SYNTHESIS OF THROUGH-BOND ENERGY TRANSFER CASSETTES AND THEIR ENCAPSULATION IN SILICA AND CALCIUM PHOSPHATE NANOPARTICLES

A DISSERTATION

by

JINEY JOSE

Submitted to the Office of Graduate Studies of
Texas A&M University
in partial fulfillment of the requirements for the degree of

DOCTOR OF PHILOSOPHY

December 2009

Major Subject: Chemistry

SYNTHESIS OF THROUGH-BOND ENERGY TRANSFER CASSETTES AND THEIR ENCAPSULATION IN SILICA AND CALCIUM PHOSPHATE NANOPARTICLES

A Dissertation

by

JINEY JOSE

Submitted to the Office of Graduate Studies of
Texas A&M University
in partial fulfillment of the requirements for the degree of

DOCTOR OF PHILOSOPHY

Approved by:

Chair of Committee,	Kevin Burgess
Committee Members,	Brian Connell
	Marcetta Y. Darensbourg
	Robert C. Burghardt
Head of Department,	David H. Russell

December 2009

Major Subject: Chemistry

ABSTRACT

Synthesis of Through-bond Energy Transfer Cassettes and Their Encapsulation in Silica and Calcium Phosphate Nanoparticles.

(December 2009)

Jiney Jose, B.S., U.I.C.T, Mumbai, India; M.S., Texas A&M University.

Chair of Advisory Committee: Dr. Kevin Burgess

Water-soluble fluorescent probes with emission in the 600-800 nm region have significant potential in biological applications such as cell imaging. Most fluorescent probes however suffer from limited fluorescence brightness in aqueous media due to aggregation and self-quenching. Their photostability for an extended period of time is also a concern. One way of improving their photophysical properties is to encapsulate them in a protective matrix to form fluorescent nanoparticles.

We have synthesized a set of six through-bond energy transfer cassettes which emit in the 600-800 nm region with Fluorescein or BODIPY as donor and benzophenoxazine dye Nile Red or cyanine dye Cy5 as acceptor. Their photophysical properties in organic and aqueous media were evaluated. These cassettes were encapsulated in silica or calcium phosphate nanoparticles (20 nm in diameter) to improve their solubility, brightness, and photostability in aqueous media. We also synthesized some water-soluble benzophenoxazine based fluorophores and the impact of different water-soluble groups on their emission characteristics in aqueous media was studied. Selected fluorophores were used for *in vitro* cellular imaging studies.

ACKNOWLEDGEMENTS

I would like to thank my research advisor, Professor Kevin Burgess for providing a conducive environment for carrying out independent research. Many thanks for his support, patience and help with all my projects. I am grateful for his enthusiasm for all of my research projects. I thank Professors Marcetta Y. Darensbourg, Brian Connell, and Robert C. Burghardt for serving on my graduate advisory committee. I really appreciate them for finding time to serve on my committee and also for their timely advice. Thanks to Jill Powers, Sandy Manning, Lauren Kulpa, Angie Medina, Angela Jade, and Whitney Ajie for assistance with office related work.

Thanks to Dr. Yuichiro Ueno for all his valuable advice and help with my projects. Thanks to Dr. Aurore Loudet for biological studies of my compounds. Thanks to Dr. Amber Schaefer for reading and correcting the dissertation. Thanks to Dr. Liangxing Wu, Dr. Jing Liu, Dr. Rakeshwar Bandicchor, Dr. Arjun Raghuraman, Dr. Andrey Malakhov, Dr. Junyan Han, and Cliferson Thivierge for their help and friendship. Thanks to Hansoo Kim and Tarun Bansal for help with nanoparticle imaging and cell imaging studies. Many thanks to Dr. Steve Silber, Dr. Sarathy, and Dr. Bhakmutov for assistance with NMR. Thanks to Lingling Li, Eunhwa Ko and Juan Castro for providing useful compounds. Thanks to everyone in Burgess group for their valuable friendship.

Finally I would like to thank my parents and friends for their encouragement and my wife for her patience and love. Above all thanks to dear Lord Jesus Christ for all his blessings and grace.

TABLE OF CONTENTS

LIST OF FIGURES

Page

Page

Page

Page

LIST OF TABLES

LIST OF SCHEMES

NOMENCLATURE

AFM	atomic force microscopy
BODIPY	4,4-difluoro-4-bora-3a,4a-diaza-*s*-indacene
BSA	bovine serum albumin
CH_2Cl_2	dichloromethane
CH_3CN	acetonitrile
Cy	cyanine
DIC	*N,N'*-diisopropylcarbodiimide
DMAP	4-dimethylaminopyridine
DMF	*N,N*-dimethylformamide
EDCI	1-ethyl-3-(3-dimethylaminopropyl)carbodiimide hydrochloride
ETE	energy transfer efficiency
EtOAc	ethylacetate
EtOH	ethanol
FRET	fluorescence resonance energy transfer
MeOH	methanol
NHS	*N*-hydroxysuccinimide
OLED	organic light emitting diodes
PEG	polyethylene glycol
TBAF	tetrabutylammonium fluoride
TBET	through-bond energy transfer
TEM	transmission electron microscopy
TFA	trifluoroacetic acid
THF	tetrahydrofuran

CHAPTER I

INTRODUCTION

1.1 Cell Imaging

Advances in imaging techniques have allowed researchers to gain a better understanding of the functions of cells, tissues and even individual biomolecules like proteins. Development of techniques such as laser-scanning microscopy, fluorescence resonance energy transfer (FRET), multiphoton microscopy, and epifluorescence microscopy has allowed imaging of cells at resolutions previously thought to be unattainable.[1] Observation of fluorescently labeled biomolecules in live cells can reveal their interaction with each other, which is useful in cell signaling studies and also for high throughput screening of drugs. Although a great number and range of fluorescent proteins are currently available, improving them to meet the ever-expanding needs of cell biologists is quite challenging.[2] Most fluorescent proteins emit light in the green to yellow region of the spectrum and only very few emit in the red region, which is a prerequisite for live cell imaging application. On the other hand there are numerous reports on small molecule organic fluorescent probes, which are much brighter and easy to access via chemical synthesis.[3-6] Fluorescent probes emitting in the 600-800 nm range have attracted much attention because (i) cellular auto fluorescence in this region is minimal and (ii) hemoglobin, water and lipid have minimum absorbance in this region. Fluorescence imaging is widely used in various research fields due to its fine temporal and spatial resolution and the ease of performing imaging studies with simple instruments and experimental setup.[7]

This dissertation follows the style of *The Journal of Organic Chemistry*.

The light in the near infrared region can penetrate deep inside tissues and is therefore suitable for *in vivo* imaging because light scattering by dense media is much reduced, resulting in deeper penetration of light. The signal to noise ratio is also maximized due to less auto fluorescence in this region.

Among the extensive array of fluorescent probes, which is available for cellular imaging studies, there is none that works with every cell type. The difference in membrane permeability, intracellular compartmentalization and photostability has made it difficult to extend the applications of probes from mammalian cells to plant cells, bacteria and yeast.[8] A careful examination of probe design with respect to their biocompatibility will help in development of new versatile probes, which may have broad utility. Fluorescent probes not only allow real-time monitoring of events, but also provide spatial information about the monitored event. For such studies it is often desirable to simultaneously observe several fluorescently tagged components in a biochemical mixture, *ie* multiplexing.[9] This can be achieved by exciting all the tags using the same laser source. However excitation using a single source is difficult because dyes that absorb near the excitation source will absorb more light than dyes that absorb farther away from the source. This results in diminishing emissions from the dyes excited with a single source. Combinations of dyes arranged to maximize FRET have been used to overcome this problem.[10,11] A variety of near-infrared fluorophores based on FRET have been developed, which are largely being used in detecting early cancers or inflammatory process in mouse cells.[12,13]

1.2 Fluorescence Resonance Energy Transfer (FRET)

As early as the 1920s the transfer of electronic excitation energy between well separated atoms or molecules was reported.[14] The simplest case is that of two atoms separated in space and the electronic excitation of one results in excitation of the other. This excitation could occur by emission of one photon of light by the first atom and reabsorption of this quantum by the second atom. Such transfers are rarely observed and were proven not to be the case by Cario and Franck in 1922 in their experiments on

fluorescence of atoms in vapor phase.[15] In their experiments they irradiated a mixture of mercury and thallium vapors with mercury light and obtained the emission spectra for both the atoms. Since thallium atoms do not absorb mercury light, energy transfer from excited mercury atoms can excite them. Therefore a transfer by reabsorption of light is not possible in this case. The transfer of excitation energy happens over a larger distance than observed in normal collision transfer. There are a number of other examples of such excitation transfer.

Perrin *et al.* reported the first observation of such excitation transfer in solution in 1929.[16] One example is described below. A solution containing both perylene (acceptor) and chloroanthracene (donor) in varying ratio was prepared. A decrease in chloroanthracene fluorescence was observed when both components were at the same concentration, which means a definite transfer of excitation energy is taking place between the donor and acceptor molecule. The transfer occurs over the mean intermolecular distances between the donor and acceptor. This excitation transfer is independent of both the volume of solution and viscosity of the solvent and is characterized by a decrease in donor fluorescence lifetime.

The mechanism of excited energy transfer can be explained with the help of Figure (1.1) where during the absorption process, the donor is excited to a higher vibrational level of its first exited state. The donor can fall to a lower vibrational level of the same excited state by a non-radiative transition. During the deactivation process when the donor returns to the ground state, it is possible that the energy of deactivation may exactly coincide with possible absorption transition in an acceptor molecule that is in the vicinity of the deactivated donor molecule. With sufficient energetic coupling an excitation energy transfer between the donor and the acceptor molecule takes place. This type of energy transfer is referred to as “resonance transfer”.[17,18] The energy transfer takes place before emission from the donor molecule takes place and requires coupling between the electronic systems of both donor and acceptor. This limits the distance over which such

an energy transfer can occur. There is also literature precedent, which shows such energy transfer occurring between electronic systems of the same molecule.

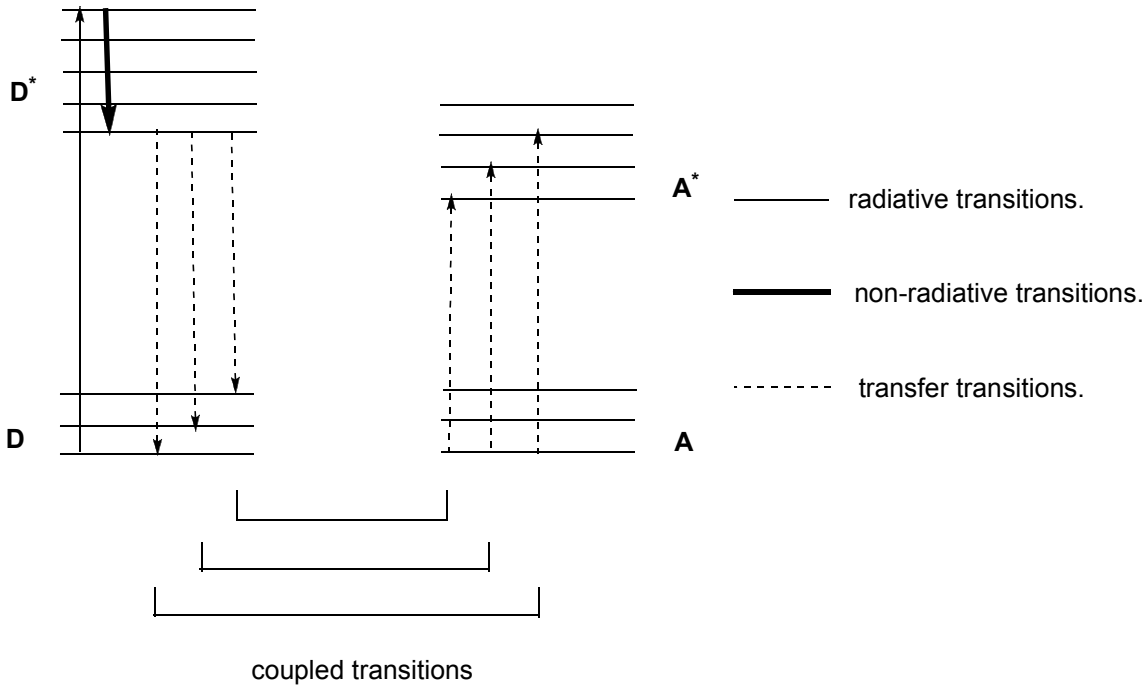

Figure 1.1. Simplified energy level diagram of energy transfer between a donor (D) and an acceptor (A).

This kind of excitation transfer process, when applied to fluorescent molecules can be defined as exciting a fluorescent molecule which is in proximity to a second fluorophore, resulting in emission occurring from the second fluorophore with minimal or almost no fluorescence seen from the excited molecule. This phenomenon is termed as Fluorescence Resonance Energy Transfer (FRET). For FRET to occur the distance between both fluorophores should be less than 10 nm. FRET was first reported by Professor Theodor Förster in 1946.[19] The excited fluorophore can be termed as a donor and the molecule emitting light can be termed as an acceptor. The energy transfer which takes place between the donor and acceptor which is separated by a distance *r*, is given by:

$$K_T(r) = Q_D\kappa^2/\tau_D\, r^6\, (9000(\ln 10)/128\pi^5 N\eta^4)_0\int^{\infty} F_D(\lambda)\varepsilon_A(\lambda)\lambda^4 d\lambda \quad \text{.....(1)}$$

Where Q_D = quantum yield of donor in the absence of the acceptor κ^2 = orientation factor (range from 0 to 4, usually assumed to be 0.67 for dynamic random averaging). κ^2 = 4 if the transition dipoles of the donor and acceptor are perfectly parallel and 0 when they are orthogonal. τ_D = lifetime of donor in the absence of the acceptor. N = 6.02 x 10^{23}. η = refractive index of the medium (usually assumed to be 1.4 for biomolecules in aqueous solution). The rate of energy transfer is inversely proportional to the sixth power of the distance, r, between the donor and the acceptor. The overlap integral J (λ) can be given as

$$J(\lambda) = \int_0^\infty F_D(\lambda)\varepsilon_A(\lambda)\lambda^4 d\lambda \quad \text{.....(2)}$$

The extent of overlap between the emission spectrum of the donor and the absorbtion spectrum of the acceptor is given by above equation. $F_D(\lambda)$ is the normalized emission spectrum of the donor. $\varepsilon_A(\lambda)$ is the extinction coefficient of the acceptor at wavelength λ.

The Förster radius, R_o, is the distance r, at which the rate of energy transfer is equal to the rate of decay of the donor ($1/\tau_D$) in the absence of the acceptor. R_o is the distance at which FRET is 50 % efficient. At $r = R_o$, $K_T = (1/\tau_D)$. Equation 1 can be written as

$$R_o = (9000(\ln 10)\, Q_D\kappa^2/128\pi^5 N\eta^4) \int_0^\infty F_D(\lambda)\varepsilon_A(\lambda)\lambda^4 d\lambda \quad \text{.....……..(3)}$$

R_o is typically in the range of 20 to 60 A^o for organic fluorophores.

Knowing R_o, one can calculate the ET rate by:

$$k_T = \frac{1}{\tau_D}\left(\frac{R_o}{r}\right)^6 \quad \text{……(4)}$$

The efficiency of energy transfer, E, is the fraction of photons absorbed by the donor that are transformed to the acceptor. E is given by

$$E = \frac{k_T}{\tau_D^{-1} + k_T} \quad \text{……...(5)}$$

this is the ratio of the energy transfer rate to the total decay rate of the donor.

The efficiency of energy transfer can be calculated from the emission intensity of the donor in the absence and presence of the acceptor.[20]

In order for FRET to occur overlap of emission of the donor fragment with the absorbtion of the acceptor is essential. This is a constraint, which limits the combination of dyes that can be used for multiplexing.

1.3 Through Bond Energy Transfer

Through-bond energy transfer systems consist of a donor and acceptor part connected via a conjugate linker that does not allow them to be planar. This nonplanar geometry allows rapid energy transfer from the donor to the acceptor part. Through-bond energy transfer is mechanistically different from Förster basis for FRET, which requires overlap of emission of the donor fragment with the absorbtion of the acceptor. There are two mechanisms proposed for the observed energy transfer. Dexter[21] and superexchange energy transfer.[22] As compared to Förster energy transfer, Dexter energy transfer is a short range phenomenon and requires the interaction between an excited donor orbital with an orbital of the acceptor in the ground state. Superexchange energy transfer can take place over a longer distance since energy is relayed through bonds connecting the donor and the acceptor (Figure 1.2).

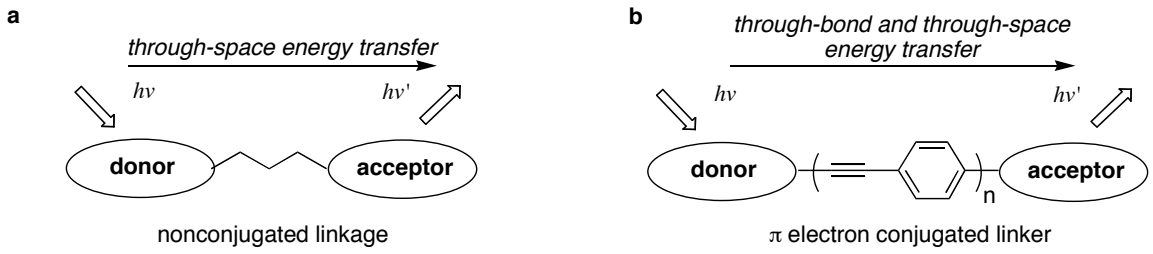

Figure 1.2. Concept of (**a**) through-space and (**b**) through-bond energy transfer.

Thus appropriately designed through-bond energy transfer cassettes could absorb photons via a donor part and transfer the energy rapidly through the conjugated linker to the acceptor fragment that emits at a longer wavelength. There is no known constraint on the difference between the donor absorbtion and acceptor emission wavelength in this scheme since no overlap is required for energy transfer to occur. Thus it is possible to design dyes that can absorb strongly at short wavelengths and emit brightly at longer

wavelengths. When the fluorescence Stokes' shift (the wavelength separation between absorption and fluorescence maxima) is small, which is usually the case in most organic fluorophores, it is difficult to maximize the excitation and detection of fluorophore and at the same time isolate the fluorescence signal from scattered excitation light. This problem can be completely overcome in through-bond energy transfer cassettes because the donor absorbtion wavelength is far apart from the acceptor emission wavelength. In summary, through bond energy transfer cassettes have the potential to increase the resolution and fluorescence intensities obtained from several probes excited by a laser source operating at a single wavelength.

Our group has expertise in designing such through-bond energy transfer cassettes.[23-28] Previous members have designed four energy transfer cassettes as shown in Figure 1.3 and studied their photophysical properties (Figure 1.4).[29] Excitation of these cassettes at 488 nm produces fluorescence characteristic of only the acceptor component, which proves 100 % energy transfer efficiency between the donor and the acceptor. The fluorescence intensities of **1-4** when excited at the donor component were compared to emission of molecule that resembles only the acceptor part. Cassettes were shown to fluoresce more brightly than the acceptor proving efficient energy transfer.

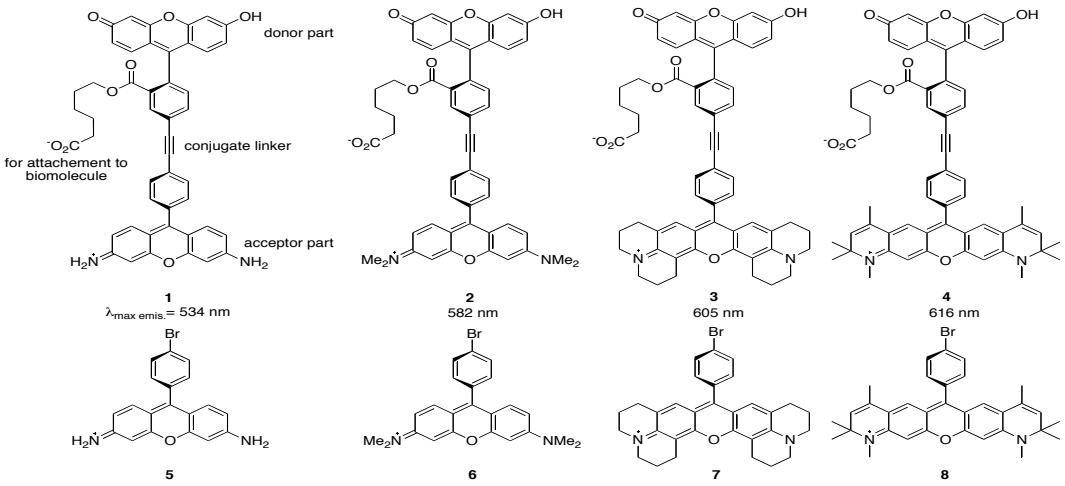

Figure 1.3. Through-bond energy transfer cassettes and acceptors synthesized by our group.

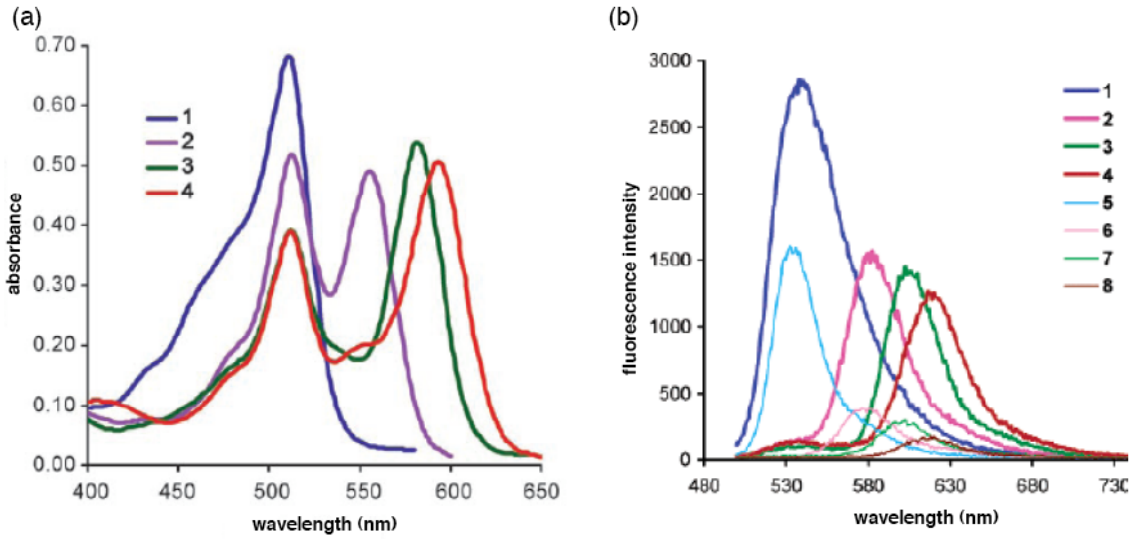

Figure 1.4. (**a**) absorbance of cassettes 1-4 in EtOH and (**b**) Fluorescence of equimolar EtOH solutions of 1-8 excited at 488 nm.

For the above-mentioned cassettes to be useful in cellular imaging, they should be soluble in aqueous media. To enhance their water solubility either the donor or acceptor should have water-soluble functional groups. Our group recently published a water-soluble through-bond energy transfer cassette, which showed approximately 80 % energy transfer in aqueous media.[30] This cassette was successfully used for intracellular imaging studies of COS-7 cells.

Our work with benzophenoxazine dyes showed that their water-soluble variant fluoresces in the 600-700 nm region with good quantum yields.[31,32] This property makes them useful as an acceptor fragment for synthesis of water-soluble cassettes. In chapter two we will explain the synthesis of water-soluble analogues of benzophenoxazine dyes. The effect of different water-soluble groups on the photophysical properties of these dyes, particularly on quantum yield, was evaluated. The synthesis and photophysical properties of cassettes based on water-soluble benzophenoxazine dyes are discussed in Chapter III.

1.4 Fluorescent Nanoparticles

With the advent of cellular imaging technologies, the need for brighter and near infrared fluorophores has increased.[2] Organic fluorophores can be synthetically fine tuned to emit in the near infrared region with sufficient water-solubility. There are few literature reports on water-soluble bright fluorophores and their brightness is heavily dependent on the surrounding media.[31,33,34] Cellular imaging studies are done at physiological pH and most organic fluorophores fluoresce with reduced efficiency in the cellular environment, mainly due to aggregation and quenching by cellular entities.[33] More demanding biological applications such as single molecule detection and studying protein-protein interaction puts restrictions on the extent to which organic fluorophores can be used. One of the most significant drawbacks is their low photostabilities in aqueous media, which makes detection of signal over extended periods of time difficult.[35]

Semiconductor quantum dots discovered by Louis E. Brus at Bell Labs, proved to be a very good alternative to organic fluorophores due to their extreme brightness and size dependent emission characteristics.[36] Quantum dots are 20 times brighter and 100 times more photostable than organic fluorophores and have a particle size range between 20-100 nm. It's emission is dependent on particle size with large nanoparticles emitting in the near IR region of the spectra. Most quantum dots are synthesized from heavy metals like cadmium and selenide and therefore suffer from cytotoxicity issues.[37-39] It is insoluble in water and must be coated with a polymer to make them water-soluble before introducing into cells, which increases their hydrodynamic radius. Recently cadmium-free quantum dots were reported but their cytotoxicity has yet to be completely evaluated.[40] Under cellular imaging conditions cadmium leaches out from the quantum dots, because the energy of UV irradiation is sufficient to break the covalent chemical bond of cadmium selenide. It also suffer from "blinking" which is the dark state of these particles and is a drawback for single molecule tracking studies.

Weisner *et al* has published extensively on fluorescent silica nanoparticles, which involves encapsulations of organic fluorophores in silica.[41,42] The particle size of silica nanoparticles fall in the sub 50 nm region and are therefore useful for cellular imaging studies. Silica is chemically stable and protects the encapsulated dye molecules from the external environment. These nanoparticles are 20 times brighter than the constituent dye itself.[42] The photostability of the encapsulated dye is shown to improve dramatically compared to the dye itself. Their small size makes them dispersible in aqueous media and they remain stable without aggregation for months. The silica surface is easily functionalizable and therefore such surface modified silica nanoparticles can be used for attachment to biomolecules.[43] The silica nanoparticles are nontoxic at biologically relevant concentrations and can be used in a broad range of imaging applications such as visualization of capillaries and macrophages, and real time imaging of tumor metastasis.[44] When used at concentration less than or equal to 0.1 mg/mL no cell death was reported over a period of 8 h.[45] We have tried to encapsulate some of our through-bond energy transfer cassettes in silica, which will be discussed in part one of Chapter IV.

Calcium phosphate nanoparticles is another interesting and simpler method to encapsulate organic fluorophores to enhance their photophysical properties in aqueous media.[46] Like silica, calcium phosphate shields the encapsulated dye from the external environment and therefore enhances their photophysical properties. These are 15-25 nm particles and are therefore optimal for cellular imaging studies. The surface of these nanoparticles can be decorated with carboxylic acid groups by which they can be attached to biomolecules or they can be further modified with groups such as glycols to improve their water-solubility. They are stable for months at physiological pH and only dissolve below pH 5.5.[47] This property makes it useful in delivering cargoes like therapeutic agents for treatment of various diseases like cancer, wherein controlled release of the drug at the specific target is important for efficient diagnosis and treatment. Calcium phosphate is bioresorbable and calcium is the most abundant metal

found in the human body. There is no reported cell cytotoxicity of calcium phosphate nanoparticles and therefore it is easy to work with. Calcium phosphate nanoparticles present an attractive tool for diagnostic imaging for both *in vivo* and *in vitro* studies. A detailed study of these particles with respect to encapsulating hydrophobic cassettes is illustrated in part two of Chapter IV.

CHAPTER II

SYNTHESIS OF WATER-SOLUBLE FLUORESCENT PROBES

2.1 Introduction

There are many application of fluorescent probes as a suitable diagnostic and imaging agent. Therefore the demand for probes that can perform imaging has also increased. These probes are mainly used as markers for cell organelles and also for conjugation to protein molecules for protein-protein interaction studies which requires them to be inherently water-soluble. A vast majority of fluorescent probes reported in the literature are only sparingly soluble in aqueous media, which reduces their fluorescence output in a cellular environment. In recent years a number of water-soluble fluorescent probes have been reported and their application for cellular imaging studies evaluated.[48-50] The presence of different water-soluble groups improves fluorescence output of these probes in aqueous media by preventing aggregation induced quenching. Much of these studies are carried out on rhodamines,[51] cyanines,[52] and BODIPY[53] derivatives. There exists an opportunity to extent these studies to other family of fluorescent probes such as benzophenoxazines, perylenes, and squarines which are traditionally used as functional materials such as organic light emitting diodes (OLED).[54] Here in we describe our efforts towards synthesized water-soluble benzophenoxazine derivatives for cellular imaging studies.

2.2 Benzophenoxazine Derivatives

Benzophenoxazine dye, Nile Red is a solvatochromic dye (solvent dependent emission).[32] It is a liphophilic stain extensively used for detection of intracellular lipid droplets.[55,56] Its emission is shifted to lower wavelengths in nonpolar solvents and to higher wavelengths in polar solvents. Its emission in the 600-700 nm region makes it a useful probe for cellular imaging,[1] but it suffers from two major drawbacks; (i) it is completely insoluble in aqueous media and (ii) it is

nonfluorescent in aqueous media due to aggregation. We hypothesized that introduction of water-solubilizing groups would improve its water-solubility and fluorescence in aqueous media. There are very few reports of water-soluble benzophenoxazine dyes in the literature.[57,58] We had previously reported two water-soluble analogues which showed good quantum yields in water.[31] Herein we report the effect of different water-soluble groups on the photophysical properties of these dyes in aqueous media.

Most organic fluorescent probes are inherently flat and self organize into supramolecular clusters in aqueous media due to aggregation resulting in reduced fluorescence efficiency. Relatively low fluorescence or complete quenching of fluorescence in solutions where aggregation is predominant is due to the fact that excited energy in these systems is usually dissipated in non-radiative processes.[59,60] Photophysical properties of fluorescent probes in aqueous media are markedly different compared to that in organic media. This can be attributed to the greater difference in polarity between fluorescent probes and water. Surfactants such as the Triton® series help in reducing the polarity difference and enhancing fluorescence. A more attractive means is to synthetically incorporate groups which will make fluorescent probes intrinsically water-soluble. Water-soluble groups such as sulfonic acids and carboxylic acids are widely used for this purpose.[61,62] Carboxylic acid groups also serve as a suitable handle for attachment of fluorescent probes to various biomolecules. Other groups such as polyethylene glycols, phenols, phosphonates are also utilized to impart water-solubility.[52,63,64] Recent reports from the Romieu group have emphasized post synthetic modification of organic dyes to impart water-solubility.[33,53] This method is particularly useful for introduction of multiple sulfonic acid groups and is a viable alternative to elaborate synthetic routes most commonly used to introduce such groups. A similar strategy to introduce multiple carboxylic acids and hydroxyl groups is explored in this work.

2.2.1 Results and Discussion

2.2.1.1 Syntheses of Benzophenoxazine Dyes

The synthesis of dye **13** was started from the dicarboxylic acid derivative of 3-aminophenol, **9** (Scheme 2.1). The starting material was prepared form a previously reported procedure.[31] Esterification of compound **9**, followed by nitrosation and condensation with 1,6-dihydroxy naphthalene in the presence of a catalytic amount of hydrochloric acid yielded dye **12**. The nitroso compound was used without additional purification due to its unstable and hygroscopic nature. Alkylation of **12** followed by removal of *t*-butyl group with trifluoroacetic acid afforded **13** in 45 % yield. Surprisingly dye **1** with only one carboxylic acid was soluble in water. The diethylester groups also helps in imparting solubility to the dye. The 2-hydroxy Nile Red, with a carboxylic handle at 2- position is reported to be soluble in water but its quantum yield is not mentioned.[65]

Scheme 2.1. Synthesis of dye **13**.

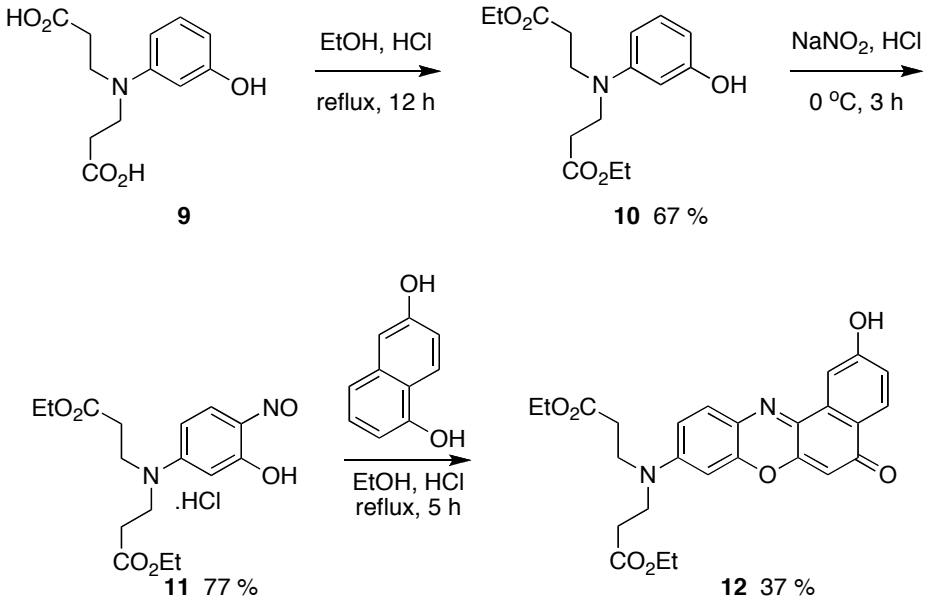

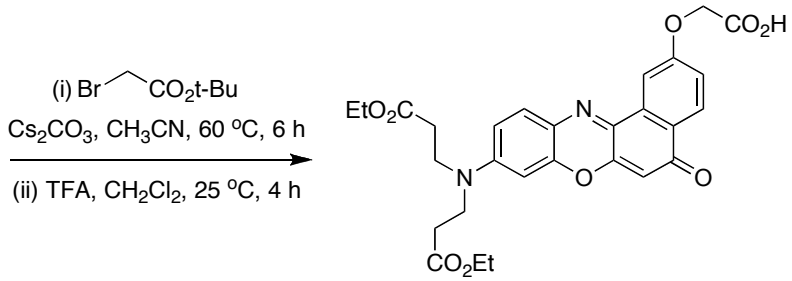

13 45 %

Sulfonic acid dye **20** (Scheme 2.2) was prepared from nitroso compound **17**.[64,66] 3-Aminophenol **14** was mono-alkylated to obtain ethyl derivative **15** in 70 % yield. Treatment of **15** with 1,3-propane sultone yielded water-soluble sulfonated aminophenol **16** in 60 % yield. Nitrosation of **16** yielded nitroso compound **17** which was used for further reaction without any purification. Purification was not attempted due to the instability of nitroso compound **17**. Reaction of **17** with 1,7- dihydroxy naphthalene in DMF at 140 °C yielded **20** in 71 % yield. A similar dye is reported in the literature but its photophysical properties in aqueous media were not measured.[57] The presence of a phenolic group and a sulfonic acid group makes dye **20** highly water-slouble.

Scheme 2.2. Synthesis of dye **20**.

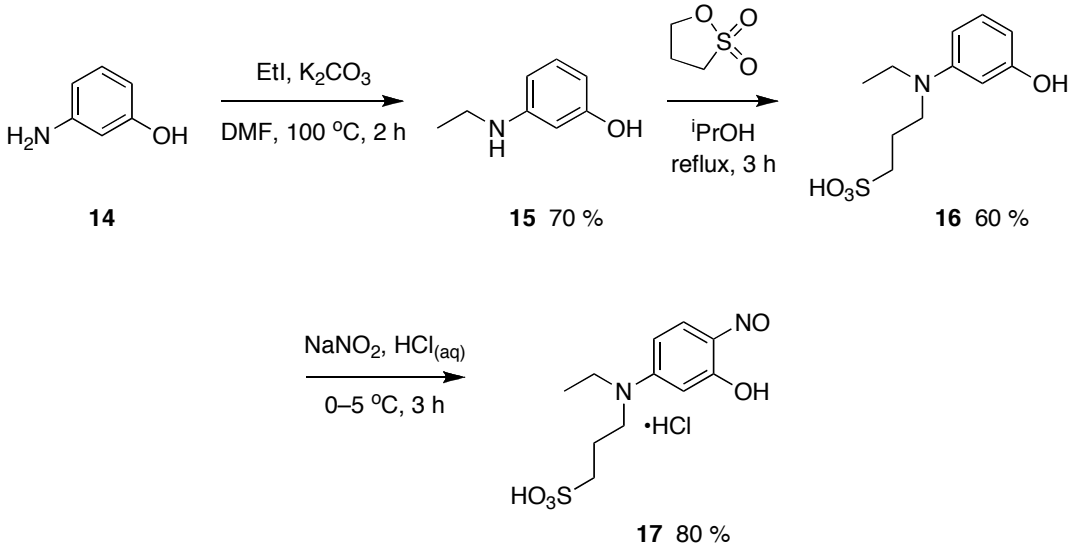

14 **15** 70 % **16** 60 %

17 80 %

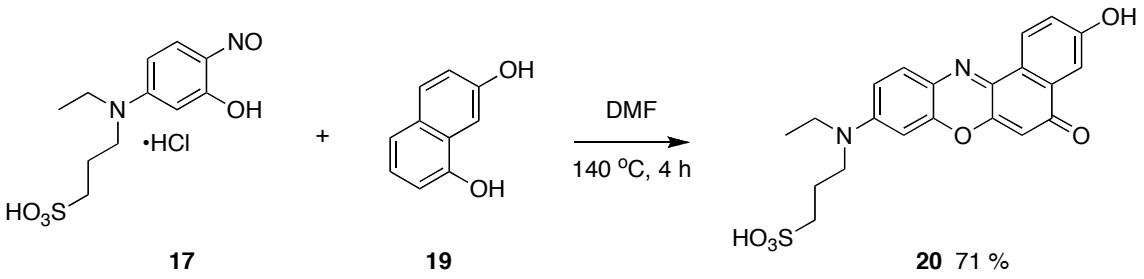

Dyes **25**, **27** and **28** incorporate water-soluble groups shown in Figure 2.1. Trizma base **21** is widely used as a buffer (pH 8.4) in immunohistochemical staining and is very soluble in water.[67] Compound **21** also acts as a useful substrate for incorporating multiple carboxylic acid groups which we assume will further improve water-solubility and serve as a handle for attachment to biomolecules. Treatment of **21** with acrylonitrile followed by acid hydrolysis yielded **22** in quantitative yield.[68] The random orientation of **21** and **22** will prevent π-stacking of dyes and help reduce aggregation in aqueous media. On the other hand, oligoethylene glycol linkers are known to improve water-solubility. Our group has expertise in synthesis of oligoethylene glycols using "click" chemistry.[69] We used a similar strategy to prepare linker **23** in gram quantities. Linker **23** was prepared by Dr. Yuichiro Yueno.

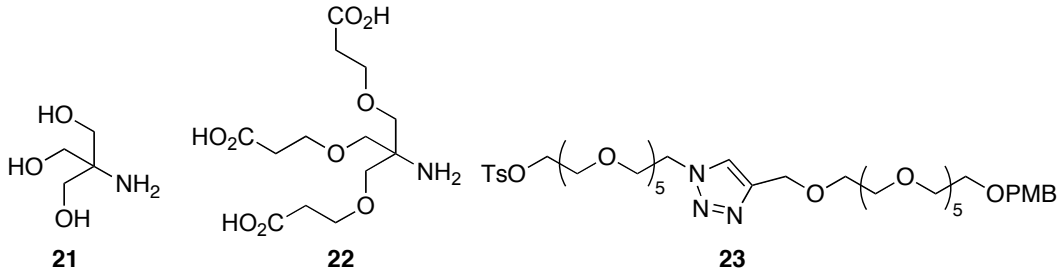

Figure 2.1. Water-soluble groups used in this study.

Scheme 2.3. Synthesis of water-soluble group **22**.

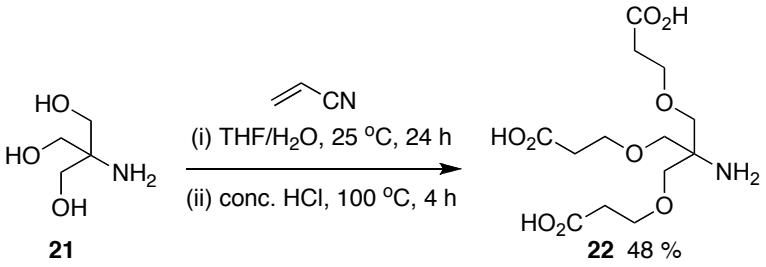

2-Hydroxy Nile Red **24**, prepared by following a reported proceudure[3] was alkylated with oligoethylene glycol linker **23** followed by removal of PMB group in TFA/CH_2Cl_2 to afford **25** in 58 % yield. We had previously reported the synthesis of water-soluble dye **26**, which has a quatum yield of 0.33 in pH 7.4 buffer. Activation of the carboxylic acids of dye **26**, followed by reaction with corresponding amines **21** and **22** yielded dyes **27** and **28** in 59 and 28 % yield respectively. A longer reaction time was required for synthesis of dye **28** and we attribute this to the steric bulk of the water-soluble group **22**. Both dyes **27** and **28** were purified on medium pressure liquid chromatography using reverse phase C-18 column and CH_3CN/H_2O as eluent.

Scheme 2.4. Synthesis of dye **25**.

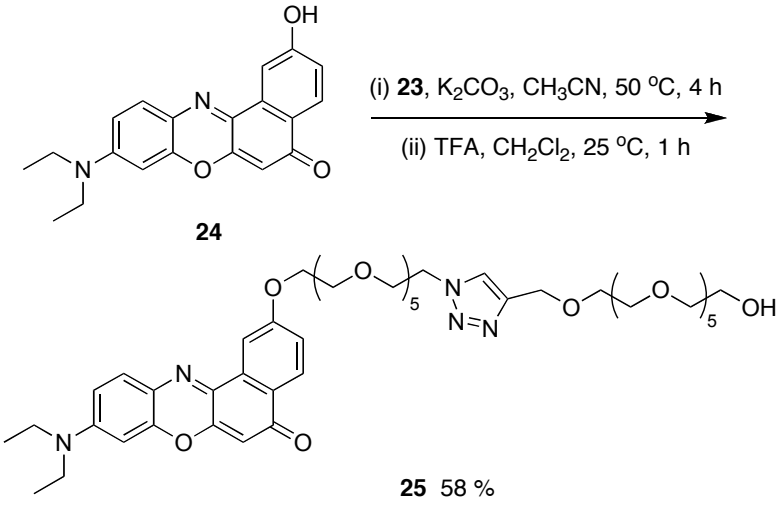

Scheme 2.5. Synthesis of dye **27** and **28**.

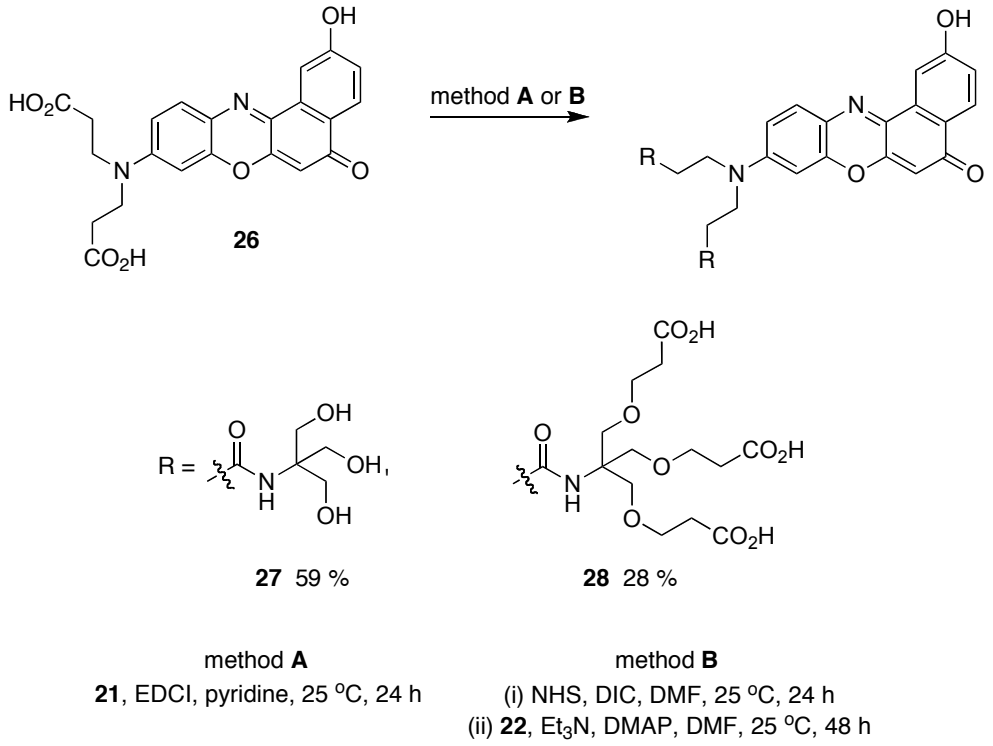

2.2.1.2 Photophysical Properties of Benzophenoxazine Dyes

All dyes showed good solubility in water, pH 7.4 phosphate buffer and EtOH. The abosrbance and fluorescence spectra of all dyes in EtOH and pH 7.4 phosphate buffer are shown in Figure 2.2 and Figure 2.3 respectively. Absorbance and fluorescence is red shifted by a value of 20-30 nm in pH 7.4 compared to their corresponding values in EtOH. This red shift is primarily due to the solvatochromic nature of benzophenoxazine dyes. The Stokes' shift of these dyes, the difference in wavelength (nm) between the absorbtion and emission maxima in pH 7.4 and EtOH varies between 78-99 nm. The large stoke shift makes it possible to excite these dyes at a lower wavelength and obtain fluorescence output at a higher wavelength which can be readily distinguished from the light source used to excite the dye. Most fluorophores have small Stokes' shifts and it is often difficult to avoid the mutual inteference between the excitation and emission wavelength. This draw back reduces

the sensitivity of such fluorophores in bioimaging studies. Benzophenoxazine dyes such as the ones synthesized, with large Stokes' shifts can be used to overcome these drawbacks.

Among the water-soluble groups used, carboxylic acid shows a greater effect on quantum yields than sulfonic acid and oligoethylene glycol linker (Table 2.2) in pH 7.4 and also in EtOH (Table 2.1). The carboxylic acid dye **13** has a quantum yield of 0.33 as compared to sulfonic acid dye **20**, which has a quantum yield of 0.17. The quantum yields of these dyes in EtOH varied from 0.47-0.73. The quantum yields obtained for dyes in pH 7.4 shows a significant improvement compared to 2-hydroxy Nile Red dye **24** which is almost non-fluorescent in pH 7.4. The different water-soluble groups used have a positive influence on the solubility and quantum yield of dyes in aqueous media, but to different extents. Groups such as carboxylic acids, which tend to disrupt the planarity of the dye molecules thereby preventing pi stacking seem to improve photophysical properties to a greater extent in aqueous media. Twisted intramolecular charge transfer[70] which is prominent in benzophenoxazine dyes tends to be lower in aqueous media due to H-bonding of water with the lone pair of electrons on nitrogen. This can only be prevented if the dye is completely isolated from water by casting them in a rigid matrix like silica.[71] Efforts in this direction will be an alternative means to improve their photophysical properties. The full width at half maxima values, which is a measure of aggregation is in fact lower in pH 7.4 (Table 2.2) for all dyes compared to their value in EtOH (Table 2.1). This reflects their reduced tendency to aggregate in aqueous media.

a

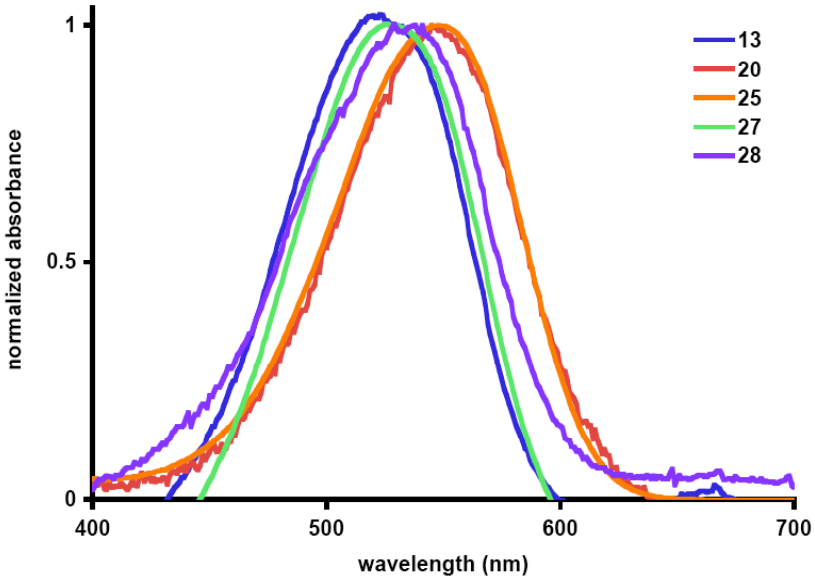

b

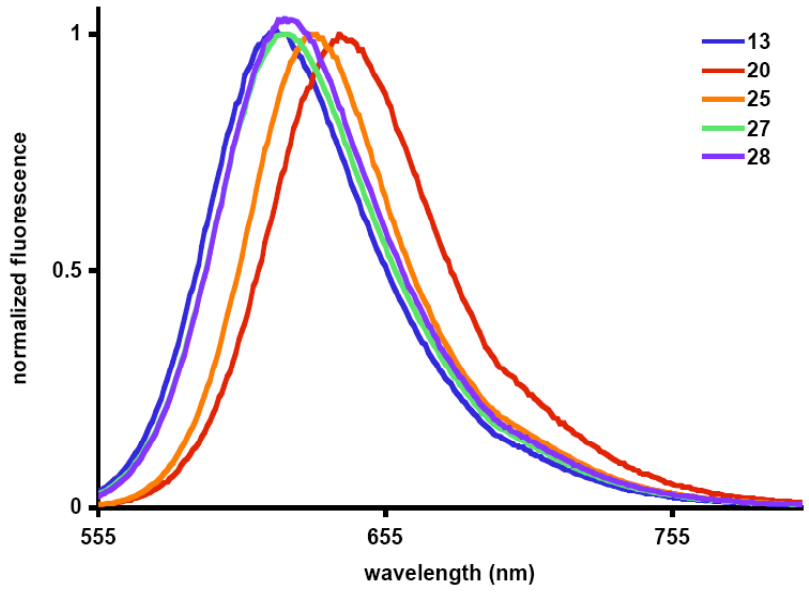

Figure 2.2. Normalized UV absorption and fluorescence emission spectra of dyes in EtOH. Concentration for absorption measurement: 10^{-6} M; concentration for fluorescence measurement: 10^{-7} M.

a

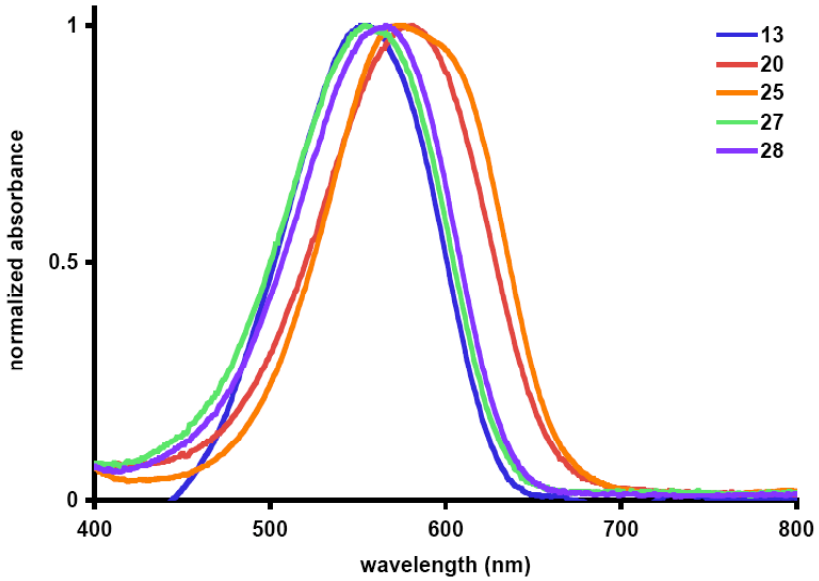

b

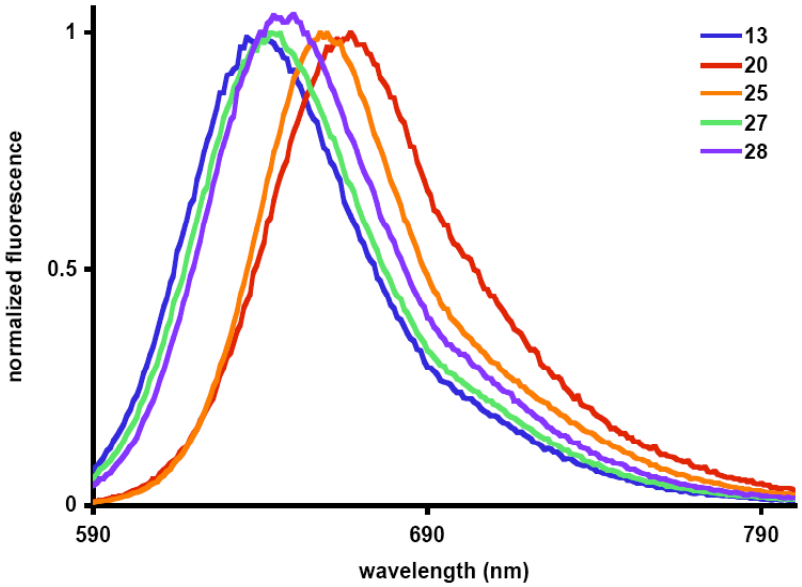

Figure 2.3. Normalized UV absorption and fluorescence emission spectra of dyes in pH 7.4 (0.1 M sodium phosphate buffer). Concentration for absorption measurement: 10^{-6} M; concentration for fluorescence measurement: 10^{-7} M.

TABLE 2.1. Spectroscopic properties of dyes in EtOH.

dye	λ_{abs} (nm)	ε ($M^{-1}cm^{-1}$)	$\lambda_{em.}$ (nm)	fwhm (nm)	Φ[a]
13	522	15400	621	65	0.73
20	545	16200	639	66	0.60
25	548	11740	631	60	0.48
27	530	9900	620	65	0.47
28	544	10200	622	67	0.63

[a] Standard used for quantum yield measurement: rhodamine 6G in EtOH (Φ : 0.94), quantum yield and extinction coefficients (at 10^{-6} M) were repeated three times.

TABLE 2.2. Spectroscopic properties of dyes in pH 7.4.

dye	λ_{abs} (nm)	ε ($M^{-1}cm^{-1}$)	$\lambda_{em.}$ (nm)	fwhm (nm)	Φ
13	554	14300	640	60	0.33[a]
20	581	15200	667	65	0.17[b]
25	572	15250	658	53	0.26[a]
27	554	7900	643	60	0.32[a]
28	566	8300	654	63	0.28[a]

Standard used for quantum yield measurement: [a]rhodamine 101 in EtOH (Φ : 1.0), [b]sulforhodamine in EtOH (Φ : 1.0), quantum yield and extinction coefficients (at 10^{-6} M) were repeated three times.

2.2.1.3 Cellular Imaging Studies using Benzophenoxazine Dyes

The subcellular localization of the Nile Red derivatives was studied in Clone 9 cells. When the cells were incubated with the hydrophobic 2-hydroxy Nile Red **24**, no specific labeling was observed and both the mitochondria and the golgi were labeled (Figure 2.4a). On the other hand, Nile Red derivatives **25** and **27** targeted different organelles (Figure 2.4b and 2.4c). Compound **25** specifically stained the mitochondria, while probe **27** accumulated in the golgi. The localization of **27** in the golgi was confirmed by comparing the staining pattern of **27** to the one of BODIPY TR ceramide complexed to BSA, a marker for golgi. Nile Red derivatives **13**, **20** and **28** did not enter the cells under normal conditions. This is probably because they are negatively charged. In an attempt to import those dyes inside the cells, **28** was mixed with Pep-1 (1:3 mol ratio) and the cells incubated with this complex. After 30 min incubation at 37 °C, the probe could be observed inside the cells, but was sequestered in lysozomes (Figure 2.4d). Dr. Aurore Loudet performed cellular imaging studies.

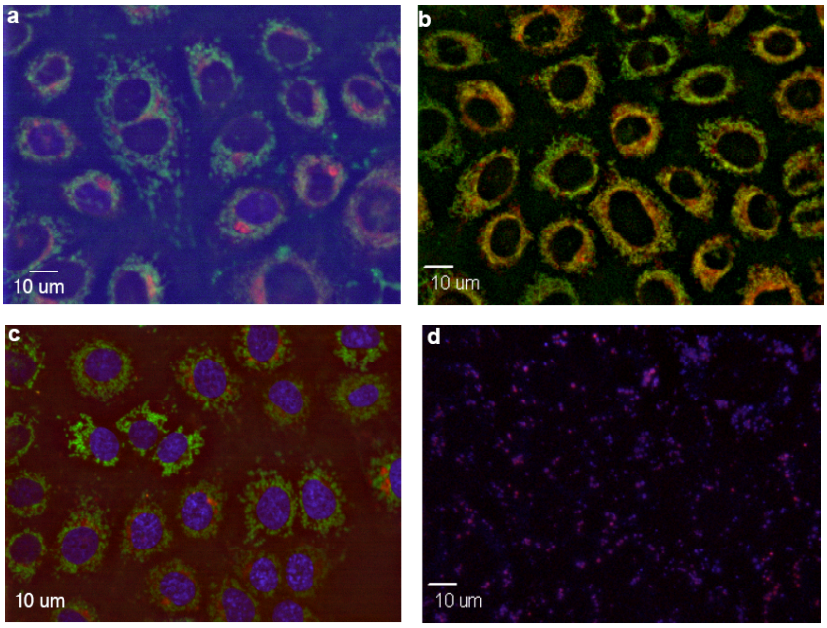

Figure 2.4. Images of Clone 9 cells treated with (**a**) 2-hydroxy Nile Red **24** (**b**) dye **25** (**c**) dye **27** and (**d**) dye **28**.

2.2.2 Conclusion

In conclusion we have prepared five water-soluble dyes with good quantum yields to study the effect of different water-soluble groups on their photophysical properties in aqueous media. The yields of these dyes were moderate to good and can be easily reproduced. In some cases the syntheses can be scaled up to gram quantities without much synthetic effort. These water-soluble dyes can be readily purified on a reverse phase column without significant loss in yield. Photophysical properties do not seem to vary much with different water-soluble groups even though carboxylic acids seem to improve quantum yields better than sulfonic acids. This is due to the ability of such groups to disrupt π stacking in aqueous media. The large Stokes' shift of the water-soluble dyes compared to commercially available dyes makes them useful in applications such as *in vitro* imaging studies. Selected dyes **25** and **27** specifically stained the mitochondria and the golgi apparatus respectively proving their applicability for bioimaging studies.

2.3 Water-soluble Nile Blue Derivatives

Nile Blue, **29** (Figure 2.5), is a fluorescent probe that has been known for over 110 years.[32,72] In polar media its absorption and emission maxima shift to the red, indicative of stabilized charge separation in the excited state; consequently, this dye has been used to monitor events that depend upon solvent polarity.[73-75] It has also been used for fluorescence resonance energy transfer (FRET) studies.[76,77] Nile Blue tends to have a higher affinity for cancerous cells than healthy ones,[78] and it is a photosensitizer for oxygen;[79,80] these two properties together can be useful in photodynamic therapy.[81] However, two properties of Nile Blue *in aqueous media* are limiting for many applications, specifically: (i) low solubility; and, (ii) low quantum yield.

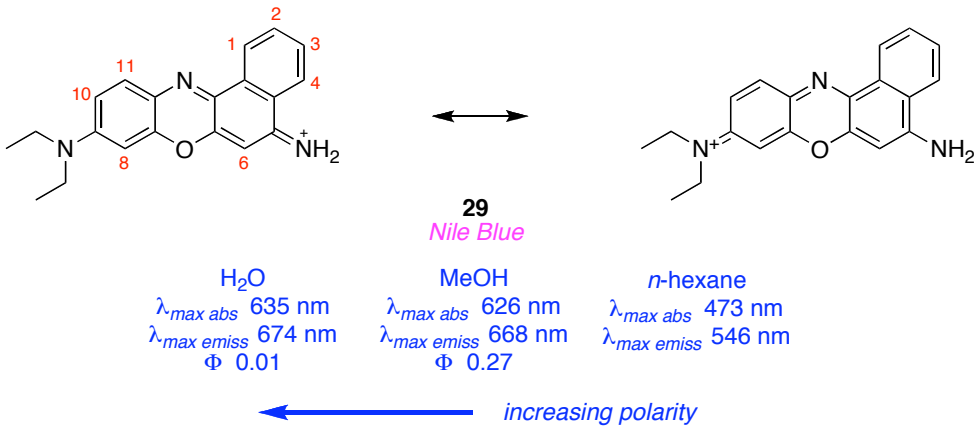

Figure 2.5. Photophysical properties of Nile Blue **29** in different solvents.

Some work has been published on Nile Blue derivatives with improved water solubilities.[82-85] Aggregation of inherently flat, lipophilic aromatic dyes is disfavored when they are functionalized with water-soluble substituents, and their quantum yields can improve as a result. Consequently, Nile Blue derivatives bearing hydrophilic groups can have improved solubilities *and* fluorescence outputs. Probes **30** and **31** are the most interesting probes to arise from these studies (Figure 2.6).[82] Their quantum efficiencies are improved by as much as a factor of ten. However, they have no carboxylic acid handle for attachment to biomolecules, and the sharpness of their emissions broaden as the solvent is changed from methanol to water, perhaps indicative of aggregation. Other work involves incorporation of groups that offer only incrementally enhanced water solubilities,[83] lack of quantum yield data,[84] and/or no experimental procedures for the syntheses.[84,85]

a

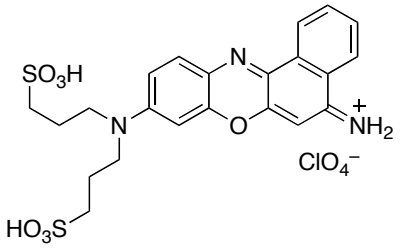

30
pH 7.4, Φ 0.10
$\lambda_{max\ abs}$ 633 nm
$\lambda_{max\ emiss}$ 675 nm

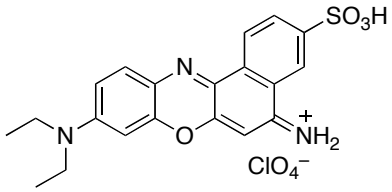

31
pH 7.4, Φ 0.03
$\lambda_{max\ abs}$ 637 nm
$\lambda_{max\ emiss}$ 677 nm

b

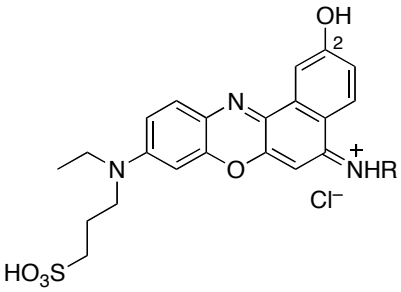

32

this work

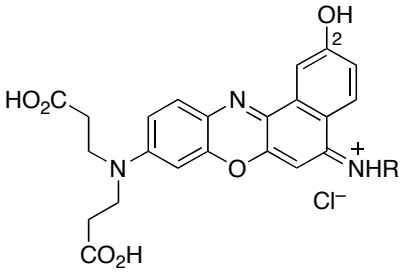

33

R = 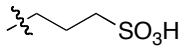 **a**

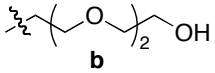 **b**

Figure 2.6. (**a**) Reported water-soluble Nile Blue derivatives **30** and **31** and (**b**) Nile Blue derivatives synthesized in this work **32** and **33**.

This work reports the syntheses of the 2-hydroxy Nile Blue derivatives **32** and **33**, and compares their fluorescence properties with those of **30** and **31**. For both probes, the 2-hydroxy substituent was incorporated to enhance water solubility, and the other hydrophilic groups are situated on both ends of the molecule to reduce the potential for aggregation. Not all possible applications of these dyes require functional groups for attachment to biomolecules, but many do, and compounds **33a** and **33b** were designed for that purpose.

2.3.1 Results and Discussion

2.3.1.2 Synthesis of Nile Blue Derivatives (32 and 33)

The western part of targets **32** and **33** were formed from functionalized nitrosophenols; these were prepared as outlined in Scheme 2.2 (compound 17) and Scheme 2.6 (compound 34). Nitroso compound **34** was formed via nitrosylation of phenol **9**, a starting material previously used in these laboratories for syntheses of Nile Red derivatives.[86] Both the aminonaphthol components **36** required for the eastern half of these molecules were made via alkylation reactions. Compound **36a** was obtained via alkylation with propane sultone (Scheme 2.7a). The triethylene glycol derivative **37** was conveniently made in a few steps from the parent diol, then this was used to *N*-alkylate 5-amino-2-naphthol as shown (Scheme 2.7b).[87-89]

Scheme 2.6. Synthesis of nitroso aminophenols.

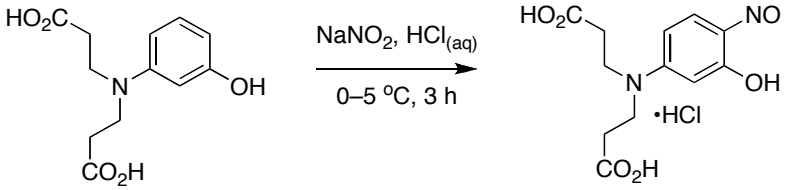

9 **34** 77 %

Scheme 2.7. Synthesis of water-soluble aminonaphthol components (**a**) and (**b**)

a

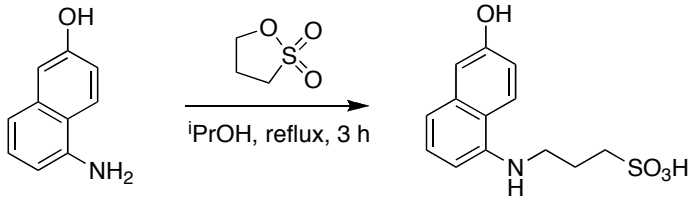

35 **36a** 33 %

b

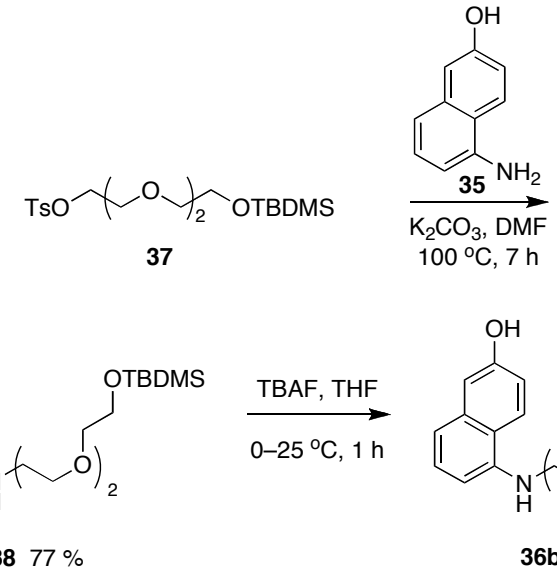

Previous syntheses of Nile Blue derivatives required relatively high temperatures and/or strong acids. Compounds **32** and **33** were made via condensation at a relatively low temperature (90 °C) without addition of any additional acids. The blue products were isolated via MPLC on a reverse phase C18 column (Scheme 2.8).

Scheme 2.8. Synthesis of water-soluble Nile Blue derivatives (**a**) without carboxylic acid handle and (**b**) with carboxylic acid handle.

a

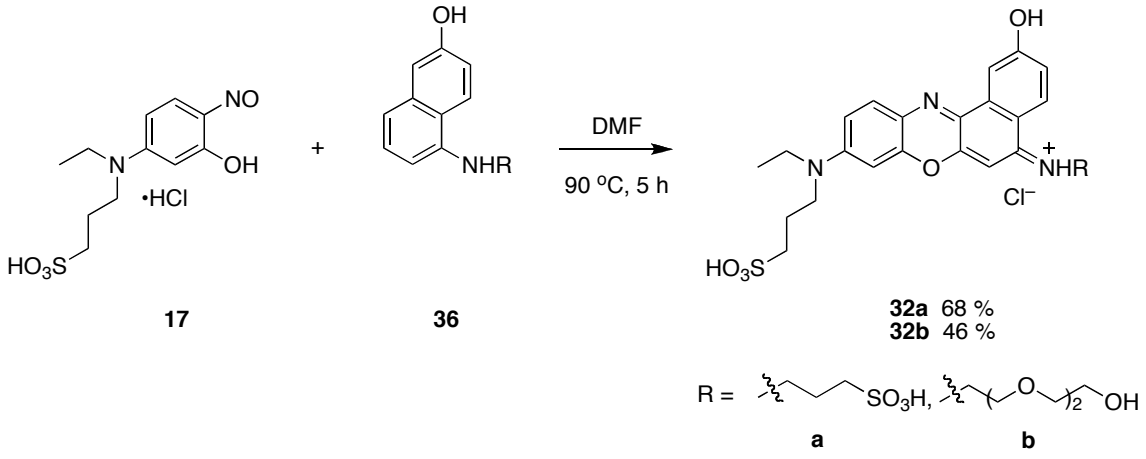

b

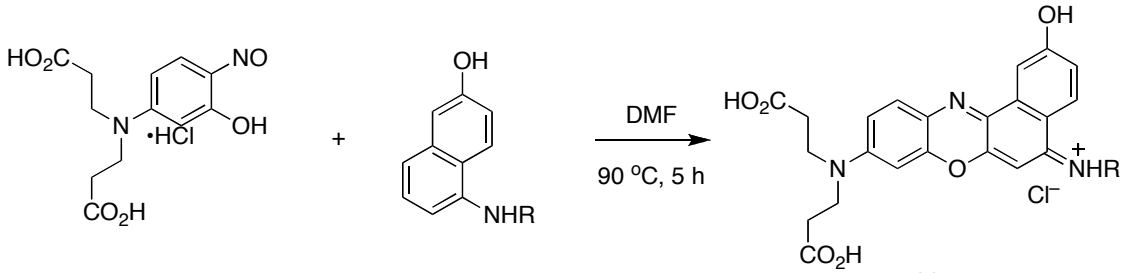

2.3.1.2 Photophysical Properties of Nile Blue Derivatives

Electronic spectra (Figure 2.7) of the dyes were recorded in methanol, as a representative polar organic solvent, in 0.1 M phosphate buffer at pH 7.4 (PB, Table 2.3), in the same buffer but with 3 % Triton X-100 (TX), and in 0.1 M pH 9 borate buffer (BB). Only **32a** and **33a** were soluble in MeOH; data for **32b** and **33b** could not be obtained in this medium. The effects of adding Triton X-100 to the medium are ambiguous; this reagent changes the solvent polarity, but also might prevent aggregation effects.[74,90,91] In borate buffer at pH 9.0 the phenolic hydroxyl of the dyes will be predominantly in the anionic form. The quantum yields of the dyes are much lower in pH 9 borate buffer compared to the ones in pH 7.4 phosphate buffer. This reduced quantum yield at higher pH can be attributed to the instability of the dyes in basic environment.

TABLE 2.3. Spectroscopic properties of the Nile Blue derivatives in different solvents.

dye	λ_{abs} (nm)	ε ($M^{-1}cm^{-1}$)	$\lambda_{em.}$ (nm)	fwhm (nm)	Φ[a]	solvent
32a	628	14400	662	47	0.56	MeOH
32a	630	42400	671	52	0.14	PB[b]
32a	631	51200	669	49	0.24	TX[c]
32a	630	28400	670	56	0.02	BB[d]
33a	629	58800	666	50	0.32	MeOH
33a	630	30300	670	58	0.10	PB[b]
33a	629	64100	669	56	0.11	TX[c]
33a	631	34500	670	73	0.02	BB[d]
32b	629	33600	671	55	0.14	PB[b]
32b	628	44400	670	47	0.23	TX[c]
32b	630	21800	672	51	0.13	BB[d]
33b	632	38100	673	56	0.13	PB[b]
33b	631	14700	672	54	0.26	TX[c]
33b	630	38000	670	54	0.08	BB[d]
29[82]	635	4000	675	115	0.01	water
30[82]	633	36000	675	86	0.10	water
31[82]	637	11000	677	93	0.03	water

[a]Standard used for quantum yield measurement: Nile Blue in MeOH (Φ: 0.27), quantum yield and extinction coefficient (at 10^{-6} M) experiments were repeated three times; [b]pH 7.4 phosphate buffer; [c]3 % Triton X-100 in pH 7.4 phosphate buffer; [d]pH 9.0 borate buffer.

All the dyes under any of the conditions described above, had absorption maxima between 628 – 632 nm; consequently, there is little variation of this parameter with solvent polarity. Extinction coefficients for the molecules, however, ranged from 10,100 – 64,100. For **32a**, **33a**, and **32b** the maximum values corresponded to the media that includes Triton X-100; such enhancement effects have been observed for fluorescent dyes,[90,91] including Nile Blue.[74] Variations in the extinction coefficients for **33b** were not as wide as for the other dyes, and the absolute values were less. Fluorescent emission maxima for the dyes varied between 662 – 673 nm. The fact that in MeOH, compounds **32a** and **33a** had fluorescence emission maxima that were within 9 nm of the values in aqueous buffers means that the solvatochromic effects for these two materials are much less than for Nile Blue. Further, lack of significant variations between the emission wavelengths in the various buffers indicates that increased pH change from physiological levels, and lipophilic co-solvents have little affect on these dyes. Sharpness of fluorescent emissions are expressed in terms of full width at half maximum peak heights (fwhm; where smaller is sharper). All the dyes **32** and **33** emitted with sharper fluorescence peaks than Nile Blue **29** or the more water-soluble forms **30** and **31** (data shown in Table 2.3 for these dyes is taken from the literature reference). Further, in aqueous media the quantum yields for these emissions were in all cases better for **32** and **33** relative to Nile Blue and its derivatives **30** and **31**.[82]

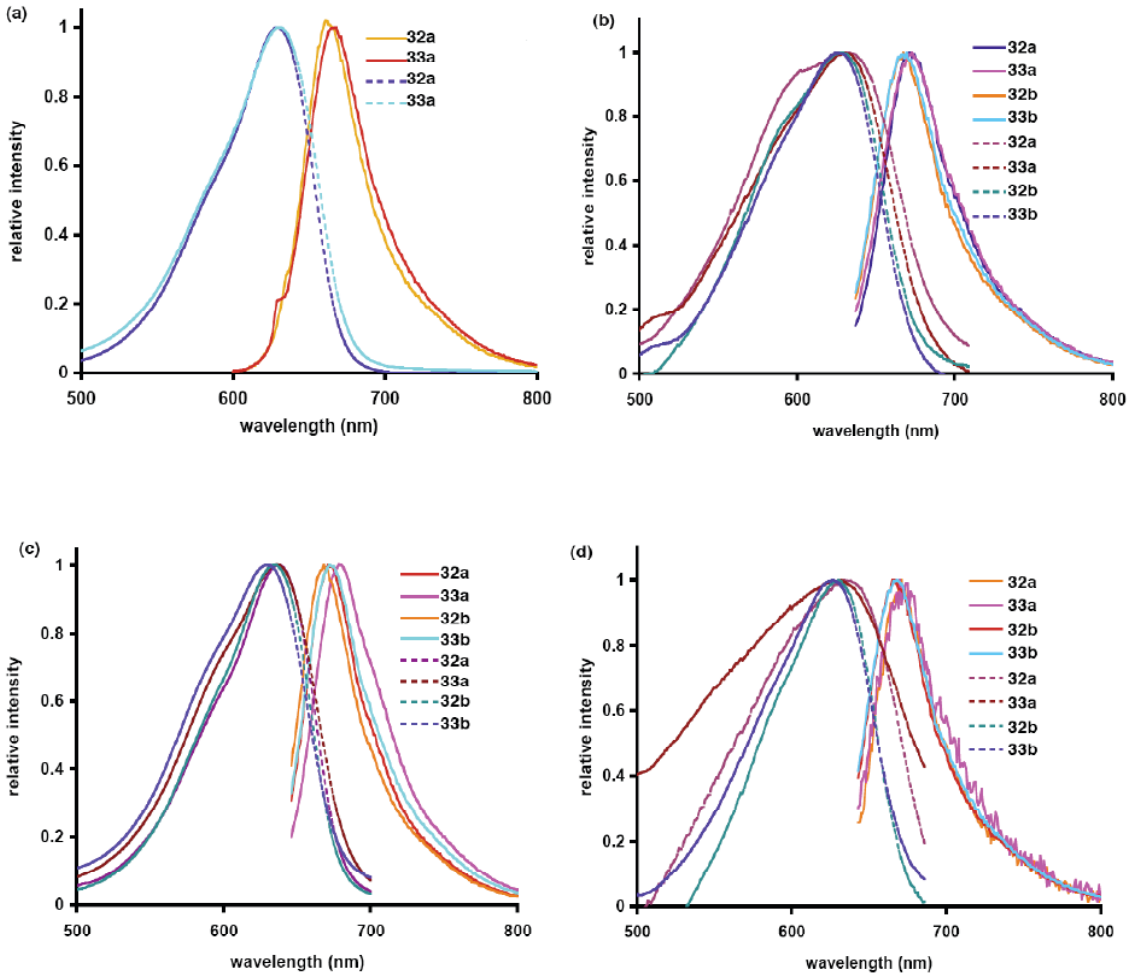

FIGURE 2.7. Absorption (dashed lines) and fluorescence (solid lines) at 2 x 10^{-6} M, of: **a** dyes **32a, 33a** in methanol; **b** dyes in phosphate buffer (pH = 7.4); **c** dyes in 3% Triton X-100 in phosphate buffer (pH 7.4); and **d** in borate buffer (pH = 9.0). All dyes excited at their corresponding λ_{max}.

Figure 2.8 outlines experiments performed to explore aggregation of the dyes in aqueous media. Plots of the normalized UV absorbance versus concentration reveal that the $\lambda_{max\ abs}$ for compound **32a** at 4μM occurs at 671 nm, with an inflection on the blue side of the peak at approximately 600 nm (Figure 2.8a). This inflection point grows as the concentration of the dye was increased; at 16 μM there are two distinct absorption maxima, and at higher concentrations, the shorter wavelength absorption becomes dominant. Figure 2.8 b shows that at concentrations of up to 4.0 μM the absorbance of

32a varies in a near linear way with concentration. Above that concentration, the absorbance deviated markedly from linear concentration dependence. Overall, these data may be interpreted to mean that the dye is aggregating at concentrations above *ca* 4.0 μM. Similar analyses using UV absorption indicate that dye **32a** deviates from Beer-Lambert behavior above this concentration. Probably the dyes are forming fluorescent J-aggregates at concentrations above *ca* 4.0 μM, rather than the non-fluorescent H-forms. Similar analyses for dyes **32b**, **33a**, and **33b** (Figures 2.8 c – h) indicate very similar behavior. Concentration versus absorbance studies indicate these materials tend to aggregate above 4.0 μM.

Finally the Nile Blue derivative, **33a** was used to label ovalbumin via activation of the dye-dicarboxylic acids (*N*-hydroxysuccinimide and *N*,*N*'-diisopropylcarbodiimide in DMF) followed by addition of this activated probe to protein in 0.1M $NaHCO_3$ solution (pH 8.3). The dye:protein ratio was calculated[25] to be 1.1 when 5 eq. of dye was used; this corresponds to 22 % labeling efficiency. This sample was used to obtain the spectral data shown in Figure 2.9a. The wavelengths for the absorption and fluorescence maxima for the free dye **33a** and the **33a**-ovalbumin conjugate were observed to be almost identical, but the fluorescence intensity was much less for **33a**-ovalbumin conjugate.

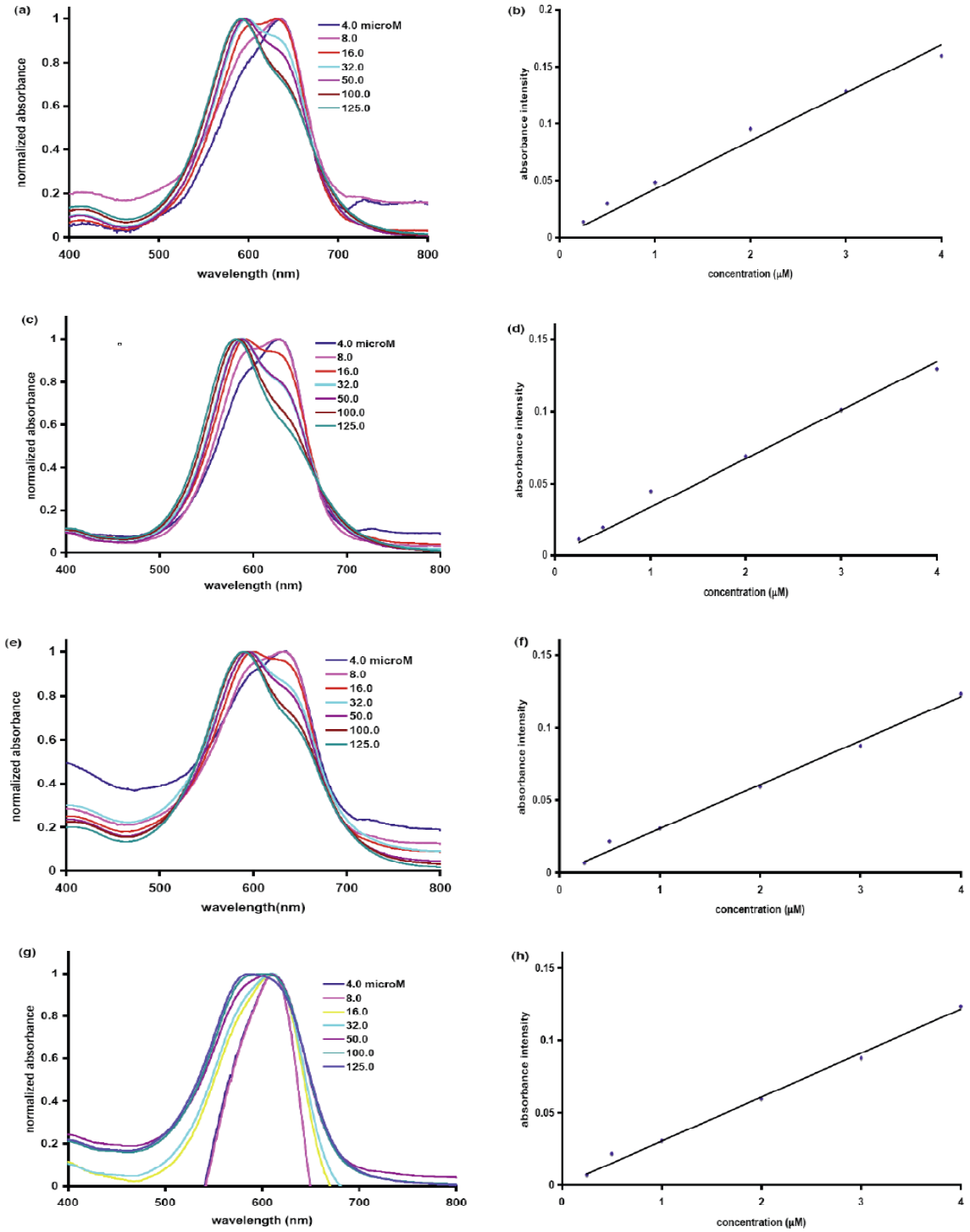

FIGURE 2.8. Aggregation studies at various concentrations for dyes (**32a-b**, **33a-b**). Normalized absorption for various concentrations (μM) in pH 7.4 phosphate buffer (plot a, c, e, g) and plot of absorbance intensity vs. concentration (plot b, d, f, h).

One application of Nile blue derivatives is to measure protein concentrations; this is possible because the fluorescence intensities of Nile blue derivatives tend to increase with protein concentration. However, one limitation of this application is the poor water solubility of Nile Blue derivatives. In this work, the Nile Blue derivative **33a** was mixed with with increasing concentrations of ovalbumin in pH 6.8 phosphate buffer. The fluorescence data for that set of experiments are shown in Figure 2.9b. The fluorescence intensity of **33a** was increased when the protein was added. These increases were small, but the concentrations of ovalbumin were only varied between 3 – 12 μM, *ie* also small changes in protein concentration that are hard to detect. Further, unlike in some previous work with lipophilic Nile Blue derivatives, use of the water-soluble form **33a** circumvented the need for any detergent additives.

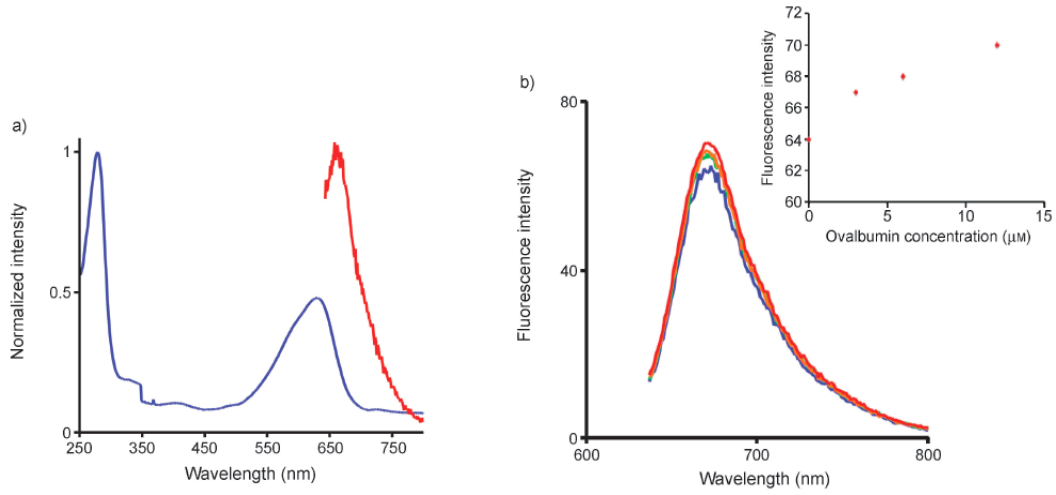

Figure 2.9. Absorption and fluorescence spectra of covalently and non-covalently bonded dye-protein conjugates. **a**: Absorbance (blue) and fluorescence (red) spectra of **33a**-ovalbumin in 0.1 M phosphate buffer (pH 7.4). **b**: Fluorescence spectra of **33a** (5 x 10^{-7} M) and blue: 0, green: 3.0, orange: 6.0, and red: 12.0 μM ovalbumin in phosphate buffer (pH 6.8), λ_{ex} = 630 nm. Inset: Variation in the fluorescence intensity of **33a** vs. ovalbumin concentration.

2.3.2 Conclusion

The Nile Blue derivatives reported here have sharper fluorescence emissions (fwhm 30 nm less), and improved quantum yields in pH 7.4 phosphate buffer relative to the known water-soluble Nile Blue derivatives **30** and **31**. They are formed via condensation reactions that do not require added acids or very harsh reaction conditions (DMF, 90 °C); this is in marked contrast to the syntheses of most other Nile Blue derivatives. Preparative HPLC purification of the products was *not* necessary: they were isolated via reverse phase medium pressure liquid chromatography (MPLC) using acetonitrile/water eluant. The phenolic OH functionalities of dyes **32** and **33** almost certainly increase the water solubilities of these compounds. Alternatively, the phenolic group provides a potential avenue for further derivatization of the dyes (*eg* via triflation and organometallic couplings, or for attachment of a handle to enable dyes **32** to be conjugated to proteins). Three other groups that promote water solubilities were included in these studies: a sulfonic acid, dicarboxylic acids, and a triethylene glycol fragment. Despite this, the fluorescence properties of the dyes, and presumably their aggregation states at elevated concentrations, did not vary significantly. All the dyes showed little tendency to aggregate below 1 - 4 μM; this characteristic would tend to make them useful for biochemical studies when used in relatively dilute solutions, but would exclude applications where quantitation is required at higher concentrations. Probably the most useful spectroscopic parameter of the dyes is their fluorescence at relatively long wavelengths, 670-680 nm, in aqueous media. Probes that emit above 650 nm are relatively few, yet they tend to be the most useful ones for tissue and intracellular imaging applications.[92,93]

Many applications of Nile Blue require it to be water-soluble. Nile Blue acts as an electron mediator for the oxidation of the 1,4-dihydronicotinamide, NAD(P)H cofactors and can be used for detection of NAD(P)H.[94] Upon interaction with NAD(P)H the fluorescence of Nile Blue is quenched due to reduction of Nile Blue by NAD(P)H.[95] Most studies use commercially available sparingly water-soluble Nile Blue and therefore

a surfactant or additive has to be used to enhance solubility of Nile Blue in aqueous media. The water-soluble Nile Blues described in this section can improve detection of such metabolites in an aqueous environment. Detection of trace amount of aluminum in food samples is performed using a kinetic method involving slow oxidation of Nile Blue with potassium bromate.[96] This oxidation reaction is catalyzed by aluminum and therefore can be used as a tool for analyzing the presence of aluminum in food samples. The reaction is carried out in aqueous acidic media and therefore a hydrophilic Nile Blue analogue can greatly enhance the sensitivity of such measurements. Nile Blue derivatives are used for detection of nanomolar concentration of toxic metals such as Hg(II) in aqueous media as a low cost alternative to other detection methods.[97] In spite of their low quantum yields (0.1), water-soluble analogues of Nile Blue are preferred to the water insoluble non fluorescent ones for sensing and detection studies.

2.4 SNAP Tag

Site specific labeling of proteins *in vivo* with fluorescent probes helps to study their functions and understand protein-protein interactions in live cells or tissues. Currently the methods available to achieve site specific labeling involve either genetically modifying the protein of interest by introducing an unnatural amino acid using nonsense codon suppression technology[98,99] or expressing them as a fusion protein with a polypeptide or protein to which a fluorescent label is attached.[100] While genetic modifications are limited to proteins which are expressed in exogenous hosts, fusion proteins often result in oligomerisation. Attachment of organic functional groups to specific locations on the protein using chemical reactions is another alternative for protein labeling but suffers from the fact that proteins may not be stable to all reaction conditions and most of these reactions involve modification of cysteine or lysine residues which are very abundant in most proteins and therefore affect specificity.[101] Introduction of organometallic intermediates, which target less common amino acids like tryptophan and tyrosine seems to have somewhat overcome the problem of specificity, the broad applicability of these reactions are still to be ascertained.[102,103]

O^6-benzylguanine derivatives commonly referred to as SNAP-Tags in literature, have gained prominence in recent years due to their small size and ability to selectively label biomolecules.[104,105] It is based on the human form of DNA repair protein O^6-alkylguanine-DNA alkyltransferase (AGT). The function of AGT is to remove alkyl groups from guanine bases of DNA to prevent mutations during cell division. The removal of alkyl group is achieved by formation of a covalent thioether bond with the alkyl group by the cysteine residue. The discovery by Johnsson *et al.*, that AGT can undergo reaction with any chemical moiety when attached to the guanine base through a benzyl group, triggered a widespread interest in using them as potential cellular imaging agents.[106] The labeling is based on the irreversible reaction of DNA alkyltransferase with O^6-benzylguanine derivative to which a fluorophore is attached (Figure 2.10). The reaction results in transfer of the fluorophore to the cysteine residue of AGT. This reaction allows any fluorescent tag with a suitable handle to be transferred to a protein of interest, which is attached to AGT. There is no known dependence of reaction rate with the type of fluorescent probe used. Wild type AGT (207 amino acids) can be mutated by removing 30 C-terminal residues without significantly altering its activity towards benzylguanine. This mutation is necessary to avoid reaction of AGT with alkyl groups on alkylguanine residues. Removal of amino acid residues also makes AGT much smaller than auto fluorescent proteins.

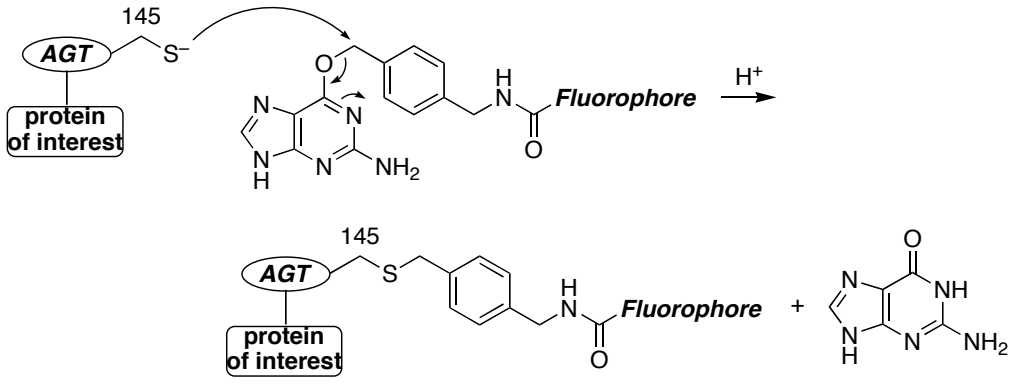

Figure 2.10. Reaction mechanism for SNAP-tag essay.

Figure 2.11 shows a list of the most commonly used fluorescent probes for synthesis of SNAP-tag. All probes are commercially available and emit in the 500-620 nm region. Presence of acetyl groups promote cell permeability, as the efficiency of labeling is dependent on the cell permeability of the substrate. In some cases the benzyl guanine is modified by addition of ester groups on guanine to promote permeability.[107]

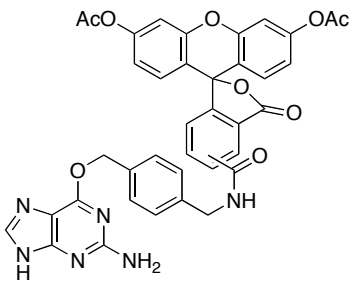

Fluorescien

$\lambda_{max\ abs}$ 499 nm
$\lambda_{max\ emiss}$ 525 nm

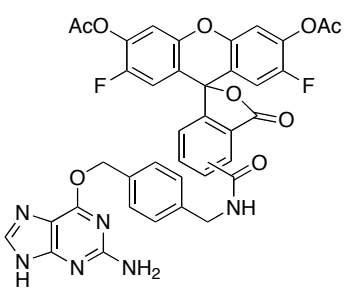

Difluorofluorescien

$\lambda_{max\ abs}$ 500 nm
$\lambda_{max\ emiss}$ 528 nm

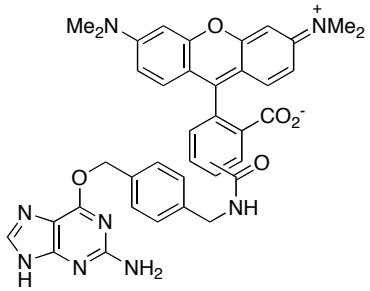

Rhodamine

$\lambda_{max\ abs}$ 555 nm
$\lambda_{max\ emiss}$ 584 nm

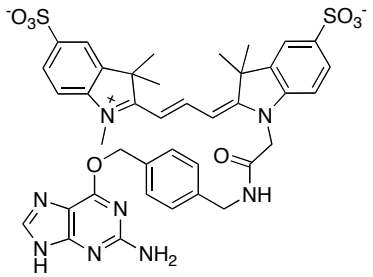

cyanine Cy3

$\lambda_{max\ abs}$ 553 nm
$\lambda_{max\ emiss}$ 572 nm

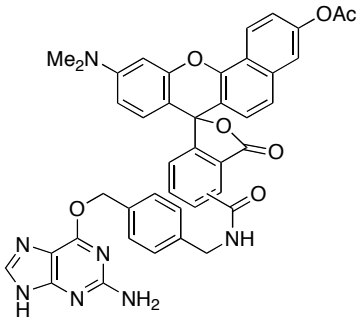

Carboxy SNARF-1

$\lambda_{max\ abs}$ 526, 562 nm
$\lambda_{max\ emiss}$ 621 nm

Figure 2.11. Commonly used SNAP-tag fluorescent labels.

The general strategy for syntheses of SNAP-tags is shown in Scheme 2.9.[108] 6-Chloroguanine is activated by treatment with N-methylpyrolidine and the activated guanine is coupled with trifluoro-N-(4-hydroxymethyl-benzyl)-acetamide to form the corresponding protected benzylguanine derivative. Deprotection of protected

benzylguanine derivative and coupling with activated fluorophores yields the SNAP-tags in 2-10 % yield. The low stability of the activated fluorophores results in poor yields in the coupling step.

Scheme 2.9. General strategy for syntheses of SNAP-tags.

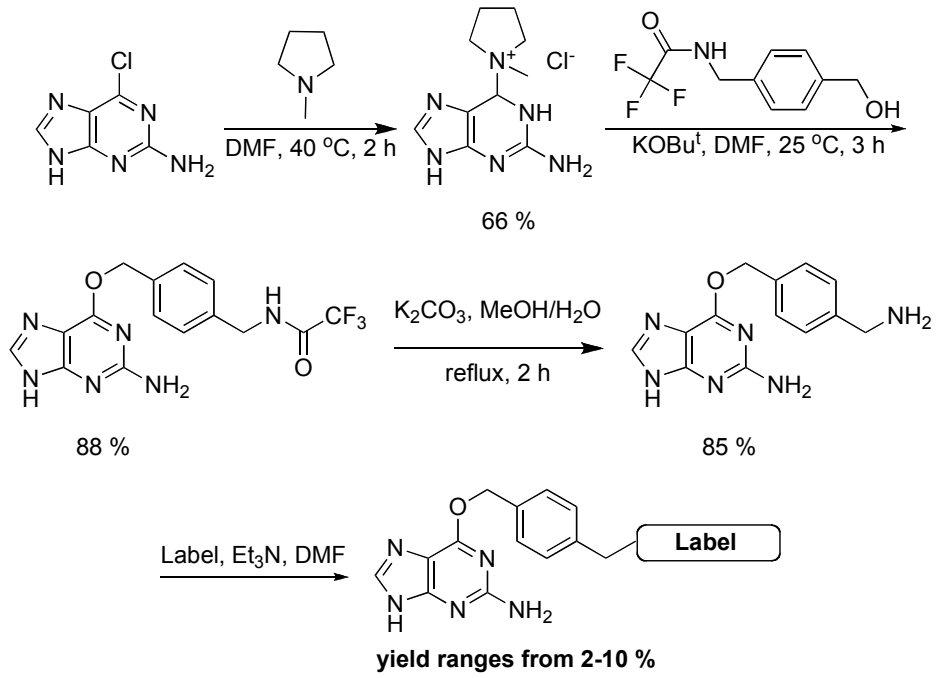

Recently Blake Peterson *et al.* have reported SNAP-tag based on Pennsylvania Green derivatives, which exhibit substantially higher cell permeability than similar Oregon Green derivatives (Figure 2.12).[109] Their work shows that a small change in molecular substitution of a carboxylate group in Oregon Green to a methyl group in Pennsylvania Green greatly enhances the cell permeability and therefore biological activity of O^6-benzylguanine derivatives. Transient transfection of CHO cells with nuclear localized AGT-H2B fusion protein showed strong nuclear fluorescence upon labeling with O^6-benzylguanine-Pennsylvania Green but only weak nuclear fluorescence signal when labeled with O^6-benzylguanine-Oregon green under same reaction conditions.

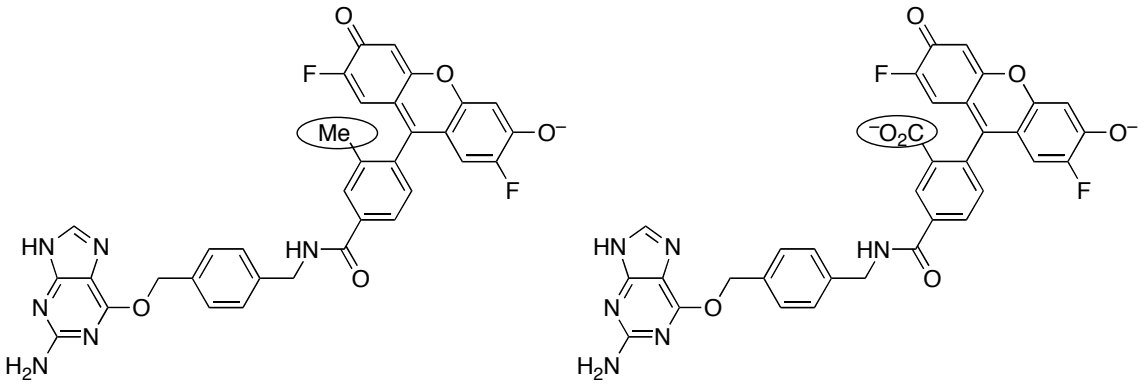

O^6-Benzylguanine-
Pennsylvania Green
Φ 0.92 (pH 7.4)
$\lambda_{max\ abs}$ 494 nm
$\lambda_{max\ emiss}$ 515 nm

O^6-Benzylguanine-
Oregon Green
Φ 0.97 (pH 7.4)
$\lambda_{max\ abs}$ 494 nm
$\lambda_{max\ emiss}$ 522 nm

Figure 2.12. Structures of *O*^{6}-benzylguanine-Pennsylvania and Oregon green.

2.4.1 Results and discussion

A major problem encountered in cellular imaging studies is the inherent auto-fluorescence of cells in the 400-600 nm region, which sometimes results in false positives and should be avoided. The way to overcome this problem is to synthesize probes, which emit in the 600-800 nm region. Nile Red and its derivatives fluoresce around 630-640 nm and its emission is solvent dependent, with a bathochromic shift in more polar solvents like water. There is no reported SNAP-tags based on Nile Red derivatives in the literature probably due to the absence of a handle such as carboxyl group which can be used to attach it to benzylguanine. We had earlier reported synthesis of a dicarboxylic acid derivative of Nile Red.[31] In collaboration with *Covalys Biosciences AG*, Switzerland, we prepared **Nile Red-SNAP-tag**, which was used for labeling studies (Figure 2.13). Transfection of CHO cells with AGT26-his fusion protein and treatment with **Nile Red-SNAP-tag** shows distinct fluorescence indicating that the compound is entering the cell (Figure 2.14). Most of the label seems to be trapped in the cytosol and no fluorescence was observed from the nuclei.

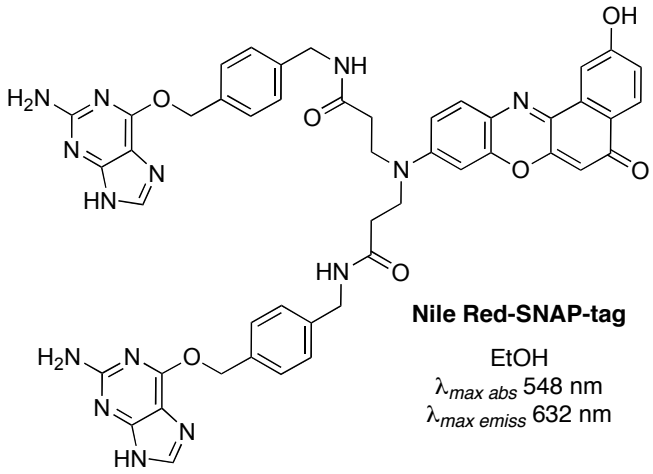

Figure 2.13. Nile Red based SNAP-tag derivative.

a

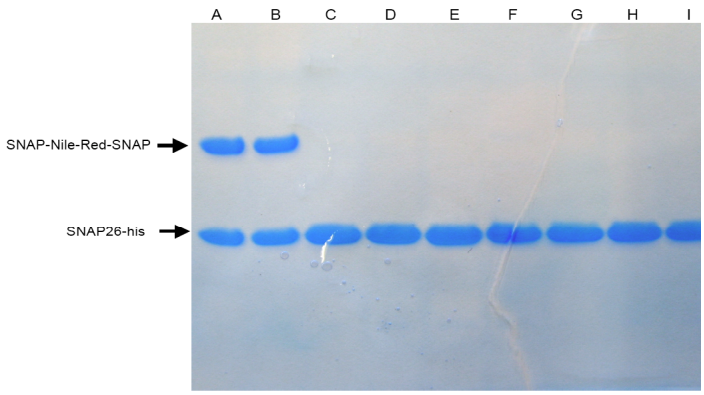

b

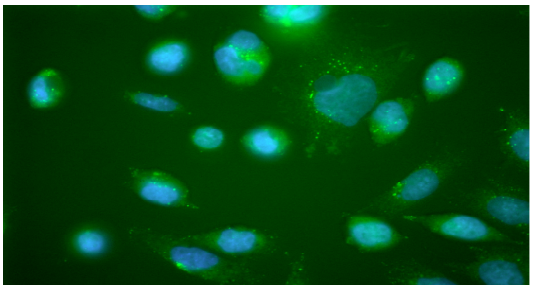

Figure 2.14. (**a**) SDS Gel shows **Nile Red-SNAP-tag** is reactive towards SNAP26-his (line A and B); (**b**) labeling of CHO-K1 cell line with **Nile Red-SNAP-tag**. Green spots shows labeling with **Nile Red-SNAP-tag** and blue is DAPI stain (control for nuclear staining).

These results prompted us to modify the structure of the Nile Red derivative to improve its nuclear permeability. The modified Nile Red derivative **13** was used to synthesize benzylguanine derivatives **13a**, **13b**, and **13c** (Figure 2.15). Transfection of CHO cell lines CHO-K1 and CHO-NLS with AGT26-his fusion protein and treatment with **13a**, **13b**, and **13c** again gave distinct fluorescence indicating that the compound is entering the cell but was trapped in either vesicles and in some cases mitochondria (Figure 2.16 and 2.17). Further studies are required to synthesize a SNAP-tag based on Nile Red derivative, which can selectively label nuclei.

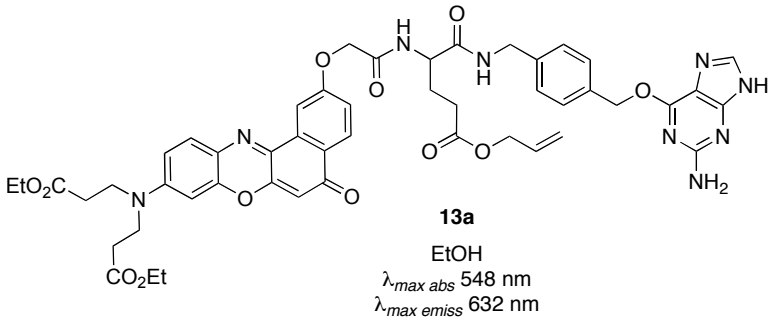

13a

EtOH
$\lambda_{max\ abs}$ 548 nm
$\lambda_{max\ emiss}$ 632 nm

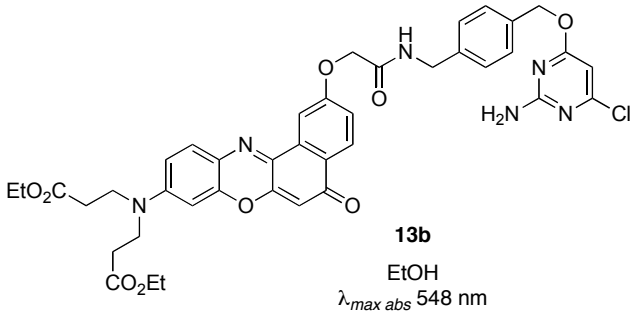

13b

EtOH
$\lambda_{max\ abs}$ 548 nm
$\lambda_{max\ emiss}$ 632 nm

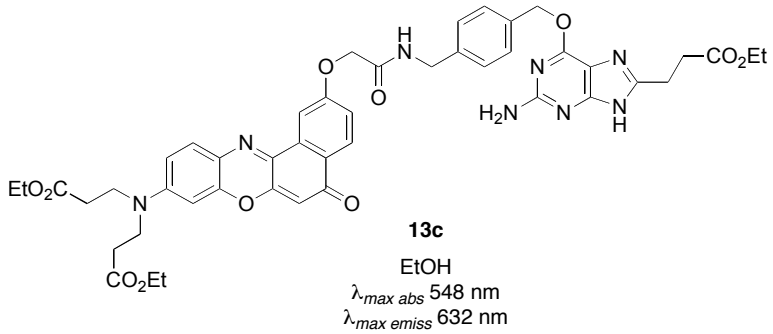

13c

EtOH
$\lambda_{max\ abs}$ 548 nm
$\lambda_{max\ emiss}$ 632 nm

Figure 2.15. SNAP-tag based on Nile Red with different benzylguanine derivatives.

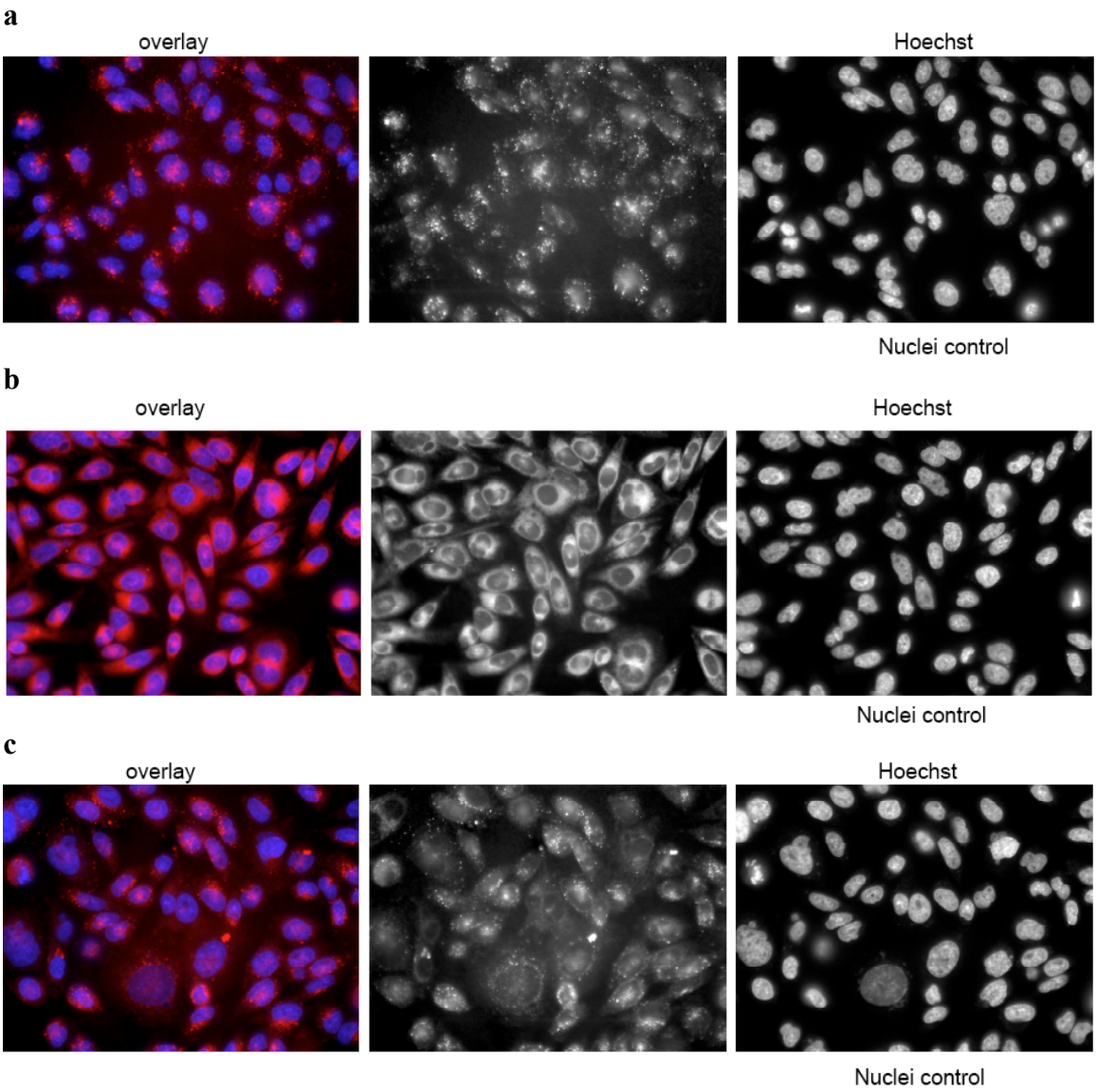

Figure 2.16. Labeling of CHO-K1 cell line with SNAP-tags (**a**) **13a** (**b**) **13b** (**c**) **13c**.

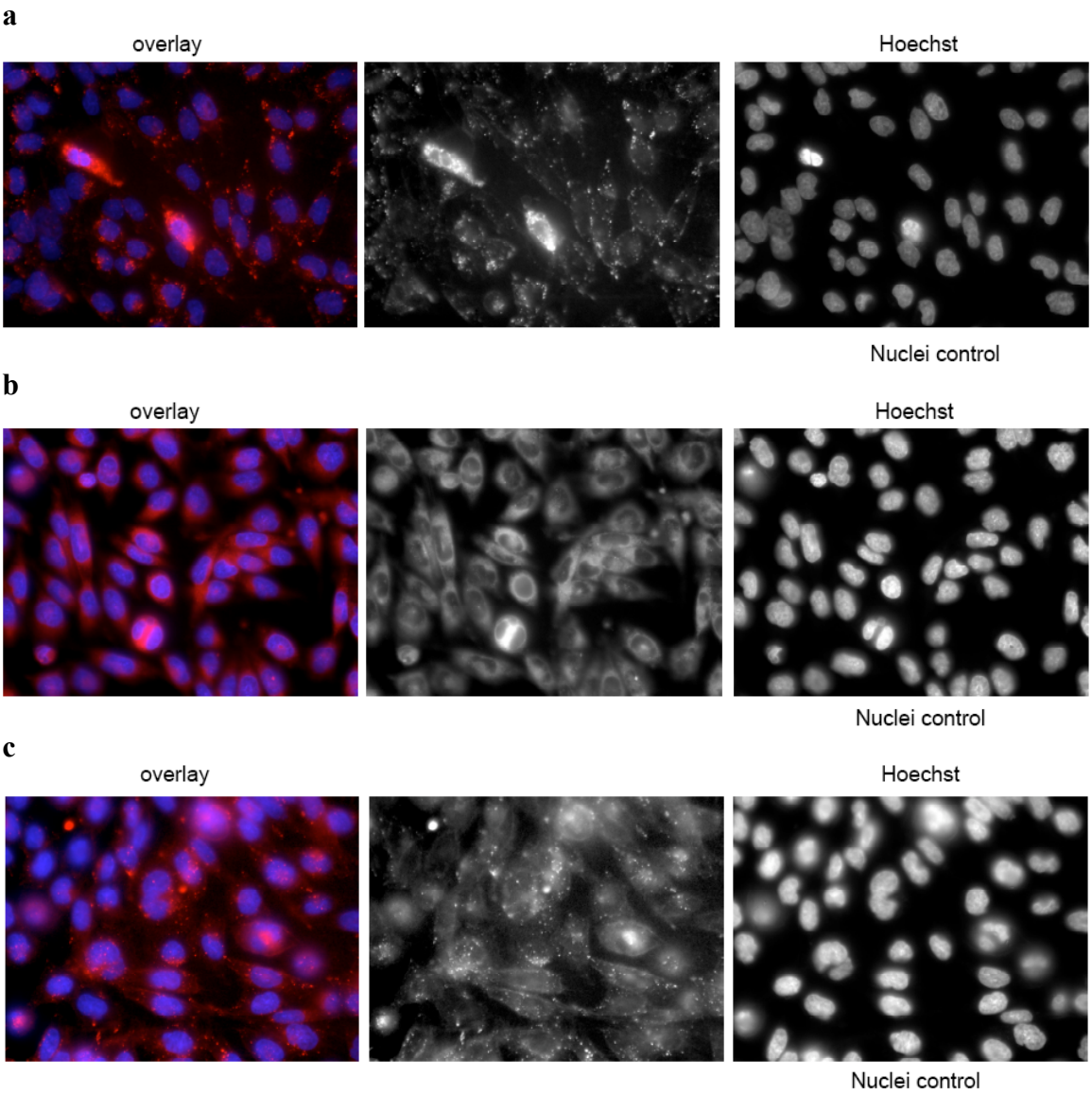

Figure 2.17. Labeling of CHO-NLS cell line with SNAP-tags (**a**) **13a** (**b**) **13b** (**c**) **13c**.

2.4.2 Conclusion

We have synthesized water-soluble derivatives of benzophenoxazine dyes and studied their photophysical properties in aqueous media. There are only a few water-soluble benzophenoxazine dyes reported in the literature and the ones that are published do not give full photophysical properties in aqueous media.[57,61] The quantum yields of these dyes in pH 7.4 phosphate buffer were in the range of 0.1-0.33, which is a great improvement from the corresponding insoluble ones. Aggregation studies on these dyes

shows that they have fewer tendencies to aggregate in the 1 - 4 μM range which tends to make them useful for biochemical studies when used in low concentration. Most applications dealing with organic fluorophores involve dilute concentrations and therefore the above mentioned range in which the dyes are in the non-aggregated state is not a serious drawback in using them. Selected dyes **25** and **27** specifically stained the mitochondria and the golgi apparatus respectively proving their applicability for bioimaging studies. There is no reported use of benzophenoxazine dyes for cellular imaging studies. Dye **13** was used to synthesize benzylguanine derivatives of SNAP-tag for cell imaging and was observed to enter cells efficiently.

Presence of a phenoxazine core in chemotherapeutic drugs such as actinomycin D (Figure 2.18) suggests that the phenoxazine derivatives may possess anticancer activities. In *vitro* and *in vivo* studies on various cancerous cell lines have shown the antitumor activities of water-soluble phenoxazines.[110] In light of these findings, it would be interesting to study the antitumor activity of the synthesized water-soluble benzophenoxazine dyes.

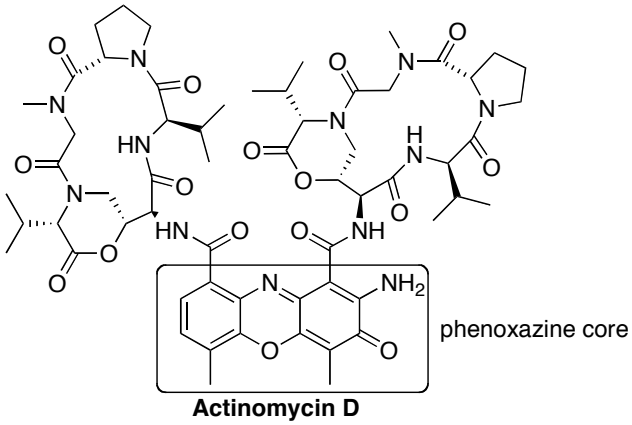

Figure2.18. Structure of actinomycin D, a chemotherapeutic drug.

Our motivation to synthesize benzophenoxazine dyes was not only to make them water-soluble but also to use them as a possible acceptor fragment in through-bond energy transfer cassettes. The syntheses of such cassettes are reported in the Chapter III.

CHAPTER III

ENERGY TRANSFER CASSETTES

3.1 Through-bond Energy Transfer Cassettes

Through-bond energy transfer (TBET) cassettes consist of two fluorophores, a donor absorbing at a lower wavelength and an acceptor emitting at a longer wavelength connected by a conjugate linker in such a manner that the entire molecule is not completely planar. Such cassettes could be particularly useful in biotechnology for multiplexing experiments in which several outputs are to be observed from a single excitation source. The advantage of such a system over traditional FRET based systems is that there is no known requirement of overlap between the donor emission and the acceptor absorbance. Therefore in principle any two fluorophores can be linked together to observe a single fluorescence output from the acceptor. Initial work from our lab proved that such systems are synthetically viable and can be constructed without much difficulty.[29,111] These TBET cassettes showed good photophysical properties and highly efficient energy transfer in organic media. In order to broaden their utility for cellular imaging studies these cassettes need to be water-soluble. Some water-soluble cassettes were reported from our group and was used for monitoring three-component interactions *in vitro* and in living cells.[112]

3.1.1 Results and Discussion

We intend to shift the emission of such TBET cassette systems further to the near IR region of the spectrum and make them water-soluble either by decorating them with water-soluble groups such as carboxylic acids and sulfonic acids or by encapsulating them in silica or calcium phosphate nanoparticles, which can then be dispersed in water. We chose to work with benzophenoxazine dye Nile Red and cyanine dye Cy5 as acceptors which emit in the 600-700 nm region. Figure 3.1 shows the structure of

cassettes **39**-**44**. Cassettes **43** and **44** are hydrophobic in nature and were synthesized to encapsulate in silica or calcium phosphate nanoparticles (Chapter 4). Cassettes **39**-**43** have Nile Red derivatives as their acceptor fragment and cassette **44** has cyanine dye Cy5 as the acceptor fragment. The donor fragment for all the cassettes are either fluorescein or BODIPY derivatives. Both of them absorb around 480-500 nm and emit in the 510-515 nm range. Cassettes **39**-**42** were designed to study the combination of donor and acceptor that would result in a TBET cassette with good energy transfer properties in aqueous media.

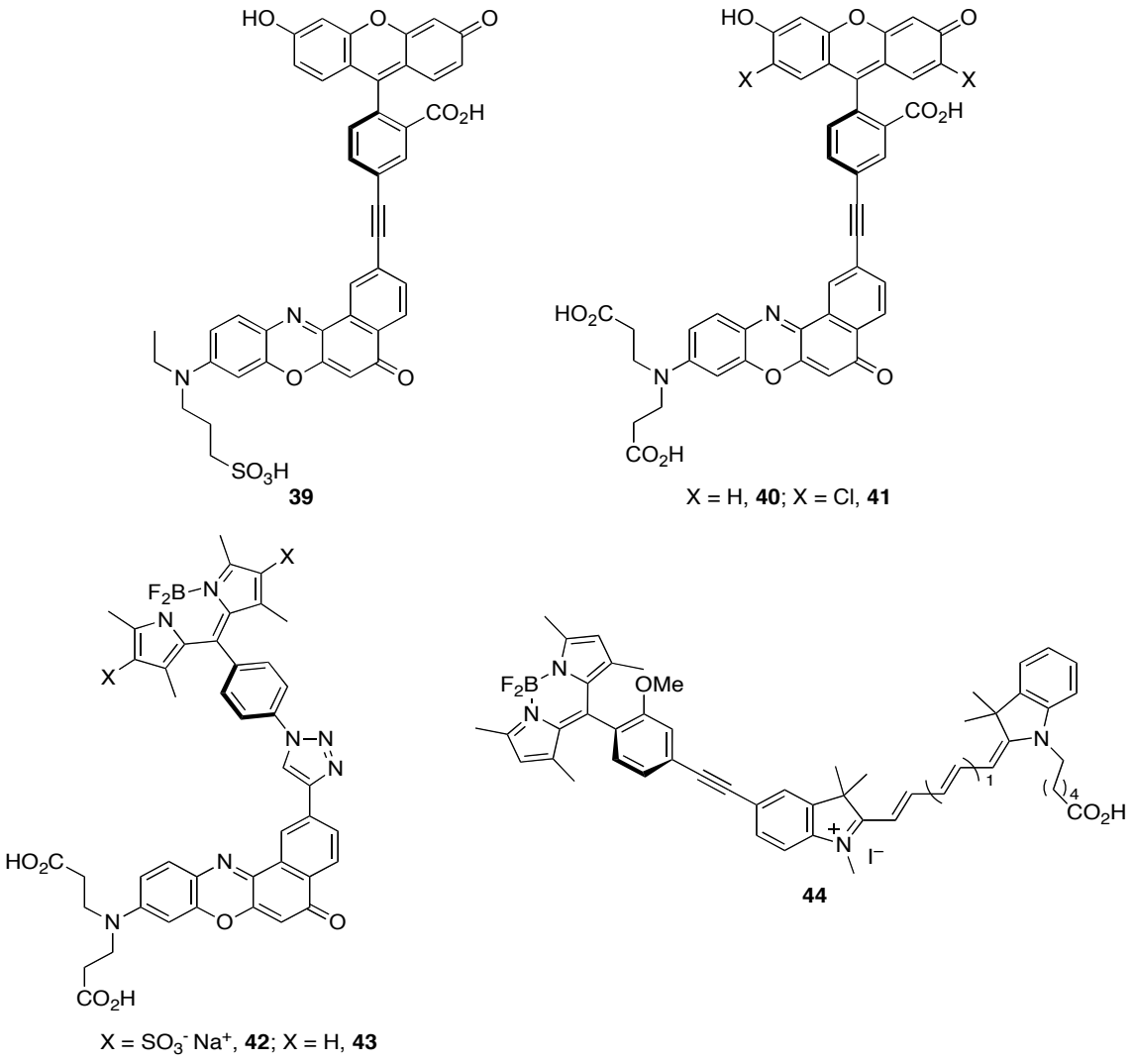

Figure 3.1. Structure of cassettes **39**-**44**.

3.1.1.1 Syntheses of Cassettes

Figure 3.2 shows donor fragments used for cassettes **39-44**. Dr. Yuichiro Ueno provided donor fragments **45** and **49**. Mr. Juan Castro provided dichlorofluorescien derivative **46** and Miss Lingling Li provided sulfonic acid BODIPY **47**. Donor fragment **48** was synthesized using a procedure reported for synthesis of BODIPY **47**.[62] The nitro BODIPY **54** was refluxed in EtOH in presence of hydrazine for 30 minutes to form the amino derivative. The amino derivative being unstable was directly subjected to diazotization at 0 ^{o}C, followed by an azide transfer reaction with sodium azide to obtain donor fragment **47**. (Scheme 3.1)

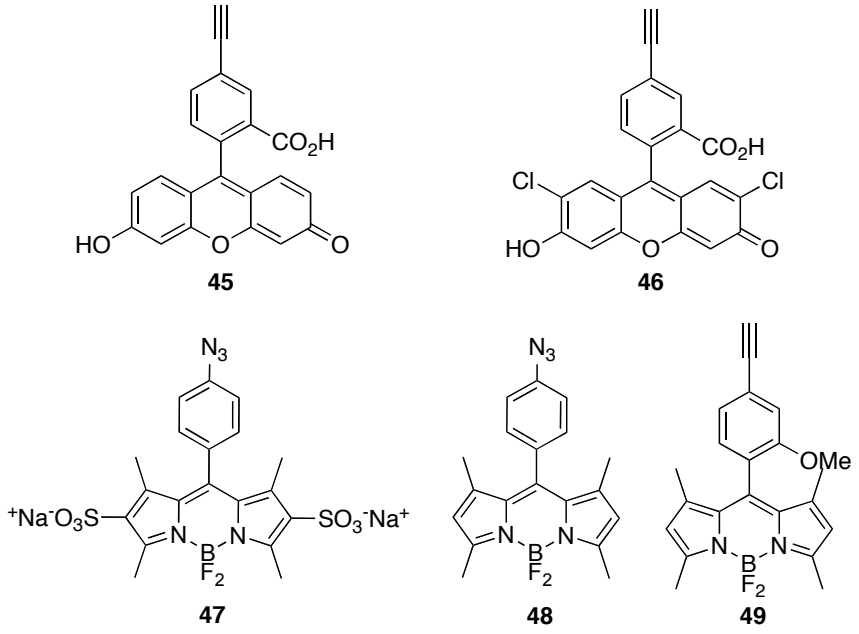

Figure 3.2. Structure of donors used for synthesis of cassettes **39-44**.

Scheme 3.1. Synthesis of donor fragment **48**.

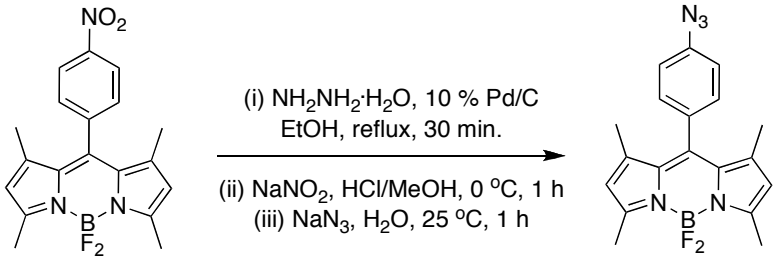

54 **48** 38 %

Acceptor fragments **50** and **51** (Figure 3.3) were synthesized via triflation reaction.[113] Nile Red derivatives **55** and **56** were treated with N-phenyltriflamide in presence of triethylamine at 25 °C for 24 h in THF to obtain the corresponding triflates **50** and **51** in 55 and 52 % yield respectively. Sonogashira coupling of **51** with trimethylsilylalkyne followed by deprotection at 25 °C for 30 minutes with TBAF afforded acceptor fragment **52** in 58 % overall yield. (Scheme 3.2b) Condensation of indolium bromide **58** with *N*,*N*'-diphenylformamidine at 120 °C in acetic anhydride for 30 min followed by treatment with indolium iodide **59** at 25 °C afforded acceptor fragment **53** in 65 % yield (Scheme 3.2c).

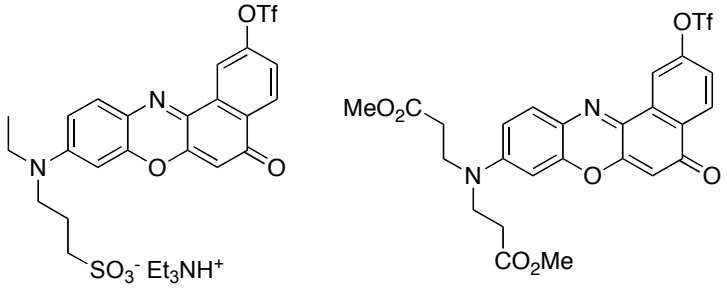

50 **51**

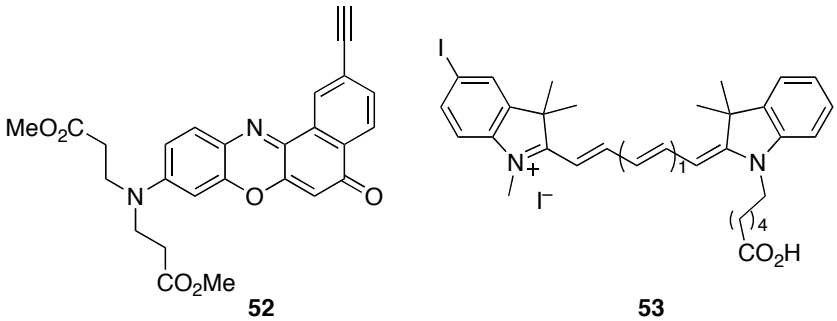

Figure 3.3. Structure of acceptors used for synthesis of cassettes **39-44**.

Scheme 3.2. Synthesis of acceptor fragment (**a**) **50** (**b**) **51**, **52** and (**c**) **53**.

a

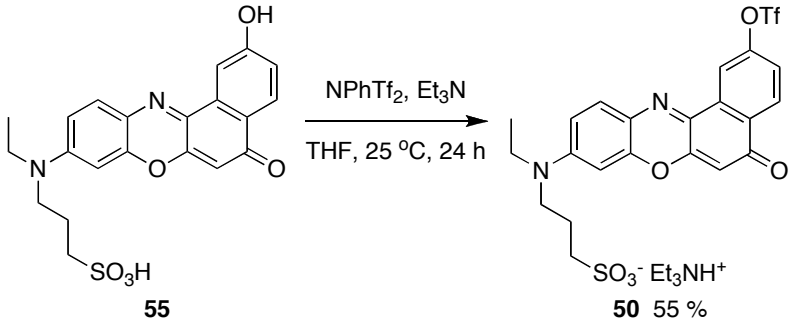

b

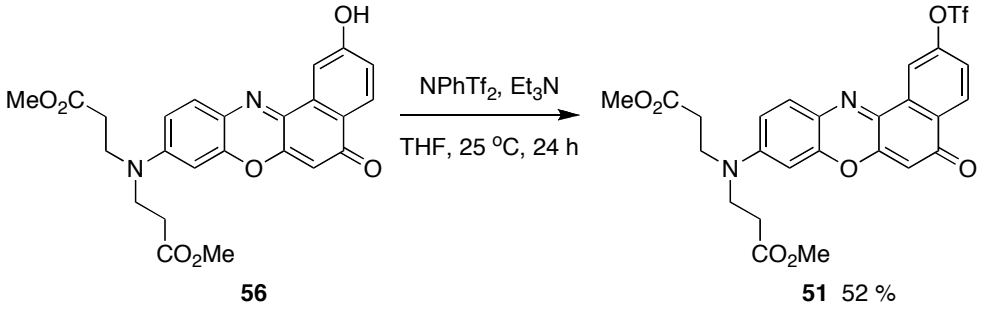

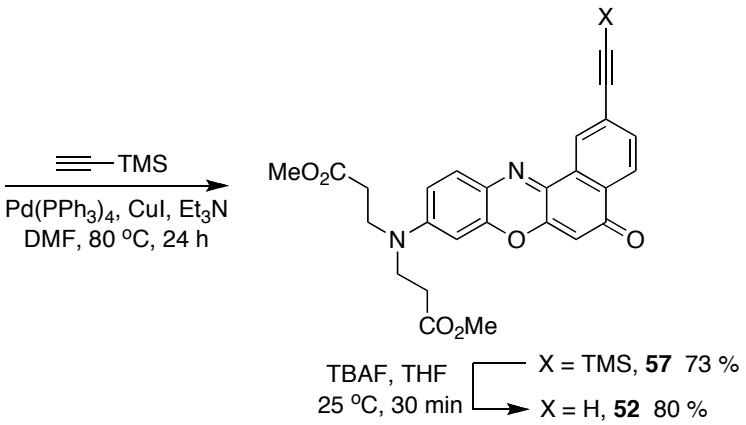

c

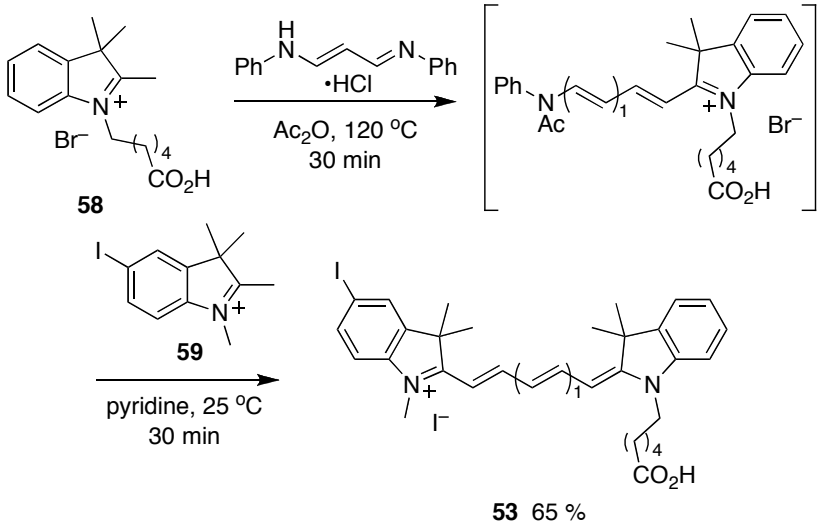

Cassette **39** (scheme 3.3) was prepared via Sonogashira coupling of Nile Red triflate **50** with fluorescein alkyne **45**. The coupling reaction proceeded only at high temperature (above 100 °C). An initial screening of reaction conditions showed that no coupling products were obtained even at high temperature when $PdCl_2(PPh_3)_2$ was used as a catalyst. Use of $Pd(PPh_3)_4$ as catalyst and heating to 130 °C afforded product **39** in 49 % yield. At temperatures lower than 130 °C, the yield was very low, and in most cases, there was no reaction at all.

Scheme 3.3. Synthesis of cassette **39**.

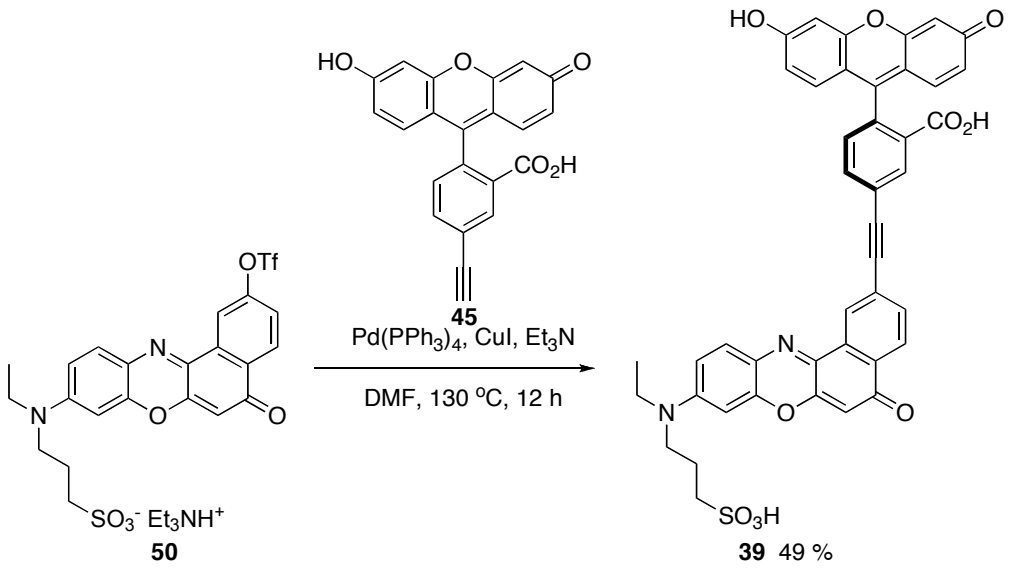

Cassettes **40** and **41** were also prepared via palladium catalyzed cross coupling reaction between the corresponding triflate and an alkyne. The reaction conditions were similar to the synthesis of cassette **39** and coupling was possible only at 130 ^{o}C. The dimethylester derivatives obtained were hydrolyzed to carboxylic acids using K_2CO_3 in MeOH/Water mixture and purified via acid base extraction and then by reverse phase HPLC to afford **40** and **41** in 59 and 21 % yield. The dichlorofluorescien alkyne is not very stable at 130 ^{o}C and therefore the yield of the coupling reaction is low in case of cassette **41**.

Scheme 3.4. Synthesis of cassettes **40** and **41**.

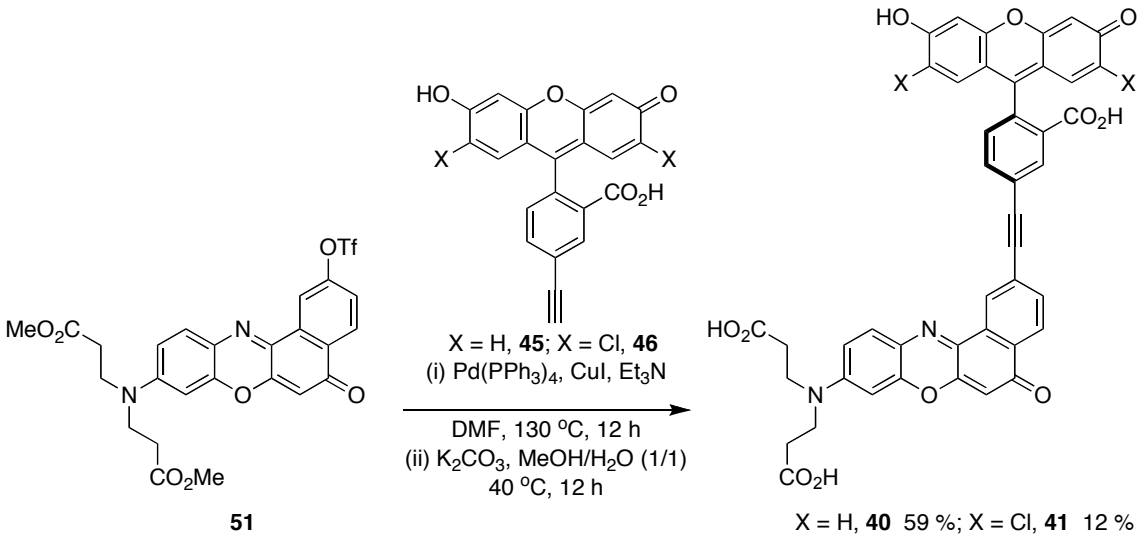

1,3 dipolar cycloadditions between an azide and an alkyne is a well established reaction.[114-116] Cassettes **42** and **43** were synthesized using copper catalyzed 1,3 dipolar cycoladditons using tris(1 - benzyl - 1H - 1,2,3 - triazol - 4 - yl)methyl amine (TBTA) ligand as a copper stabilizer (Scheme 3.5). Reaction without the TBTA ligand resulted in poor yields of cycloaddition products. Reaction of water-soluble BODIPY **47** with Nile Red alkyne **52**, followed by hydrolysis in aqueous methanol with K_2CO_3 afforded cassette **42**. The product was purified on a reverse phase medium pressure liquid chromatography (MPLC) C-18 column using CH_3CN/H_2O (1/1) as eluent to afford cassette **42** as a dark purple colored material in 39 % yield. Cassette **43** was obtained in 30 % yield under similar reaction conditions and purified on a reverse phase medium pressure liquid chromatography (MPLC) C-18 column using CH_3CN/H_2O (7/3) as eluent. The low yield of these two cassettes is due to the apparent instability of BODIPY in basic media.

Scheme 3.5. Synthesis of cassettes **42** and **43**.

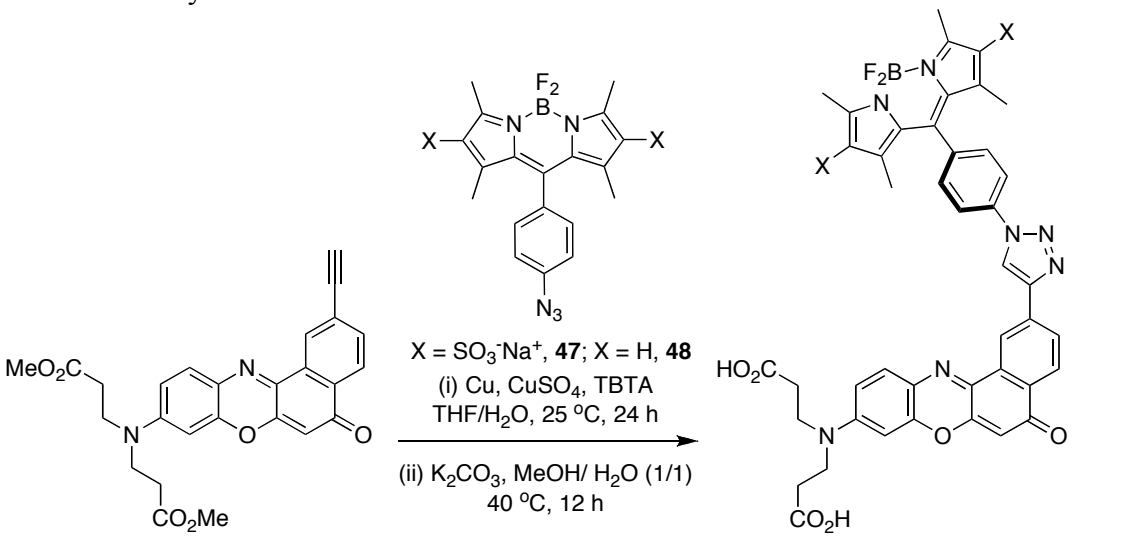

The final cassette **44** was synthesized via palladium catalyzed cross coupling reaction between BODIPY alkyne **48** and iodocyanine **53** (Scheme 3.6). Cyanine dyes are chemically unstable at temperatures above 40 ^{o}C and therefore the coupling reaction was carried out at 40 ^{o}C for 1 h. Attempted reactions at 25 and 30 ^{o}C resulted in either no reaction or very poor conversion, which was confirmed by TLC. Flash chromatography purification using 10 to 50 % MeOH/CH_2Cl_2 afforded cassette **44** as a dark purple solid in 26 % yield.

Scheme 3.6. Synthesis of cassette **44**.

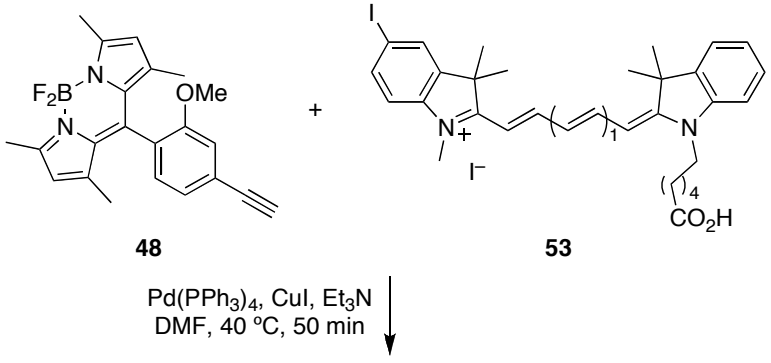

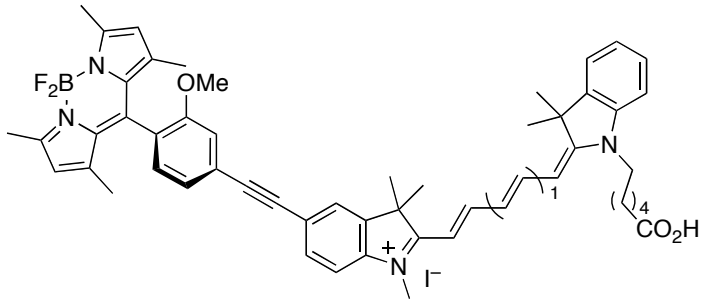

44 26 %

3.1.1.2 Photophysical Properties of Cassettes

The absorbtion and emission profiles of cassettes **39**-**44** in EtOH are shown in Figure 3.4. As expected the absorbtion of cassettes shows the presence of two distinct absorbtion maxima corresponding to the donor and acceptor fragments of each cassette. The fluorescence of cassettes **39**-**44** in EtOH shows efficient energy transfer without significant leakage from the donor fragment. The prominent emissions from all the cassettes are seen from the acceptor fragment. The quantum efficiency of all cassettes in EtOH was in the range of 0.31 to 0.41 when excited at the donor. The energy transfer efficiency (ETE) calculated for cassettes **39**-**44** ranged from 77 to 97 % (Table 3.1).

a

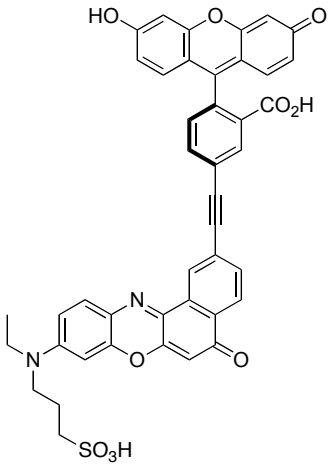

39

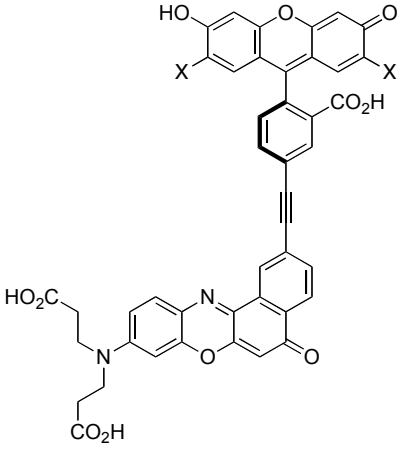

X = H, **40**; X = Cl, **41**

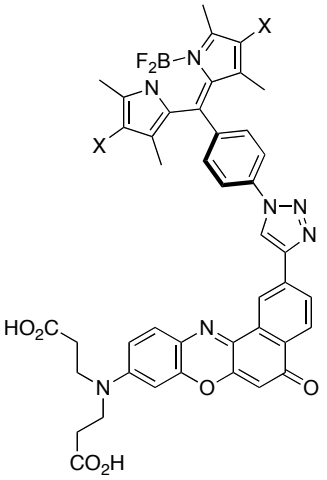

X = SO_3^- Na^+, **42**; X = H, **43**

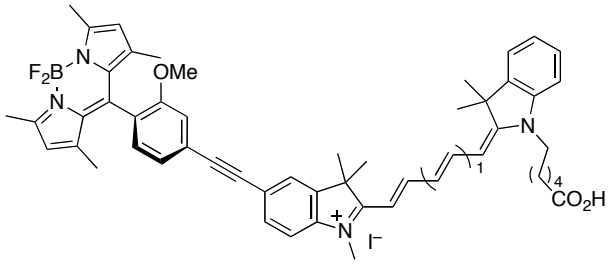

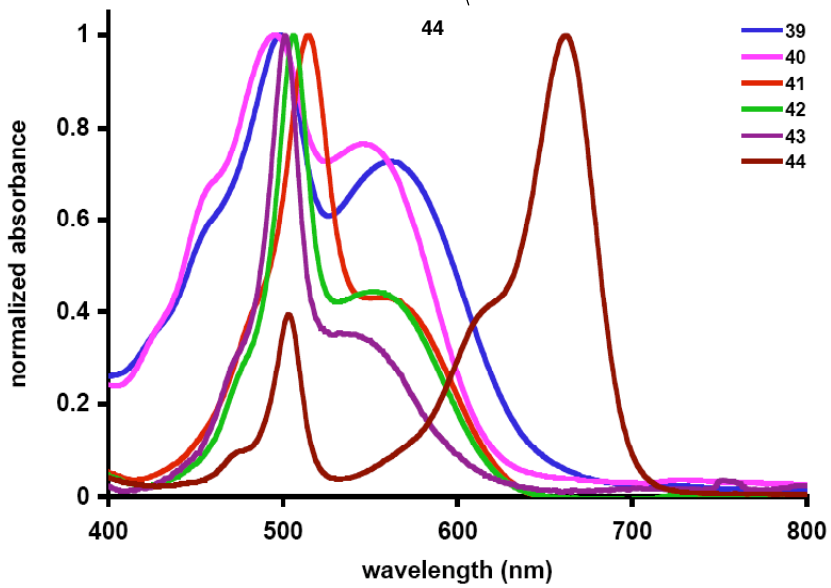

b

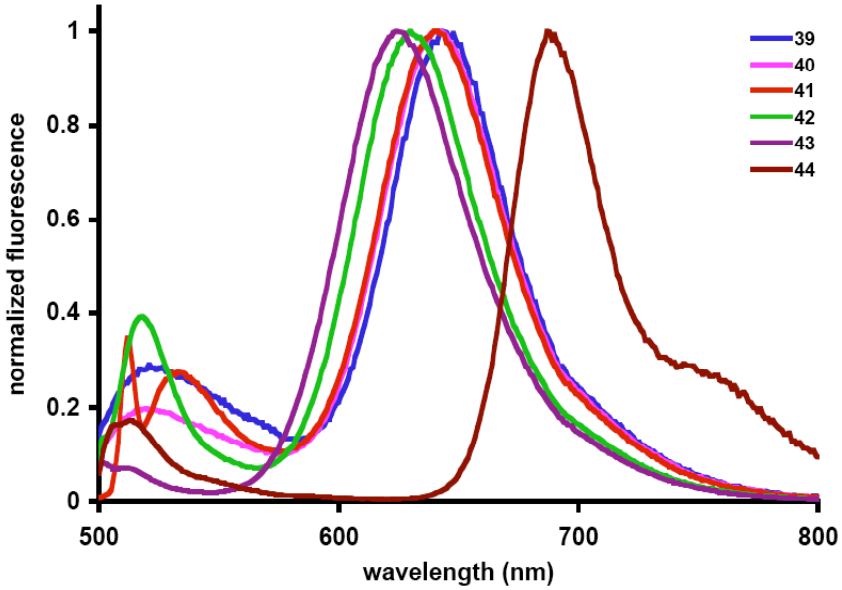

Figure 3.4. Normalized absorbance (**a**) and fluorescence (**b**) of cassettes **39-44** in EtOH. Concentration for absorbance measurement 10^{-6} M; concentration for fluorescence measurement 10^{-7} M.

Table 3.1. Photophysical properties of cassettes **39-44** in EtOH.

dye	λ_{abs}(nm)	$\lambda_{em.}$(nm)	Φ_D	Φ_A[c]	ETE % (Φ_D/Φ_A)
39	498, 561	648	0.31+/-0.02[a]	0.40+/-0.03	77
40	495, 546	644	0.34+/-0.01[a]	0.38+/-0.01	89
41	515, 555	645	0.36+/-0.03[b]	0.43+/-0.02	83
42	506, 553	632	0.41+/-0.02[b]	0.49+/-0.02	81
43	501, 541	624	0.36+/-0.02[b]	0.37+/-0.01	97
44	504, 662	687	0.35+/-0.01[b]	0.40+/-0.02[d]	90

Φ_D: quantum yield of cassette when excited at the donor. Φ_A: quantum yield of cassette when excited at the acceptor. Standard used for quantum yield measurement: [a]Fluorescien in 0.1 M NaOH (Φ: 0.92), [b]rhodamine 6G in EtOH (Φ: 0.94), [c]rhodamine 101 in EtOH (Φ: 1.0); [d]Nile Blue (Φ: 0.27 in EtOH). Quantum yield measurements were repeated three times and averaged.

The photophysical properties of the cassettes in pH 7.4 phosphate buffer were not that encouraging (Figure 3.5). Water-soluble cassettes **39-41** showed almost no energy transfer (Table 3.2). Cassette **42** showed 42 % energy transfer with a reduced quantum yield of 0.1 when excited at the donor. These results show that in cassettes **39-42** non-radiative processes predominate in aqueous media, which result in poor energy transfer. Cassettes **39-41** all had fluorescein derivatives as the donor and in all cases almost no fluorescence output from the acceptor Nile Red was seen. The presence of water-soluble groups in these cassettes did not prevent it from aggregating in aqueous media, which contributes to their poor energy transfer efficiency.

a

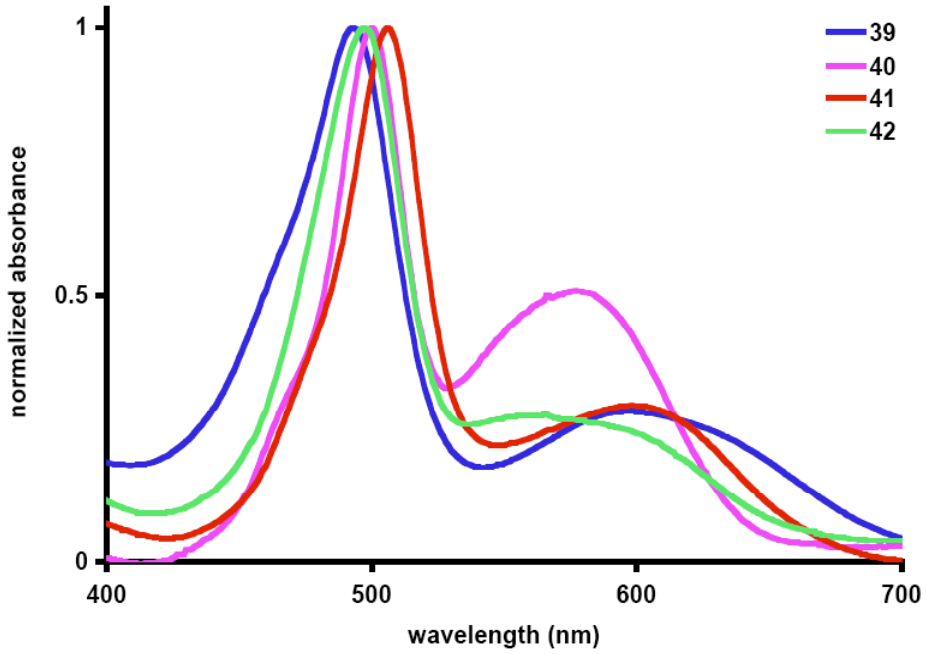

b

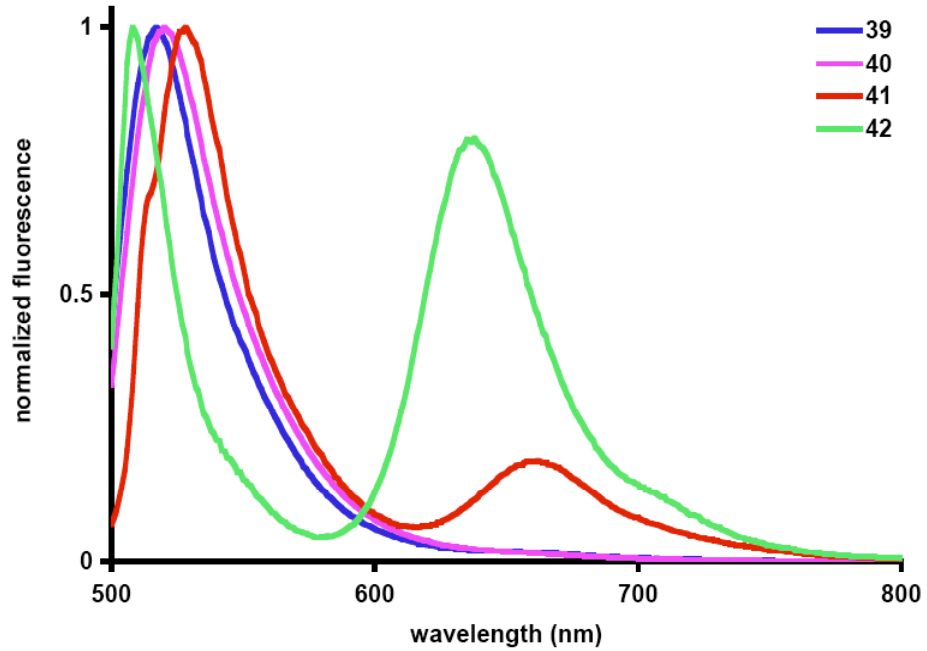

Figure 3.5. Normalized absorbance (**a**) and fluorescence (**b**) of cassettes **39-42** in pH 7.4 (0.1 M sodium phosphate buffer). Concentration for absorbance measurement 10^{-6} M; concentration for fluorescence measurement 10^{-7} M.

Table 3.2. Photophysical properties of cassettes **39-42** in pH 7.4 (0.1 M sodium phosphate buffer).

dye	λ_{abs}(nm)	$\lambda_{em.}$(nm)	Φ_D	Φ_A[c]	ETE % (Φ_D/Φ_A)
39	493, 591	517	0.010[a]	0.14+/-0.02	7
40	500, 577	520	0.008[b]	0.12+/-0.01	6
41	506, 593	528, 662	0.016[b]	0.11+/-0.03	14
42	497, 575	509, 637	0.10[a]	0.24+/-0.01	42

Φ_D: quantum yield of cassette when excited at the donor. Φ_A: quantum yield of cassette when excited at the acceptor. Standard used for quantum yield measurement: [a]Fluorescien in 0.1 M NaOH (Φ: 0.92), [b]rhodamine 6G in EtOH (Φ: 0.94), sulforhodamine in EtOH (Φ: 1.0); quantum were repeated three times and averaged.

3.1.2 Conclusion

Through-bond energy transfer cassettes based on Nile Red derivatives and cyanine dye Cy5 were synthesized to study their behavior in organic and aqueous media. TBET cassettes based on Nile Red derivatives showed good energy transfer in organic media but very poor energy transfer in aqueous media. TBET cassettes with a Nile Red derivative as the acceptor and fluorescein derivative as the donor showed almost no energy transfer in aqueous media. When the donor was changed to water-soluble BODIPY we observed 40 % energy transfer from the donor to the acceptor. These findings show that fluorescein is not a good donor for synthesis of water-soluble TBET cassettes. Another reason may be the low quantum yield and molar extinction coefficient of acceptor Nile Red derivatives compared to the fluorescein donor. Energy transfer is not properly mediated in such a system and non-radiative processes dominate in aqueous media. Substituting the alkyne linker with a triazole linker in these cassettes may help to some extent in improving energy transfer efficiency.

In conclusion we have prepared six cassettes based on Nile Red and cyanine acceptors and fluorescein or BODIPY fragments as donors. These show efficient energy transfer in ethanol and fluoresce with a quantum yield of 0.31- 0.41. Their long wavelength emission and large Stokes' shifts are useful for fluorescence studies in polar, hydrogen-bonding, organic solvents. Our current efforts are focused on making similar cassettes with improved photophysical properties for use in biological media. Cassettes **43** and **44** were prepared for encapsulation in silica and calcium phosphate nanoparticles and will be discussed in Chapter IV.

3.2 Chemiluminescent Energy Transfer Cassettes

The two most common ways to induce chemiluminescence in purely organic, non-biological, systems are to treat either oxalate esters or luminol derivatives with basic hydrogen peroxide.[117,118] Both these types of mixtures give light of relatively short wavelengths that are not ideal for applications in biotechnology. Luminol, for instance, emits in the range 420 - 450 nm, depending on the solvent media.[119] Intimate mixtures of oxalate esters or luminol,[120] an oxidant, and an acceptor dye give longer wavelength emissions via intermolecular energy transfer. This results in the mesmerizing, long-lived emissions seen in "light stick toys". However, the options for forming discrete probes for biotechnology that emit at longer, and generally more useful, wavelengths are limited.[121-124,125] All our published research to date features cassettes based on UV-absorbing donors, like compound **3** (Figure 3.6). We thought it would be intriguing to make cassettes where the donor might be activated chemically instead. Oxalate esters are not useful donors for through-bond energy transfer cassettes because it is impossible to conjugate an acceptor to the oxalate fragment. Consequently, luminol-based systems were selected. Described here are the syntheses and spectroscopic properties of the fluorescein- and Nile Red-based, chemically activated, cassettes **60** and **61**.

a

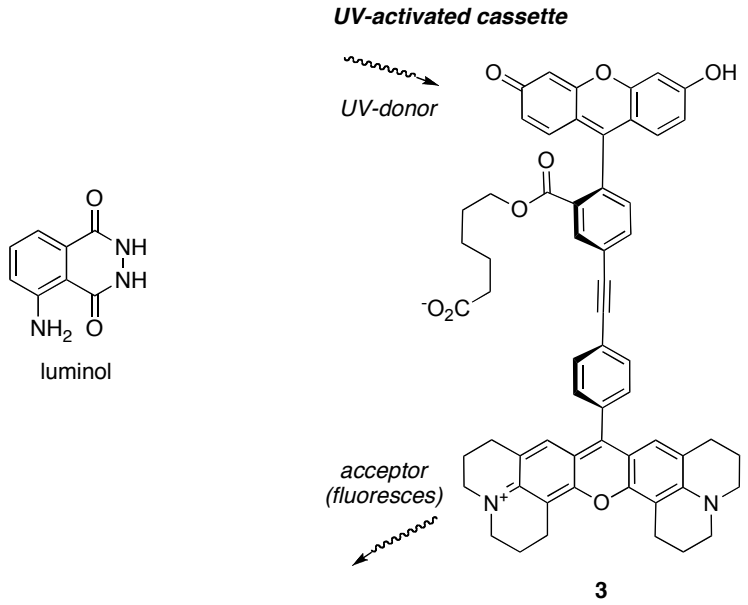

b

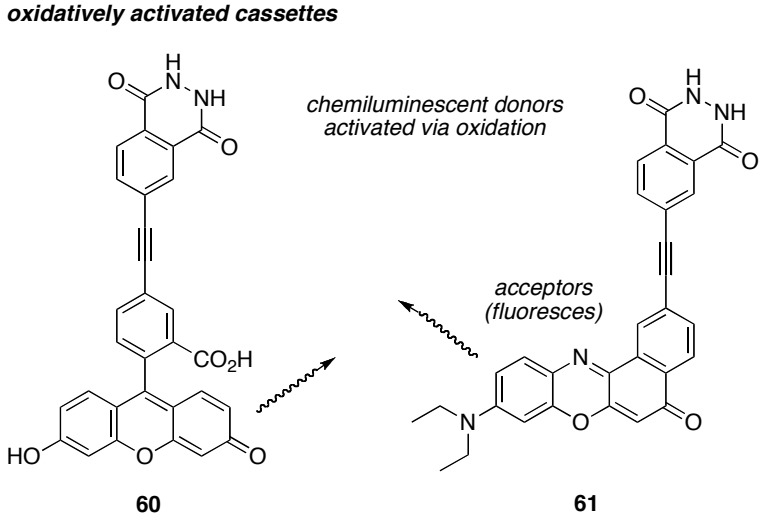

Figure 3.6. Structure of (**a**) light activated and (**b**) chemically activated TBET cassettes.

3.2.1 Results and Discussions

3.2.1.1 Synthesis of Chemiluminescent Cassettes

Nearly all luminol derivatives are insoluble in most organic media, and this makes them extremely difficult to manipulate. After considerable experimentation, one solution to this problem emerged: bis(*N*-protection) of compounds like **3** with 4-methoxybenzyl (PMB) groups. This approach gave organic-soluble, easily chromatographed, intermediates, and the PMB group is removed in the closing stages of the synthesis via treatment with TFA. Thus, Scheme 3.7 shows the syntheses that evolved for compounds **60** and **61**. In both routes, the cyclic hydrazide **63** was bis-*N*-protected, then elaborated via Sonogashira reactions.[126] These featured derivatives of 5-bromofluorescein[127] and 2-hydroxy Nile Red.[128] The route to the cassettes would have been more convergent if an alkyne derivative of luminol could have been coupled with halogenated/triflated acceptors, but that approach was ineffective.

Scheme **3.7.** Preparation of (a) fluorescein cassette **60** and (b) Nile Red cassette **61**.

a

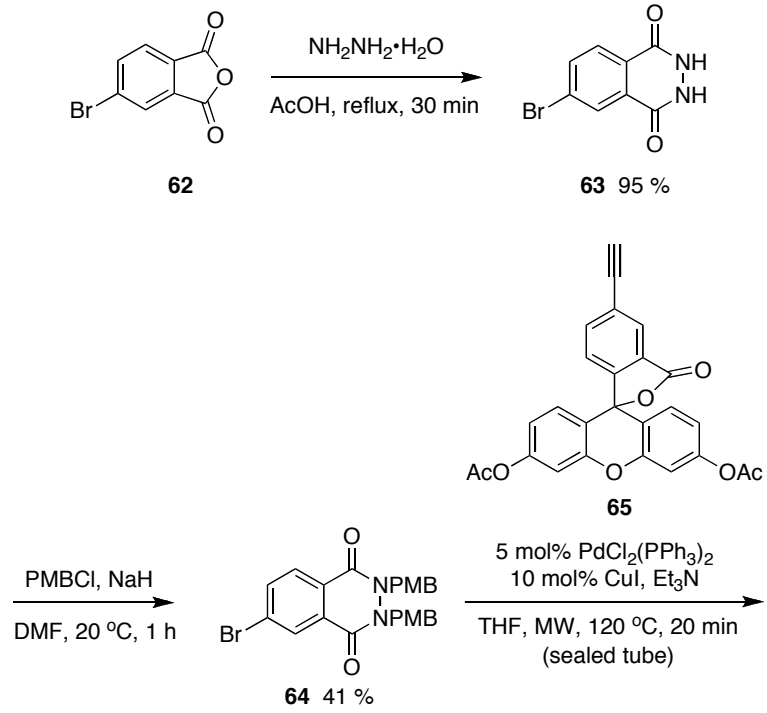

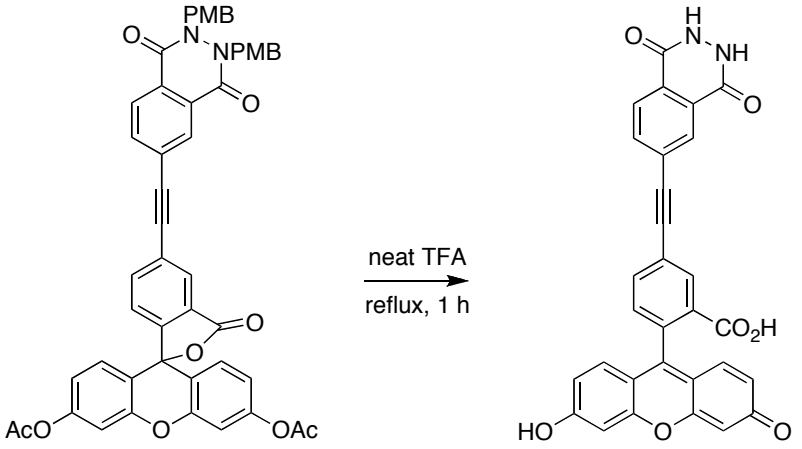

66 58 %

60 88 %

b

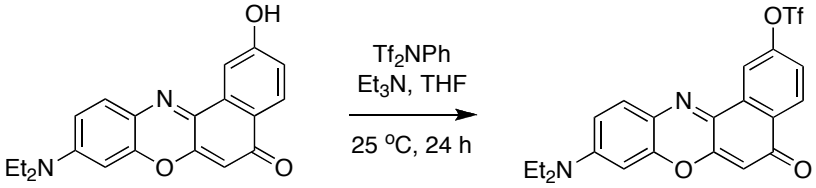

24

67 75 %

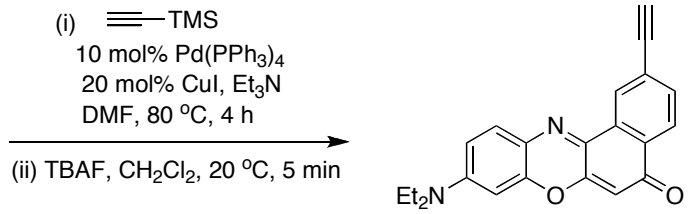

68 73 %

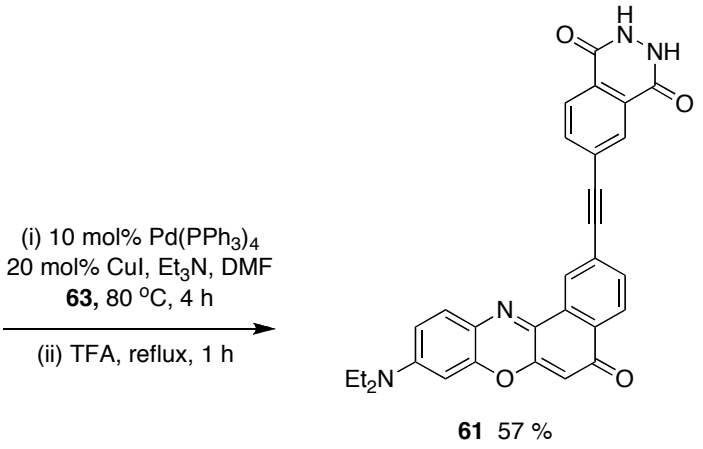

61 57 %

3.2.1.2 Photophysical Properties of Chemiluminescent Cassettes

It is hard to describe the spectacular chemiluminescence of these compounds without showing pictures of the experiments to support the words (Figure 3.7). For cassette **60**, a 100 μl aliquots of the compound (10^{-5} M, in pH = 10 aqueous $Na_2CO_3/NaHCO_3$ buffer) was added to a sample cell containing $CuSO_4$ (1.5 x 10^{-3} M) and H_2O_2 (2.0 x 10^{-3} M) with stirring. Cassette **61** is not very soluble in aqueous media and, in any case, the quantum yield for Nile Red emission is less than 0.1 in water. Consequently, for **61**, potassium *tert*-butoxide in THF (10^{-2} M) was added to the compound dissolved in dry DMF (10^{-5} M). This experiment is done open to the air and oxygen is presumed to be the oxidant. Luminol under the conditions used for cassette **60** gives a bright blue emission. If efficient energy transfer occurred for compounds **60** and **61** then we were expecting them to emit yellow/green for fluorescein cassette **60** and red chemiluminescence for Nile Red cassette **61** instead, characteristic of fluorescein and Nile Red, respectively. This is exactly what we saw. Cassette **60** gave a bright yellow/green emission, while **61** glowed with a less intense red color. No trace of blue in the emission was seen in either case.

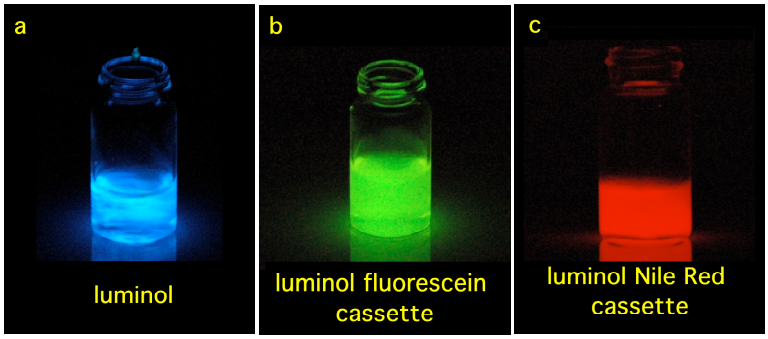

Figure 3.7. Pictures of **a** luminol**, b** cassette **60**, and **c** cassette **61** when activated with an oxidant.

Compounds **69** and **70** (Figure 3.8) were prepared as controls since it is thought that the excited species from luminol derivatives involves the corresponding phthalate dianions. Indeed, ESI-MS analysis of cassettes **60** and **61** after the oxidative activation revealed the presence of **69** and **70**, respectively. This was confirmed via HPLC analyses in the case of **60**.

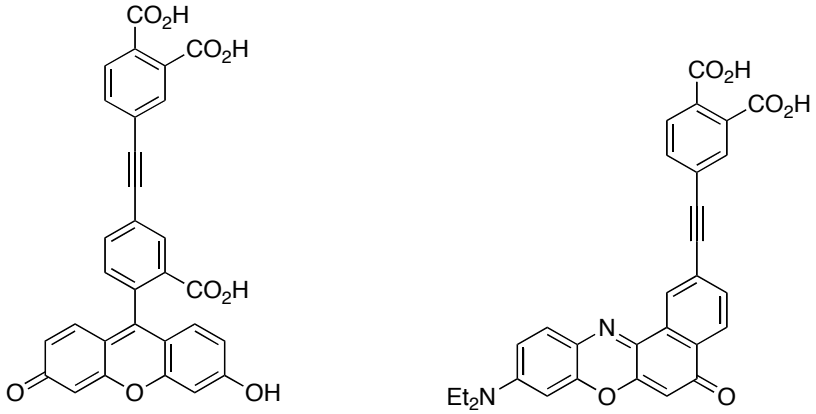

Figure 3.8. Control compounds **69** and **70**.

Figure 3.9a shows normalized UV absorption and fluorescence spectra for **69**, and **70**. The extent of overlap between the chemiluminescence output of the phthalate derived from luminol and the UV absorption of the acceptor part of cassettes **69** and **70** is shown in Figure 3.9b. Normalized chemiluminescence emissions for **60** and **61** are shown in

Figure 3.9c. The emissions of **60** and **61** are sharp and characteristic of the acceptors only; no chemiluminescence from the donor was detected.

a

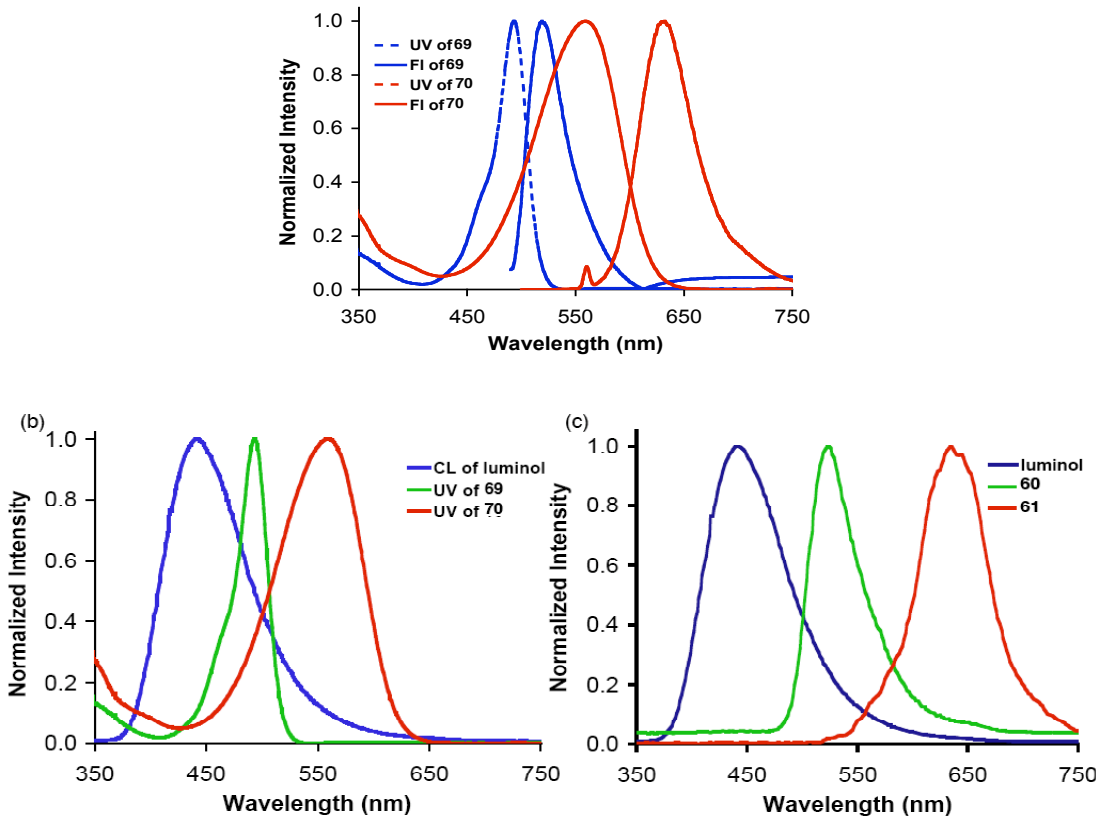

Figure 3.9. Normalized UV and fluorescence spectra of cassettes. **a** UV/visible and fluorescence spectra of **69** in pH: 10 aqueous sodium carbonate/bicarbonate buffer solution, and of **70** in dry DMF; **b** chemiluminescence spectrum of luminol (blue), UV/vis absorption bands of compound **69** (green) and compound **70** (red); **c** chemiluminescence spectra of luminol (blue), cassette **60** (green), and cassette **61** (red).

Sometimes, the eyes can play tricks on the brain, and that is partially true in this case. The chemiluminescence from cassette **61** appears to be weaker than that for **60**, but the quantitative data collected in Table 3.3 indicates this is not the case. Chemiluminescent quantum yields measured relative to luminol indicate **61** actually emits more strongly. Probably, chemiluminescence from **61** appears to be weaker than that from **71** because the human eye is about five times more sensitive to light near the emission maximum of fluorescein than it is to light emitted from the Nile Red acceptors.[129]

Table 3.3. Selected spectroscopic properties of luminol, **60**, **69, 61, 70** and **71**.

compound	UV	fluorescence	chemiluminesence	
	$\lambda_{abs\ max}$ (nm)	$\lambda_{fluor\ max}$ (nm)[b]	$\lambda_{chemi\ max}$ (nm)[b]	Relative Φ_{chemi}
luminol[a]	-	-	442	100[a]
60[a]	494	518	524	61[b]
69[a]	493	519	-	-
61[b]	558	628	634	>100[b]
70[b]	558	628	-	-
71	-	-	412	0.02[d]

[a] In carbonate/bicarbonate buffer. [b]In dry DMF. [c]From ref. 84.

The relative quantum yields for chemiluminescence that are presented in Table 3.3 use luminol as a standard. However, the donor fragments of cassettes **60** and **61** do not have the amino substituent of luminol. Small changes to the luminol structure tend to reduce its chemiluminescence dramatically.[119] If the emissions from cassettes **60** and **61** were compared with the hydrazide **71** (which has a much lower absolute quantum yield for chemiluminescence) then the data for cassettes **60** and **61** would appear to be even more impressive.

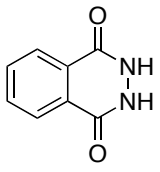

71

Experimentally, it is extremely challenging to determine the extent of energy transfer through bonds and through space in twisted but otherwise conjugated cassettes. For the UV-activated system **3** we asserted that through-bond energy transfer must be fast and

efficient by considering rates of energy transfer.[130] However, direct observation of rates is hard in chemically activated systems where excitation of the donor occurs continuously. Further, we have so far been unable to prepare the logical control compounds for comparison: those in which the alkyne linker of cassettes **60** or **61** are replaced by an ethylene fragment. In any case, *through-space* energy transfer for those controls might differ considerably from that occurring in **60** or **61** because the orientation of the donor and acceptor fragments would be dynamic in the reduced compounds. However, the *through-space* energy transfer cassette **72**, based on luminol, was prepared approximately four decades ago and does provide an interesting comparison.[131-133] The reported relative chemiluminescence quantum yield for this compound (luminol standard) is significantly less than that measured here for cassettes **60** and **61**. It may be that, just as in our UV-activated cassettes like **3**, rapid and efficient energy transfer can occur for the systems that facilitate the possibility of through-bond energy transfer.

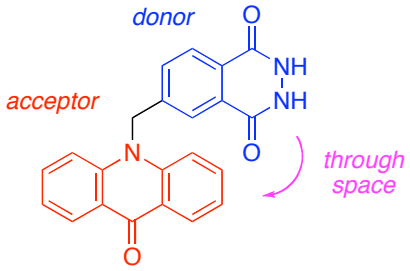

72
relative Φ_{chemi} = 8
(luminol = 100)

Calculations of Förster energy transfer for systems that have donor and acceptor fragments arranged within a few Ångstroms are not reliable because the theory implies a point dipole approximation which fails when the distance becomes less than the special size of the donor and acceptor charge distributions. Nevertheless, these calculations were performed; the dipole-dipole energy transfer efficiency was smaller (39 and 42% for **60** and **61**, respectively) than actually observed.

3.2.2 Conclusion

Chemiluminescence provides detection methods that approach the sensitivity of ones based on radioactivity.[134] In the context of intracellular imaging, it has the advantage that no excitation irradiation is required. Simple *in vitro* experiments show that cassettes **60** and **61** can be activated via treatment with peroxidase under physiological conditions, and they emit in longer wavelength regions that are more transparent to cellular tissues than the 420 - 450 nm range where luminol chemiluminesces. Consequently, there is a possibility that probes based on chemically activated energy transfer can be applied in biotechnology. Dr. Junyan Han performed most work in synthesis of chemiluminescent energy transfer cassettes.

CHAPTER IV

ENCAPSULATION OF ORGANIC FLUOROPHORES INTO WATER DISPERSIBLE NANOPARTICLES

4.1 Organic Fluorophores Encapsulated in Silica Nanoparticles

Recent work from several groups have shown that organic fluorophores can be encapsulated in silica nanoparticles thereby improving the photophysical properties of the fluorophores.[135-137] These particles can be prepared with a uniform size, often smaller than 50 nm as shown by transmission electron microscopy (TEM) and scanning electron microscopy (SEM). They are well dispersed in water and remain without aggregations for several months. Under similar excitation conditions, a single silica nanoparticle can emit as many photons as the number of dye molecules in the nanoparticles as compared to a single photon from the corresponding unencapsulated fluorophore resulting in better resolution.[138] The most promising characteristic of silica nanoparticles is that they are expected to be biologically inert and thus potentially non-cytotoxic for cellular imaging studies at concentrations below 0.1 mg/mL.[139]

4.1.1 Synthesis of Silica Nanoparticles

The synthesis of spherical silica nanoparticles can be broadly divided into two categories: (i) Reverse microemulsion and (ii) sol-gel synthesis. Reverse microemulsion relies on the controlled aqueous environment within surfactant-confined micelles in a nonpolar solvent such as cyclohexane to create monodisperse spherical colloids (Figure 4.1).[140] This method is used even today by various groups and has been shown to yield highly monodispersed particles suitable for incorporating nonpolar molecules into the silica matrix. The major drawback of this approach is the lack of non-covalent attachment of the fluorophore to the silica matrix, which results in leaching of the fluorophore out of the dye matrix over time, thereby reducing per particle brightness.[138]

This method of synthesis usually yields low amounts of silica nanoparticles and requires extensive washing procedures to remove surfactants.

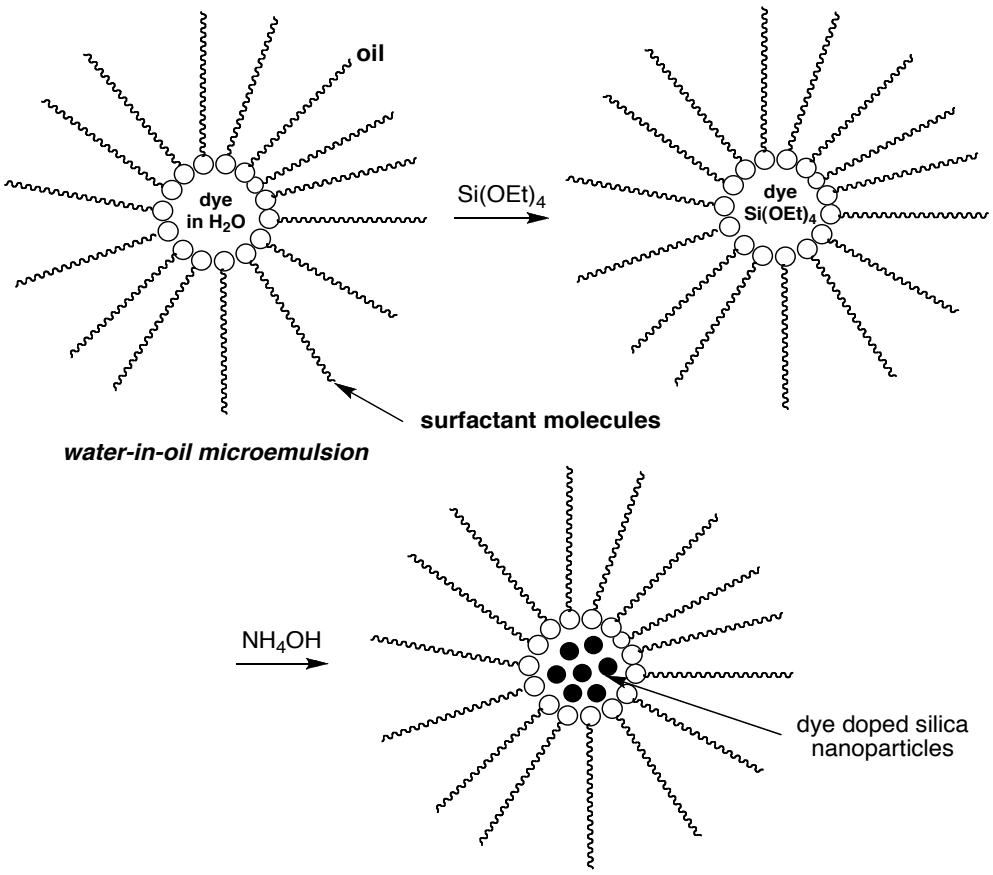

Figure 4.1. Microemulsion method for synthesis of silica nanoparticles.

In the late 1960s, Stoeber and coworkers developed a synthetic method for growing monodisperse 100 nm spherical silica nanoparticles based on sol-gel chemistry of silicon alkoxides.[141] This method involves hydrolysis and self-condensation of tetraethoxysilicate (TEOS) in EtOH in the presence of water and ammonia (used as a catalyst) to produce monodispersed 100 nm spherical silica nanoparticles. This method was improved upon by Van Blaaderen *et al.* to covalently incorporate organic fluorophores into the silica matrix by reacting them with organosilicates.[142,143] However, the particle size of silica nanoparticles obtained by these methods were always in the 100

nm region, which is much larger than an organic fluorophore or fluorescent proteins and therefore, the nanoparticles have limited use in cellular imaging studies.[144,145] In 2004, Weisner *et al.* reported the synthesis of fluorescent silica nanoparticles with hydrodynamic radii of 10-15 nm by modifying the procedure reported by Van Blaaderen *et al*. The procedure can be explained briefly as follows.[42]

An organic dye is conjugated via an isothiocyanate group or an activated carboxylic acid group to 3-aminopropyltriethoxysilane (APTS) at a molar ratio of 1:50 (fluorophore:APTS) in degassed absolute EtOH (Figure 4.2). The resulting solution is then diluted to a concentration of 1.7 x 10^{-5} M in an ethanolic ammonia solution and deionized water. This forms the silica core that is made up of the organic fluorophores. To this, a pure silica precursor tetraethoxysilane (TEOS) is added to grow the silica shell. The reaction is continued for 8 h and then further TEOS is added and allowed to react for a further 24 h period (total 32 h) followed by dialyzed to deionized water and stored. Particle size was determined by transmission electron micrography (TEM) and dynamic light scattering (DLS). In this particular example, tetramethylrhodamine isothiocyanate (TRITC) was used as a fluorophore.

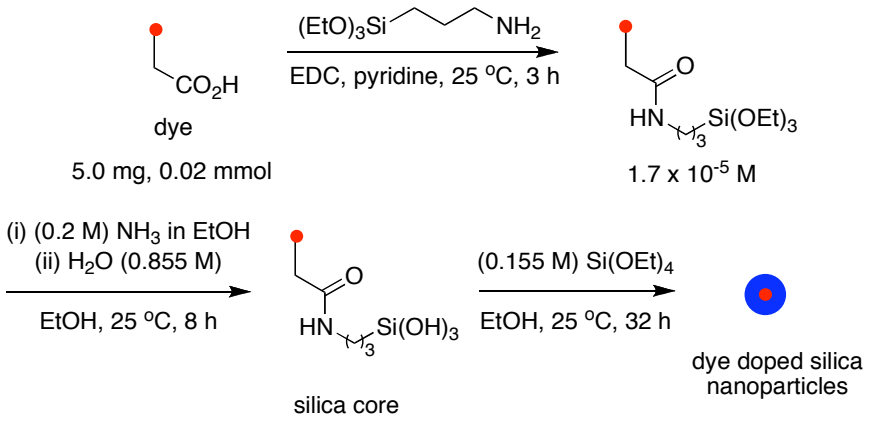

Figure 4.2. Covalent incorporation of dye molecule into silica matrix.

The versatility of this approach enables incorporation of various classes of organic fluorophores into the silica matrix. Figure 4.3 shows organic fluorophores encapsulated in silica nanoparticles using the above method. There are some report that suggest certain cyanine dyes that are particularly sensitive to reaction conditions used for silica nanoparticles synthesis cannot be incorporated due to their low synthetic stability.[146]

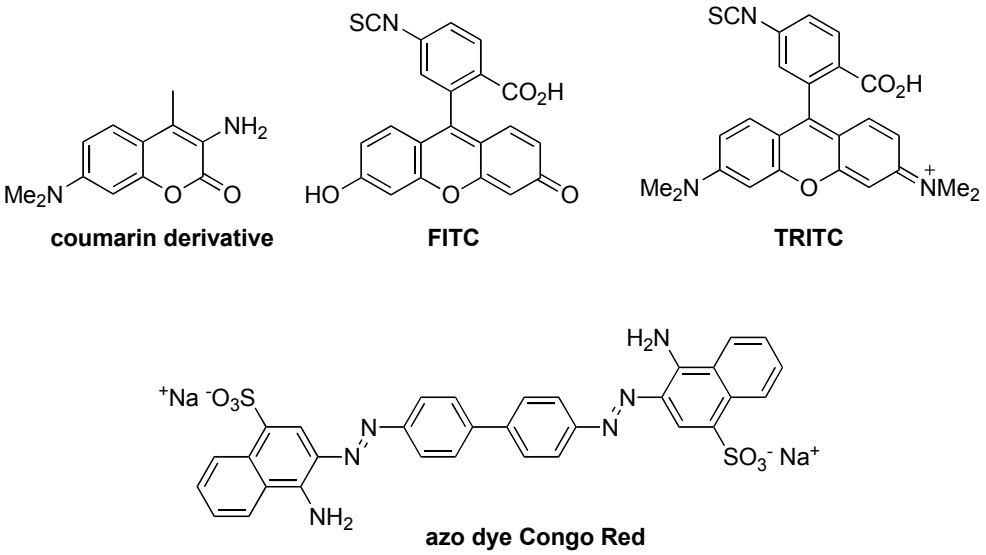

Figure 4.3. Structure of commonly used organic fluorophores for silica nanoparticle synthesis.

4.1.2 Photophysical Properties of Silica Nanoparticles

The photophysical properties of fluorescent silica nanoparticles were determined using multi-photon fluorescence correlation spectroscopy (FCS).[41,147] This technique is similar to dynamic light scattering (DLS) except that the fluorescence is analyzed instead of scattered light. The particle size of the nanoparticles can be calculated using the Stokes-Einstein equation, using the measured diffusion coefficients of the particles obtained by FCS.

$D = k_B T/6\pi\eta r$

D is diffusion coefficient, k_B is Boltzmann's constant, T is temperature in Kelvin, η is viscosity of the medium and r is the spherical particle radius.

The per particle brightness of the silica core containing multiple fluorophores is less than both the free fluorophore as well as the fluorescent silica nanoparticles. This can be attributed to the quenching effect, which is dominant when dye molecules are very near each other. The enhancement in the brightness of the silica nanoparticle is due to an increase in the radiative and a decrease in non-radiative decay rates of the fluorophores inside the silica shell. Silica also protects the fluorophore from external environmental factors such as oxygen, water and other solvent molecules, which are known to induce non-radiative decays. Most fluorophores usually undergo a solvatochromic shift, a change in fluorescence emission with respect to solvent. This shift is owing to the changes in excited state energies in solvents with different polarities and is more prominent in polar solvents. Fluorophores encapsulated in silica nanoparticles are completely devoid of this shift; this proves that the fluorophores in silica nanoparticles are effectively removed form the external solvent environment and therefore produce a consistent fluorescence output in any solvent. The silica shell is also beneficial in reducing photobleaching of the fluorophore; in most cases a two-fold enhancement in photostability is reported because of the protection given by the silica shell.[148]

Comparison of brightness of fluorescent silica nanoparticles with quantum dots shows that their brightness is 2-3 times less than quantum dots. An organic fluorophore is 30 times less bright than quantum dots and is also prone to photobleaching. This result shows that an organic fluorophore can be encapsulated in silica to enhance its brightness significantly and comparable to quantum dots. An advantage of silica nanoparticles over quantum dots is that quantum dot fluorescence occurs by single exciton transitions whereas in silica nanoparticles the multiple dye molecules within the particles each absorb and emit independently. This overcomes the issues of stochastic blinking suffered by quantum dots by providing multiple emitters within a single silica particle.[138] Furthermore, the silica matrix ensures that the dye molecules are separated from each other to avoid self-quenching. Each particle core is separated from its neighbors by twice the pure silica thickness creating high spatial emitter density without permitting energy

transfer between neighboring fluorophores.[138] The dense packing of silica nanoparticles also helps in brightness enhancement, which is not possible with organic fluorophores. Most water-soluble organic fluorophores have a reduced fluorescence output in water when compared to their output in organic solvents; and this reduces their applicability in cellular imaging. This drawback coupled with synthetic difficulties in imparting water-solubility makes them less attractive for single molecule detection studies. Fluorescence of silica nanoparticles is independent of the solvent media and can replace traditional organic fluorophores for such studies.

4.1.3 Surface Modification of Silica Nanoparticles

The surface of silica nanoparticles is amenable to chemical modification due to the presence of reactive hydroxyl groups. This is an advantage for performing fluorescent bioassays and bioimaging wherein these particles can be conjugated to different biomolecules such as proteins, antibodies and oligonucleotides via functional groups on their surface and specificity in targeting can be achieved.[149] These functional groups also serve to improve the water disperability of particles and prevent aggregation. Introduction of polyethylene glycol (PEG) on the surface of silica nanoparticles is a common way to improve water solubility. PEG also serves to improve the colloidal stability of nanoparticles and therefore increases their bench life (Scheme 4.1a).[150] Sulfonic acid groups can also be introduced onto the silica surface by reaction with corresponding trimethoxysilyl aminopropyl thiol followed by oxidation with peroxide (Scheme 4.1b).[151]

Carboxylic acid groups serve to improve water-solubility and are a suitable handle for conjugation to proteins and other biomolecules. The negative charge on a carboxylate group helps reduce aggregation and keeps the particle in a monodispersed state. Reaction with carboxyethylsilane triol in pH 7.4 sodium phosphate buffer affords carboxyl modified particles in quantitative yields (Scheme 4.1c).[35]

Scheme 4.1. Surface modification of silica nanoparticles with (**a**) PEG and (**b**) sulfonic acid and (**c**) carboxyl groups.

a

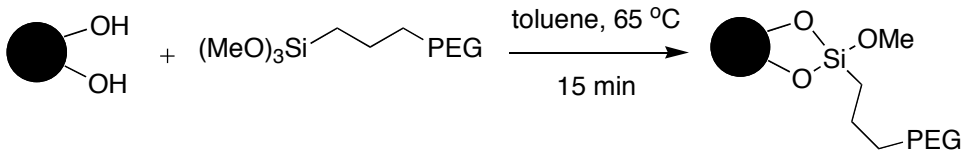

b

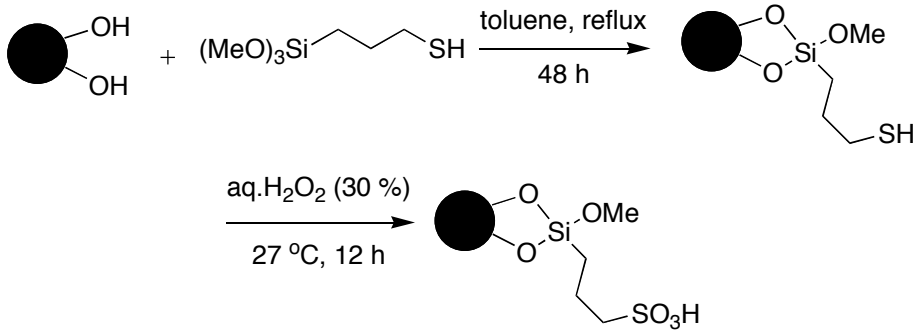

c

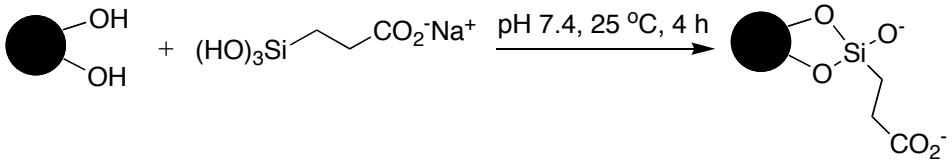

The introduction of amino groups on the surface of silica nanoparticles is straightforward.[152] Reaction of 3-aminopropyltriethoxysilane (APTS) with silica nanoparticles in toluene at 95 ^{o}C for 3 h yields amine functionalized nanoparticles in quantitative yield (Scheme 4.2). Amino group is particularly attractive because it can be readily coupled with carboxylic acids on proteins and antibodies. A similar approach also yields alkyne and azide terminated linkers on the surface which can be used for performing 1,3-cycloaddition reactions with modified proteins or biotin substrates. It is also possible to quantify the amine moiety on a silica surface by performing the Fmoc test. Briefly the amine-functionalized nanoparticles in anhydrous DMF is added to a solution of FmocCl DMF. The mixture is stirred overnight under nitrogen for the reaction to go to completion and washed thoroughly with MeOH and dried. The dried

nanoparticles are weighed and redispersed in DMF by sonication. To this solution piperidine is added and reaction continued for 20 min. Amine quantification is performed using standard Fmoc protocol by detecting the UV absorbtion of the supernatant solution at λ = 300 nm after centrifugation at 13000 rpm for 20 min. The extinction coefficient at this wavelength is 7800 $M^{-1}cm^{-1}$.[153]

Scheme 4.2. Surface modification of silica nanoparticle with amino, azido and alkyne groups.

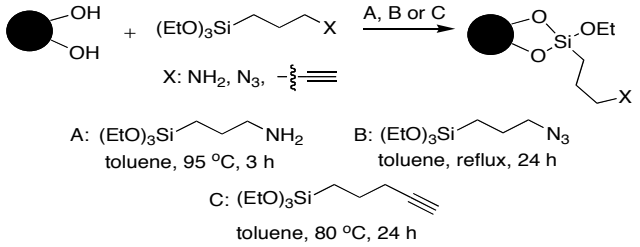

Folic acid, also known as vitamin B9, is a vital vitamin for survival and proliferation of animal cells. Animal cells cannot produce folic acid and therefore express folate receptors, which can capture exogenous folates. Cancerous cells overexpress these receptors because of rapid cell division. Any biomarker used for tracking such cancerous cells will be easily taken up if its surface is conjugated to folic acid. Amine functionalized fluorescent silica nanoparticles can be conjugated to folic acid using carbodiimide chemistry and used for detection of cancer cells (Scheme 4.3).[154]

Scheme 4.3. Folic acid conjugation to silica nanoparticles.

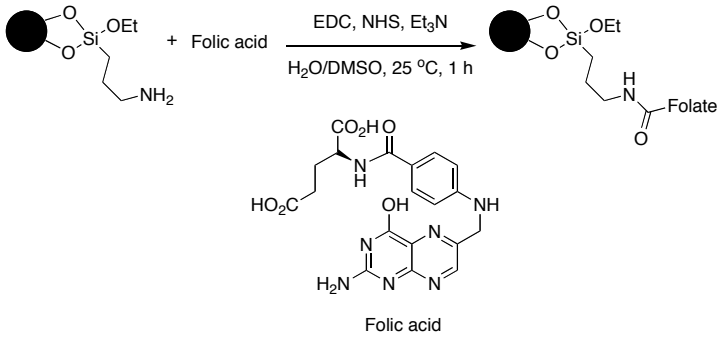

Folic acid is insoluble in water so it is important not to overload silica nanoparticles with folic acid to prevent aggregation. Presence of one or two folic acid molecules on a single nanoparticle is enough for cancer cells to uptake these particles.

Surface characterization of silica nanoparticles is done by solid-state ^{29}Si NMR, IR spectroscopy and X-ray diffraction (XRD). Silicon-29 NMR is used to probe detailed solid-state chemistry of silica materials. The chemical shift of various silica groups spans 120 ppm, which allows all types of chemical functionalities to be readily observed. Presence of different functional groups on the surface changes the chemical environment of silica that can be detected by ^{29}Si NMR. IR spectroscopy is used to determine the presence of different functional groups on the surface. XRD is a non-destructive technique, which reveals information about chemical composition and physical properties of materials. The diffraction pattern formed when X-rays are focused on a material is interpreted to give information about the surface morphology and chemical composition.

4.1.3 Toxicology Studies on Fluorescent Silica Nanoparticles

Toxicity is a major roadblock in implementing any imaging agents for clinical use. This is evident from the fact that even though quantum dots are the brightest imaging agents available, they are not widely used due to the toxicity of heavy metals associated with such particles. The cytotoxicity and genotoxicity studies of fluorescent silica nanoparticles on A549 cancer cell lines suggests that they are safe to use at the molecular and cellular levels below 0.1 mg/mL and cells live at least 24 h after exposure to silica nanoparticles.[139] Labeling of the A549 cancer cell line with 50 nm silica nanoparticles results in an induction of DNA repair protein which prevents DNA injury, and therefore, less genotoxicity. Cell death observed when working with concentration of nanoparticles above 0.1 mg/mL were mainly due to cellular organelle destruction rather than genome damage. However, accumulated silica can cause chronic or acute toxicity in animal models if exposed for a longer period of time (weeks), which is of less

concern because imaging experiments are usually done for not more than 3 days. Cytotoxicity is more prevalent with aggregated particles than with monodispersed ones. The surface charge of silica nanoparticles, which is negative at physiological pH, helps to prevent aggregation due to repulsion between like charges. Several studies also indicate that fibroblast cells with long doubling time (average time between two cell divisions) are more prone to injury induced by silica nanoparticles than tumor cells with short doubling time,[139] which suggests that the cytotoxicity of silica nanoparticles also varies depending on the cell lines used. Experiments on cultured human bronchoalveolar carcinoma-derived cells with 15 nm and 46 nm silica nanoparticles reveal that dosage levels between 10-100 μg/mL for a period of 48 h decreased cell viability in a dose dependent manner. Cell deaths were observed even at the lower limit 10 μg/mL.[45]

Nanoparticles with sizes ranging from 10-50 nm have large specific surface area and are not affected by gravitational force. This may raise a potential problem for in vitro imaging studies in which the cell adhering to the bottom of the culture vessel is not exposed to the majority of nanoparticles in suspension. Thus, we may assume the effective dose (the number or mass of particles that actually affect the cells) is different from the administered dose. A detailed experimental study on three different cell lines (A549 epithelial cells, EAHY926 endothelial cells, and J774 monocyte-macrophage) with silica nanoparticles proved otherwise.[155] This is because the majority of particles reach the cell and induce cytotoxicity due to the convection force usually present in solution. Although a minor finding, this shows that the toxicity observed is mainly due to the entire administered dose of nanoparticles.

Available reports on toxicological effects show that colloidal silica is less toxic than crystalline forms in animal models. There are studies suggesting that colloidal silica with particle size less than 100 nm induces greater lung inflammation and lung damage than larger particles in mice. These studies were carried out by intratracheally administering silica nanoparticles of different sizes to mice models. Fluorescent silica nanoparticles

with average particle size of 30 nm showed no apparent toxicity in mice when administered through tail vein injection. The discrepancy with previous studies is likely due to the different administration route. Intraperitonial administration of silica nanoparticles (particle size 50 nm) into mice and examination after four weeks revealed their presence in brain indicating that such particles can cross blood-brain barrier without disturbing its function. The particles were present in various organs without producing any toxicity.[153]

4.1.4 Biological Applications of Fluorescent Silica Nanoparticles

One important method for determining spread of cancer is sentinel lymph node mapping which helps in performing more accurate biopsies and gaining information that reduces the amount of surgery needed. It is usually done by injecting an imaging agent or a radioactive tracer into the tumor site and visualizing the tracer as it drains into the lymphatic basin. The sentinel lymph node collects the imaging agent and can be removed for biopsy. Further analysis of the node may reveal whether or not the lymph nodes contain any cancer cells and provides an efficient means to monitor the spread of cancer through the body. Mapping experiments with fluorescent silica nanoparticles were able to detect sentinel lymph nodes with much greater accuracy and can be substituted for radioactive tracers, which is associated with long term side effects.[44]

The surface of fluorescent silica nanoparticles can be easily modified to attach different functional groups and molecules. This is an advantage for applications such as imaging cancer cell lines to determine their response to various therapeutic drugs. Fluorescent silica nanoparticles that were surface functionalized with cell penetrating peptides were used to label the cells and track metastatic prostate carcinoma cells through the body.[44]
The interaction between cancer cells and bone marrow cells is a field of intense research due to the findings that such interaction induces osteoclastogenesis, a type of bone metastase in the bone microenvironment. These interactions were tested by labeling prostate cancer cells and bone marrow cells in vivo using TAT-conjugated fluorescent

silica nanoparticles loaded with fluorophores emitting at different wavelength. The localization of the silica nanoparticles were detected by multiphoton microscopy and showed that the cancer cells and bone marrow cells are co-localized which results in metastasis of bone.

Silica nanoparticles are also used for photodynamic therapy (PDT) of certain types of cancer.[156] Photodynamic therapy is a targeted treatment and involves administering photosensitizers, a molecule which can be activated by an appropriate wavelength of light from the UV-Vis region, to the malignant tissue. The irradiation of light results in formation of reactive oxygen species (ROS), which are toxic to cells and tissues. PDT is very selective in its mode of action because the cancerous cells take up more of the photosensitizer and retain them for a longer duration of time than normal cells. Commonly used photosensitizers such as 5-aminolevulinic acid and methyl aminolevulinate are hydrophobic in nature and no one has yet developed a formulation that can be easily injected *in vivo*. Silica nanoparticles with covalently attached photosensitizer molecules were prepared and *in vitro* treatment with RIF-1 cancer cells, a human colon cancer cell line, shows ready uptake of these particles which then show phototoxicity upon irradiation with light, thus demonstrating the potential use of these nanoparticles for PDT.[157]

Targeted delivery of therapeutic drugs and imaging agents, which involves delivering medication in a manner that increases the concentration of the medication at the required site relative to others, has become a very important part of cancer diagnosis and treatment. This not only improves efficacy of the drug, but also reduces side effects associated with treatment. Silica nanoparticles stand out as an ideal platform for preparing such targeted delivery systems because their surface can be synthetically modified to accommodate many functional groups that can be attached to targeting ligands. Any desired drug, polar or nonpolar, and imaging agent can be covalently incorporated into silica nanoparticles, and after modifying the nanoparticle surface with

appropriate ligands, they can be used for treatment and diagnosis. In one such example, 20 nm fluorescent silica nanoparticles were conjugated to biotargeting molecules such as Transferrin[158], anti-claudin 4 and antimesothelin via a carboxyl functional group on their surface. Confocal microscopy studies were performed to monitor the uptake of these particles in pancreatic cancer cell lines *in vitro*. It was shown that the uptake is greatly enhanced with bioconjugated silica nanoparticles as compared to the non-bioconjugated ones. The enhanced efficiency is due to the receptor-mediated uptake of these bioconjugated nanoparticles with their corresponding receptors, which are known to be overexpressed on the surface of the cell line used.

Surface modified silica nanoparticles are used in protein purification studies. Tetramethylrhodamine doped silica nanoparticles (particle size 23 nm) were surface modified with nitrilotriaceticacid (NTA) and exposed to $NiCl_2$ to generate fully functionalized (Ni-NTA) nanoparticles. Ni-NTA is known to have great affinity for histidine-tagged proteins, and if exposed to a cell lysate containing many different proteins, will selectively react with only histidine-tagged proteins. Thus, fluorescent silica nanoparticles with Ni-NTA surface functionality, when exposed to a cell lysate containing histidine-tagged protein (in this case Estrogen receptor, ERα) as a minor component, showed very high binding specificity enabling protein purification in a single step. Such studies cannot be performed using organic fluorophores because their fluorescence is often quenched in presence of metals like Nickel.[159]

Use of silica as a host material for encapsulating fluorophores looks promising due to the number of biological applications reported based on them. Improving the performance of organic fluorophores by encapsulating them in water-dispersible silica nanoparticles will significantly reduce the cost of synthesis of water-soluble fluorophores because any nonpolar organic fluorophore can be encapsulated in silica. By combining functionalities such as targeting, imaging and treatment, silica nanoparticles can be envisioned as a "guided missile" for selectively attacking cancerous cells without affecting normal cells.

These particles would give feedback on the activity of the therapeutic agents rather than simply identifying the cancerous cells.

4.1.5 Results and Discussions

Some of the TBET cassettes prepared in our laboratory showed poor energy transfer efficiency and low fluorescence quantum yields in aqueous media in spite of having water-soluble groups, presumably due to aggregation induced fluorescence quenching. We hypothesized that encapsulating such cassettes in silica nanoparticles will minimize their interaction with external solvents and will enable them to fluoresce with improved energy transfer efficiency. Described here is research undertaken to compare the properties of the energy transfer cassettes **43**, **44**, **73**, and **74** encapsulated in silica with the free fluorophores in solution (Figure 4.4). The acceptor fragments of these cassettes were also encapsulated in silica nanoparticles to study the improvement in photophysical properties in aqueous media (Figure 4.5). Silica nanoparticle are easily dispersible in water and therefore provide an alternate pathway for solubilizing any organic fluorophore in aqueous media.

This project is part of a broader effort to produce fluors that can absorb UV strongly at a convenient wavelength (*eg* 488 nm), and emit it efficiently at much higher wavelengths. Our experience has been that it is relatively easy to prepare cassettes that do this in organic media, much harder to make them water soluble, and extremely difficult to design water-soluble cassettes that have good quantum yields in aqueous media. This goal was reached for some cassette designs, but **43**, **44**, **73**, and **74** are illustrative of ones that *failed* to reach it, primarily for solubility reasons (Figure 4.4). Cassette **73** in pH 7.4 phosphate buffer has poor solubility, even for fluorescence experiments, and it dissolves extremely slowly. The other cassettes are even less soluble in aqueous media. Thus, we sought to understand how encapsulation of these cassettes in silica nanoparticles would impact their compatibility with aqueous media. Further, the influence of nanoparticle

formation on the photophysical properties of these "through-bond energy transfer cassettes" was an unknown that was to be probed in this study.

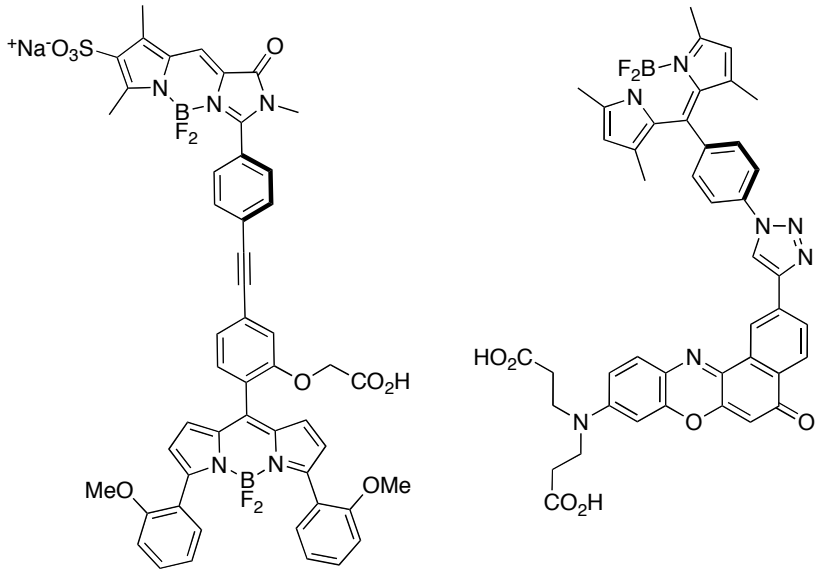

73 **43**

74; n = 0, **44**; n = 1

Figure 4.4. Structure of cassettes encapsulated in silica.

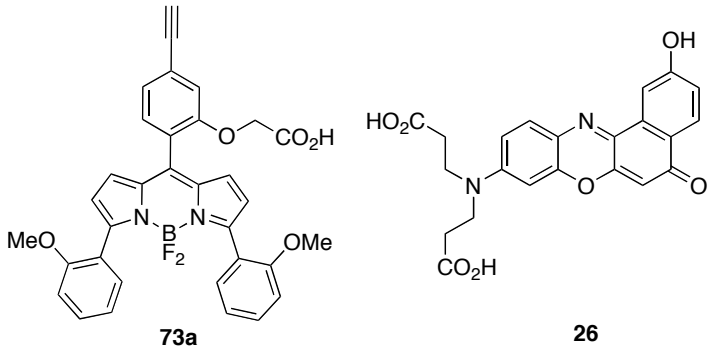

73a **26**

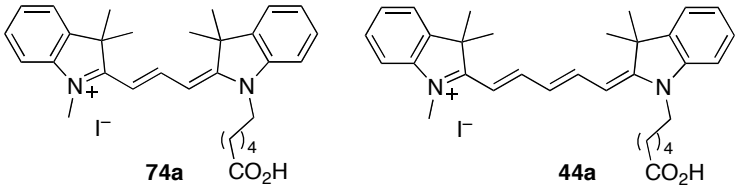

Figure 4.5. Structure of acceptors of cassettes encapsulated in silica.

4.1.5.1 Synthesis

The encapsulation of cassettes and corresponding acceptors were achieved by following a reported procedure by Wiesner *et al* (Scheme 4.4).[41,42] The organic dye is conjugated via activated carboxylic acid group to 3-aminopropyltriethoxysilane (APTS) at a molar ratio of 1:50 (fluorophore:APTS) in degassed absolute EtOH under nitrogen. The above dye solution (0.14 mL, 1.7 x 10^{-5} M) was added to EtOH along with water (1.52 mL, 1.71 M) and NH_3 in EtOH (5.0 mL, 0.2 M) at 25 ^{o}C to make up a final volume of 50 mL and stirred for 12 h at 25 ^{o}C. TEOS (1.63 mL, 0.155 M) was then added in aliquots of 0.4 mL every fifteen minutes and stirring continued for another 12 h at 25 ^{o}C. The resulting silica nanoparticles were dialyzed into EtOH to remove unreacted starting materials. Further dialysis was performed to transfer the formed silica nanoparticles from EtOH to deionized water and finally to pH 7.4 (0.1 M sodium phosphate buffer). Consequently, it was possible to study the encapsulated cassettes in aqueous media whereas the parent systems are insufficiently soluble to do this.

Scheme 4.4. Syntheses of dye doped silica nanoparticles.

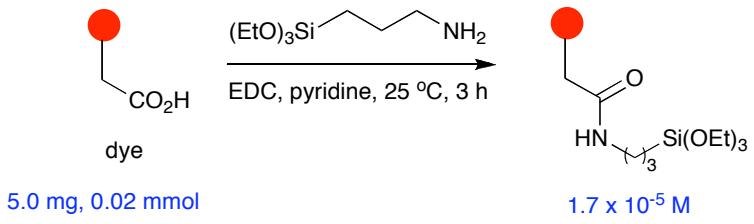

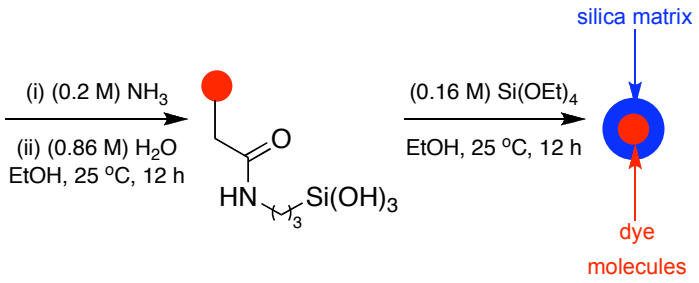

Transmission electron microscopy (TEM) images were obtained for the synthesized nanoparticles (Figure 4.6). Particles were spherical, well dispersed, and homogeneous in size with an average diameter of 20-24 nm. The silica nanoparticles did not undergo any degradation in spite of continuous exposure to the electron beam from the TEM instrument thereby proving to be a robust encapsulation material. The TEM measurements were performed by Dr. Hansoo Kim from the micropscopy and imaging center at Texas A&M University.

a

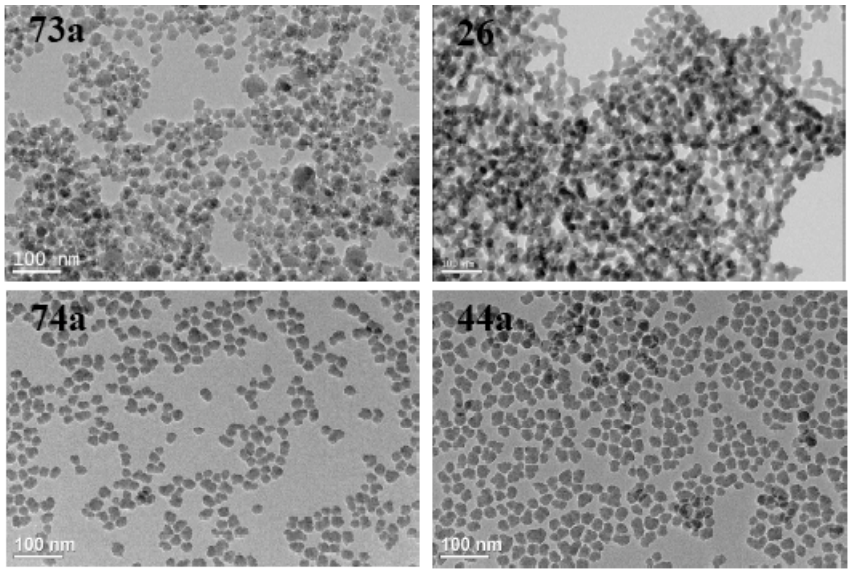

Figure 4.6. Transmission electron microscopy (TEM) images of (**a**) acceptors and (**b**) cassettes. Particle size: 20-24 nm.

b

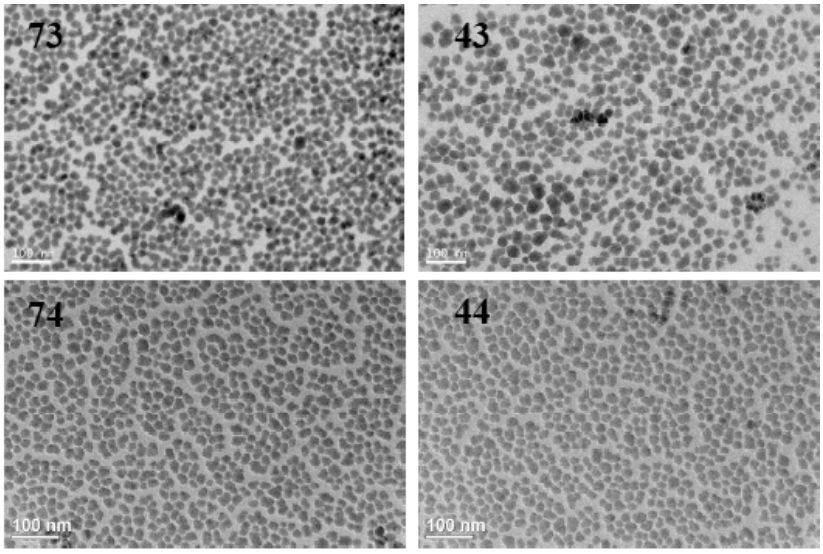

Figure 4.6. Continued.

4.1.5.2 Photophysical Properties

The absorbance and emission maxima of the acceptors **26**, **44a**, **73a**, and **74a** encapsulated in silica nanoparticles and dispersed in pH 7.4 phosphate buffer are shown in Figure 4.7a and 4.7b. Figure 4.8a shows the normalized absorbance of the particles from cassettes **43**, **44**, **73**, and **74** under the same conditions. The cassettes each have two distinct absorbance maxima corresponding to their donor and acceptor fragments. Direct comparison of the free and encapsulated cassettes in phosphate buffer is not possible because the unencapsulated systems are insufficiently soluble. For this reason, the following discussion compares the free cassettes in EtOH with the corresponding nanoparticles in phosphate buffer. Encapsulation in silica did not change the relative intensities of the donor and acceptor absorption peaks relative to the free cassettes (in EtOH, please see Appendix C). We have defined the ratio of the fluorescence quantum yields of cassettes when excited at the donor to that when excited at the acceptor as the *energy transfer efficiency* (ETE). This parameter for the encapsulated cassettes is very high: 74 – 93 %. However, the overall quantum yield decreases in the order **73** > **43** > **74** > **44**. In other words, the overall quantum yields for the cassettes excited at the donors are a function of the ETE, and the quantum yields of the acceptor fragments.

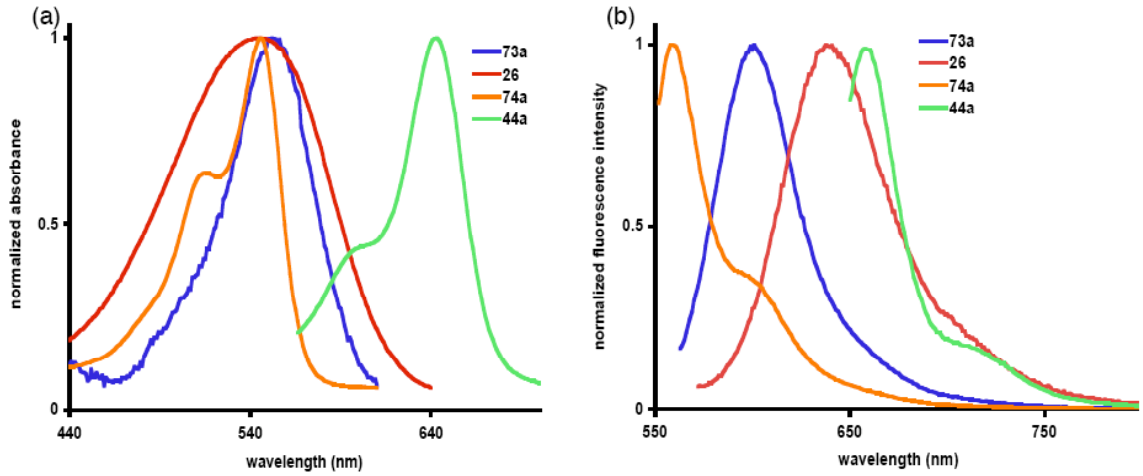

Figure 4.7. Normalized absorbance (**a**) and fluorescence (**b**) of acceptors encapsulated in silica in pH 7.4.

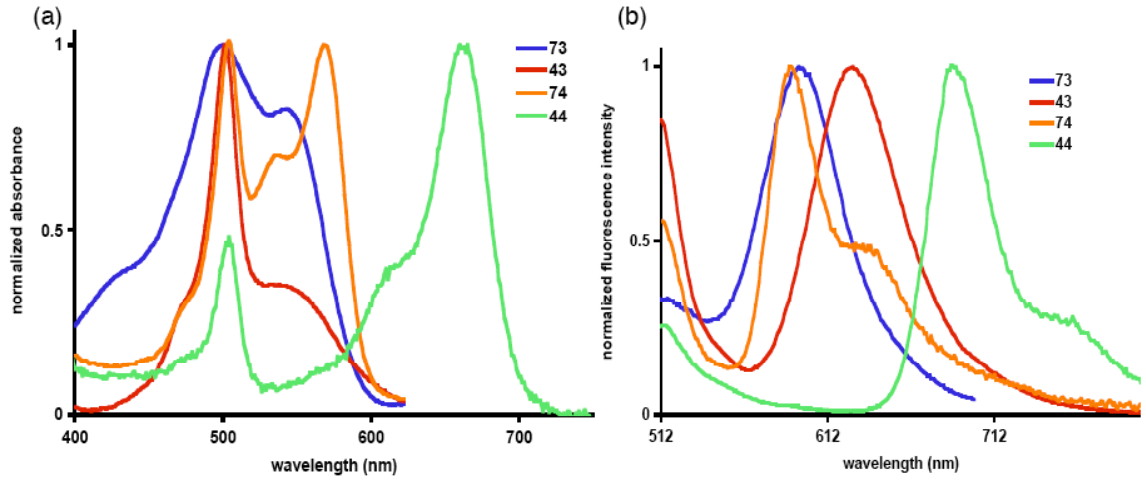

Figure 4.8. Normalized absorbance (**a**) and fluorescence (**b**) of cassettes encapsulated in silica in pH 7.4.

The quantum yields of these acceptors in silica nanoparticles, except Nile Red acceptor **26** showed marked improvement in aqueous media (Table 4.1). Particularly acceptor **74a** showed a ten fold improvement in quantum yield as compared to the bare dye in aqueous media, which is reported to have a quantum yield of 0.037.[160,161] The Nile Red acceptor **26** is water-soluble and the fluorescence quantum yield does not improve upon encapsulation in silica nanoparticles. The acceptors **73a** and **44a** are by themselves

insoluble in water and therefore nonfluorescent. Encapsulating these acceptors in silica nanoparticles not only made them water-soluble but also fluorescent.

Table 4.1. Photophysical properties of acceptors encapsulated silica in pH 7.4.

dye	λ_{abs}(nm)	$\lambda_{em.}$(nm)	fwhm (nm)	Φ
73a	548	601	49	0.32+/-0.01[a]
26	532	637	57	0.27+/-0.01[a]
74a	550	566	37	0.30+/-0.02[a]
44a	646	666	39	0.09+/-0.02[b]

Standards used for quantum yield measurement: [a]rhodamine 6G (Φ 0.92 in EtOH); [b]Nile Blue (Φ 0.27 in EtOH). Quantum yields were measured three times and averaged.

Encapsulating these cassettes in silica nanoparticles made them easily dispersed in water. Cassettes **43** and **44** have quantum yields of 0.31 and 0.18 when excited at the donor in pH 7.4 buffer (Table 4.2). However, the quantum yields of cassettes **73** and 7**4** when excited at the donor were very low, even after encapsulation. Both these cassettes showed good energy transfer in pH 7.4 phosphate buffer, so energy loss can be attributed to the acceptor fragments.

Table 4.2. Energy transfer efficiency of cassette encapsulated silica in pH 7.4.

dye	λ_{abs}(nm)	$\lambda_{em.}$(nm)	Φ_D[a]	Φ_A	ETE % (Φ_D/Φ_A)
73	499, 544	597	0.31+/-0.02	0.33+/-0.01[a]	93
43	502, 539	512, 627	0.18+/-0.03	0.24+/-0.02[a]	74
74	504, 568	592	0.04	0.05[b]	78
44	504, 659	687	0.02	0.03[c]	81

Φ_D: quantum yield of cassette when excited at the donor absorbtion maxima. Φ_A: quantum yield of cassette when excited at the acceptor absorbtion maxima. Standards used for quantum yield measurement: [a]rhodamine 6G (Φ 0.92 in EtOH); [b]rhodamine 101 (Φ 1.0 in EtOH); [c]Nile Blue (Φ 0.27 in EtOH). Quantum yields were measured three times and averaged.

Photostabilities of dyes used for intracellular imaging is a significant issue; probes that readily photobleach tend to be less useful. The photostability of the encapsulated cassettes **73**, **74** and acceptor **74a** were studied and compared to the corresponding bare cassettes and acceptor. In all cases the encapsulated fluorophores were found to be more photostable than the unencapsulated ones. Photobleaching, which is usually a result of interaction between the fluorophore and dissolved oxygen in the solvent, is less severe in the encapsulated silica nanoparticle. The silica matrix protects the encapsulated fluorophore from dissolved oxygen, which often leads to photobleaching (Figure 4.9). An argon ion laser (Spectra-Physics) fitted with notch filter to remove 514 nm wavelength light was used to perform the photostability studies and samples were irradiated with 488 nm wavelength light with power density of 1.2W/cm^2 for **73** and 12W/cm^2 for sample **74a** and **74**.

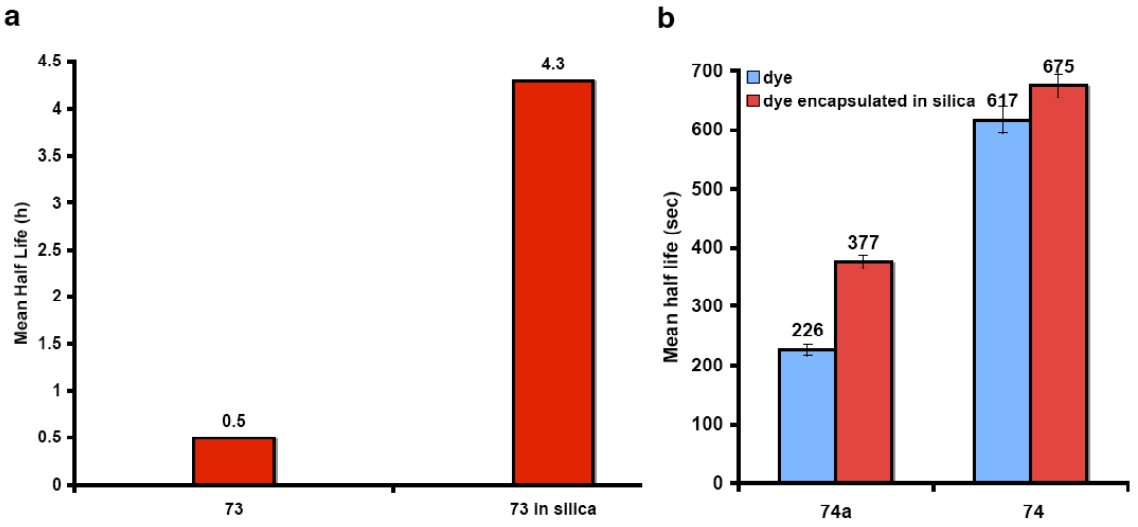

Figure 4.9. Photostability studies of silica nanoparticles. (**a**) Half life for cassette **73** and cassette **73** doped silica nanoparticles and (**b**) half life comparison for acceptor **74a** and cassette **74**.

4.1.5.2 Cellular Imaging Studies

Cassettes **73** and **74** encapsulated in silica nanoparticles were used for *in vitro* cellular imaging studies with COS7 cells. Incubation with 0.02 mg/mL (**73**) and 0.01 mg/mL (**74**) of the silica nanoparticles in pH 7.4 phosphate buffer at 37 ^{o}C for 2 h resulted in efficient uptake of these particles. Upon excitation at 488 nm, no significant output was observed in the green channel (503 – 553 nm; Figure 4.10a) but strong fluorescence was observed in the red one (575 – 625 nm; Figure 4.10b) for cassette **73**. This demonstrates that the encapsulated cassette **73** gave good energy transfer *inside cells*. The ETE for the encapsulated cassette **74** was less than for **73** (78% relative to 93%, see Table 4.2) so for this probe emission from the green and red channels was expected, and it was observed (Figure 4.10c and 4.10d). No significant cytotoxicity was observed after uptake of either of these nanoparticles types, however some vacuoles could be observed (yellow arrows in Figure 4.10b) indicative of some adverse effects on the cells at this particle concentration.

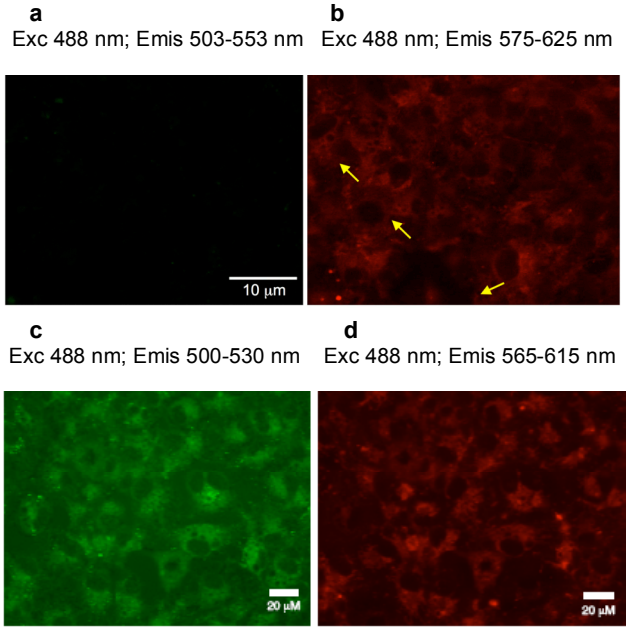

Figure 4.10. Cellular uptake of cassette (**a**) **73** and (**b**) **74** doped silica nanoparticles. Intracellular fluorescence of SiO_2-nanoparticles from cassette **73** excited at 488 nm and observed at: **a** 503 – 553 nm; and, **b** 575 – 625 nm. Images **c** and **d** are the corresponding ones for SiO_2-nanoparticles from cassette **74**.

4.1.5 Conclusion

In conclusion, we have shown that cassettes that have very poor water solubility can be encapsulated in silica nanoparticles, and they can be easily dispersed in water. SiO_2-encapsulation of the cassettes **73** and **74** improved their photostability with respect to photobleaching. The silica nanoparticles could be imported into cells without use of reagents to induce this, and without noticeable levels of cytotoxicity. Leaching of the dyes out of the silica nanoparticles would be highly unlikely since they are covalently attached to the silica when the nanoparticles are formed. Methods to provide surface modifications of silica nanoparticles are known.[162,163] Consequently, this work may lay foundations for applications of encapsulated energy transfer cassettes in intracellular imaging.

4.2 Encapsulation of Organic Fluorophores in Calcium Phosphate Nanoparticles

Many advances have been achieved in diagnosis as well as treatment of diseases each with its own level of sensitivity and efficacy. Early detection and treatment is the best way to confront any type of disorder and developments of tools to accomplish this simultaneously are always in the forefront of research. Recent advances in our knowledge of nanoparticles such as gold, iron oxide, polymer, silica have paved the way for many new technologies to be utilized in biological assays in basic research setup. They have the potential to radically change cancer therapy by allowing for effective and targeted drug delivery by overcoming the many biological, biophysical and biomedical barriers an animal model presents against conventional drugs and imaging agents. These particles help us to detect cells and biomolecules that cannot be detected by conventional imaging agents. The ability to clearly observe changes in a cancer cell is critical to the success of any treatment. To realize their full potential, as a potent tool for widespread application in clinical trials and eventually on humans requires a deeper understanding of their mode of action and the toxicity associated with such nanoparticles. Ensuring that nanoparticles are safe for use in humans will be a key factor in determining their impact

on imaging and treatment. Concerns are growing as to whether they have unintended consequences when exposed to humans or the environment.

4.2.1 Calcium Phosphate Nanoparticles Synthesis

4.2 Encapsulation of Organic Fluorophores in Calcium Phosphate Nanoparticles

Calcium phosphate is a biomineral present in the body mainly in bone and tooth enamel. It is distributed in intra and extracellular spaces and also in blood streams in millimolar concentrations.[164] It plays important roles in blood clotting, nerve impulse transmission, muscle contraction and enzyme regulation[165,166] mediates constriction and relaxation of blood vessels[167] and the secretion of hormones.[168] Their presence in the human body and their biodegradability makes them safe in handling and administering. Moreover they can be easily cleared from human body once imaging is done unlike other agents. Calcium phosphate is stable at physiological pH and becomes completely soluble at pH levels below 5.5,[47] which makes it an efficient transporter of bioactive agents.

4.2.1 Calcium Phosphate Nanoparticles

Nanoparticles have the potential to change cancer diagnosis by allowing detection of cells and biomolecules that cannot be traced by conventional imaging agents. Development of such nanoparticles with low cytotoxicity is the focus of this section. Some early literature reports describes syntheses of plasmid DNA loaded calcium phosphate nanoparticles.[169] Water in oil microemulsion method is used to synthesize these nanoparticles. They range in size from 30-40 nm. Recently Adair *et al* reported a similar method to encapsulate hydrophobic and hydrophilic organic fluorophores in calcium phosphate nanoparticles with an average particle size of 16-20 nm.[46,170] The calcium phosphate shell apparently improves the colloidal stability and the photophysical properties of the encapsulated fluorophore.[171] Figure 4.12 shows fluorophores encapsulated in calcium phosphate nanoparticles.[170]

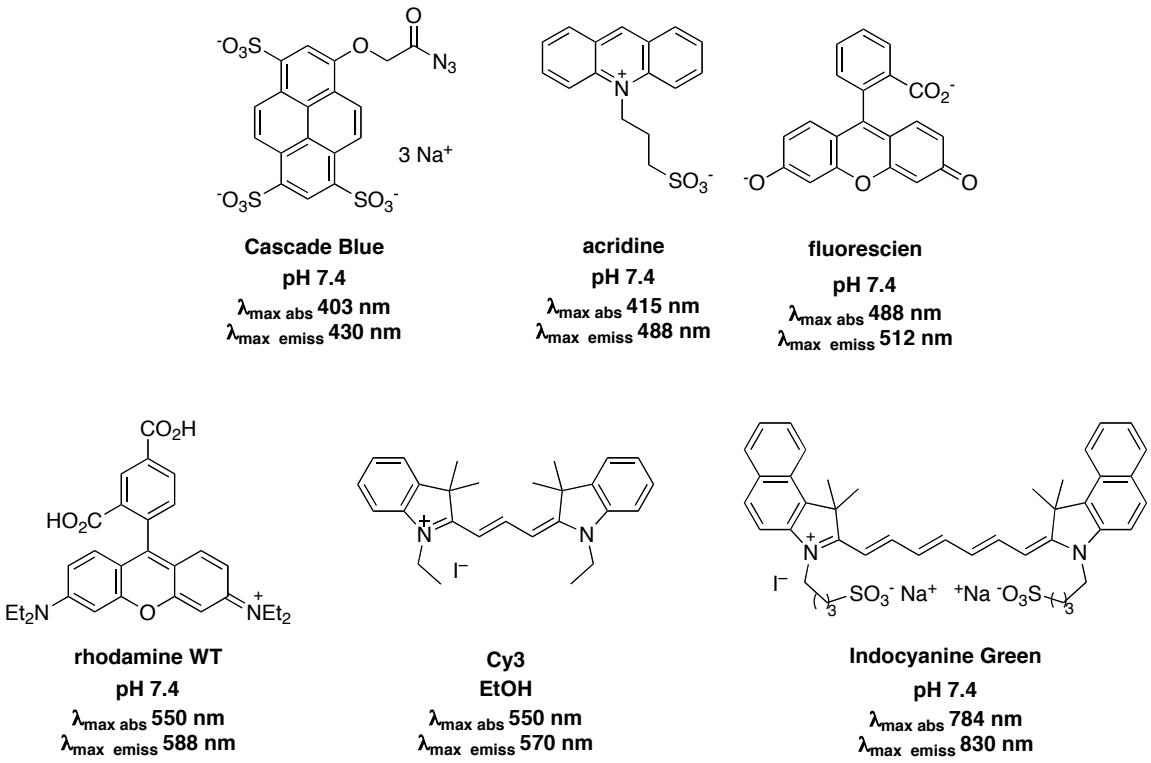

Figure 4.11. Structures of organic fluorophores doped in calcium phosphate nanoparticles.

The brightness of the fluorophore doped calcium phosphate nanoparticles is reported to be enhanced significantly compared to the parent fluorophore. In one such example one indocyanine green-doped calcium phosphate nanoparticle is 1000 times better than one indocyanine green molecule.[46] The improved brightness results from a decrease in non-radiative process inside the calcium phosphate matrix and the protection it gives the fluorophore from out side quenching agents like solvents and dissolved gases. The improvement in brightness also signifies that the fluorophore is not self-aggregating inside the matrix, which would result in quenching. The fluorescence quantum yield, is twice for the fluorophore encapsulated in calcium phosphate nanoparticles compared to the bare fluorophore in some cases which proves that radiative processes dominate non-radiative ones inside the matrix.[171] Most organic fluorophores show solvent-dependent fluorescence characteristics due to hydrogen bonding with solvents and also due to intermolecular charge transfer. In contrast the fluorescence spectra of encapsulated dyes

are stable regardless of solvents used proving minimum interaction between the solvent and the encapsulated fluorophore.[170] The encapsulated fluorophore has higher photostability than the bare fluorophore because it is protected from environmental oxygen by the calcium phosphate matrix.

4.2.2 Surface Modification of Calcium Phosphate Nanoparticles

Particle surfaces are modified to improve their water-solubility, colloidal stability, and for bioconjugation to biomolecules. Most nanoparticles possess a surface charge known as zeta potential, the overall charge the particle acquires in a particular medium. The magnitude of this charge is a measure of the repulsive forces present and can give an idea about the long-term stability of the particle solution. If all the particles in the solution have a large negative or positive zeta potential, then they will repel each other and no aggregates will be formed. Lower zeta potential values often result in lower colloidal stability due to particles coming together and forming clumps. The pH of the medium, concentration of the additives and the polarity of the solvent used affect zeta potential.

Negatively charged carboxylate functional groups on the surface of calcium phosphate nanoparticles provide them with colloidal stability. Such carboxylate groups are formed by adsorption to the surface of calcium phosphate during nanoparticle synthesis. Apart from carboxylate functionality, there are few reported surface modifications of calcium phosphate nanoparticles. One such modification involved attachment of polyethylene glycol (PEG) amine to carboxylic acid functionalized particles (Scheme 4.5). A carbodiimide activation of the carboxylate on the surface of the nanoparticle followed by reaction with the amine resulted in PEG functionalized nanoparticles.[172] In *in vivo* imaging experiments with animal models, PEGylation is known to provide physiological dispersion and inhibits protein absorption providing maximum retention in circulatory systems.

Scheme 4.5. Surface modification of calcium phosphate nanoparticles with PEG.

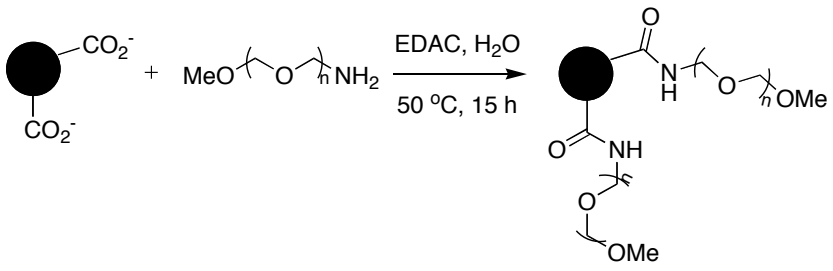

4.2.3 Biological Applications of Calcium Phosphate Nanoparticles

In vivo imaging helps in understanding a living organism with respect to its metabolic processes and cancer related changes in the body. PEGylated calcium phosphate nanoparticles doped with indocyanine green fluorophore accumulated in solid, 5 mm diameter xenograft breast adenocarcinoma tumors within 24 h after tail vein injection in nude mouse model.[46] The fluorescence of these nanoparticles were significantly prolonged compared to the bare fluorophore. Most near IR organic fluorophores suffer from quenching in physiological environment. The fluorescence signal from the nanoparticles was visible even after 4 days of administering them albeit with reduced intensity proving their robustness in a physiological environment. Dissection of the specimen after 10 min of administering shows only minor renal imaging, suggesting very low potential for renal toxicity. The PEGylated calcium phosphate nanoparticles, unlike organic fluorophores have a longer circulatory time in animal models, which helps in their collection in tumors. The fluorophore encapsulated calcium phosphate nanoparticles were also used to image the rat sympathetic stellate ganglion neurons.[173]

Biological tissues are highly scattering media and therefore imaging them at a significant tissue depth is always very difficult and conventional fluorophores cannot be used to perform such studies due to their low penetration. The dense muscle tissue has a total optical attenuation coefficient $\mu_\tau = 541\ cm^{-1}$ at 515 nm wavelength and it is very difficult for light to penetrate. Detectable penetration and emission depths were seen with

calcium phosphate nanoparticles up to 3 cm tissue depth in muscle tissues of nude mice compared to only weakly fluorescent bare fluorophore indocyanine green at only 2 cm.[46]

4.2.4 Encapsulation of Cassettes in Calcium Phosphate Nanoparticles

Incorporating water-soluble groups in TBET cassettes is difficult and time consuming. Purification of such water-soluble systems is often achieved via reverse phase HPLC or medium pressure liquid chromatography, which reduces the yield of product, and scale up is often not possible. Calcium phosphate serves as an excellent matrix, for imparting water-solubility to hydrophobic TBET cassettes and to improve their photophysical properties in water. We modified the literature methods to encapsulate TBET cassettes in calcium phosphate nanoparticles. The major difference in our method and Adair's method[46] is the reaction time (24 h compared to 5 min). An increase in reaction time was found to improve the photophysical properties of encapsulated dyes in some cases but not all. We performed dialysis to exchange the nanoparticles from organic media to aqueous media which is not attempted by Adair *et al*. The important parameters in our method and the published methods are shown in Table 4.3. The fluorophores are not covalently attached to the encapsulating material, which may result in their leaching out. The particles are stable without aggregation for at least a month. Figure 4.12 shows structures of cassettes and the corresponding acceptors encapsulated in calcium phosphate.

Table 4.3. Important parameters in different methods used for synthesis of calcium phosphate nanoparticles.

	early methods	**Adair's method**	**our method**
type of synthesis	oil in water microemulsion	oil in water microemulsion	oil in water microemulsion
reaction time	12 h	5 min	24 h
purification	centrifugation followed by EtOH wash	HPLC with 20 μm silica embedded column	column chromatography with 15 μm silica followed by dialysis
particle size	30-40 nm	16-20 nm	14-29 nm
encapsulated material	plasmid DNA	organic fluorophores	TBET cassettes

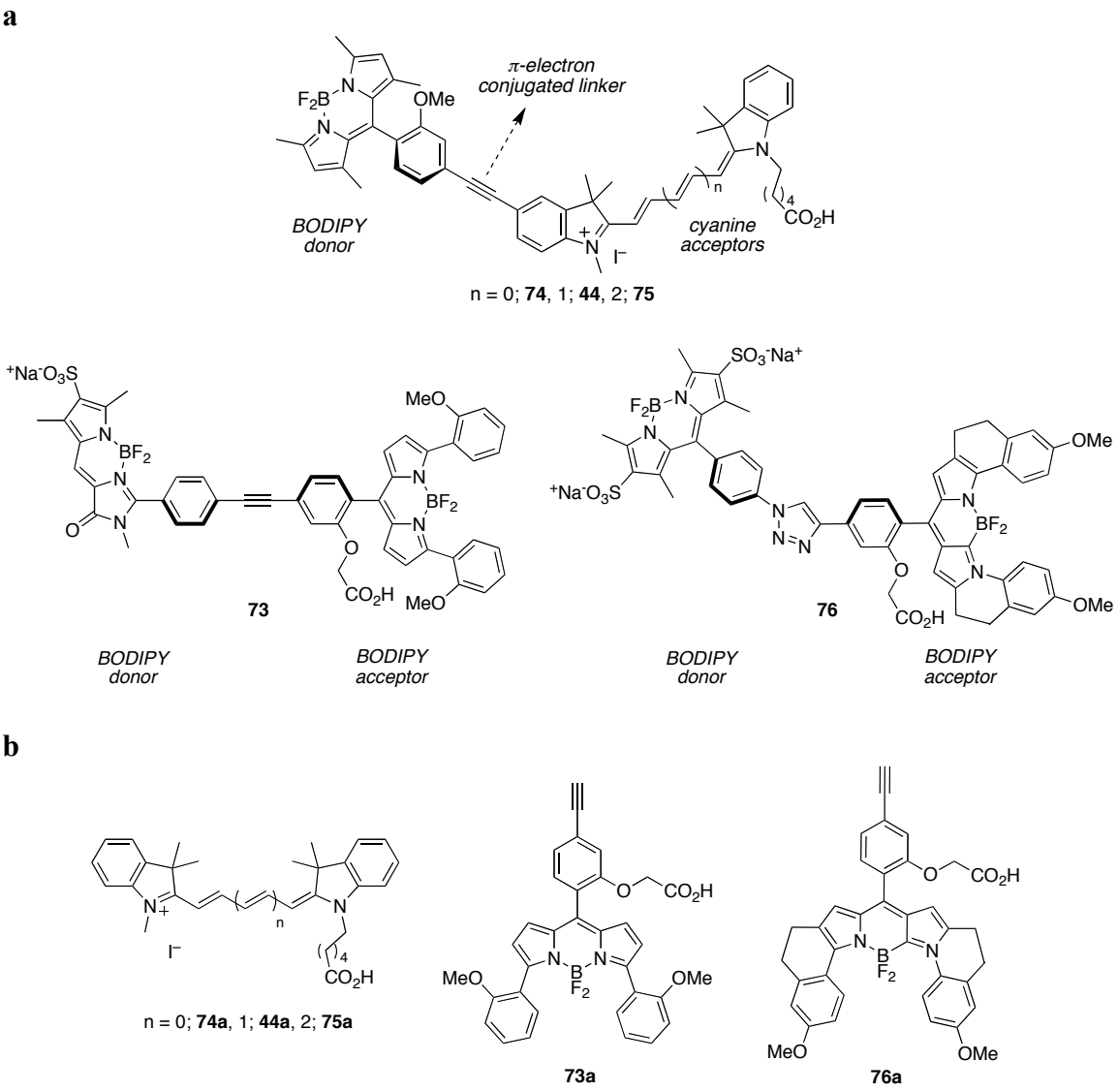

Figure 4.12. Structures of cassettes (**a**) and corresponding acceptors (**b**).

4.2.4.1 Synthesis of TBET Cassette Encapsulated Calcium Phosphate Nanoparticles

Synthesis of calcium phosphate nanoparticles is shown in Figure 4.13. Two water in oil reverse microemulsions are formed one with aqueous $CaCl_2$ and the second one with aqueous disodium phosphate in Igepal CO-520 in cyclohexane. Both microemulsions are stirred for 1 h and then mixed with each other for 24 h to form calcium phosphate nanoparticles. The reaction is quenched by addition of sodium citrate and the nanoparticles formed are purified by column chromatography. Details of synthesis are outlined in the appendix.

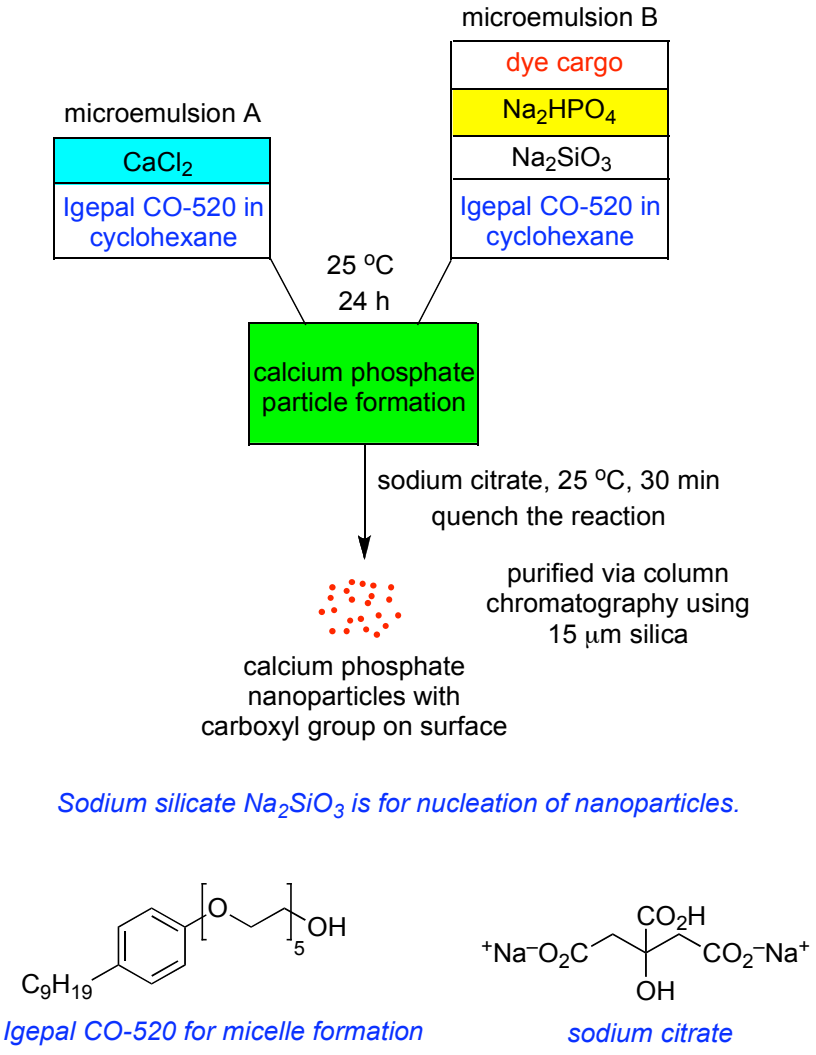

Figure 4.13. Synthesis of cassette doped calcium phosphate nanoparticles.

4.2.4.2 Photophysical Properties of Acceptors and TBET Cassettes Encapsulated Calcium Phosphate Nanoparticles

The absorbance and emission of the acceptor fragments encapsulated in calcium phosphate nanoparticles were measured in pH 7.4 buffer (Figure 4.14). A direct comparison between the encapsulated acceptors and the nonencapsulated acceptors in aqueous media was not possible due to the insolubility of the acceptors used. The fluorescence quantum yields of all acceptors in pH 7.4 buffer were in the acceptable range and did not change much with changes in reaction time (Table 4.4).

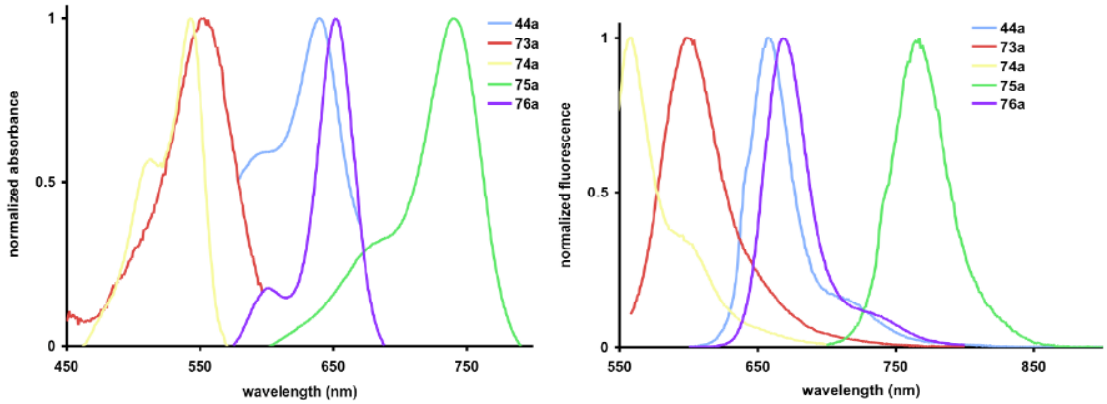

Figure 4.14. Normalized absorption and fluorescence of acceptors doped calcium phosphate particles in pH 7.4.

Table 4.4. Photophysical properties of acceptor encapsulated calcium phosphate nanoparticles in pH 7.4.

acceptors (reaction time)	$\lambda_{max\ abs}$ (nm)	$\lambda_{max\ emiss}$ (nm)	Φ
74a (5 min)	543	564	0.07[a]
74a (24 h)	543	564	0.08
44a (5 min)	643	663	0.21+/-0.01[b]
44a (24 h)	643	665	0.20+/-0.02
75a (5 min)	748	774	0.14+/-0.01[c]
75a (24 h)	748	774	0.16+/-0.01
73a (24 h)	548	602	0.35+/-0.02[d]
76a (24 h)	654	672	0.34+/-0.01[b]

Standards used for quantum yield measurements: [a]rhodamine 101 (Φ 1.0 in EtOH); [b]Nile Blue (Φ 0.27 in EtOH); [c]Cardiogreen (Φ 0.04 in MeOH); [d]rhodamine 6G (Φ 0.92 in EtOH); Quantum yields were measured three times and averaged.

The absorbance of the cassettes encapsulated in calcium phosphate nanoparticles shows two distinct peaks corresponding to donor and acceptor fragments respectively. In all cases except cassette **76** we observed almost complete energy transfer in pH 7.4 buffer (Figure 4.15). Cassette **76** is an exception because the donor and acceptor absorbance are

separated by a distance of 260 nm and therefore suffers from loss of energy via non-radiative processes. The energy transfer efficiency for cassettes **44**, **73**, **74** and **76** were in the range of 86-90 %. Energy transfer calculation for cassette **75** was not possible due to non-availability of a suitable standard. Cassettes **73** and **74** have quantum yields of 0.38 and 0.26 in pH 7.4 buffer whereas cassettes **44** and **76** had lower quantum yields of 0.063 and 0.14 in pH 7.4 buffer (Table 4.5).

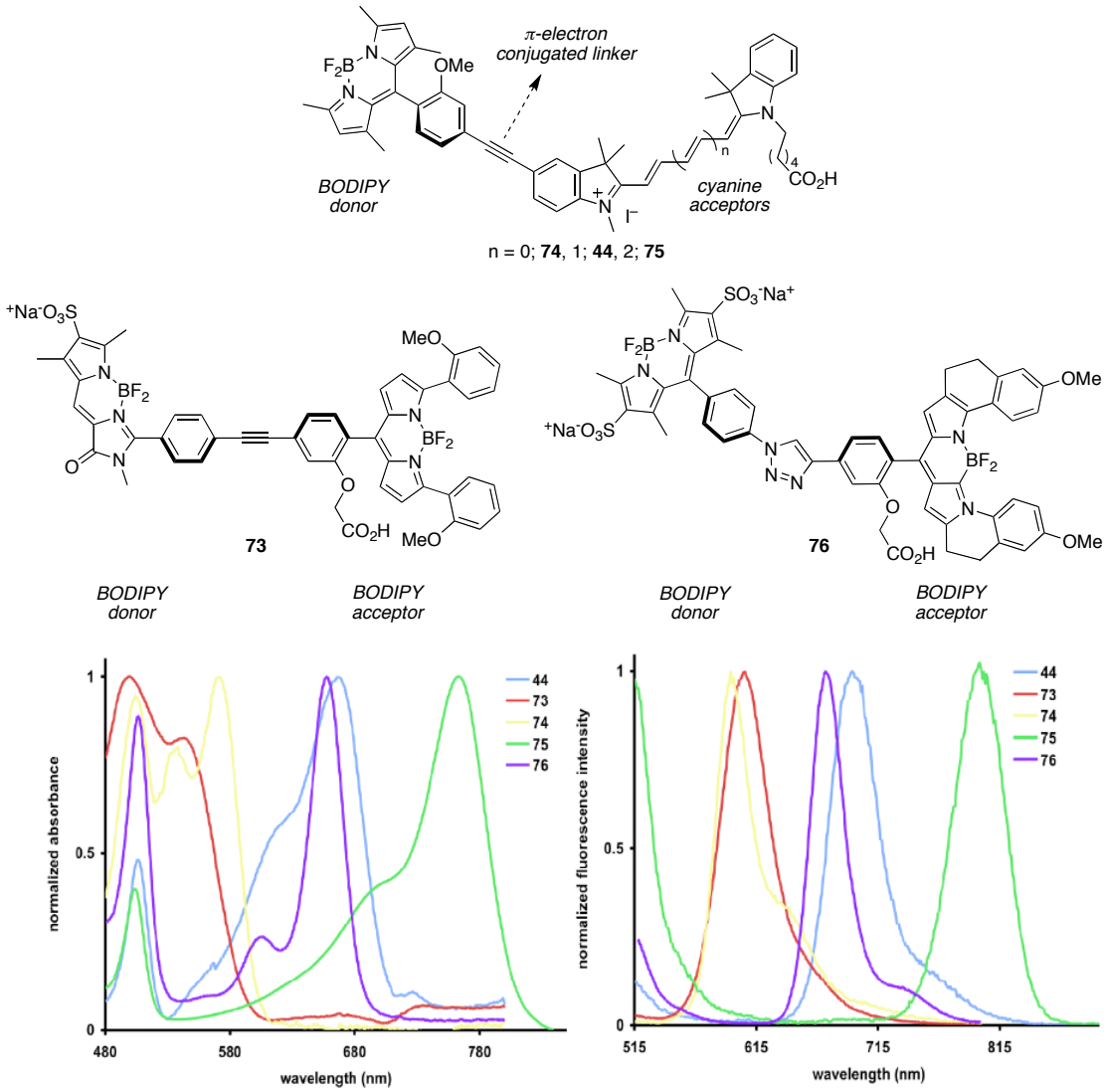

Figure 4.15. Normalized absorption and fluorescence of cassettes doped calcium phosphate nanoparticles in pH 7.4.

Table 4.5. Photophysical properties of cassette doped calcium phosphate nanoparticles in pH 7.4 (0.1 M sodium phosphate buffer).

cassettes (reaction time)	$\lambda_{max\ abs}$ (nm)	$\lambda_{max\ emiss}$ (nm)	Φ_d[a]	Φ_a[b]	ETE (%) = Φ_d/Φ_a x 100
74 (5 min)	504, 569	590	0.037	0.041[b]	90
74 (24 h)	504, 568	592	0.26+/-0.01	0.29+/-0.02 [b]	88
44 (5 min)	504, 659	687	0.051	0.057[c]	90
44 (24 h)	504, 659	687	0.063	0.071[c]	89
75 (5 min)	504, 764	793	0.039	-	40
75 (24 h)	504, 764	793	0.053	-	41
73 (24 h)	499, 543	606	0.38+/-0.01	0.44+/-0.03[a]	86
76 (24 h)	506, 657	674	0.14+/-0.01	0.16+/-0.02[c]	88

Φ_d: excited at donor; Φ_a: excited at acceptor. Standards used for quantum yield measurements: [a]rhodamine 6G (Φ 0.92 in EtOH); [b]rhodamine 101 (Φ 1.0 in EtOH); [c]Nile Blue (Φ 0.27 in EtOH). Quantum yields were measured three times and averaged.

A comparison of absorbance of cassette **76** and **76** encapsulated in calcium phosphate in pH 7.4 buffer shows that the absorbtion of the acceptor fragment of cassette encapsulated in calcium phosphate is greater than that of the donor fragment, whereas in the unencapsulated cassette the absorbtion of donor fragment is greater than the acceptor fragment (Figure 4.16). This difference in absorbance is due to the relative insolubility of the acceptor in the free cassette in aqueous media, which leads to reduced fluorescence output. Once encapsulated inside calcium phosphate, the cassette becomes water-soluble and therefore does not suffer from any aggregation related quenching. The fluorescence output of the encapsulated cassette **76** is 3.7 fold higher than the cassette itself when excited at the donor absorbance maxima. The quantum yield of the encapsulated cassette **76** is 0.14 whereas the free cassette **76** has a quantum yield of 0.032 (Table 4.6). The enhancement in quantum yield further proves that calcium phosphate shields the cassette from solvents and prevents quenching.

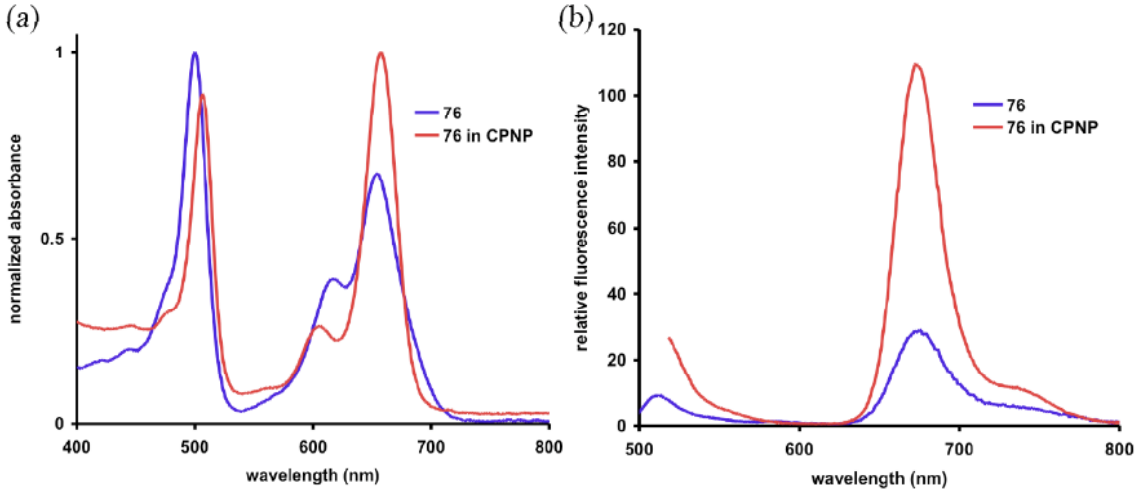

Figure 4.16. (a) Absorbtion and (b) relative fluorescence of cassette **76** and **76** doped calcium phosphate nanoparticles (CPNP) in pH 7.4. Concentration for absorbance: 10^{-6} M; concentration for fluorescence: 10^{-7} M.

Table 4.6. Comparison of photophysical properties of encapsulated and un encapsulated cassette **76** in pH 7.4 (0.1 M sodium phosphate buffer).

cassettes	$\lambda_{max\ abs}$ (nm)	$\lambda_{max\ emiss}$ (nm)	Φ_d[a]	Φ_a[b]	ETE (%) = Φ_d/Φ_a x 100
76	500, 655	674	0.032	0.037	86
76 in CPNP	506,657	674	0.14+/-0.01	0.16+/-0.02	88

CPNP: calcium phosphate nanoparticles;; [a]Φ_d excited at donor relative to rhodamine 6G (Φ 0.92 in EtOH); [b]Φ_a excited at acceptor relative to Nile Blue (Φ 0.27 in EtOH). Quantum yields were measured three times and averaged.

The reaction time for nanoparticle formation did not seem to improve the photophysical properties of the encapsulated fluorophores significantly except in case of cassette **74** where the quantum yield of calcium phosphate nanoparticles formed after 24 h reaction was 7 fold higher than the ones obtained after 5 min reaction (Figure 4.17 and 4.18). In most cases the reaction between calcium chloride and sodium phosphate to form calcium phosphate is very rapid and is completed in a short period of time. A graph of integrated fluorescence intensity against absorbtion for acceptors and cassettes for different

reaction times did not show any significant difference except for cassette **74** (Figure 4.18).

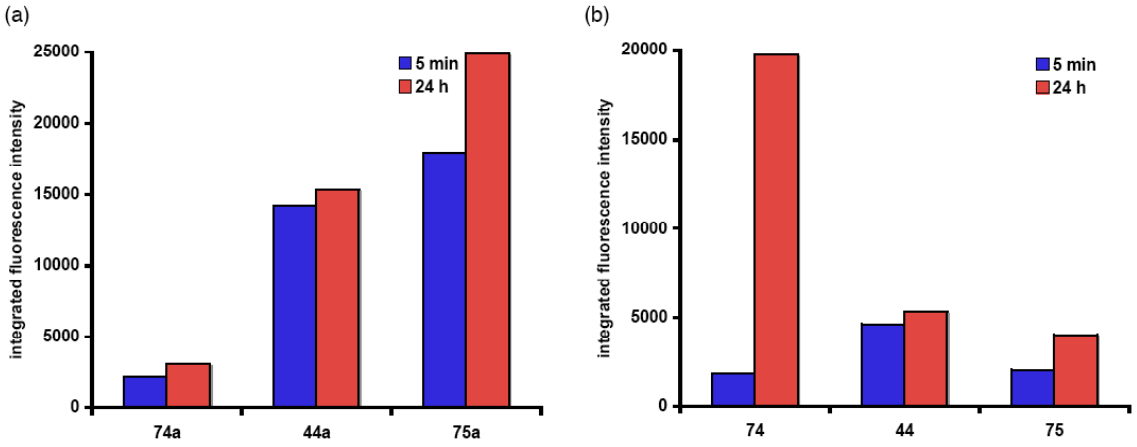

Figure 4.17. Effect of reaction time on fluorescence output of encapsulated fluorophores. Integrated fluorescence intensity of: (**a**) cyanine acceptor doped calcium phosphate nanoparticles and (**b**) cassette doped calcium phosphate nanoparticles in pH 7.4 (0.1 M sodium phosphate buffer) for reaction time 5 min (blue) and 24 h (red). All acceptors excited at their corresponding λ_{max} and all cassettes excited at their corresponding donor $\lambda_{max.}$ All measurements done for similar absorbance range for each sample.

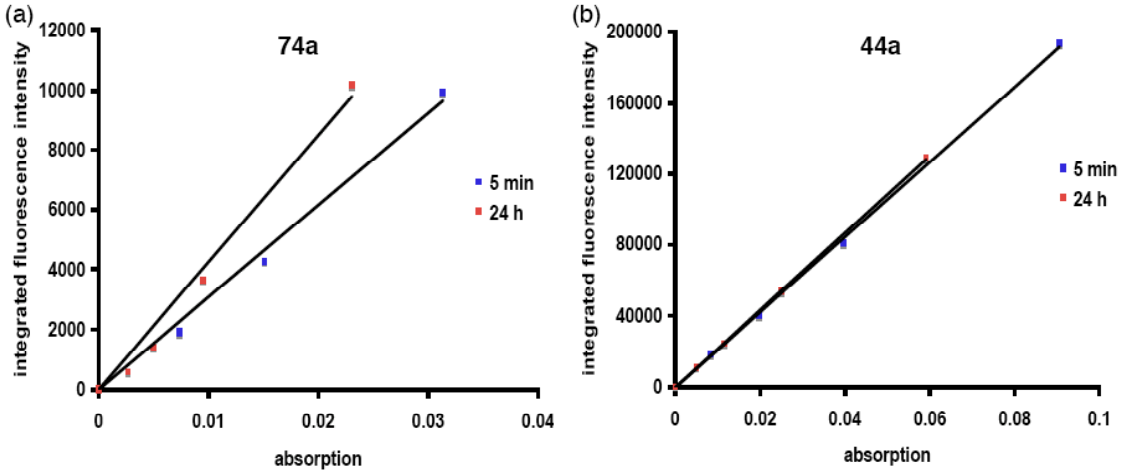

Figure 4.18. Effect of reaction time on fluorescence output of encapsulated fluorophores. Comparison of integrated fluorescence intensity of cyanine acceptor doped calcium phosphate particles **a**, **b**, **c** and cassette doped calcium phosphate particles **d**, **e**, **f** in pH 7.4 (0.1 M sodium phosphate buffer) for reaction time 5 min (blue) and 24 h (red).

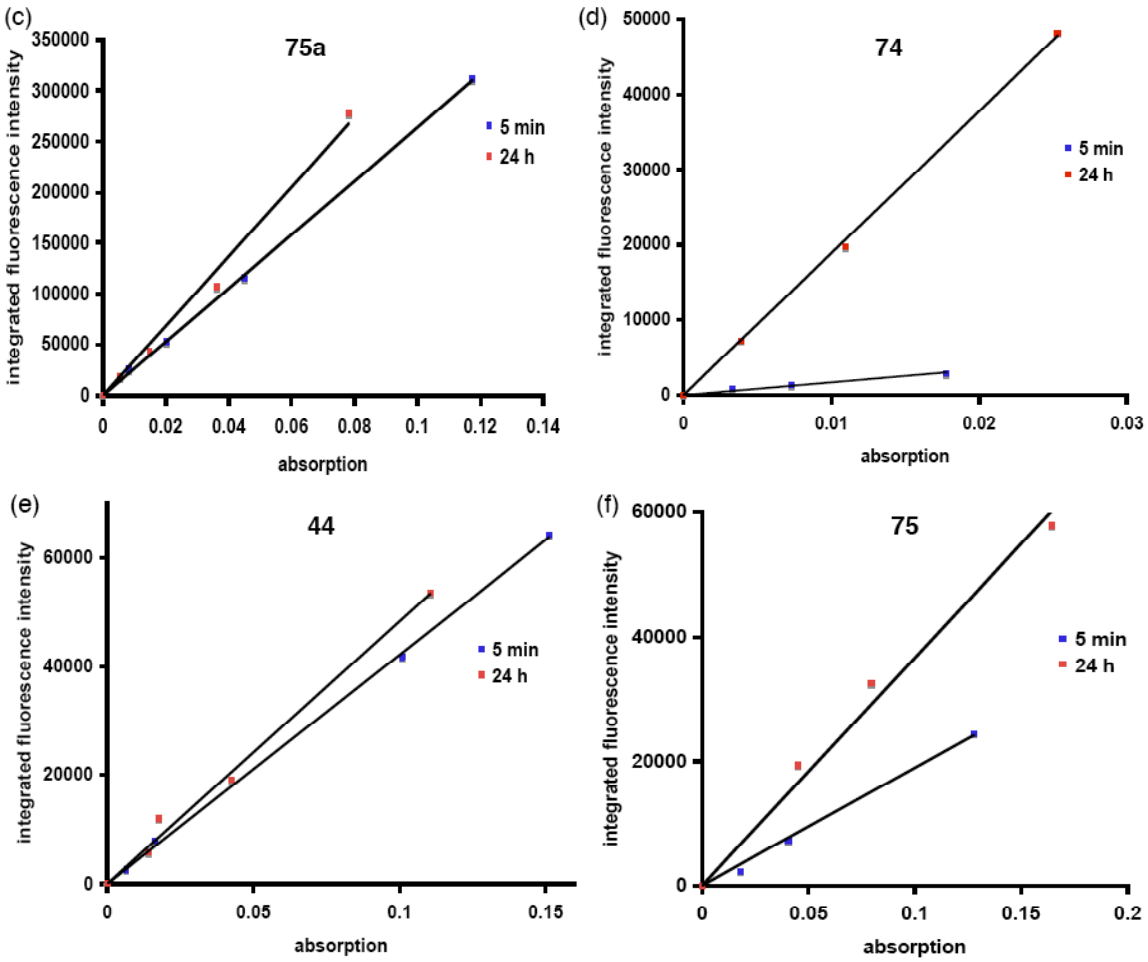

Figure 4.18. Continued

Particle size of the calcium phosphate nanoparticles formed was measured using atomic force microscopy (AFM). A freshly cut mica surface was pressed with adhesive tape and peeled off to clean the mica surface. A drop of nanoparticle dispersion in water was placed on the mica surface and dried with compressed nitrogen for 5 min. The surface was scanned with Digital Instruments Nanoscope AFM in tapping mode. An SPM ULTRASHARP silicon cantilever of the NSC15 series with a resonance frequency of 325 KHz was used for scanning. The typical tip curvature radius of the uncoated probe was < 10.0 nm. Particle size of the calcium nanoparticles was in the range of 14-29 nm and they were spherical in shape and well dispersed (Figure 4.19 and 4.20).

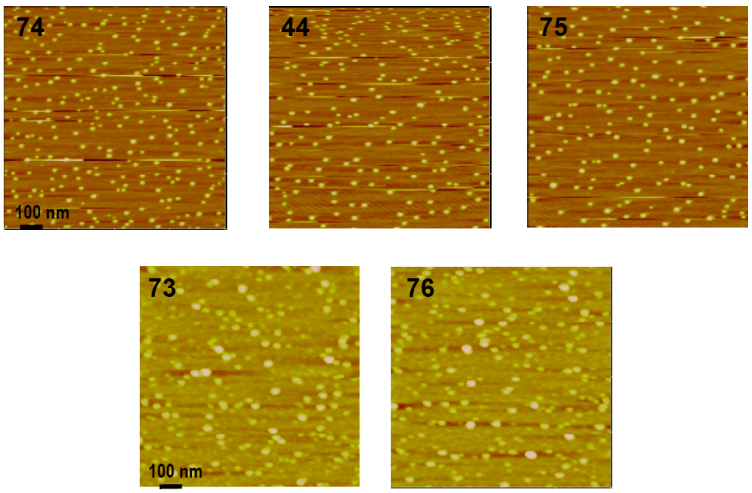

Figure 4.19. AFM images for cyanine cassettes encapsulated in calcium phosphate nanoparticles. Particle size: 14- 29 nm.

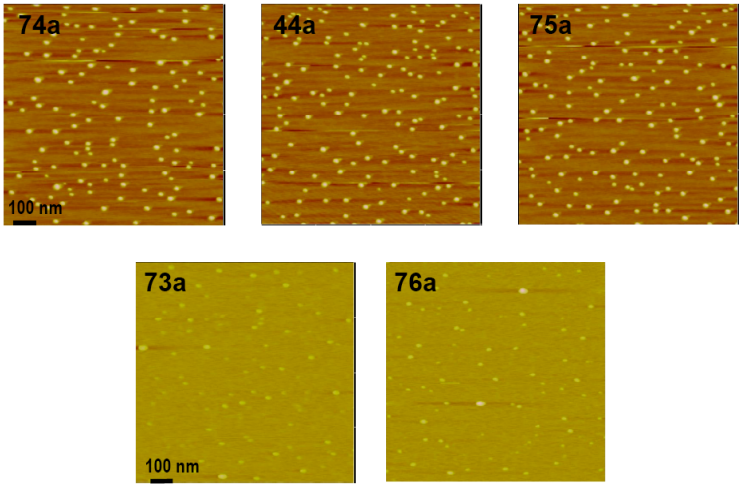

Figure 4.20. AFM images for cyanine cassette acceptors encapsulated in calcium phosphate nanoparticles. Particle size: 16- 28 nm.

4.2.5 Conclusion

TBET cassettes were successfully encapsulated in silica and calcium phosphate nanoparticles. These fluorescent nanoparticles are completely water dispersible and can encapsulate either hydrophilic or lipophilic fluorophores. This serves as a novel method to make any organic fluorophore water-soluble. The advantage of these nanoparticles is the improvement in the photophysical properties of the encapsulated fluorophores. In most cases we observed an improvement in quantum yield and energy transfer efficiency in cassettes encapsulated.

Silica nanoparticles involve covalent attachment of the fluorophore within the silica matrix. This prevents leaking of the fluorophore from the nanoparticle for a prolonged period of time (for at least a month). Surface modifications of these particles are reported[152,174,175] and can be attempted to attach these particles to protein and other biomolecules. Selected silica nanoparticles were used for cellular imaging studies and stained COS7 cells.

Calcium phosphate nanoparticles are easy to synthesize and also biocompatible. Their unique property of being stable at physiological pH and increased solubility in acidic pH makes them an imaging agent as well as a delivery vehicle for carrying therapeutic drugs. Their nontoxic nature and ease of preparation makes them a superior choice over silica nanoparticles for future biological applications.

CHAPTER V

OUTLOOK AND CONCLUSIONS

5.1 Outlook

The demand for understanding cells on a microscopic level continues to fuel development of new imaging agents. Organic fluorophores emitting in the near IR region are most preferred but their robustness in the cellular environment is usually a concern. The ones that are available suffer from low photostability, aggregation and quenching issues which hampers their widespread use in imaging studies. Nevertheless there are literature reports, which try to over come these issues by synthetic manipulation of fluorophores mainly by introduction of water-soluble groups[4,33,176,177] and structural designs[3,12,178] that make them more photostable. Molecular probes® is one of the leading providers of novel fluorophores for biomedical applications and have a wide range of products for imaging different regions of the cell.[179] The advantage of organic fluorophores over other imaging agents such as nanoparticles is their size which is usually 2-3 nm, almost 10 times smaller than fluorescent quantum dots and similar nanoparticles. The cytotoxicity associated with such nanoparticles is also a cause of concern for their widespread use in imaging studies.

The current state of the art involves encapsulating organic fluorophores in a relatively nontoxic matrix like calcium phosphate and formation of nanoparticles, which can then be used for cellular imaging studies. This approach is advantageous because the photophysical property of the fluorophore is enhanced inside the calcium phosphate matrix. There is, however, a limit to the extent to which the properties of a fluorophore can be enhanced. For example, brightness of a fluorophore depends on the number of photons it absorbs and the quantum efficiency, the fraction of photons absorbed that are emitted as light. These two parameters are inherent properties of the fluorophore and calcium phosphate does not increase or decrease the number of photons absorbed by the

fluorophore. Thus focus should be on synthesizing fluorophores with high molar extinction coefficients. Among organic fluorophores cyanines have high molar extinction coefficient[5] but suffer from low quantum efficiency and chemical instability.

5.1.1 Conjugated Organic Polymers

Conjugated organic polymers are mainly organic compounds with an extended π orbital system through which an electron can move from one end of the polymer to the other. Their extended π conjugation renders it with a molar extinction coefficient much higher than traditional organic fluorophores. Most conjugated organic polymers reported in literature are used in applications such as electrochemical sensors,[180] polymer based solar cells,[181] optical amplifiers,[182] and flat panel displays using OLEDS.[36,54] One of the main drawbacks of conjugated organic polymers is their insolubility in aqueous media, which makes them less useful for biological applications such as cell imaging. This problem can be overcome by developing polymers with saccharide groups attached to conjugated polymers. These saccharides not only impart water-solubility but also interact specifically with cell surface receptor proteins. Such polymers are known as glycopolymers and they are useful candidates for imaging and targeted drug delivery. Currently such glycopolymers are widely used for imaging lectins and bacteria.[183] Two such glycopolymers are shown in Figure 5.1. They are fluorine-based polymers with a polyethylene glycol chain and a glucose residue to impart water-solubility. The use of long flexible polyethylene glycol as tethered spacers helps reduce steric hindrance for cellular recognition and prevents non-specific interactions. The strong interactions between the carbohydrates on the polymer with bacteria such as *E. coli* results in significant red shifts in UV/Vis absorbtion and fluorescence spectra.

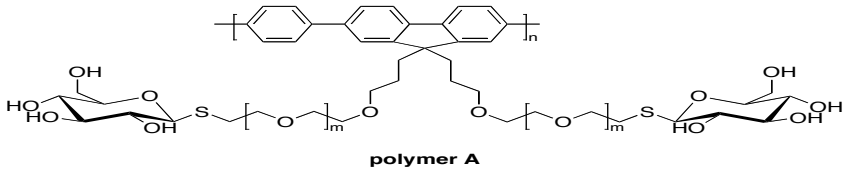

polymer A

Figure 5.1. Structures of water-soluble conjugated polymers.

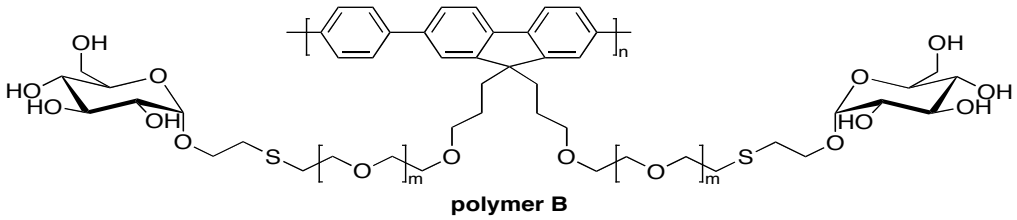

Figure 5.1. Continued.

Synthesis of such polymers (Scheme 5.1) involves Suzuki cross coupling of phenyldiboronic acid and a bromide bearing monomer, **E** to form polymer **F** bearing polyethylene glycol tethers. The bromide bearing monomer **E** was prepared by reacting compound **C** with polyethylene glycol mono laurate in the presence of sodium hydride in THF at 25 ^{o}C, followed by hydrolysis under basic conditions to afford intermediate **D**. Bromination of **D** with bromine and triphenylphosphine in acetonitrile yielded **E** which was used for the polymerization reaction. Post polymerization reaction of polymer **F** with 1-thiol-β-D-glucose tetraacetate and 1-thioethyl-α-D-mannose tetraacetate under basic conditions afforded polymers **G** and **H**. These polymers were subjected to de-acetylaion under Zemplen conditions in methanol with sodium methoxide to yield polymer **A** and **B**.

Scheme 5.1. Synthesis of water-soluble polymers **A** and **B**

a

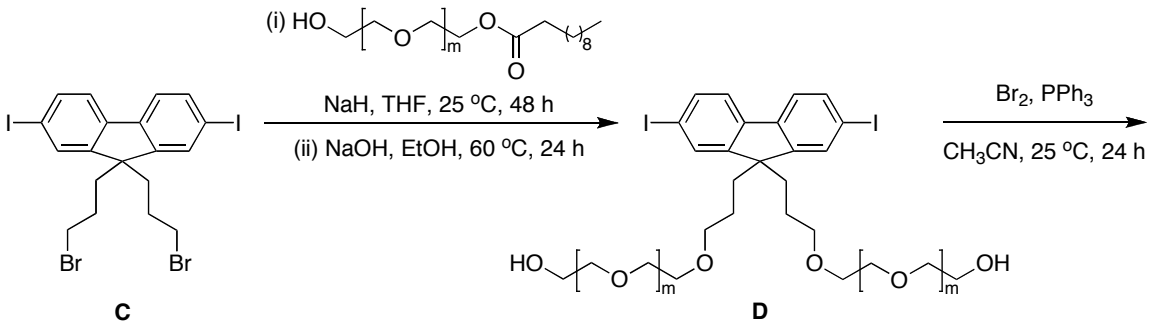

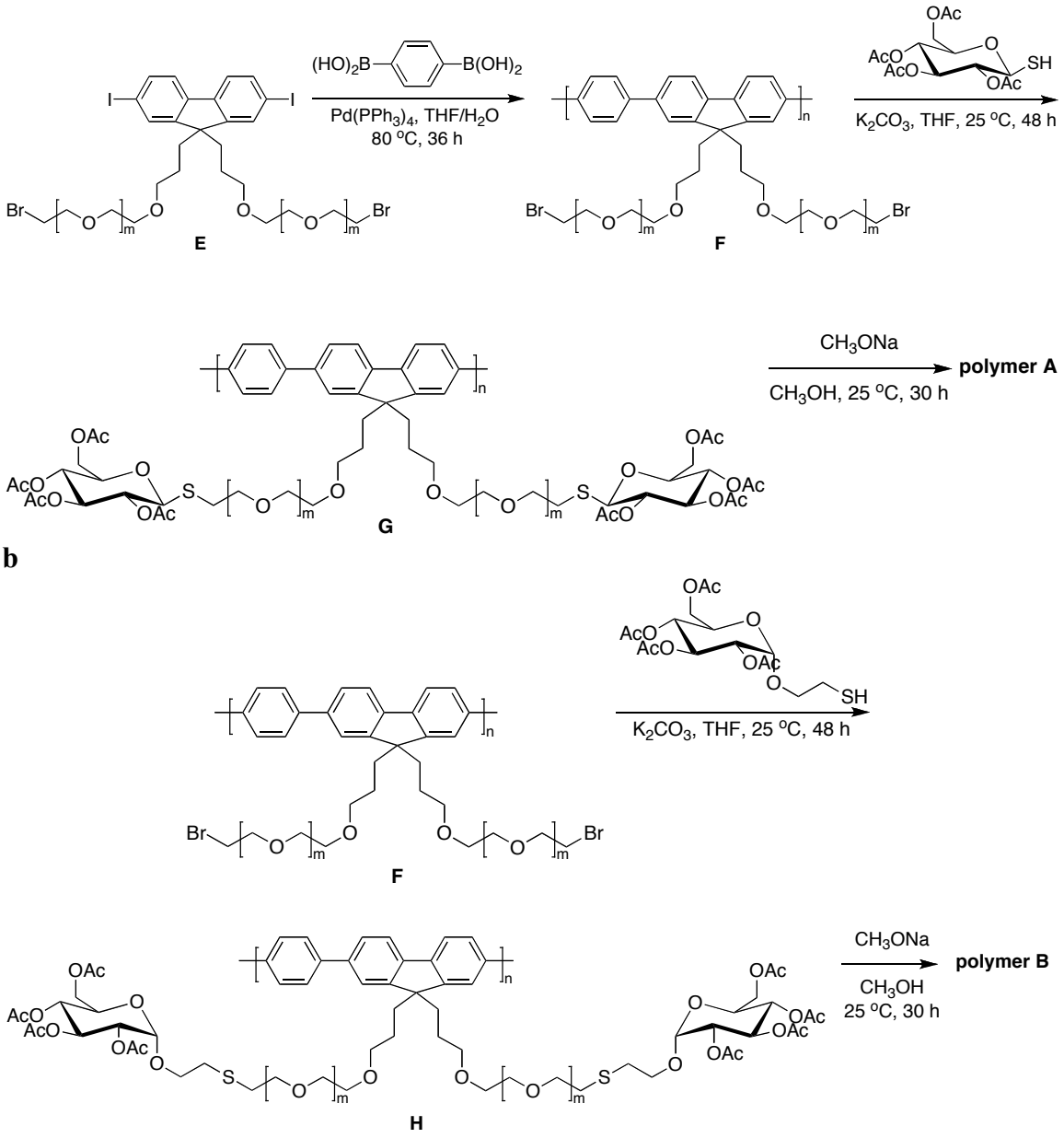

Polymers **A** and **B** are highly water-soluble and fluoresce with a quantum yield of about 44 % in pH 7.4 phosphate buffer. They exhibit absorbtion maximum peak at 380 nm and emission maximum peak at 426 nm. Polymer **B** was used for imaging studies of ORN178 strain of *E.coli* that expresses wild type 1 pili, which specifically binds to mannose. Pili is a hair like appendage found on the surface of many bacteria. Pili connect a bacterium to another of its species and build a bridge between the cytoplasm

of the cells and allows for exchange of plasmids between the bacteria. Incubation of polymer **B** with the ORN178 strain resulted in the formation of fluorescently stained bacterial clusters from which the polymer was not removed by rinsing and centrifugation. There was a significant red shift in UV/Vis absorbtion and fluorescence spectra of polymer **B** in the presence of bacteria indicating enhanced π conjugation of the polymer with bacterial pili through multivalent interactions. The polymer absorbtion maximum was shifted to 400 nm and emission maximum to 460 nm in the presence of bacteria. These glycopolymers look promising for biosensing applications for cells and viruses.

5.1.2 Conjugated Polymer Nanoparticles

A simpler approach towards integrating conjugated polymers for biological applications was put forth by McNeill *et al* whose work involves formation of nanoparticles from conjugated polymers, which are dispersible in aqueous media.[184] The polymers used for synthesis of nanoparticles need not be water-soluble to begin with thereby saving considerable synthetic effort and time. Conjugated polymer nanoparticles possess several advantageous properties for fluorescence labeling applications such as short excited state life time, high quantum yields and large absorbtion cross section per particle which makes them extremely bright.

The preparation of these nanoparticles is simple and straightforward and does not involve emulsion polymerization or surfactants. This method can be applied to a wide range of conjugated polymers that are soluble in organic solvents. The method is based on addition of a solution of conjugated polymer dissolved in an organic water miscible solvent to water, followed by rapid mixing. The particle size of these nanoparticles ranges between 5-10 nm and they are stable in aqueous suspensions.

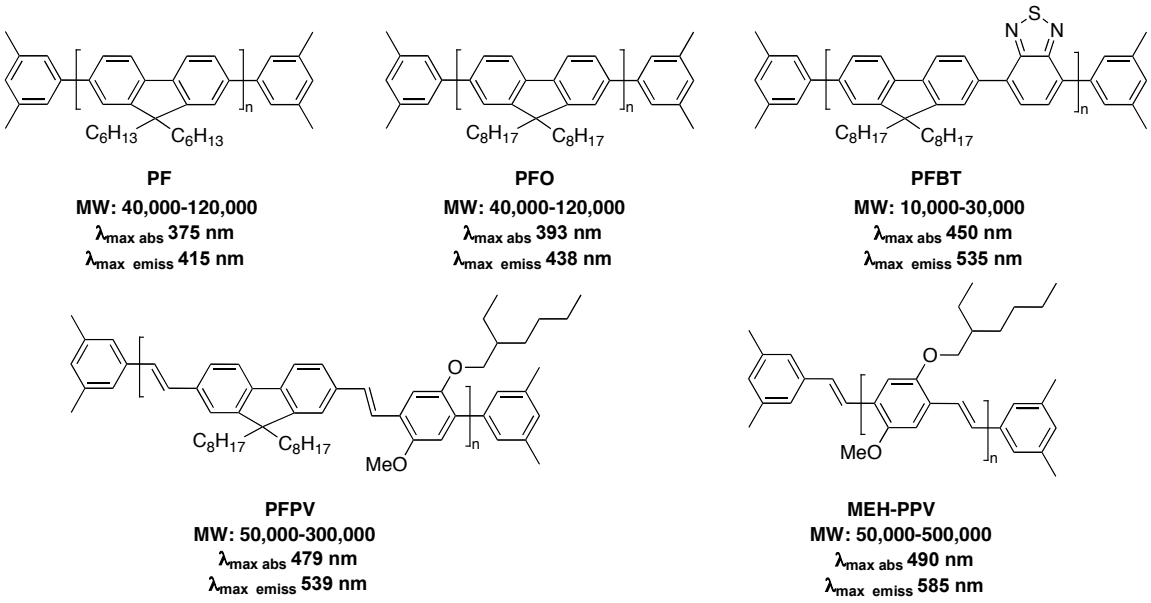

Figure 5.2. Structure of commercially available conjugated polymers used for nanoparticle synthesis. Photophysical properties measured in THF. MW denotes molecular weight.

Figure 5.2 shows commonly used conjugated polymers for nanoparticle synthesis and they are sold by ADS Dyes, Inc®. The procedure for preparing these nanoparticles can be described as follows (Scheme 5.2). The polymer was dissolved overnight by stirring in THF under an inert atmosphere. The solution was filtered and diluted to a concentration of 20 ppm. A part of this solution is added to deionized water with sonication. The resulting solution was again filtered to remove any aggregates and any starting material remaining. The THF was removed by partial evaporation under vacuum and the resulting solution was further filtered to obtain a clear solution with well-dispersed nanoparticles. The particle size was determined by atomic force microscopy (AFM) and transmission electron microscopy (TEM). The suspension is reported to be stable for weeks without any aggregation.[185]

Scheme 5.2. Synthesis of nanoparticles from conjugated polymer PFO.

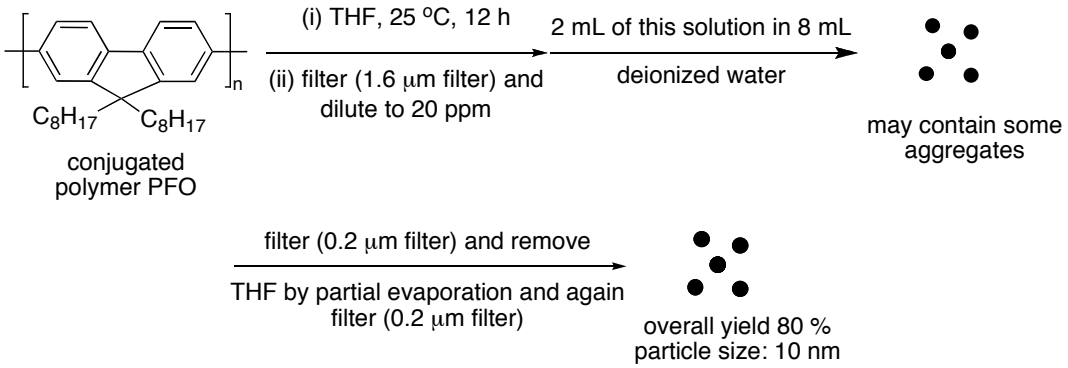

The nanoparticle dispersion in water displays blue shifted, broadened absorbtion spectra and a red-shifted emission spectra as compared to their parent polymer in THF (Figure 5.3). The blue shifted absorbtion spectra can be attributed to bending or kinking of the polymer backbone.[185] This is also in agreement with simple geometric consideration *ie* the diameter of a nanoparticle is roughly 50 % of the effective conjugation length of the unconstrained polymer. The presence of some aggregates due to interactions between segments of polymer chain is evident from the red tail in the absorbtion spectra. The red shift in the fluorescence spectra of these nanoparticles can be ascribed to the increasing interaction between segments of the polymer chain in a compact nanoparticle which leads to energy transfer to low energy chromophores and weakly fluorescent interchain aggregates. The fluorescence quantum yields of these nanoparticles in water were in the range of 0.1 with a molar extinction coefficient of approximately 5 x 10^7 $M^{-1}cm^{-1}$. It should be mentioned that the quantum yields of these nanoparticles are 4-fold less for PFO, 7-fold less for PFPV and 25 –fold less for MEH-PPV as compared to their parent polymer in THF. Nevertheless the comparison of quantum yield and molar extinction coefficient of one such nanoparticle dispersion in water prepared from PFPV with that of fluorescent dye rodhamine 6G, a widely used biological stain indicates that the PFPV nanoparticles are 50 times brighter than rodhamine 6G.

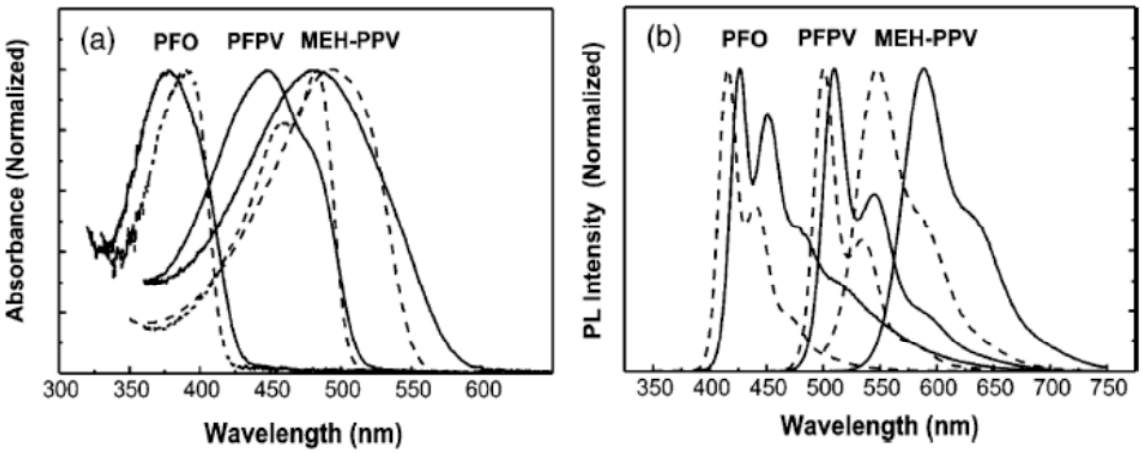

Figure 5.3. Normalized absorbtion (a) and fluorescence spectra (b) of the conjugated polymer nanoparticle dispersions (solid lines). Their comparison to corresponding polymers in THF solution (dashed lines).

As mentioned before conjugated organic polymers have high fluorescence quantum yields and broad emission spectra with full width at half maxima (fwhm) of around 50-100 nm, meeting the requirement for an efficient donor in FRET based systems. They also have high molar extinction coefficients and can harvest light very efficiently. These characteristics make them suitable for FRET based systems in which these polymers can act as donors to fluorescent dyes which absorb and emit at a longer wavelength compared to the polymer.[186] Scheme 5.3 shows preparation of dye doped fluorescent nanoparticles with an average particle size of 30 nm. The procure is similar to preparing undoped polymer nanoparticles, except that a given 100 ppm solution of fluorescent dye in THF is added in varying amounts of 0-10 % to the polymer solution. In order to make sure that the dye is primarily located inside the nanoparticles and not as free dye molecules in solution, the dye doped polymer nanoparticle solution was concentrated by a factor of 6 using centrifugal concentrators with a molecular weight cut off of 30,000. A very weak absorbtion and fluorescence from the dopant dye was observed in the filtrate proving that most of the dye was encapsulated in the polymer nanoparticle. The repetition of the above procedure after two weeks also did not result in any absorbance or fluorescence of the dopant dye in the filtrate indicating minimal dye leakage.

Scheme 5.3. Synthesis of dye doped polymer nanoparticles.

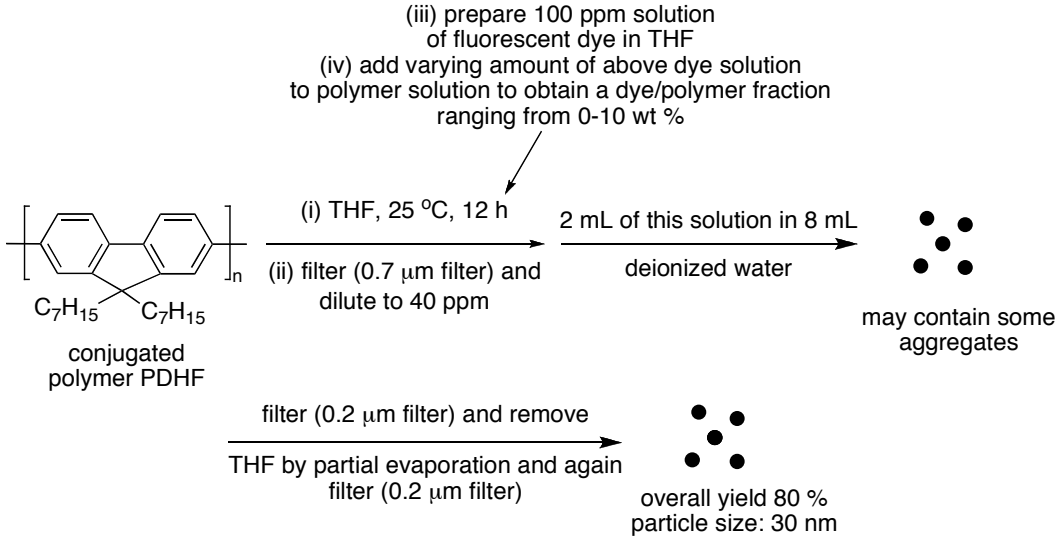

Polymer PDHF was used as a host polymer in preparing these dye doped polymer nanoparticles because of its high molar absorptivity and broad emission spectrum, which provides favorable spectral overlap with dopant dyes. Structure and photophysical properties of dopant dyes are shown in Figure 5.4. Figure 5.5a represents normalized fluorescence emission spectrum of the PDHF nanoparticles in water and absorbtion spectra of perylene, coumarin 6, Nile Red and TPP in THF solution. The fluorescence of the polymer PDHF in the 400-550 nm region possess good overlap with the absorbtion spectra of all the dyes, a key requirement for energy transfer via Forster mechanism. Figure 5.5b shows the normalized absorbtion (dashed line), fluorescence excitation and emission spectra (solid line) of the undoped PDHF and the four dye doped nanoparticles in water. The dominant absorbtion peak around 375 nm of the dye-doped nanoparticles is due to PDHF and the weak absorbtion is from the dopant dye. When excited at 375 nm, the fluorescence emission from PDHF is almost completely quenched and the nanoparticle exhibits fluorescence characteristic of the dopant fluorescent dye. This proves efficient energy transfer between the host polymer PDHF and the dopant dye within the nanoparticles.

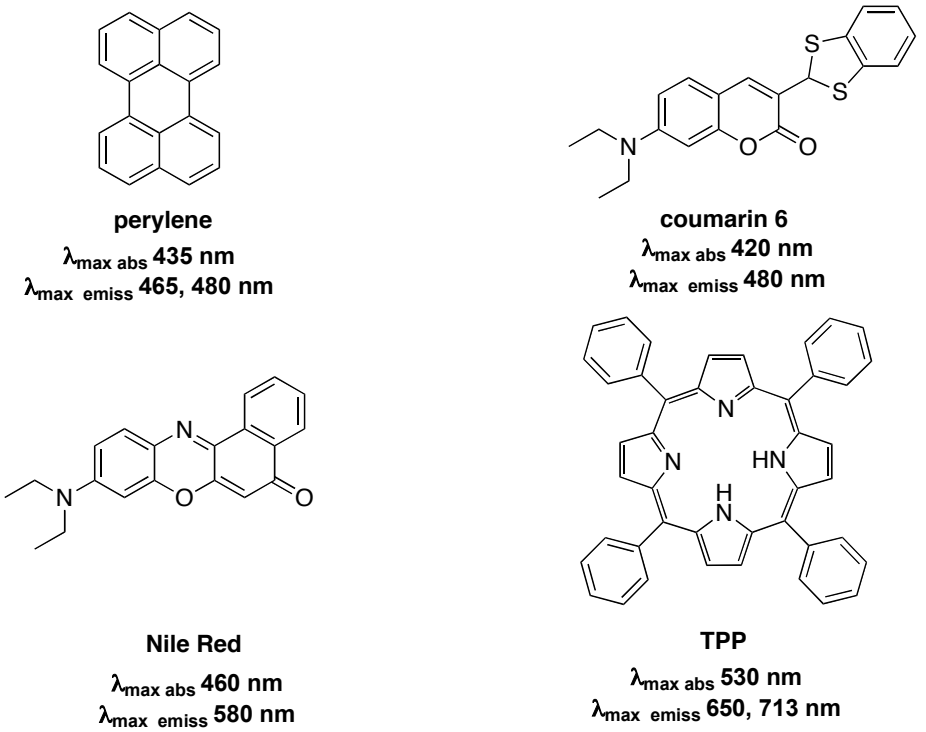

Figure 5.4. Dopant dyes used for nanoparticle synthesis. Photophysical properties measured in THF.

The fluorescence energy transfer increases with increasing concentration of the dopant dye and reaches a maximum at 1.0 wt % of the dopant dye. Further increase in the concentration of the dopant dye caused a significant reduction in the fluorescence energy transfer. The reduction in fluorescence energy transfer is caused by formation of dye aggregates at higher concentrations. The dye doped polymer nanoparticles are many times brighter than inorganic quantum dots and dye loaded silica nanoparticles of similar dimensions.[186] The quantum yields of nanoparticles were approximately 0.4 with a molar extinction coefficient of 1.5×10^9 M^{-1} cm^{-1}. The photostability of the dye doped polymer nanoparticles was analyzed using a 1.0 mW, 380 nm UV light source. The dye doped polymer nanoparticles showed a 4 fold improvement in photostability compared to the undoped nanoparticles. The efficient energy transfer between the host polymer and the dopant dye gives an alternate path for energy dissipation thereby improving photostability of the nanoparticle as a whole.

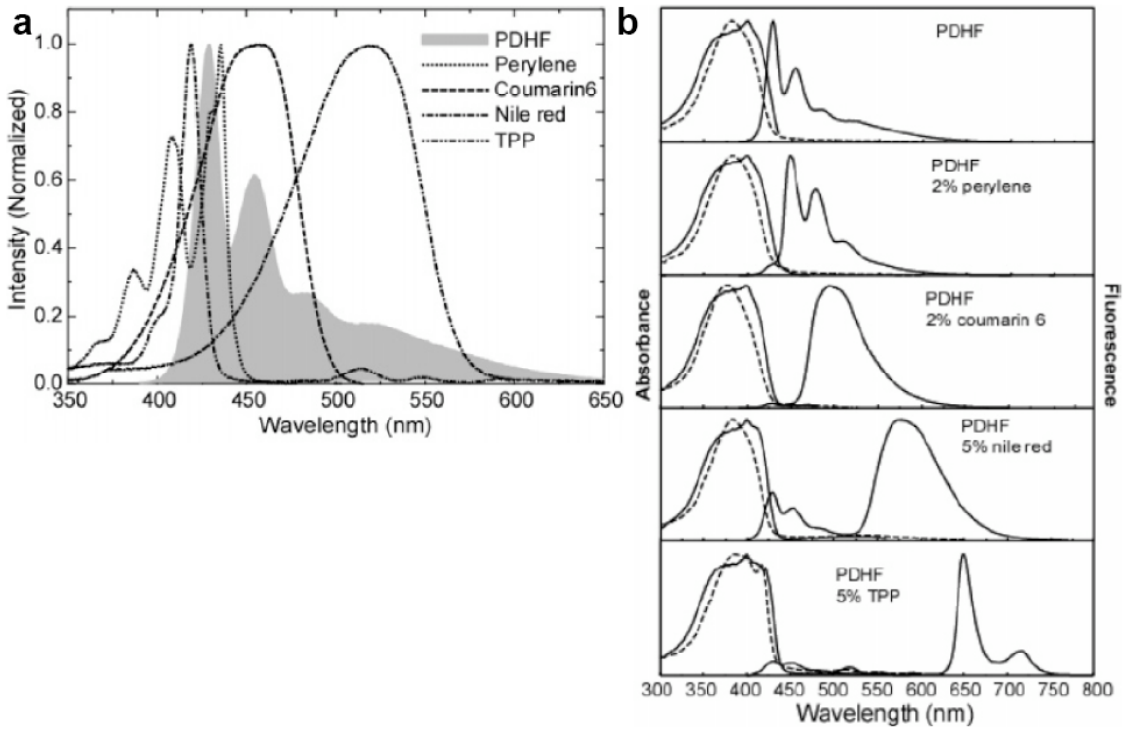

Figure 5.5. (a) Normalized fluorescence spectrum of PDHF nanoparticles in water and absorbtion spectra of dopant dyes in THF. (b) Normalized absorbtion (dashed), fluorescence excitation and emission spectra (solid) of pure and dye doped PDHF nanoparticles in water.

The nondoped polymer nanoparticles were used for bioimaging studies in cells.[187] J774.A1 macrophage cells were used for this particular study based on the ability of the macrophage cell line to efficiently ingest cellular debris and small particles such as nanoparticles. Figure 5.6 shows differential interference contrast (DIC) and fluorescence images of the cells incubated with PPE, PFPV, PFBT and MEH-PPV nanoparticles. The images indicate internalization of the nanoparticles by cells. The nanoparticle appears to be stable in the cell culture medium and most nanoparticle fluorescence is seen from the cytoplasm indicating that most of them crossed the cell membrane.

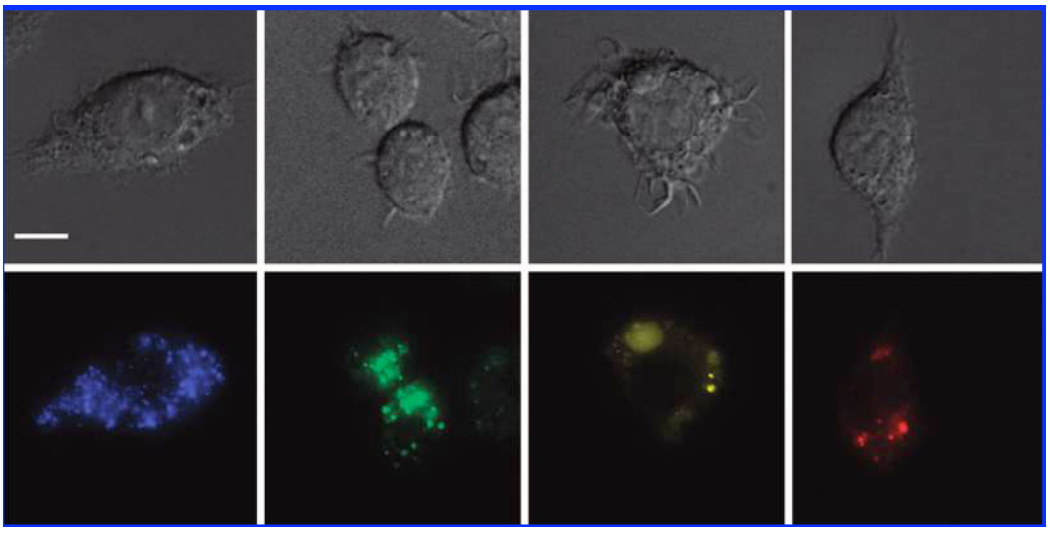

Figure 5.6. Differential interference contract (DIC) images (top) and fluorescence images (bottom) of macrophage cells labeled with PPE, PFPV, PFBT, and MEHPPV polymer nanoparticles. Scale bar: 10 μm.

5.1.3 Encapsulation of Conjugated Polymers in Calcium Phosphate Nanoparticles

5.1.3.1 Preliminary Data

Conjugated organic polymer nanoparticles show promise as an imaging agent for biological studies because of their extreme brightness and ease of preparation. Photostability of these nanoparticles are reported to be similar to fluorescent organic dyes and further investigation is required to ascertain their long-term stability in order for them to be useful for *in vivo* animal imaging. Macrophages are a type of white blood cell involved in cleaning up any foreign debris and as such can uptake any material, therefore cellular imaging studies with other more widely used cell lines such as HeLa cells should be carried out to study the broad applicability of these nanoparticles. The cytotoxicity of these nanoparticles should also be evaluated on different cell lines with respect to particle size and polymer used in their preparation.

The widespread use of these polymer nanoparticles in biological studies can be envisioned only if they are modified so as to make them (i) more photostable (ii) have emission characteristics shifted closer to the near infrared region (iii) minimally cytotoxic and (iv) biocompatible. In order to achieve these objectives a rational design

comprising conjugated organic polymers, near infrared fluorophore and calcium phosphate nanoparticle can be put forward. The idea is to covalently attach fluorophores to the polymer backbone in such a way to facilitate through-bond energy transfer from the polymer to the fluorophore and then encapsulate these modified polymers in biocompatible and non-cytotoxic calcium phosphate nanoparticles to improve their photostability. As mentioned earlier there need not be any overlap of the emission of the polymer with the absorbance of the fluorophore for energy transfer to occur.

We modified the published procedure for calcium phosphate nanoparticle synthesis so that polymer nanoparticles from **PFO** could be used as the organic cargo, and cast calcium phosphate around the organic nanoparticle. Since polymer nanoparticles are unstable in organic media no surfactant was used in their encapsulation in calcium phosphate. Briefly 1.0 mL of the polymeric nanoparticles 20 nm in diameter and 40 ppm in concentration were stirred along with sodium phosphate 0.1 mL (6×10^{-3} M) and sodium silicate 0.05 mL (8×10^{-4} M) for 5 min and calcium chloride 0.1 mL (10^{-2} M) was added. The solution was stirred for 10 or 20 minutes for calcium phosphate nanoparticle formation and then quenched with 0.1 mL sodium citrate (10^{-3} M). Overall these particles were 90- 110 nm in diameter (atomic force microscopy, AFM, Figure 5.7).

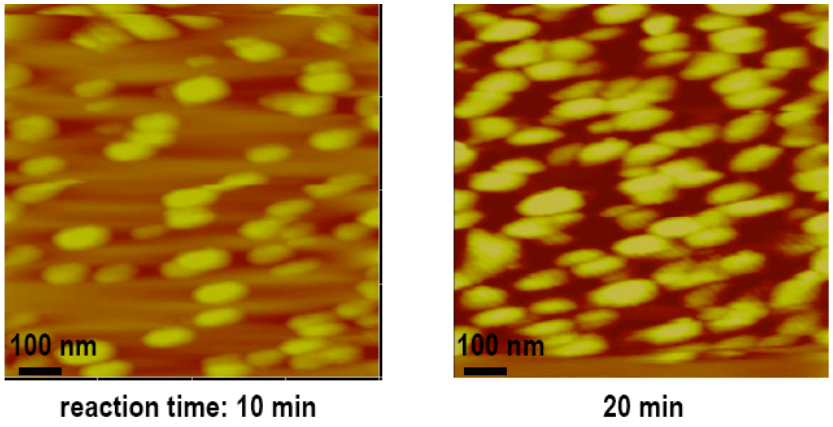

Figure 5.7. AFM images of polymer nanoparticles encapsulated in calcium phosphate at different reaction times.

The large size of these particles makes them less useful for imaging studies because large particles have a tendency to aggregate and they are less cell permeable. An optimum size for nanoparticles for cellular imaging studies is 20-30 nm as is the case with silica and calcium phosphate nanoparticles.[170,174] We reasoned that instead of encapsulating polymer nanoparticles in calcium phosphate, the polymer could be directly encapsulated in calcium phosphate to obtain nanoparticles in the size range of 20-30 nm. The synthetic procedure for polymer encapsulated calcium phosphate nanoparticles is shown in Figure 5.8. The procedure is similar to the published procedure,[170] except the reaction time, which is 6 h instead of the usual 5 min. We believe the increase in reaction time will help achieve complete encapsulation of the polymer and help in formation of a compact shell. The concentration of the polymer cargo used was 10^{-5} M and 1.0 mL of polymer solution in THF was used for nanoparticle synthesis. The polymer was not very soluble in THF or any other solvents and therefore the encapsulation process was not very efficient.

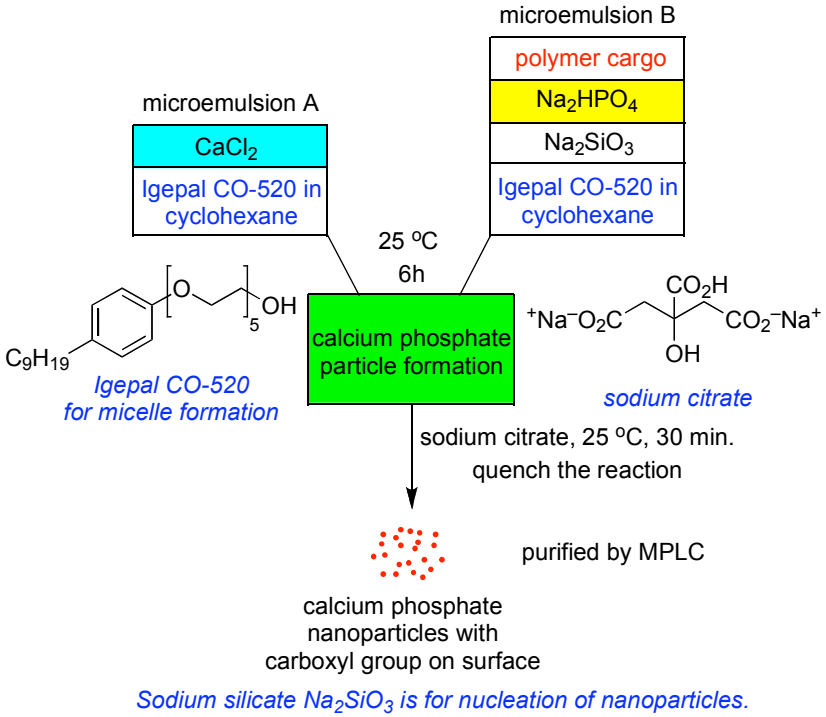

Figure 5.8. Synthesis of polymer doped calcium phosphate nanoparticles.

Figure 5.9 shows the normalized absorbance and emission spectra of PFPV encapsulated calcium phosphate nanoparticles. The absorbtion and emission properties of these particles are similar to the parent polymer, indicating that unlike polymer nanoparticles, polymer inside calcium phosphate matrix exists as dispersed single molecules, thereby reducing intermolecular quenching.

a

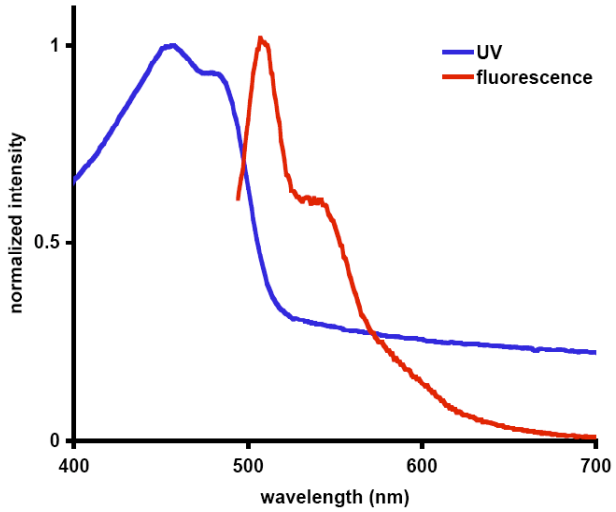

b

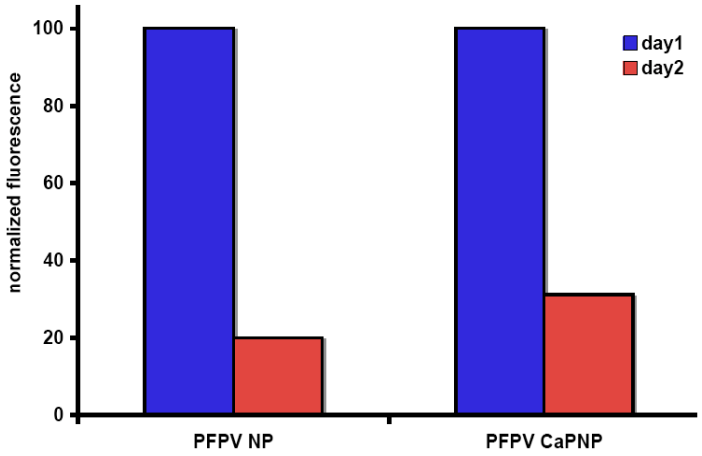

Figure 5.9. (**a**) Normalized absorbtion and emission of polymer doped calcium phosphate nanoparticles and (**b**) comparison of photostability of PFPV polymer nanoparticles and PFPF encapsulated calcium phosphate nanoparticles in pH 7.4 phosphate buffer.

The photostability of polymer encapsulated calcium phosphate nanoparticles is greater than the corresponding polymer nanoparticles by a factor of 10 % (Figure 5.9b). These measurements were done by exposing the nanoparticle samples to ambient light for two days. The sharp decrease in fluorescence intensity from day one to day two for both sets of nanoparticles is due to the extreme instability of PFPV towards light. Calcium phosphate does seem to provide some protection to the encapsulated polymer as evident from the fluorescence output of the samples on day two. The photostability studies were repeated two times and averaged. PFPV being the least light stable among all the available polymers, we expect the photostability of calcium phosphate nanoparticles prepared from other conjugated polymers to be better.

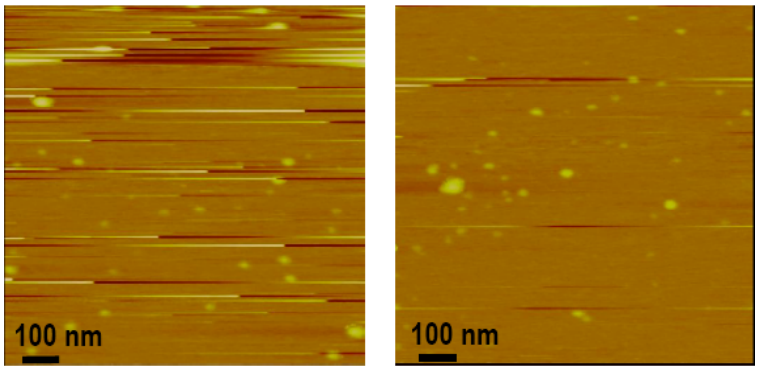

Figure 5.10. AFM images of PFPV and PFO encapsulated calcium phosphate nanoparticles.

Atomic microscopy images (AFM) show well dispersed particles with particle size ranging from 12 -31 nm (Figure 5.10). These smaller particles are better suited for imaging purposes than the larger ones previously prepared. With this preliminary data in hand we will try to encapsulate polymers covalently linked to near infrared fluorophores into calcium phosphate nanoparticles.

5.1.3.2 Future Goals

The most important step in our approach is the synthesis of polymer with a fluorophore covalently attached to it. This is somewhat similar to the synthesis of through-bond

energy transfer cassettes, the major difference being the ratio of donor and acceptor used. From reported literature,[186] it is known that for FRET based systems efficient energy transfer form the polymer to the dopant dye is possible at a dopant concentration of 1.0 wt %. A further increase in dopant concentration results in decreased energy transfer due to intermolecular quenching of the dopant dye molecules. Therefore our synthesis will be modified to include relatively small amounts of acceptor fragments that fluoresce at long wavelengths relative to the polymer donor, and that become electronically conjugated to the polymer. Thus acceptor-containing monomers will be added to the polymer syntheses at relatively low levels (around one acceptor molecule per 100 donor monomers used in the polymerization would be a good starting point). For instance, the **PF** polymer derivatives will be made using Suzuki coupling procedures that have been used extensively for these polymer types. In the proposed work relatively low concentrations of acceptor fragments will also be added to the syntheses. The part of the acceptor that becomes integrated into the main polymer chain may modulate the spectroscopic properties of the polymer and is therefore called "modulator". These modulators might be significantly more or less electron donating than the core of polymer, thus improving its "push-pull" characteristics, increasing its one- and two-photon cross sections (Figure 5.11b).

a

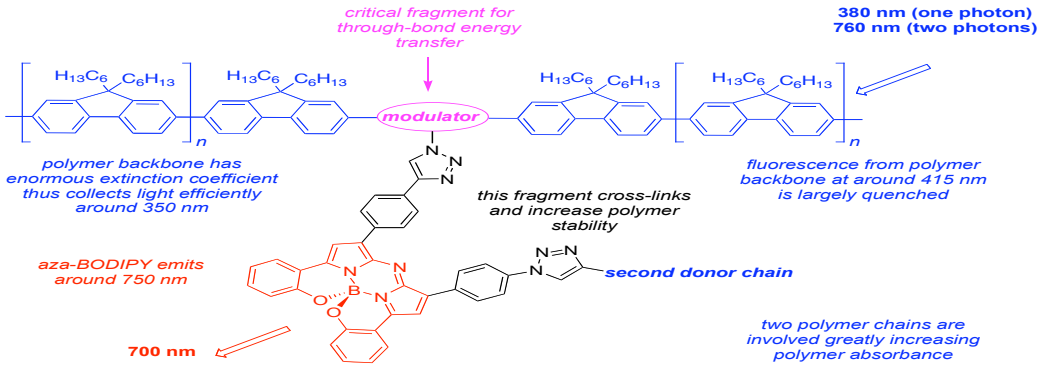

Figure 5.11. (a) Proposed backbone modified conjugated organic polymer with an acceptor fluorophore. (b) Modulator fragments for efficient energy transfer. (c) Fluorophores for polymer synthesis.

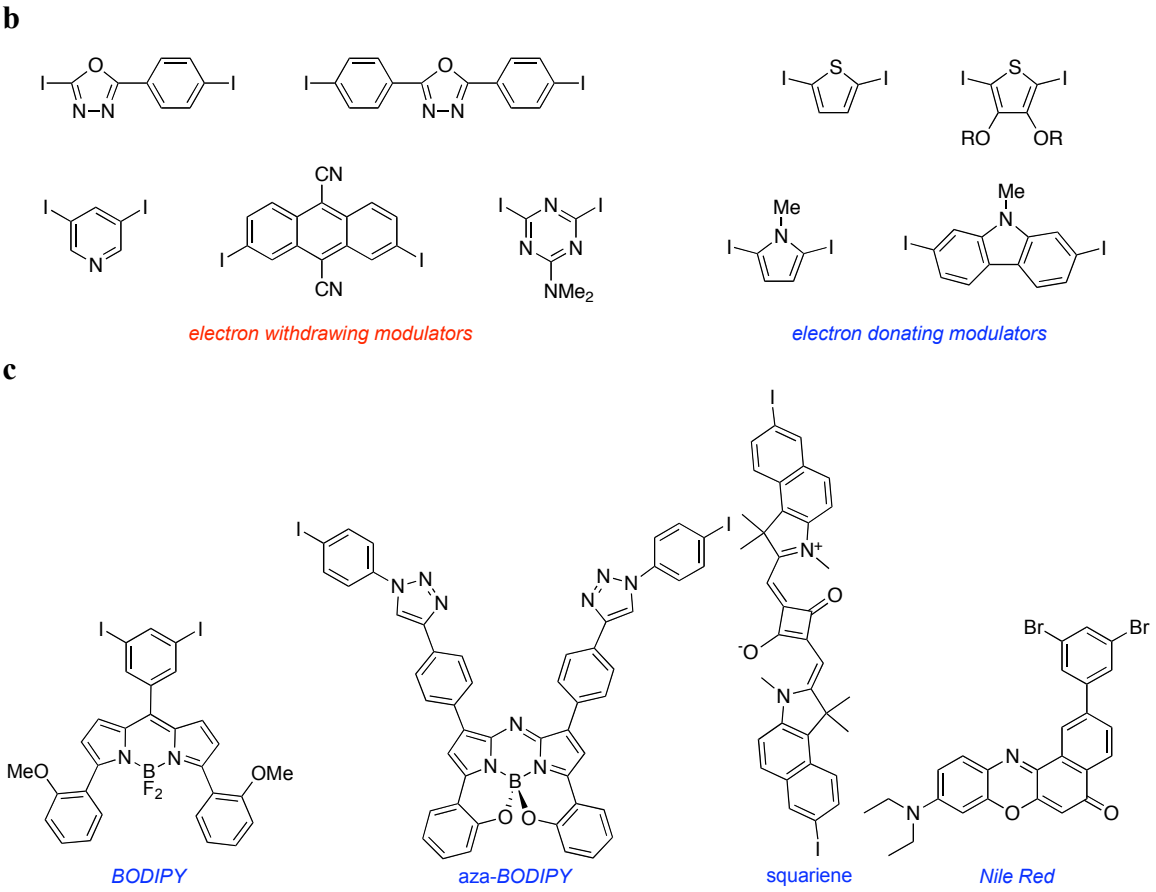

Figure 5.11. Continued.

Polymer encapsulated calcium phosphate nanoparticles holds promise because of their high per particle brightness and nontoxic nature. Through-bond energy transfer systems where conjugated polymers act as donors and near infrared emitting fluorophores act as acceptors is a novel approach towards channeling the vast photon energy absorbed by the polymer to the fluorophore thereby shifting the emission of the system to a longer wavelength. Non-radiative processes can be minimized by encapsulating them in calcium phosphate, which gives sufficient shielding from quenchers such as oxygen and solvents. A further advantage of such nanoparticles is their biocompatibility because calcium and phosphate ions are ubiquitously present in human beings and possess no toxic side effects at millimolar concentrations.

5.1.4 Sensing and Detecting Explosives Using Organic Fluorophores

Detection of explosives in aqueous media as well as in gaseous environment is gaining widespread research interest for security reasons.[188-190] Detection techniques need to be sensitive with low detection limit, accurate and less time consuming to ensure the safety of everyone and reduce damages in the event of an explosion. The most widely studied explosives are nitro compounds such as TNT, RDX and PETN (Figure 5.12). Most of these chemical compounds have low vapor pressures and are therefore difficult to detect. Most explosives are fluorescence quenchers and therefore the decrease in fluorescence of a fluorophore can be monitored for the detection of such compounds. Fluorescence based methods for detection requires only an excitation source and a detector, which can be easily incorporated into a hand held device for field detection of explosives. Explosives are inherently non-fluorescent and therefore background interference in such measurements is minimal.

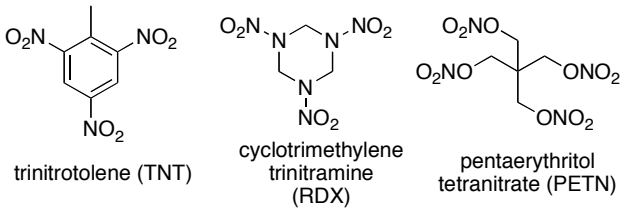

Figure 5.12. Structure of common nitro explosives.

Figure 5.13 shows some commonly used organic fluorophores for detection of nitro explosives.[190,191] These fluorophores are able to detect nitro explosives in picomolar and even ppb levels, which can be quantified by the reduction in their fluorescence upon interaction with the explosives. Detection of explosives via fluorescence can be classified into the following three categories: (i) indirect fluorescence methods (ii) indirect laser induced fluorescence (iii) fluorescence immunoassays. All three methods detect the decrease in fluorescence of the fluorophore upon interaction with an explosive. Detection is either done in solution phase or in solid state. For field detection of explosives it is beneficial for the fluorophore to be solid state, due to ease of handling.

Most often fluorophores are incorporated into a poly(vinylchloride) membrane or into a silica monolith. Polymers and silica beads have also been used as a solid support for organic fluorophores. The fluorophore doped particles are fixed on to a glass slide or onto the end of an optical fiber and then exposed to the explosive vapor. The rate of reduction in fluorescence of the fluorophore is related to the diffusion of the vapor into the particles which allows the identity of the explosive to be determined.

Indirect laser induced fluorescence approaches involve displacement of the fluorophore by the explosive based on either charge or space considerations, leading to a local decrease in fluorescence. The fluorophore is usually contained in a micelle such as sodium dodecyl sulfate that favors radiative processes and therefore the fluorophore is highly fluorescent. The presence of an explosive will disturb the equilibrium between the fluorophore and the micelle there by reducing the fluorescence intensity. In this method a laser is used to excite the fluorophore and reduction in fluorescence is correlated to the concentration of fluorophore.

Fluorescence immunoassays are widely used for detecting nitrated explosives. An explosive specific antibody is saturated with a fluorescently labeled analog of the explosive molecule. When this antibody is exposed to an explosive, the explosive displaces the fluorescent label. This causes a change in the fluorescence properties of the fluorescent label and enables detection. These immunoassays have been incorporated into a number of field devices and tested on real samples.

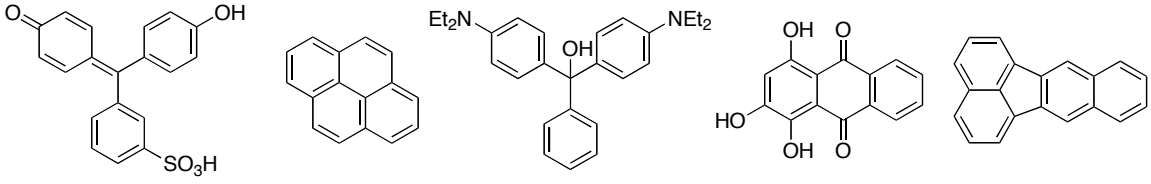

phenol red $\lambda_{max\ abs}$ 325 nm $\lambda_{max\ emiss}$ 369 nm

pyrene $\lambda_{max\ abs}$ 325 nm $\lambda_{max\ emiss}$ 375 nm

malachite green $\lambda_{max\ abs}$ 325 nm $\lambda_{max\ emiss}$ 379 nm

purpurin $\lambda_{max\ abs}$ 325 nm $\lambda_{max\ emiss}$ 413 nm

benzo[*k*]fluoranthene $\lambda_{max\ abs}$ 308 nm $\lambda_{max\ emiss}$ 435 nm

Figure 5.13. Structure of commonly used organic fluorophores for detection of nitrated explosives. Photophysical properties measured in THF.

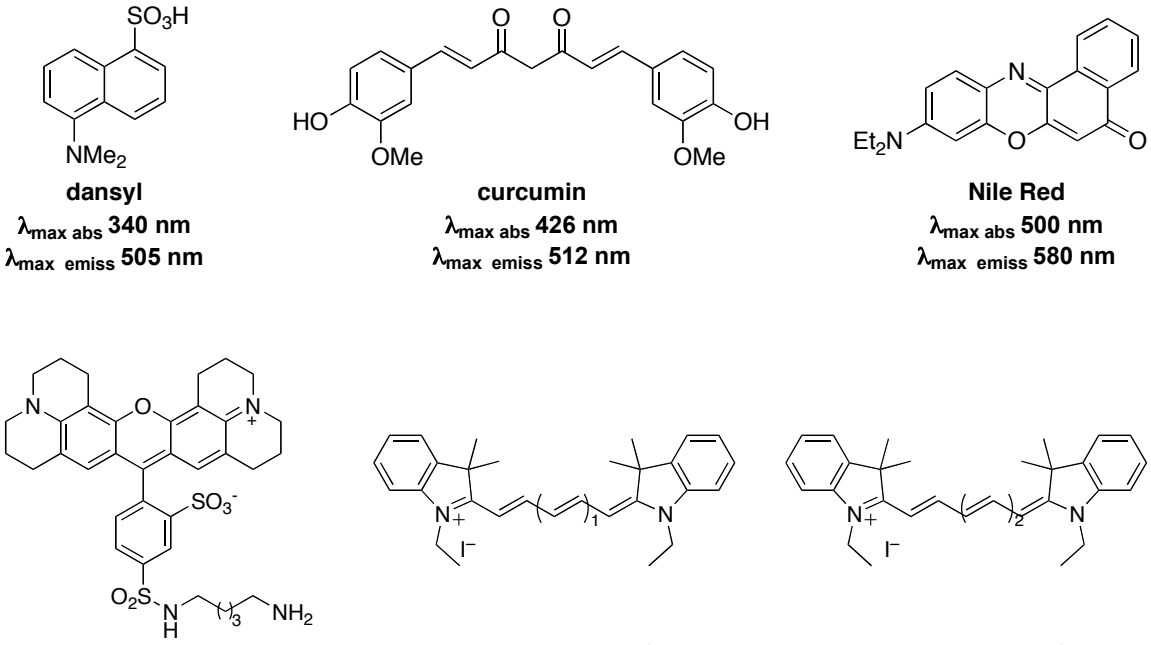

Figure 5.13. Continued.

From the above fluorescence based detection methods used, it is clear that the solubility of the fluorophore in aqueous media is very important for their success in field measurements because most often explosives are found in a hydrophilic environment. Water-soluble analogues of above mentioned fluorophores and ones that emit to the far red could be easily synthesized, thereby improving detection limits and sensitivity. Some examples of such fluorophores are shown in figure 5.14. Since most of these fluorophores are used in field detection studies, their photostability to ambient light is very important. Their photostability can be improved by encapsulating them in mesoporous silica nanoparticles. In this particular type of application control of particle size need not be very stringent and can be in the range of 100-200 nm.

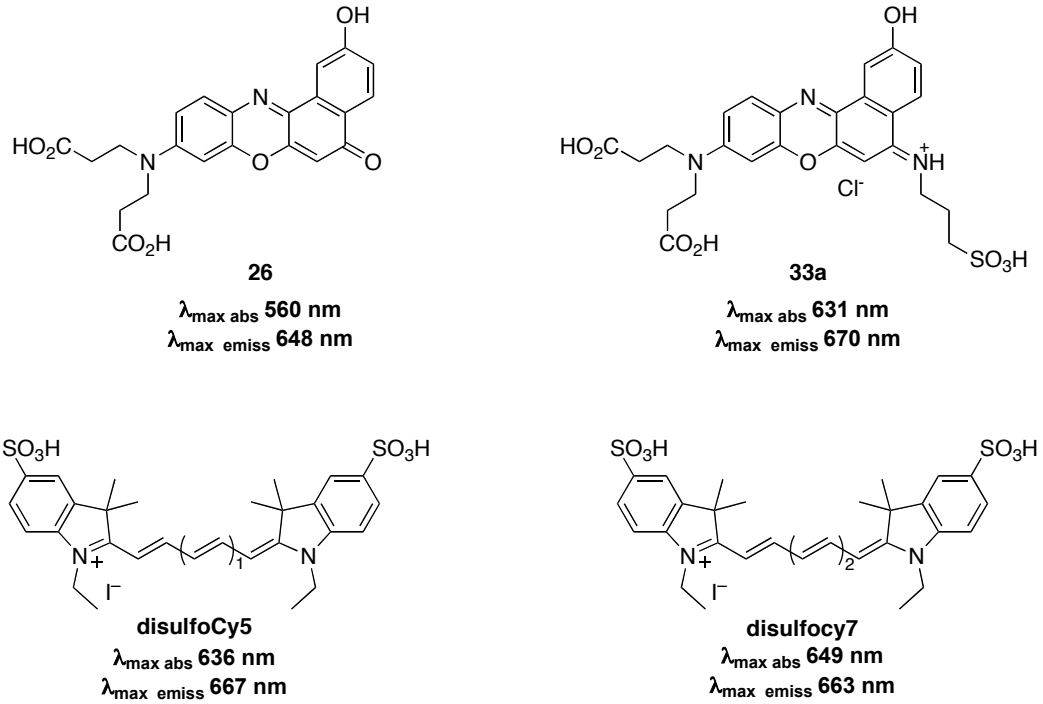

Figure 5.14. Water-soluble organic fluorophores for detection and sensing of nitrated explosives. Absorbance and emissions measured in pH 7.4 (0.1 M phosphate buffer).

Conjugated organic polymers are the most widely used materials for the detection of nitrated explosives and the process was first developed by Swager *et al.*[192] These polymers are characterized by a "molecular wire" effect, in which the conjugated backbone of the polymer helps in efficient delocalization of electron density due to the absorbtion of light and they emit in the visible region of the spectrum.[193] Perturbation in electron delocalization by any external factor, in this case by the interaction of explosive with the polymer chain results in a significant reduction in the fluorescence output. The sensitivity of such conjugated polymers towards nitrated explosives are 50 fold higher than organic fluorophores. The quenching occurs via an electron transfer mechanism and is dominated by a static interaction between the explosive and the polymer. This nonbonding electrostatic interaction between the electron rich polymer and the electron deficient nitrated explosives is critical in the detection process. The response of the polymer was initially verified using paraquat, a well known electron transfer quenching agent (Figure 5.15).

Most of the conjugated polymers used are iptycene based and their response to explosives is dependent on the vapor pressure of the explosives and the charge distribution of the polymer and the explosives (Figure 5.15).[194] Presence of the iptycene moiety in the polymer backbone prevents π stacking or excimer formation and thus prevents self quenching of the polymers. The rigid iptycene moiety also provides cavities for the explosives to bind to the polymer, an important reason behind their high sensitivity.[195] The response time of such polymers is usually measured in seconds.

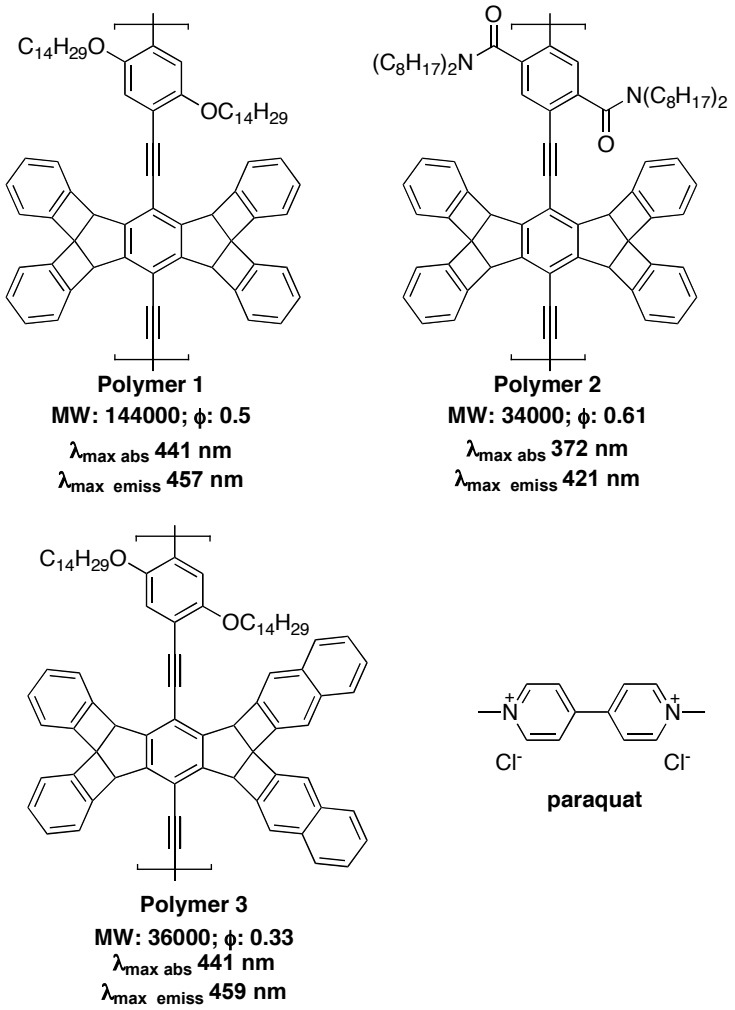

Figure 5.15. Structure of iptycene based polymers and paraquat. Photophysical properties measured in dichloromethane.

Synthesis of such polymers (Scheme 5.4) involves palladium catalyzed cross coupling reaction of corresponding disubstituted diiodobenzenes with iptycene diacetylenes.[194] The iptycene diacetylenes are obtained from the corresponding iptycene quinones, which in turn are obtained from reaction of benzoquinone and anthracene or pentacene. As evident from the reaction scheme the synthesis of iptycene precursors is low yielding and accompanied by isomers that makes purification difficult. This step is a bottleneck in the synthesis of iptycene based polymers.

Scheme 5.4. Synthesis of polymer **1** and iptycene precursor.

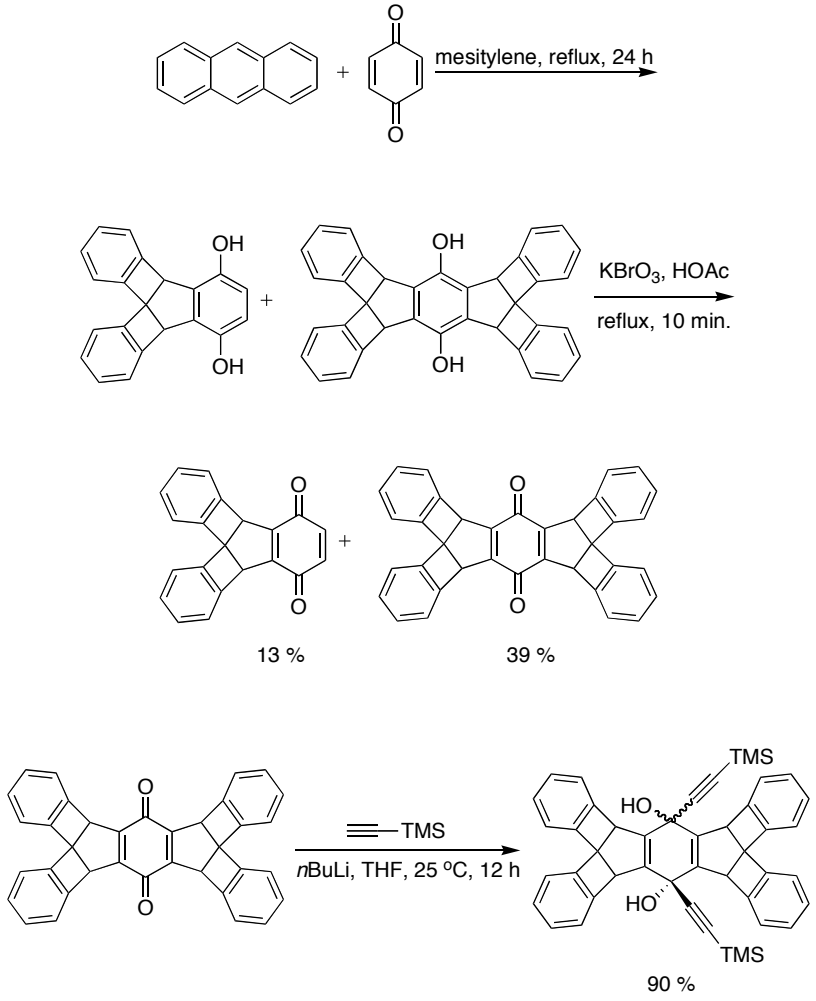

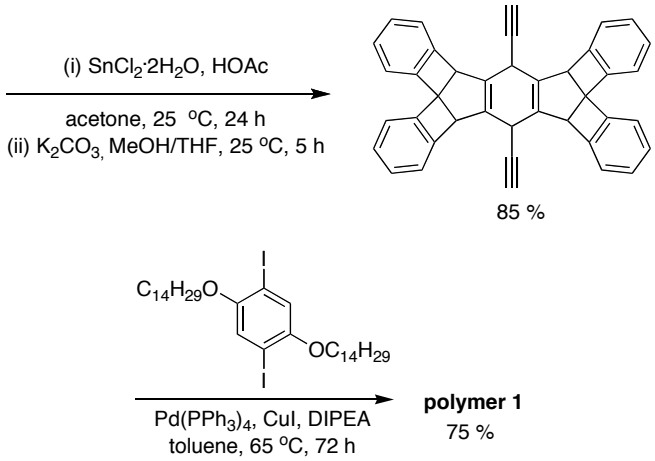

The absorbance and emission of iptycene based polymers are in the 400-500 nm region. There are hardly any literature reports on fluorene based polymers for explosive sensing and detection. We believe that electron rich fluorene based polymers will be a useful addition to the growing number of polymers used for such applications. It would be interesting to synthesize a copolymer from iptycene and fluorene and study its photophysical properties (Figure 5.16). Most polyfluorenes have a red shifted emission compared to the iptycene polymers and by following the strategy described in the previous section (covalent attachment of an organic fluorophore to the polyfluorene back bone to form through-bond energy transfer system) the emission wavelength can be shifted to any desired wavelength. One important draw back of polymers in field detection of explosives is their photo instability in ambient light. This can be overcome by either encapsulating these polymers in calcium phosphate or silica to form nanoparticles with improved photostability and dispersibility in aqueous media.

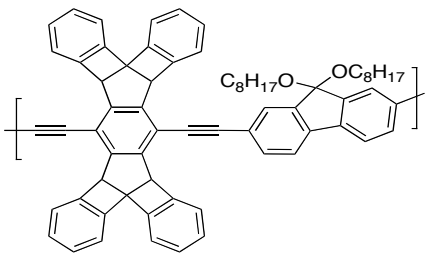

Figure 5.16. Proposed copolymer from iptycene and fluorene.

5.1.5 Solid Emissive Organic Fluorophores

Solid emissive organic fluorophores is the focus of intense research because of their possible application in optoelectronics such as organic light emitting diodes (OLED).[54,196] OLED is any light emitting diode whose emissive electroluminescent layer is composed of a film of organic dye deposited by a polymer coat. OLED finds widespread application in television screens, computer displays, cell phones and can be used as a general light source. A significant benefit of OLED is that they do not require any backlight to function and therefore draw far less power than liquid crystal displays (LCD).

In OLED applications efficient green and blue emitting materials have been developed[197] and commercialized whereas red emitting material is still proving to be a stumbling block. Organic fluorophores with emissions in the 600-800 nm region in solution and solid phase are very rare. This is because their dense packing in amorphous or crystalline state leads to quenching of the fluorescence. Most organic fluorophores have high planarity in molecular structures and result in well-ordered π stacking leading to aggregation in solid states. Aggregation in solid state can be prevented by introducing bulky substituents thereby disrupting the ordered π stacking and minimizing quenching effects.

BODIPY dyes with their fine tunable emission and ease in synthetic manipulation appear to be a suitable candidate for investigation in solid-state emissive materials. Akkaya *et al*[198] reported the synthesis of solid emissive BODIPY dyes with bulky substituents to prevent π stacking and quenching. They introduced *tert*-butyl and 3,5-di-*tert*-butyl phenyl substituents and found that these groups are very effective in keeping the π system apart. Scheme 5.5 shows the synthesis of BODIPY dyes **1** and **2**. The reaction of appropriate aldehyde with corresponding pyrrole following standard BODIPY synthesis conditions afforded **1** and **2** in 45 and 26 % yield respectively. Crystal structures obtained for dyes **1** and **2** showed that the distance between the closest

overlapping near-parallel π-surfaces in compound **1** and **2** are considerably larger than BODIPY dyes with no substituents. This indicates that *tert*-butyl group acts as a molecular separator in these dyes and reduces quenching in the solid state. Both dyes showed a red shifted emission in solid state (BODIPY **1**: 590 nm and **2**: 610 nm) as compared to their emission in solution (BODIPY **1**: 500 nm and dye **2**: 520 nm). The absorbtion of both dyes in solid phase were **1**: 490 nm and **2**: 510 nm respectively and absorbtion in solution phase were not reported.

Scheme 5.5. Synthesis of BODIPY with bulky *tert*-butyl substituents to prevent π stacking.

a

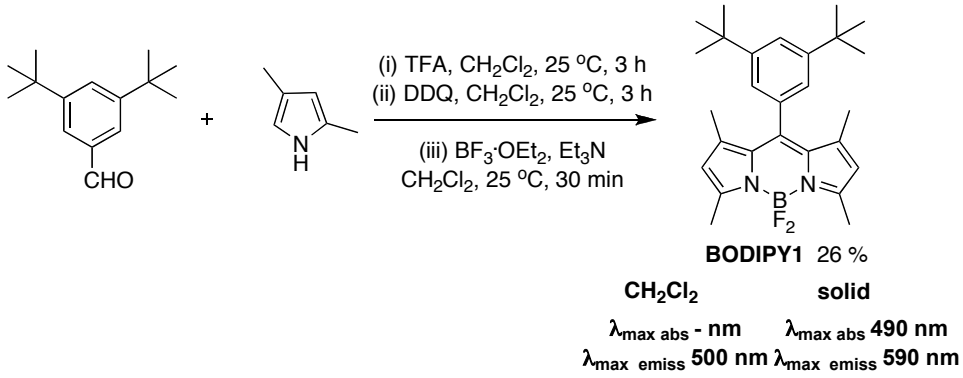

b

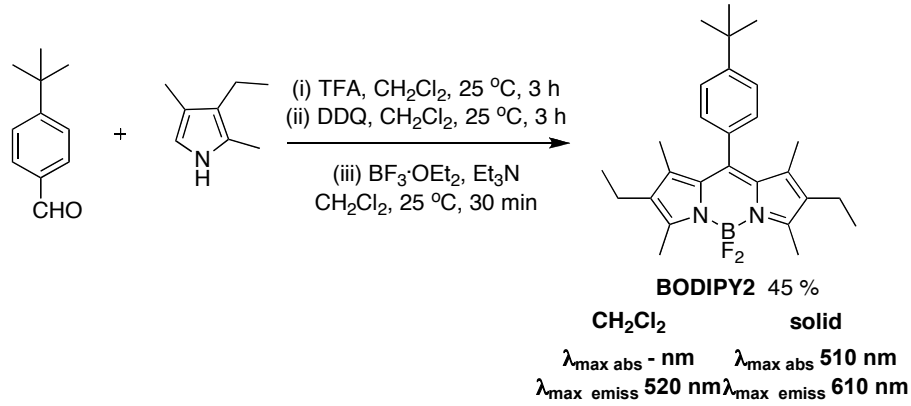

Qian *et al*[199] reported a similar modification of BODIPY dyes with bulky trityl groups and found that the introduction of the trityl group caused a significant red shifted

emission compared to parent BODIPY dye in solid state possibly due the extended conjugation afforded by the trityl groups. Thus the trityl groups serve the dual purpose of disrupting π stacking and extending conjugation. Scheme 5.6 illustrates the synthesis of BODIPY3. Trityl chloride is converted to the corresponding tritylalkyne in four steps via palladium catalyzed cross coupling. The tritylalkyne is coupled to diiodo BODIPY to afford BODIPY3 in 71 % yield.

Scheme 5.6. (a) Synthesis of (a) Trityl alkyne **A** and (b) BODIPY decorated with trityl groups.

a

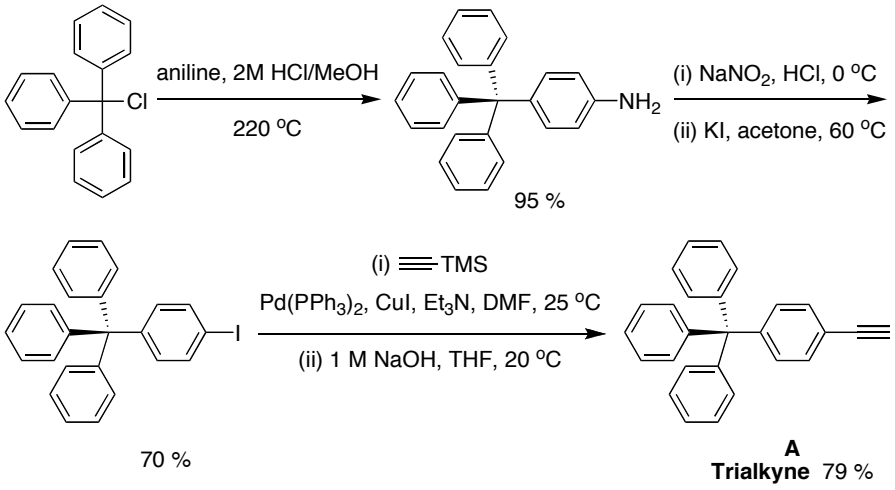

b

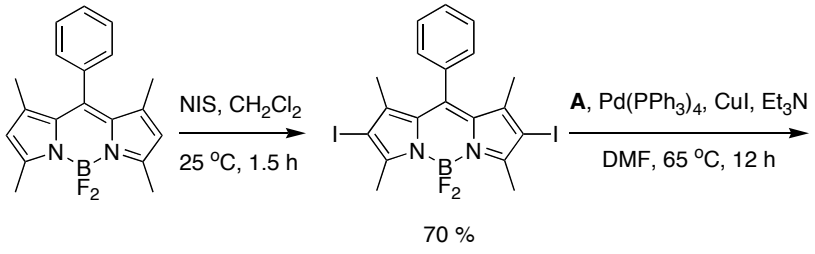

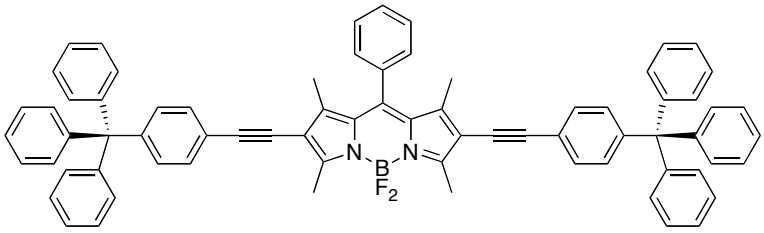

BODIPY3 71 %

CH_2Cl_2	solid
$\lambda_{max\ abs}$ 575 nm	$\lambda_{max\ abs}$ 575 nm
$\lambda_{max\ emiss}$ 610 nm	$\lambda_{max\ emiss}$ 610 nm

The photophysical properties of BODIPY3 in dichloromethane were measured and found to have a quantum yield of 0.79 with an absorbtion at 575 nm and emission at 610 nm. The dye exhibited similar photophysical properties in solid state. The enhanced fluorescence emission in solid state can be attributed to the steric bulk of the trityl group, which prevents π stacking of the molecules, weakens intermolecular interactions and inhibits self-quenching.

Another bulky group used for improving the photophysical properties of a dye in solid state is the perfluoropropylene trimer (Figure 5.17) derived substituents. Benzophenoxazine dye Nile Red with trimer **A** at the 2 position showed exceptional fluorescence emission in solid state; where as Nile Red with no substitution is completely non fluorescent.[200]

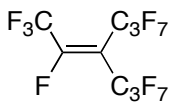

trimer A

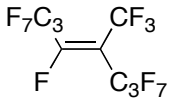

trimer B

Figure 5.17. Perfluoropropylene trimers.

Scheme 5.7. Synthesis of solid emissive Nile Red dye.

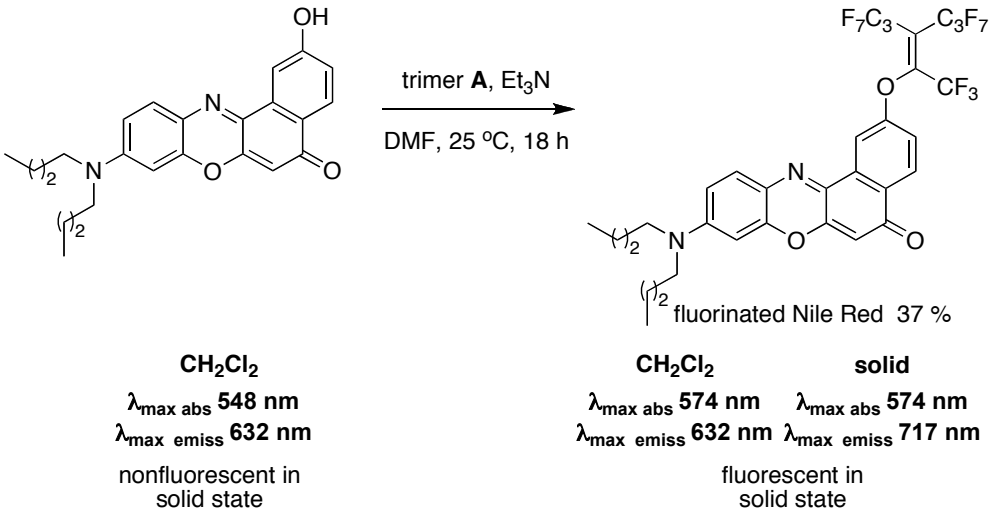

The emission profile of fluorinated Nile Red is vastly different in solid phase and solution phase. The fluorescence emission in solid state has maxima at 717 nm where as in solution phase the fluorescence maxima is at 632 nm. The authors attribute this bathochromic shift to an increased intermolecular interaction between dye molecules in solid phase compared to solution phase. The quantum yield of the fluorinated Nile Red in dichloromethane is 0.69 and in solid state it is 0.024 which shows that inspite of the presence of trimer **A** in the dye structure there is significant quenching of the dye in solid state and a more bulky group is required to prevent π stacking.

A more direct way of overcoming quenching interactions in fluorescent dyes in solid state is to encapsulate them in a matrix such as silica or calcium phosphate. Results obtained from our laboratory have shown that Nile Red dye upon encapsulation in silica nanoparticles (20 nm dimension) is bright red fluorescent in solid state (Figure 5.18). We do not find any bathocromic shift in fluorescence emission probably due to less intermolecular interaction between dye molecules inside the silica matrix. Since any organic fluorophore except few cyanine dyes (Cy7 and similar ones) can be encapsulated in silica using simple synthetic procedures, fluorescent silica nanoparticles can be used as a possible substitute for organic dyes in preparation of organic light emitting diodes

(OLED). The most important draw back of organic dyes is their photo instability, which greatly effects the lifetime of OLED. The lifetime of OLED is nearly half of the traditional liquid crystal display (LCD).[201] Encapsulation of organic dyes in silica nanoparticles is known to improve their photostability and therefore will improve the lifetime of OLED and make it cost efficient.

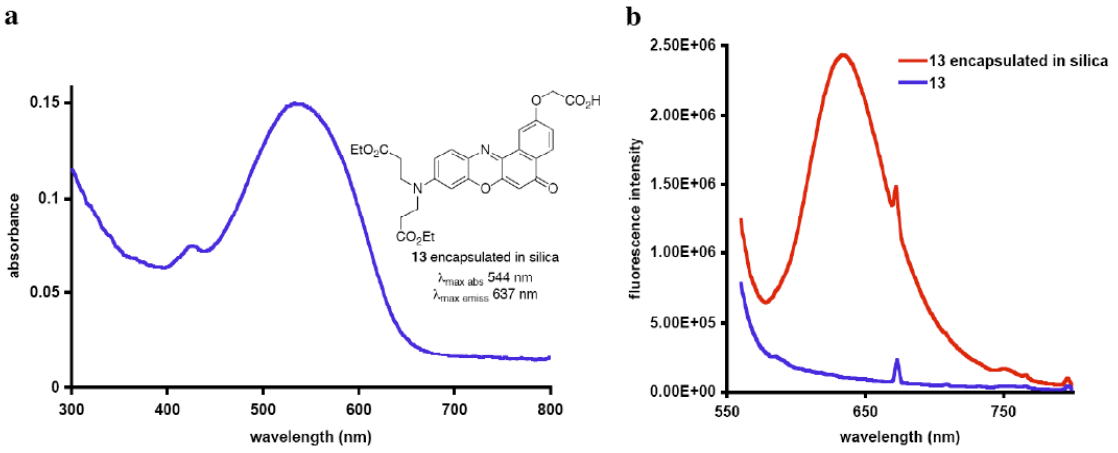

Figure 5.18. (**a**) Absorbance of **13** encapsulated in silica nanoparticles in solid state and (**b**) comparison of solid-state emission of **13** and **13** encapsulated in silica nanoparticles.

5.2 Conclusions

Nine water-soluble benzophenoxazine dyes were prepared and their photophysical properties in aqueous media evaluated (Figure 5.19). It was found that carboxylic acid and hexaethylene glycol chains have a greater impact on fluorescence output in aqueous media compared to sulfonic acid groups. This is probably because these groups are better suited to disrupt π stacking of dyes than sulfonic acids, thereby preventing self quenching of the dye molecules. The quantum yields of these dyes were in the range of 0.1-0.33 in pH 7.4 phosphate buffer. Selected dyes **25** and **27** specifically stained the mitochondria and the golgi apparatus respectively proving their applicability for bioimaging studies. Dye **13** was used for preparation of so called "SNAP-tag" by attaching it to benzylguanine derivatives. Transfection of CHO cell lines CHO-K1 and CHO-NLS with AGT26-his fusion protein and treatment with **13a**, **13b**, and **13c** gave

distinct fluorescence, indicating that the compound is entering the cell but was trapped in either vesicles and in some cases mitochondria. Further investigation is required for constructing a SNAP-tag that can track specific organelles. Dye **33a** was used for conjugate addition to ovalbumin with a labeling efficiency of 22 %. The fluorescence intensity of the dye-ovalbumin conjugate was much less than the dye itself. This dye was also used to measure ovalbumin concentrations in dilute samples. It was found that with increasing addition of small amounts of ovalbumin there was a corresponding increase in fluorescence output of the dye. The water-solubility of the dye circumvents the need for any detergent additives for such studies.

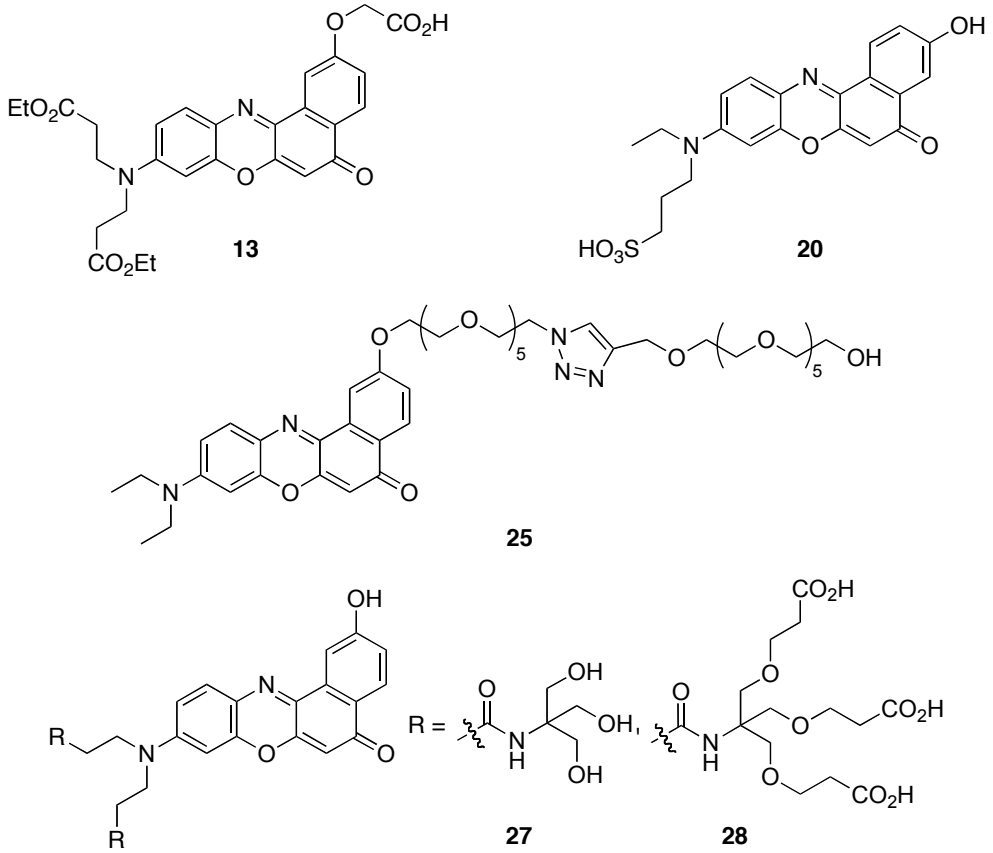

Figure 5.19. Structure of synthesized water-soluble benzophenoxazine dyes.

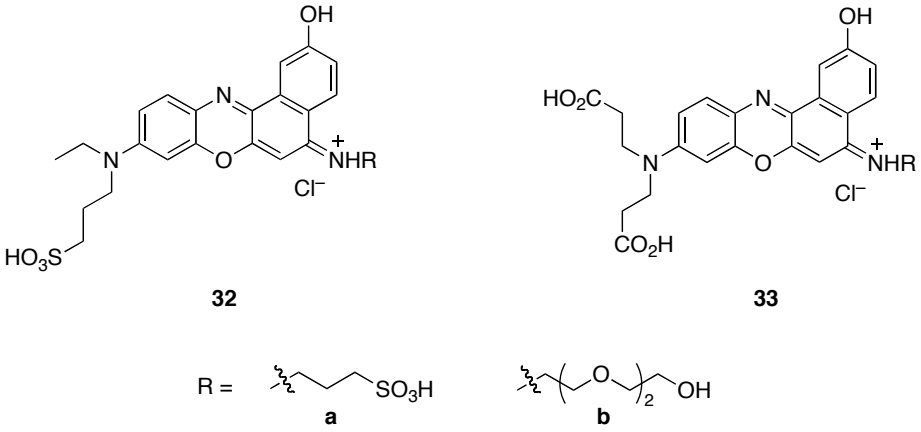

Figure 5.19. Continued.

We synthesized six through-bond energy transfer cassettes that showed good energy transfer in organic media but poor energy transfer in aqueous media. Presence of water-soluble groups did not improve energy transfer in these cassettes. Therefore some of these cassettes were encapsulated in a silica or calcium phosphate matrix to form 20-30 nm nanoparticles. These nanoparticles were easily dispersible in pH 7.4 phosphate buffer after dialysis and improved energy transfer efficiency of the encapsulated cassettes. The cassettes encapsulated in silica nanoparticles were used for cellular imaging studies and showed good uptake in COS7 cell lines. Silica and calcium phosphate nanoparticles serve as a useful matrix to encapsulate both water-soluble and insoluble fluorophores. The encapsulation indirectly makes these fluorophores water-soluble and also improves their photophysical properties.

For almost 80 years fluorescence has been used as a sensitive technique for biological studies and most recently in detection of explosives and for preparation of optoelectronics such as OLED. Organic fluorophores due to their low toxicity and tunable fluorescence properties continue to hold a prominent place in all the above applications. Their drawbacks such as low photostability, poor water-solubility and aggregation can be over come by either synthetic manipulation or more conveniently by their encapsulation in matrixes such as silica and calcium phosphate to form nanoparticles.

REFERENCES

(1) Lang, P.; Yeow, K.; Nichols, A.; Scheer, A. *Nat. Rev. Drug Discovery* **2006**, *5*, 343-356.

(2) Weissleder, R.; Ntziachristos, V. *Nat. Med.* **2003**, *9*, 123-128.

(3) Kiyose, K.; Kojima, H.; Nagano, T. *Chem.--Asian J.* **2008**, *3*, 506-515.

(4) Bouteiller, C.; Clave, G.; Bernardin, A.; Chipon, B.; Massonneau, M.; Renard, P.-Y.; Romieu, A. *Bioconjugate Chem.* **2007**, *18*, 1303-1317.

(5) Masotti, A.; Vicennati, P.; Boschi, F.; Calderan, L.; Sbarbati, A.; Ortaggi, G. *Bioconjugate Chem.* **2008**, *19*, 983-987.

(6) Hintersteiner, M.; Enz, A.; Frey, P.; Jaton, A.-L.; Kinzy, W.; Kneuer, R.; Neumann, U.; Rudin, M.; Staufenbiel, M.; Stoeckli, M.; Wiederhold, K.-H.; Gremlich, H.-U. *Nat. Biotechnol.* **2005**, *23*, 577-583.

(7) Xu, X.; Brzostowski Joseph, A.; Jin, T. *Methods Mol. Biol.* **2006**, *346*, 281-296.

(8) Johnson, I. *Histochem. J.* **1998**, *30*, 123-140.

(9) Waggoner, A. *Methods Enzymol.* **1995**, *246*, 362-373.

(10) Ju, J.; Glazer, A. N.; Mathies, R. A. *Nat. Med.* **1996**, *2*, 246-249.

(11) Metzker, M. L.; Lu, J.; Gibbs, R. A. *Science* **1996**, *271*, 1420-1422.

(12) Kikuchi, K.; Takakusa, H.; Nagano, T. *TrAC, Trends Anal. Chem.* **2004**, *23*, 407-415.

(13) Caturla, F.; Enjo, J.; Bernabeu, M. C.; Le Serre, S. *Tetrahedron* **2004**, *60*, 1903-1911.

(14) Stark, J. *Ann. Phys.* **1928**, *87*, 909-926.

(15) Cario, G. *Z. Phys.* **1922**, *10*, 185-199.

(16) Perrin, J.; Choucroun *Compt. Rend.* **1929**, *189*, 1213-1216.

(17) Weiss, J. *Trans. Faraday Soc.* **1938**, *34*, 451-456.

(18) Weiss, J. *Nature* **1938**, *141*, 248-249.

(19) Forster, T. *Naturwiss.* **1946**, *6*, 166-175.

(20) Lackowicz, J. R. *Principles of Fluorescent Spectroscopy*; 2nd ed.; Kluwer Academic/Plenum Publishers: New York, 1999.

(21) Dexter, D. J. *J. Chem. Phys.* **1953**, *21*, 836-850.

(22) Ghiggino, K. P.; Yeow, E. K. L.; Haines, D. J.; Scholes, G. D.; Smith, T. A. *J. Photochem. Photobiol., A* **1996**, *102*, 81-86.

(23) Burgess, K.; Burghart, A.; Chen, J.; Wan, C.-W. *Proc. SPIE-Int. Soc. Opt. Eng.* **2000**, *3926*, 95-105.

(24) Burgess, K.; Gibbs, R. Anthracene derivatives and BODIPY fragments in fluorescent dyes using through bond energy transfer in labeling biological molecules and in high throughput DNA sequencing. U.S. Patent 6340750, Jan. 22, **2002**.

(25) Jiao, G.-S.; Kim, T. G.; Topp, M. R.; Burgess, K. *Org. Lett.* **2004**, *6*, 1701-1704.

(26) Loudet, A.; Jiao, G. S.; Burgess, K. *Abstracts of Papers, 228th ACS National Meeting*, Philadelphia, PA, Aug. 22-26, **2004**.

(27) Burgess, K. Fluorescent through-bond energy transfer cassettes based on xanthine and pyronin derivatives. U.S. Patent 7402677, July 22, **2008**.

(28) Kim, T. G.; Castro, J. C.; Loudet, A.; Jiao, J. G. S.; Hochstrasser, R. M.; Burgess, K.; Topp, M. R. *J. Phys. Chem. A* **2006**, *110*, 20-27.

(29) Jiao, G.-S.; Thoresen, L. H.; Burgess, K. *J. Am. Chem. Soc.* **2003**, *125*, 14668-14669.

(30) Bandichhor, R.; Petrescu, A. D.; Vespa, A.; Kier, A. B.; Schroeder, F.; Burgess, K. *J. Am. Chem. Soc.* **2006**, *128*, 10688-10689.

(31) Jose, J.; Burgess, K. *J. Org. Chem.* **2006**, *71*, 7835-7839.

(32) Jose, J.; Burgess, K. *Tetrahedron* **2006**, *62*, 11021-11037.

(33) Romieu, A.; Brossard, D.; Hamon, M.; Outaabout, H.; Portal, C.; Renard, P.-Y. *Bioconjugate Chem.* **2008**, *19*, 279-289.

(34) Chen, X.-L.; Zou, J.-L.; Zhao, T.-T.; Li, Z.-B. *J. Fluoresc.* **2007**, *17*, 235-241.

(35) He, X.; Chen, J.; Wang, K.; Qin, D.; Tan, W. *Talanta* **2007**, *72*, 1519-1526.

(36) Brus, L. *Curr. Opin. Colloid Interface Sci.* **1996**, *1*, 197-201.

(37) Shiohara, A.; Hoshino, A.; Hanaki, K.-i.; Suzuki, K.; Yamamoto, K. *Microbiol. Immunol.* **2004**, *48*, 669-675.

(38) Gagne, F.; Maysinger, D.; Andre, C.; Blaise, C. *Nanotoxicology* **2008**, *2*, 113-120.

(39) Tarantola, M.; Schneider, D.; Sunnick, E.; Adam, H.; Pierrat, S.; Rosman, C.; Breus, V.; Soennichsen, C.; Basche, T.; Wegener, J.; Janshoff, A. *ACS Nano* **2009**, *3*, 213-222.

(40) Li, L.; Daou, T. J.; Texier, I.; Kim Chi, T. T.; Liem, N. Q.; Reiss, P. *Chem. Mater.* **2009**, *21*, 2422-2429.

(41) Ow, H.; Larson, D. R.; Srivastava, M.; Baird, B. A.; Webb, W. W.; Wiesner, U. *Nano Lett.* **2005**, *5*, 113-117.

(42) Wiesner, U.; Ow, H. Fluorescent silica-based nanoparticles. WO Patent 2004063387, Sept. 22, **2005**.

(43) Pham, K. N.; Fullston, D.; Sagoe-Crentsil, K. *J. Colloid Interface Sci.* **2007**, *315*, 123-127.

(44) Choi, J.; Burns, A. A.; Williams, R. M.; Zhou, Z.; Flesken-Nikitin, A.; Zipfel, W. R.; Wiesner, U.; Nikitin, A. Y. *J. Biomed. Opt.* **2007**, *12*, 64001-64011.

(45) Lin, W.; Huang, Y.-w.; Zhou, X.-D.; Ma, Y. *Toxicol. Appl. Pharmacol.* **2006**, *217*, 252-259.

(46) Altinoglu, E. I.; Russin, T. J.; Kaiser, J. M.; Barth, B. M.; Eklund, P. C.; Kester, M.; Adair, J. H. *ACS Nano* **2008**, *2*, 2075-2084.

(47) Mukesh, U.; Kulkarni, V.; Tushar, R.; Murthy, R. S. R. *J. Biomed. Nanotechnol.* **2009**, *5*, 99-105.

(48) Boyarskiy, V. P.; Belov, V. N.; Medda, R.; Hein, B.; Bossi, M.; Hell, S. W. *Chem.--Eur. J.* **2008**, *14*, 1784-1792.

(49) Kuznetsova, V. E.; Luk'yanova, T. A.; Vasiliskov, V. A.; Kharitonova, O. V.; Chudinov, A. V.; Zasedatelev, A. S. *Russ. Chem. Bull.* **2007**, *56*, 2438-2442.

(50) Matschke, M.; Beckert, R.; Kubicova, L.; Biskup, C. *Synthesis* **2008**, 2957-2962.

(51) Bandichhor, R.; Petrescu Anca, D.; Vespa, A.; Kier Ann, B.; Schroeder, F.; Burgess, K. *Bioconjugate Chem.* **2006**, *17*, 1219-1225.

(52) Reddington, M. V. *Bioconjugate Chem.* **2007**, *18*, 2178-2190.

(53) Niu, S. L.; Ulrich, G.; Ziessel, R.; Kiss, A.; Renard, P.-Y.; Romieu, A. *Org. Lett.* **2009**, *11*, 2049-2052.

(54) Wong, K.-T.; Chien, Y.-Y.; Chen, R.-T.; Wang, C.-F.; Lin, Y.-T.; Chiang, H.-H.; Hsieh, P.-Y.; Wu, C.-C.; Chou, C. H.; Su, Y. O.; Lee, G.-H.; Peng, S.-M. *J. Am. Chem. Soc.* **2002**, *124*, 11576-11577.

(55) Fowler, S. D.; Greenspan, P. *J. Histochem. Cytochem.* **1985**, *33*, 833-836.

(56) Greenspan, P.; Mayer, E. P.; Fowler, S. D. *J. Cell Biol.* **1985**, *100*, 965-973.

(57) Briggs, M. S. J.; Bruce, I.; Miller, J. N.; Moody, C. J.; Simmonds, A. C.; Swann, E. *J. Chem. Soc., Perkin Trans. 1* **1997**, 1051-1058.

(58) Simmonds, A.; Miller, J. N.; Moody, C. J.; Swann, E.; Briggs, M. S. J.; Bruce, I. E. Benzophenoxazine dyes for labeling of biomolecules. US Patent 6166202, Dec. 26, **2000**.

(59) Wang, J. C. *Adv. Color Sci. Technol.* **2000**, *3*, 20-31.

(60) Valdes-Aguilera, O.; Neckers, D. C. *Acc. Chem. Res.* **1989**, *22*, 171-177.

(61) Ho, N.-h.; Weissleder, R.; Tung, C.-H. *Tetrahedron* **2006**, *62*, 578-585.

(62) Li, L.; Han, J.; Nguyen, B.; Burgess, K. *J. Org. Chem.* **2008**, *73*, 1963-1970.

(63) Tung, C.-H.; Bredow, S.; Mahmood, U.; Weissleder, R. *Bioconjugate Chem.* **1999**, *10*, 892-896.

(64) Jose, J.; Ueno, Y.; Burgess, K. *Chem.--Eur. J.* **2009**, *15*, 418-423.

(65) Black, S. L.; Stanley, W. A.; Filipp, F. V.; Bhairo, M.; Verma, A.; Wichmann, O.; Sattler, M.; Wilmanns, M.; Schultz, C. *Bioorg. Med. Chem.* **2008**, *16*, 1162-1173.

(66) Kina, K.; Horiguchi, D. Water-soluble nitrosophenols. JP Patent 57-091969, Oct. 6, **1980**.

(67) Suzuki, H.; Delano, F. A.; Jamshidi, N.; Katz, D.; Mori, M.; Kosaki, K.; Gottlieb, R. A.; Ishii, H.; Schmid-Schonbein, G. W. *Am. J. Physiol.* **1999**, *276*, H2135-H2140.

(68) Kikkeri, R.; Traboulsi, H.; Humbert, N.; Gumienna-Kontecka, E.; Arad-Yellin, R.; Melman, G.; Elhabiri, M.; Albrecht-Gary, A.-M.; Shanzer, A. *Inorg. Chem.* **2007**, *46*, 2485-2497.

(69) Lu, G.; Lam, S.; Burgess, K. *Chem. Commun.* **2006**, 1652-1654.

(70) Golini, C. M.; Williams, B. W.; Foresman, J. B. *J. Fluoresc.* **1998**, *8*, 395-404.

(71) Qian, J.; Li, X.; Wei, M.; Gao, X.; Xu, Z.; He, S. *Opt. Express* **2008**, *16*, 19568-19578.

(72) Mohlau, R.; Uhlmann, K. *Justus Liebigs Ann. Chem.* **1896**, *289*, 94-128.

(73) Lee, S. H.; Suh, J. K.; Li, M. *Bull. Korean Chem. Soc.* **2003**, *24*, 45-48.

(74) Das, K.; Jain, B.; Patel, H. S. *Spectrochim. Acta, Part A* **2004**, *60A*, 2059-2064.

(75) Krihak, M.; Murtagh, M. T.; Shahriari, M. R. *J. Sol-Gel Sci. Technol.* **1997**, *10*, 153-163.

(76) Maliwal, B. P.; Kusba, J.; Lakowicz, J. R. *Biopolymers* **1995**, *35*, 245-255.

(77) Lakowicz, J. R.; Piszczek, G.; Kang, J. S. *Anal. Biochem.* **2001**, *288*, 62-75.

(78) Nikas, D. C.; Foley, J. W.; Black, P. M. *Lasers Surg. Med.* **2001**, *29*, 11-17.

(79) Lin, C. W.; Shulok, J. R.; Wong, Y. K.; Schanbacher, C. F.; Cincotta, L.; Foley, J. W. *Cancer Res.* **1991**, *51*, 1109-1116.

(80) Lin, C.-W.; Shulok, J. R. *Photochem. Photobiol.* **1994**, *60*, 143-146.

(81) Juzeniene, A.; Peng, Q.; Moan, J. *Photochem. Photobiol. Sci.* **2007**, *6*, 1234-1245.

(82) Ho, N.-h.; Weissleder, R.; Tung, C.-H. *Tetrahedron* **2006**, *62*, 578-585.

(83) Frade, V. H. J.; Coutinho, P. J. G.; Moura, J. C. V. P.; Goncalves, M. S. T. *Tetrahedron* **2007**, *63*, 1654-1663.

(84) Lopez-Calle, E.; Fries, J. R.; Mueller, A.; Winkler, D. *Innovation Perspect. Solid Phase Synth. Comb. Libr : Collect. Pap., Int. Symp. 7th* **2002**, 129-136.

(85) Yan, X.; Yuan, P. M. Sulfonated [8,9]benzophenoxazine dyes and the use of their labelled conjugates. WO Patent 2001083621, May 01, **2001**.

(86) Jose, J.; Burgess, K. *J. Org. Chem.* **2006**, *71*, 7835-7839.

(87) Yoshida, Y.; Sakakura, Y.; Aso, N.; Okada, S.; Tanabe, Y. *Tetrahedron* **1999**, *55*, 2183-2192.

(88) Hansen, T. M.; Engler, M. M.; Forsyth, C. J. *Bioorg. Med. Chem. Lett.* **2003**, *13*, 2127-2130.

(89) Burns, C. J.; Field, L. D.; Petteys, B. J.; Ridley, D. D. *Aust. J. Chem.* **2005**, *58*, 738-748.

(90) Mishra, V. N.; Datt, N. *Ind. J. Chem., Sect. A: Inorg., Phys., Theor. Anal. Chem.* **1985**, *24A*, 597-600.

(91) Mathur, A. K.; Agarwal, C.; Pangtey, B. S.; Singh, A.; Gupta, B. N. *Int. J. Cos. Sci.* **1988**, *10*, 213-218.

(92) Sun, C.; Yang, J.; Li, L.; Wu, X.; Liu, Y.; Liu, S. *J. Chromatogr., B* **2004**, *803*, 173-190.

(93) Frangioni, J. V. *Curr. Opin. Chem. Biol.* **2003**, *7*, 626-634.

(94) Malinauskas, A.; Ruzgas, T.; Gorton, L.; Kubota, L. T. *Electroanalysis* **2000**, *12*, 194-198.

(95) Freeman, R.; Gill, R.; Shweky, I.; Kotler, M.; Banin, U.; Willner, I. *Angew. Chem., Int. Ed.* **2009**, *48*, 309-313.

(96) Abbasi, S.; Farmany, A.; Gholivand, M. B.; Naghipour, A.; Abbasi, F.; Khani, H. *Food Chem.* **2009**, *116*, 1019-1023.

(97) Lee, M. H.; Lee, S. W.; Kim, S. H.; Kang, C.; Kim, J. S. *Org. Lett.* **2009**, *11*, 2101-2104.

(98) Liu, W.; Brock, A.; Chen, S.; Chen, S.; Schultz, P. G. *Nat. Methods* **2007**, *4*, 239-244.

(99) Zhang, Z.; Smith, B. A. C.; Wang, L.; Brock, A.; Cho, C.; Schultz, P. G. *Biochemistry* **2003**, *42*, 6735-6746.

(100) Ohana Rachel, F.; Encell Lance, P.; Zhao, K.; Simpson, D.; Slater Michael, R.; Urh, M.; Wood Keith, V. *Protein Expr. Purif.* **2009**, *68*, 110-120.

(101) De Simone, A.; Corrie, J. E. T.; Dale, R. E.; Irving, M.; Fraternali, F. *J. Am. Chem. Soc.* **2008**, *130*, 17120-17128.

(102) Antos, J. M.; McFarland, J. M.; Iavarone, A. T.; Francis, M. B. *J. Am. Chem. Soc.* **2009**, *131*, 6301-6308.

(103) Scheck, R. A.; Dedeo, M. T.; Iavarone, A. T.; Francis, M. B. *J. Am. Chem. Soc.* **2008**, *130*, 11762-11770.

(104) Damoiseaux, R.; Keppler, A.; Johnsson, K. *Chembiochem* **2001**, *2*, 285-287.

(105) Juillerat, A.; Gronemeyer, T.; Keppler, A.; Gendreizig, S.; Pick, H.; Vogel, H.; Johnsson, K. *Chem. Biol.* **2003**, *10*, 313-317.

(106) Keppler, A.; Pick, H.; Arrivoli, C.; Vogel, H.; Johnsson, K. *Proc. Nat. Acad. Sci. U.S.A.* **2004**, *101*, 9955-9959.

(107) Gendreizig, S.; Keppler, A.; Juillerat, A.; Gronemeyer, T.; Johnsson, K. *Highlights Bioorg. Chem.* **2004**, 344-351.

(108) Keppler, A.; Gendreizig, S.; Gronemeyer, T.; Pick, H.; Vogel, H.; Johnsson, K. *Nat. Biotechnol.* **2003**, *21*, 86-89.

(109) Mottram, L. F.; Maddox, E.; Schwab, M.; Beaufils, F.; Peterson, B. R. *Org. Lett.* **2007**, *9*, 3741-3744.

(110) Suzuki, F.; Hashimoto, K.; Ishihara, M.; Westman, G.; Samuelsson, K.; Kawase, M.; Motohashi, N.; Sakagami, H. *Anticancer Res.* **2007**, *27*, 4233-4238.

(111) Jiao, G.-S.; Thoresen, L. H.; Kim, T. G.; Haaland, W. C.; Gao, F.; Topp, M. R.; Hochstrasser, R. M.; Metzker, M. L.; Burgess, K. *Chem.--Eur. J.* **2006**, *12*, 7816-7826.

(112) Wu, L.; Loudet, A.; Barhoumi, R.; Burghardt, R. C.; Burgess, K. *J. Am. Chem. Soc.* **2009**, *131*, 9156-9157.

(113) Okamoto, A.; Tainaka, K.; Fujiwara, Y. *J. Org. Chem.* **2006**, *71*, 3592-3598.

(114) Huisgen, R.; Knorr, R.; Moebius, L.; Szeimies, G. *Chem. Ber.* **1965**, *98*, 4014-4021.

(115) Kolb, H. C.; Finn, M. G.; Sharpless, K. B. *Angew. Chem., Int. Ed.* **2001**, *40*, 2004-2021.

(116) Chan, T. R.; Hilgraf, R.; Sharpless, K. B.; Fokin, V. V. *Org. Lett.* **2004**, *6*, 2853-2855.

(117) Haas Jr., J. W. *J. Chem. Ed.* **1967**, *44*, 396-402.

(118) Gundermann, K.-D. *Angew. Chem. Int. Ed.* **1965**, *4*, 565-572.

(119) White, E. H.; Roswell, D. F. *Acc. Chem. Res.* **1970**, *3*, 54-62.

(120) Diaz, A. N.; Garcia, J. A. G.; Lovillo, J. *J. Biolumin. Chemilumin.* **1997**, *12*, 199-205.

(121) Wei, C. C.; White, E. H. *Tetrahedron Lett.* **1971**, 3559-3562.

(122) Spruit-Van Der Burg, A. *Recl. Trav. Chim. Pays-Bas* **1950**, *69*, 1536-1544.

(123) White, E. H.; Bursey, M. M. *J. Org. Chem.* **1966**, *31*, 1912-1917.

(124) Stanely, P. E.; Kricka, L. J. *Bioluminescence and Chemiluminescence: Progress and Current Applications*, Cambridge, UK, , **2002**.

(125) Campbell, A. K. *Chemiluminescence. Principles and Applications in Biology and Medicine*; VCH: Weinheim, 1988.

(126) Sonogashira, K.; Tohda, Y.; Hagihara, N. *Tetrahedron Lett.* **1975**, *16*, 4467-4470.

(127) Jiao, G.-S.; Han, J. W.; Burgess, K. *J. Org. Chem.* **2003**, *68*, 8264-8267.

(128) Briggs, M. S. J.; Bruce, I.; Miller, J. N.; Moody, C. J.; Simmonds, A. C.; Swann, E. *J. Chem. Soc., Perkin Trans. 1* **1997**, *7*, 1051-1058.

(129) *Documenta Geigy, Scientific Tables*; 6 ed.; Diem, K., Ed.; Geigy Pharmaceuticals: Ardsley, NY, 1962.

(130) Kim, T. G.; Castro, J. C.; Loudet, A.; Jiao, J. G. S.; Hochstrasser, R. M.; Burgess, K.; Topp, M. R. *J. Phys. Chem. A* **2006**, *110*, 20-27.

(131) White, E. H.; Roswell, D. F. *J. Am. Chem. Soc.* **1967**, *89*, 3944-3945.

(132) Roberts, D. R.; White, E. H. *J. Am. Chem. Soc.* **1970**, *92*, 4861-4867.

(133) Roswell, D. F.; Paul, V.; White, E. H. *J. Am. Chem. Soc.* **1970**, *92*, 4855-4860.

(134) Wampler, J. E. In *Chemi- and Bioluminescence*; Burr, J. G., Ed.; Marcel Dekker: New York, 1985, p 1-44.

(135) Burns, A.; Sengupta, P.; Zedayko, T.; Baird, B.; Wiesner, U. *Small* **2006**, *2*, 723-726.

(136) Kim, S.; Ohulchanskyy, T. Y.; Baev, A.; Prasad, P. N. *J. Mater. Chem.* **2009**, *19*, 3181-3188.

(137) Legrand, S.; Catheline, A.; Kind, L.; Constable, E. C.; Housecroft, C. E.; Landmann, L.; Banse, P.; Pieles, U.; Wirth-Heller, A. *New J. Chem.* **2008**, *32*, 588-593.

(138) Burns, A.; Ow, H.; Wiesner, U. *Chem. Soc. Rev.* **2006**, *35*, 1028-1042.

(139) Jin, Y.; Kannan, S.; Wu, M.; Zhao, J. X. *Chem. Res. Toxicol.* **2007**, *20*, 1126-1133.

(140) He, X.; Duan, J.; Wang, K.; Tan, W.; Lin, X.; He, C. *J. Nanosci. Nanotechnol.* **2004**, *4*, 585-589.

(141) Stoeber, W.; Fink, A.; Bohn, E. *J. Colloid Interface Sci.* **1968**, *26*, 62-69.

(142) Van Blaaderen, A.; Vrij, A. *Langmuir* **1992**, *8*, 2921-2931.

(143) Van Blaaderen, A.; Van Geest, J.; Vrij, A. *J. Colloid Interface Sci.* **1992**, *154*, 481-501.

(144) Van Blaaderen, A.; Vrij, A. *J. Colloid Interface Sci.* **1993**, *156*, 1-18.

(145) Verhaegh, N. A. M.; Blaaderen, A. v. *Langmuir* **1994**, *10*, 1427-1438.

(146) Bringley, J. F.; Penner, T. L.; Wang, R.; Harder, J. F.; Harrison, W. J.; Buonemani, L. *J. Colloid Interface Sci.* **2008**, *320*, 132-139.

(147) Larson, D. R.; Ow, H.; Vishwasrao, H. D.; Heikal, A. A.; Wiesner, U.; Webb, W. W. *Chem. Mater.* **2008**, *20*, 2677-2684.

(148) Folling, J.; Polyakova, S.; Belov, V.; van Blaaderen, A.; Bossi Mariano, L.; Hell Stefan, W. *Small* **2008**, *4*, 134-142.

(149) Mader, H.; Li, X.; Saleh, S.; Link, M.; Kele, P.; Wolfbeis, O. S. *Ann. New York Acad. Sci.* **2008**, *1130*, 218-223.

(150) Jana, N. R.; Earhart, C.; Ying, J. Y. *Chem. Mater.* **2007**, *19*, 5074-5082.

(151) Shylesh, S.; Sharma, S.; Mirajkar, S. P.; Singh, A. P. *J. Mol. Catal. A: Chem.* **2004**, *212*, 219-228.

(152) Liu, S.; Zhang, H.-L.; Liu, T.-C.; Liu, B.; Cao, Y.-C.; Huang, Z.-L.; Zhao, Y.-D.; Luo, Q.-M. *J. Biomed. Res., A* **2007**, *80A*, 752-757.

(153) Yoon, T.-J.; Yu, K. N.; Kim, E.; Kim, J. S.; Kim, B. G.; Yun, S.-H.; Sohn, B.-H.; Cho, M.-H.; Lee, J.-K.; Park, S. B. *Small* **2006**, *2*, 209-215.

(154) Santra, S.; Liesenfeld, B.; Dutta, D.; Chatel, D.; Batich, C. D.; Tan, W.; Moudgil, B. M.; Mericle, R. A. *J. Nanosci. Nanotechnol.* **2005**, *5*, 899-904.

(155) Lison, D.; Thomassen, L. C. J.; Rabolli, V.; Gonzalez, L.; Napierska, D.; Seo, J. W.; Kirsch-Volders, M.; Hoet, P.; Kirschhock, C. E. A.; Martens, J. A. *Toxicol. Sci.* **2008**, *104*, 155-162.

(156) Ohulchanskyy, T. Y.; Roy, I.; Goswami, L. N.; Chen, Y.; Bergey, E. J.; Pandey, R. K.; Oseroff, A. R.; Prasad, P. N. *Nano Lett.* **2007**, *7*, 2835-2842.

(157) Prasad, P. N.; Kim, S.; Ohulchanskyy, T. Y.; Pandey, R. K. Nanoparticles for two-photon activated photodynamic therapy and imaging. U.S. Patent 20090035576 Feb. 05, **2009**.

(158) Kumar, R.; Roy, I.; Ohulchanskyy, T. Y.; Goswami, L. N.; Bonoiu, A. C.; Bergey, E. J.; Tramposch, K. M.; Maitra, A.; Prasad, P. N. *ACS Nano* **2008**, *2*, 449-456.

(159) Kim, S. H.; Jeyakumar, M.; Katzenellenbogen, J. A. *J. Am. Chem. Soc.* **2007**, *129*, 13254-13264.

(160) Mujumdar, R. B.; Ernst, L. A.; Mujumdar, S. R.; Lewis, C. J.; Waggoner, A. S. *Bioconjugate Chem.* **1993**, *4*, 105-111.

(161) Southwick, P. L.; Ernst, L. A.; Tauriello, E. W.; Parker, S. R.; Mujumdar, R. B.; Mujumdar, S. R.; Clever, H. A.; Waggoner, A. S. *Cytometry* **1990**, *11*, 418-430.

(162) Liu, S.; Zhang, H.-L.; Liu, T.-C.; Liu, B.; Cao, Y.-C.; Huang, Z.-L.; Zhao, Y.-D.; Luo, Q.-M. *J. Biomed. Mater. Res., Part A* **2007**, *80A*, 752-757.

(163) Bagwe, R. P.; Hilliard, L. R.; Tan, W. *Langmuir* **2006**, *22*, 4357-4362.

(164) Guerin, A.; Pannier, B.; London, G. *Adv. Cardiol.* **2007**, *44*, 187-198.

(165) Axen, N.; Ahnfelt, N. O.; Persson, T.; Hermansson, L.; Sanchez, J.; Larsson, R. *Ceram. Eng. Sci. Proc.* **2005**, *26*, 71-77.

(166) Reynolds, E. C.; Riley, P. F.; Adamson, N. J. *Anal. Biochem.* **1994**, *217*, 277-284.

(167) Fay, F. S. *Science* **1995**, *270*, 588-589.

(168) Fournier, A.; Mansour, J.; Harbouche, L.; el Esper, I.; Brazier, M. *Recent Res. Dev. Endocrinol. Metab.* **2003**, *1*, 169-183.

(169) Truong-Le, V. L.; Walsh, S. M.; Schweibert, E.; Mao, H. Q.; Guggino, W. B.; August, J. T.; Leong, K. W. *Arch Biochem. Biophys.* **1999**, *361*, 47-56.

(170) Morgan Thomas, T.; Muddana Hari, S.; Altinoglu Erhan, I.; Rouse Sarah, M.; Tabakovic, A.; Tabouillot, T.; Russin Timothy, J.; Shanmugavelandy Sriram, S.; Butler Peter, J.; Eklund Peter, C.; Yun Jong, K.; Kester, M.; Adair James, H. *Nano Lett.* **2008**, *8*, 4108-4115.

(171) Muddana, H. S.; Morgan, T. T.; Adair, J. H.; Butler, P. J. *Nano Lett.* **2009**, *9*, 1559-1566.

(172) Ramachandran, R.; Paul, W.; Sharma, C. P. *J. Biomed. Mater. Res., Part B* **2008**, *88B*, 41-48.

(173) Kester, M.; Heakal, Y.; Fox, T.; Sharma, A.; Robertson, G. P.; Morgan, T. T.; Altinoglu, E. I.; Tabakovic, A.; Parette, M. R.; Rouse, S.; Ruiz-Velasco, V.; Adair, J. H. *Nano Lett.* **2008**, *8*, 4116-4121.

(174) Fuller, J. E.; Zugates, G. T.; Ferreira, L. S.; Ow, H. S.; Nguyen, N. N.; Wiesner, U. B.; Langer, R. S. *Biomat.* **2008**, *29*, 1526-1532.

(175) Zhao, X.; Hilliard, L. R.; Wang, K.; Tan, W. *Encyclopedia Nanosci. Nanotechnol.* **2004**, *1*, 255-268.

(176) Lopez-Calle, E.; Winkler, D.; Muller, A.; Fries, J. R.; Klumpp, M.; Wrobel, M. *Chimica Oggi* **2001**, *19*, 18-20.

(177) Fries, J.; Lopez-Calle, E. Phenoxazinium fluorescent dyes, their production and their use. U.S. Patent 20060240455, Oct. 26, **2006**.

(178) Mottram, L. F.; Boonyarattanakalin, S.; Kovel, R. E.; Peterson, B. R. *Org. Lett.* **2006**, *8*, 581-584.

(179) Molecular Probes; http://probes.invitrogen.com. Invitrogen Corporation, Eugene, OR. Accessed in May, **2006**.

(180) Zhang, L.; Sun, H.; Li, D.; Song, S.; Fan, C.; Wang, S. *Macromol. Rapid Commun.* **2008**, *29*, 1489-1494.

(181) Huo, L.; Hou, J.; Chen, H.-Y.; Zhang, S.; Jiang, Y.; Chen, T. L.; Yang, Y. *Macromolecules* **2009**, *42*, 6564-6571.

(182) Grunnet-Jepsen, A.; Thompson, C. L.; Moerner, W. E. *Science* **1997**, *277*, 549-552.

(183) Xue, C.; Jog, S. P.; Murthy, P.; Liu, H. *Biomacromolecules* **2006**, *7*, 2470-2474.

(184) Szymanski, C.; Wu, C.; Hooper, J.; Salazar Mary, A.; Perdomo, A.; Dukes, A.; McNeill, J. *J. Phys. Chem. B* **2005**, *109*, 8543-8546.

(185) Wu, C.; Szymanski, C.; McNeill, J. *Langmuir* **2006**, *22*, 2956-2960.

(186) Wu, C.; Zheng, Y.; Szymanski, C.; McNeill, J. *J. Phys. Chem. C* **2008**, *112*, 1772-1781.

(187) Wu, C.; Bull, B.; Szymanski, C.; Christensen, K.; McNeill, J. *ACS Nano* **2008**, *2*, 2415-2423.

(188) Hughes, A. D.; Glenn, I. C.; Patrick, A. D.; Ellington, A.; Anslyn, E. V. *Chem.--Eur. J.* **2008**, *14*, 1822-1827.

(189) Bart, J. C.; Judd, L. L.; Kusterbeck, A. W. *Sens. Actuators, B* **1997**, *B39*, 411-418.

(190) Meaney, M. S.; McGuffin, V. L. *Anal. Bioanal. Chem.* **2008**, *391*, 2557-2576.

(191) Meaney, M. S.; McGuffin, V. L. *Anal. Chim. Acta* **2008**, *610*, 57-67.

(192) Zhou, Q.; Swager, T. M. *J. Am. Chem. Soc.* **1995**, *117*, 12593-12602.

(193) Swager, T. M. *Acc. Chem. Res.* **1998**, *31*, 201-207.

(194) Yang, J.-S.; Swager, T. M. *J. Am. Chem. Soc.* **1998**, *120*, 11864-11873.

(195) Yang, J.-S.; Swager, T. M. *J. Am. Chem. Soc.* **1998**, *120*, 5321-5322.

(196) Mizobe, Y.; Tohnai, N.; Miyata, M.; Hasegawa, Y. *Chem. Commun.* **2005**, 1839-1841.

(197) Ooyama, Y.; Hayashi, A.; Okamoto, T.; Egawa, H.; Mamura, T.; Yoshida, K. *Eur. J. Org. Chem.* **2008**, 3085-3094.

(198) Ozdemir, T.; Atilgan, S.; Kutuk, I.; Yildirim, L. T.; Tulek, A.; Bayindir, M.; Akkaya, E. U. *Org. Lett.* **2009**, *11*, 2105-2107.

(199) Zhang, D.; Wen, Y.; Xiao, Y.; Yu, G.; Liu, Y.; Qian, X. *Chem. Commun.* **2008**, 4777-4779.

(200) Park, S.-Y.; Kubota, Y.; Funabiki, K.; Shiro, M.; Matsui, M. *Tetrahedron Lett.* **2009**, *50*, 1131-1135.

(201) Nuyken, O.; Bacher, E.; Braig, T.; Faber, R.; Mielke, F.; Rojahn, M.; Wiederhirn, V.; Meerholz, K.; Muller, D. *Des. Monomers Polym.* **2002**, *5*, 195-210.

(202) http://probes.invitrogen.com In *Molecular Probes*; Invitrogen Corporation, Eugene, OR. Accessed in May, **2006**.

(203) Williams, A. T. R.; Winfield, S. A.; Miller, J. N. *Analyst* **1983**, *108*, 1067-1071.

(204) Klotz, E. J. F.; Claridge, T. D. W.; Anderson, H. L. *J. Am. Chem. Soc.* **2006**, *128*, 15374-15375.

(205) Kvach, M. V.; Ustinov, A. V.; Stepanova, I. A.; Malakhov, A. D.; Skorobogatyi, M. V.; Shmanai, V. V.; Korshun, V. A. *Eur. J. Org. Chem.* **2008**, 2107-2117.

(206) Chang, H.-T.; Jeganmohan, M.; Cheng, C.-H. *Org. Lett.* **2007**, *9*, 505-508.

(207) Sonogashira, K.; Tohda, Y.; Hagihara, N. *Tetrahedron Lett.* **1975**, 4467-4470.

APPENDIX A

EXPERIMENTAL DATA FOR CHAPTER II

General Experimental Methods

All reactions were carried out under an atmosphere of dry nitrogen. Glassware were oven-dried prior to use. Unless otherwise indicated, common reagents or materials were obtained from commercial source and used without further purification. All solvents were dried prior to use with appropriate drying agents. Dry distilled DMF was obtained from Acros and used as such. Flash column chromatography was performed using silica gel 60 (230-400 mesh). Analytical thin layer chromatography (TLC) was carried out on Merck silica gel plates with QF-254 indicator and visualized by UV. Fluorescence spectra were obtained on a Varian Cary Eclipse fluorescence spectrophotometer at room temperature. Absorbance spectra were obtained on a Varian 100 Bio UV-Vis spectrophotometer at room temperature. IR spectra were recorded on a Bruker Tensor 27 spectrometer. Preparative HPLC data were obtained on a Beckmann Coulter preparative HPLC instrument with a C18 reverse phase column. Solvent system used (20-95% CH_3CN/1%TFA in H_2O. Analytical HPLC data were obtained on a Beckmann Coulter Analytical HPLC instrument with a C18 reverse phase column. Solvent system used 10-90% CH_3CN/0.1% TFA in H_2O.

^1H and ^{13}C spectra were recorded on a Varian 300 (300 MHz ^1H; 75 MHz ^{13}C) or Varian 500 (500 MHz ^1H; 125 MHz ^{13}C) spectrometer at room temperature. Chemical shifts were reported in ppm relative to the residual $CDCl_3$ (δ 7.26 ppm ^1H; δ 77.16 ppm ^{13}C), CD_3OD (δ 3.31 ppm ^1H; δ 49.0 ppm ^{13}C), DMSO-*d*$_6$ (δ 2.54 ppm ^1H; δ 39.52 ppm ^{13}C) or acetone-*d*$_6$ (δ 2.05 ppm ^1H; δ 29.84 and 206.26 ppm ^{13}C). Trichloro-fluoro-methane ($CFCl_3$, δ 0.00 ppm ^{19}F) was used a standard for fluorine NMR. Coupling constants (*J*) were reported in Hertz.

Photophysical Properties and Determination of Quantum Yields

Steady-state fluorescence spectroscopic studies were performed on a Cary Eclipse fluorometer. The slit width was 5 nm for both excitation and emission. The relative quantum yields of the samples were obtained by comparing the area under the corrected emission spectrum of the test sample with that of a solution of Nile Blue in ethanol, which has a quantum yield of 0.27 according to literature reports.[202] The quantum efficiencies of fluorescence were obtained from three measurements with the following equation:

$$\Phi_x = \Phi_{st} (I_x/I_{st}) (A_{st}/A_x) (\eta_x^2/\eta_{st}^2)$$

Where Φ_{st} is the reported quantum yield of the standard, **I** is the area under the emission spectra, **A** is the absorbance at the excitation wavelength and η is the refractive index of the solvent used, measured on a pocket refractometer from ATAGO. **X** subscript denotes unknown, and **st** denotes standard.[203] A dye concentration of 10^{-6} M was used for the measurement of quantum yield.

Molar extinction coefficients were obtained from the slope of a graph of absorbance *vs* concentration for each dye with five different concentrations (10^{-6} M). 0.25, 0.5, 1.0, 1.5, and 3.0 x 10^{-6} M were the concentration used.

Experimental Section

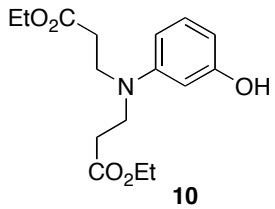

10

A solution of dicarboxylic acid **9** (2.0 g, 7.9 mmol) in ethanol (100 mL) along with HCl (10 M, 0.2 mL) was refluxed for 12 h. The reaction mixture was cooled and ethanol evaporated under reduced pressure. The residue obtained was dissolved in dichloromethane (20 mL) and organic layer washed with water (5 mL x 5). The organic layer was dried under Na_2SO_4 and solvent evaporated to obtain a residue which was purified by passing through a short flash chromatography normal phase silica column eluting with 1/1 EtOAc/hexanes to yield **10** as an yellow oil (1.64 g, 67 %). R_f = 0.8 (1/1 EtOAc/hexanes). **^{1}H NMR** (500 MHz, $CDCl_3$) δ 7.05 (t, 1H, *J* = 5.0 Hz), 6.99 (s, 1H), 6.24 (br, 2H), 4.13 (q, 4H, *J* = 7.1 Hz), 3.61 (t, 4H, *J* = 7.0 Hz), 2.58 (t, 4H, *J* = 7.0 Hz), 1.24 (t, 6H, *J* = 7.1 Hz); **^{13}C NMR** (125 MHz, $CDCl_3$) δ 172.9, 157.7, 148.4, 130.6, 105.0, 104.6, 99.9, 61.1, 47.1, 32.8, 14.4. **MS (ESI)** m/z $(M+H)^+$ 310.32; **IR (neat)** 3387, 2962, 1732 cm $^{-1}$.

^{1}H NMR ($CDCl_3$)

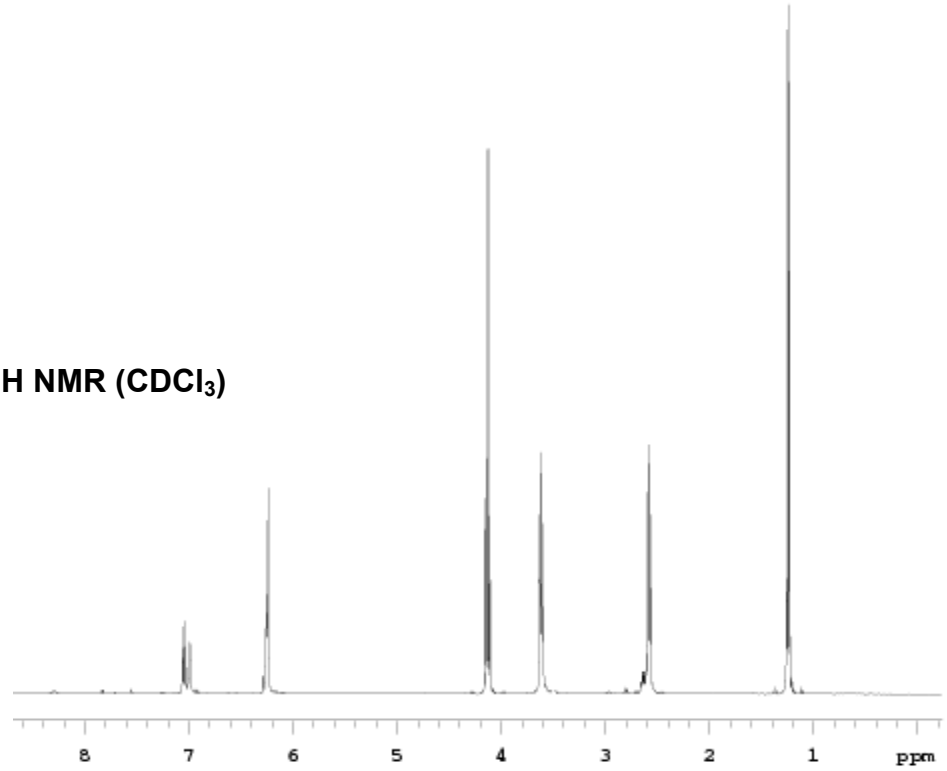

^{13}C NMR ($CDCl_3$)

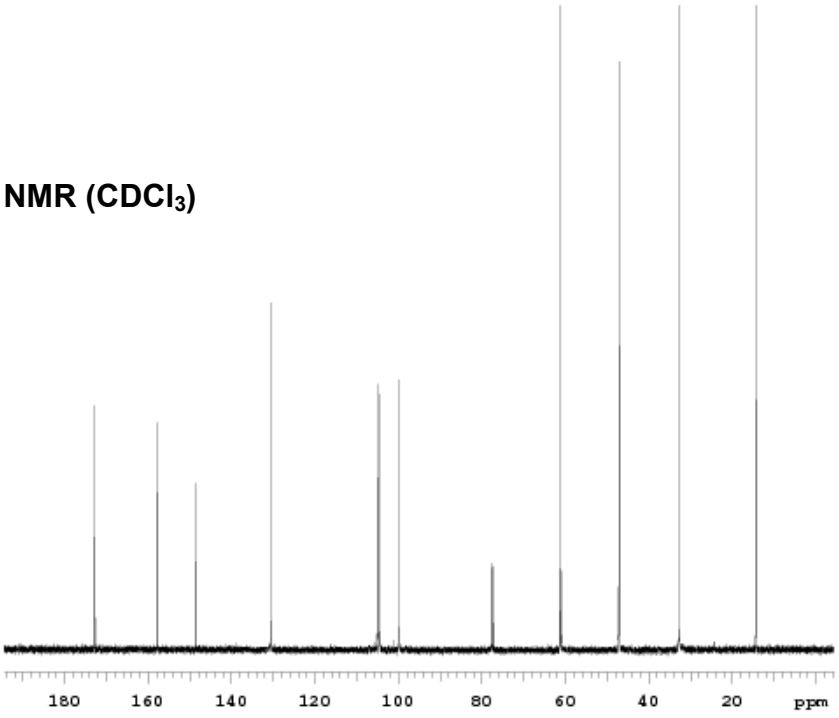

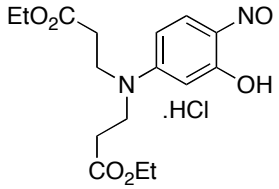

11

Sodium nitrite (0.24 g, 3.5 mmol) in water (3 mL) was added, over a period of 15 min, via a syringe pump at the rate of 0.2 mL/min, to a solution of **10** (1.0 g, 3.2 mmol) in HCl (3 mL, 10 M) and water (1.5 mL) at 0 ºC. The mixture was stirred for 3 h at 0 ºC and filtered to remove residual impurities. The filtrate was evaporated under reduced pressure to yield **11** as a yellow solid (0.92g, 77 %). The crude product was very moisture sensitive and therefore directly used without further purification for the next step.

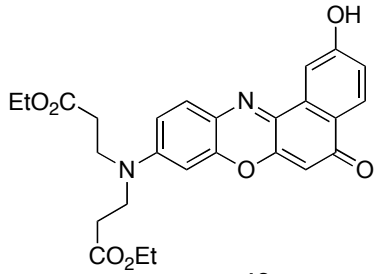

12

1,6-Dihydroxynaphthol (0.34 g, 2.1 mmol) with HCl (0.1 mL, 10 M) was added to a solution of **11** (0.8 g, 2.1 mmol) in EtOH (30 mL) all in one portion. The reaction mixture was refluxed for 5 h. The solvent was evaporated and residue purified by flash chromatography eluting with 1/1 EtOAc/hexanes and 10 % MeOH/EtOAc to afford **12** as a red solid (372 mg, 37 %). R_f = 0.8 (10 % MeOH/EtOAc). **^{1}H NMR** (300 MHz, acetone-d_6) δ 8.07 (d, 1H, J = 8.5 Hz), 8.0 (s, 1H), 7.62 (d, 1H, J = 8.5 Hz), 7.19 (dd, 1H, d, J = 9.1, 2.6 Hz), 6.89 (dd, 1H, d, J = 9.1, 2.6 Hz), 6.72 (s, 1H), 6.14 (s, 1H), 4.13 (q, 4H, J = 7.0 Hz), 3.89 (t, 4H, J = 7.0 Hz), 2.74 (t, 4H, J = 7.0 Hz), 1.22 (t, 6H, J = 7.0 Hz); **^{13}C NMR** (125 MHz, CD_3OD) δ 183.8, 172.1, 161.2, 153.5, 152.8, 146.8, 139.9, 134.3, 131.5, 127.6, 125.8, 125.5, 110.8, 106.9, 104.3, 97.1, 95.0, 60.8, 32.2, 29.6, 13.3. **MS (ESI)** m/z $(M)^+$ 478.33. **IR (neat)** 3427, 2944, 1736 cm^{-1}.

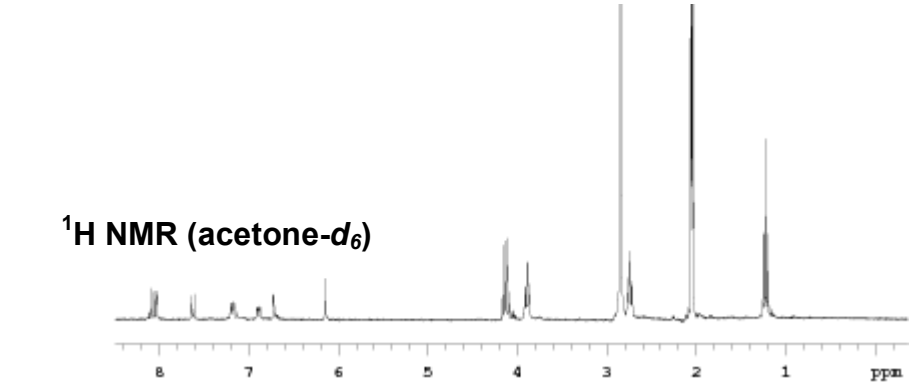

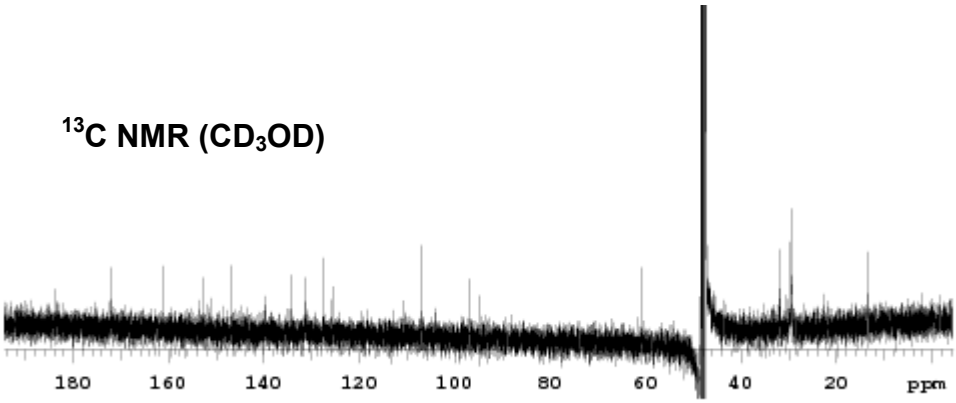

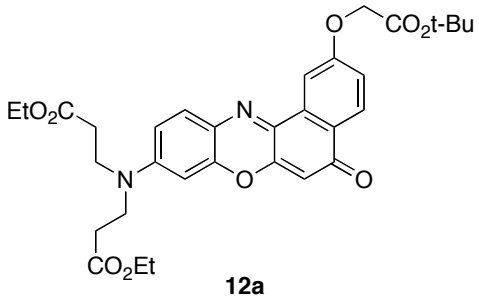

12a

Compound **12** (0.42 g, 0.9 mmol) and Cs_2CO_3 (1.43 g, 4.4 mmol) was dissolved in CH_3CN (5 mL). Tertiary butyl bromoacetate (0.86 g, 4.4 mmol) was added after 5 min. and the reaction mixture heated to 60 ^oC for 6 h. The solvent was evaporated under reduced pressure and the residue purified by flash chromatography eluting with 1/1 EtOAc/hexanes to afford **12a** as a red solid (360 mg, 69 %). R_f = 0.6 (1/1 EtOAc/hexanes). **^{1}H NMR** (500 MHz, $CDCl_3$) δ 8.12 (d, 1H, J = 9.3 Hz), 7.94 (s, 1H),

7.53 (d, 1H, *J* = 9.3 Hz), 7.17 (dd, 1H, *J* = 8.7, 4.2 Hz), 6.60 (dd, 1H, *J* = 8.7, 4.2 Hz), 6.43 (s, 1H), 6.22 (s, 1H), 4.86 (s, 2H), 4.11 (q, 4H, *J* = 4.8 Hz), 3.72 (br, 4H), 2.64 (br, 4H), 1.41 (s, 9H), 1.18 (t, 6H, *J* = 4.8 Hz); **^{13}C NMR** (125 MHz, $CDCl_3$) δ 183.0, 172.1, 168.9, 161.3, 152. 2, 150.0, 146.8, 141.9, 133.8, 131.4, 128.8, 127.0, 125.7, 118.9, 110.3, 107.1, 106.4, 97.9, 83.3, 66.2, 61.4, 47.3, 33.1, 28.2, 14.3. **MS (ESI)** m/z $(M)^+$ 592.21. **IR (neat)** 3423, 2941, 1747 cm^{-1}.

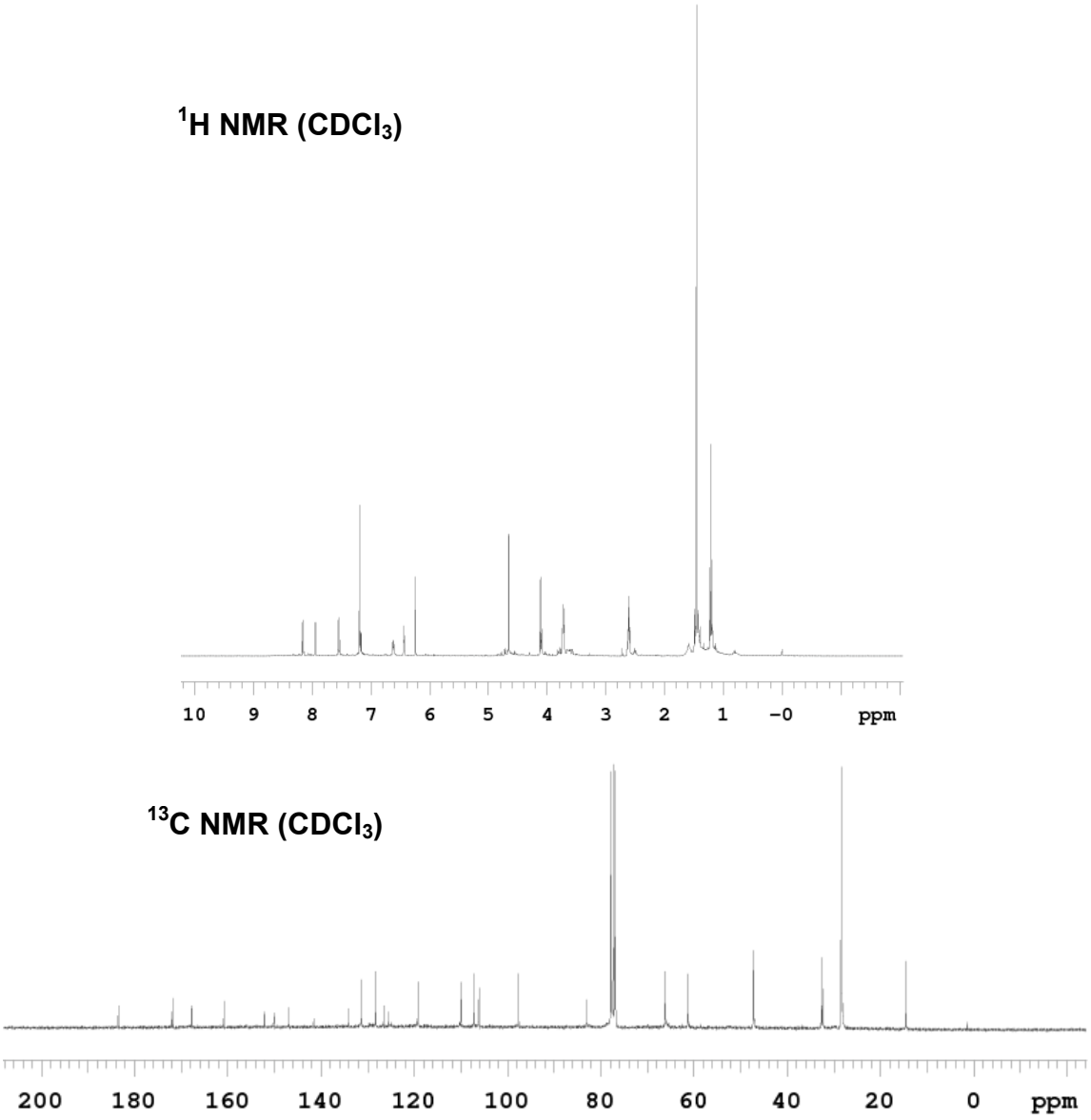

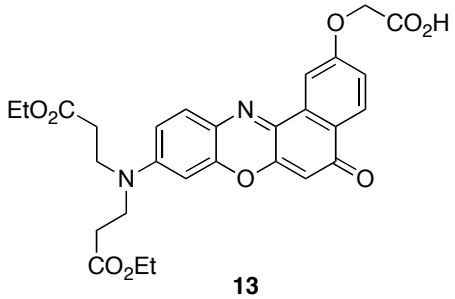

13

A solution of **12a** (100 mg, 0.17 mmol) in trifluoroacetic acid (3 mL) and dichloromethane (3 mL) was stirred for 4 h. The excess trifluoroacetic acid was neutralized by adding sodium hydroxide solution (2 mL, 2 M). The solvent was evaporated and residue purified by flash chromatography eluting with 20 % MeOH/EtOAc to afford **13** as a purple solid (60 mg, 66 %). R_f = 0.6 (EtOAc). **^{1}H NMR** (500 MHz, DMSO-d_6) δ 8.03 (d, 1H, J = 10.0 Hz), 7.88 (s, 1H), 7.61 (d, 1H, J = 10.0 Hz), 7.27 (dd, 1H, J = 10.0, 5.0 Hz), 6.82 (dd, 1H, J = 10.0, 5.0 Hz), 6.73 (s, 1H), 6.19 (s, 1H), 4.88 (s, 2H), 4.08 (q, 4H, J = 5.0 Hz), 3.73 (t, 4H, J = 5.0 Hz), 2.63 (t, 4H, J = 5.0 Hz), 1.19 (t, 6H, J = 5.0 Hz); **^{13}C NMR** (125 MHz, DMSO-d_6) δ 182.2, 172.3, 170.6, 161.3, 152.4, 151.3, 146.9, 140.1, 134.1, 131.7, 128.1, 126.0, 124.9, 118.7, 111.1, 107.3, 105.1, 97.8, 65.6, 60.9, 47.1, 32.4, 14.9. **MS (ESI)** m/z $(M+H)^+$ 537.18. **IR (neat)** 3389, 2954, 1721 cm^{-1}.

^{1}H NMR (DMSO-d_6)

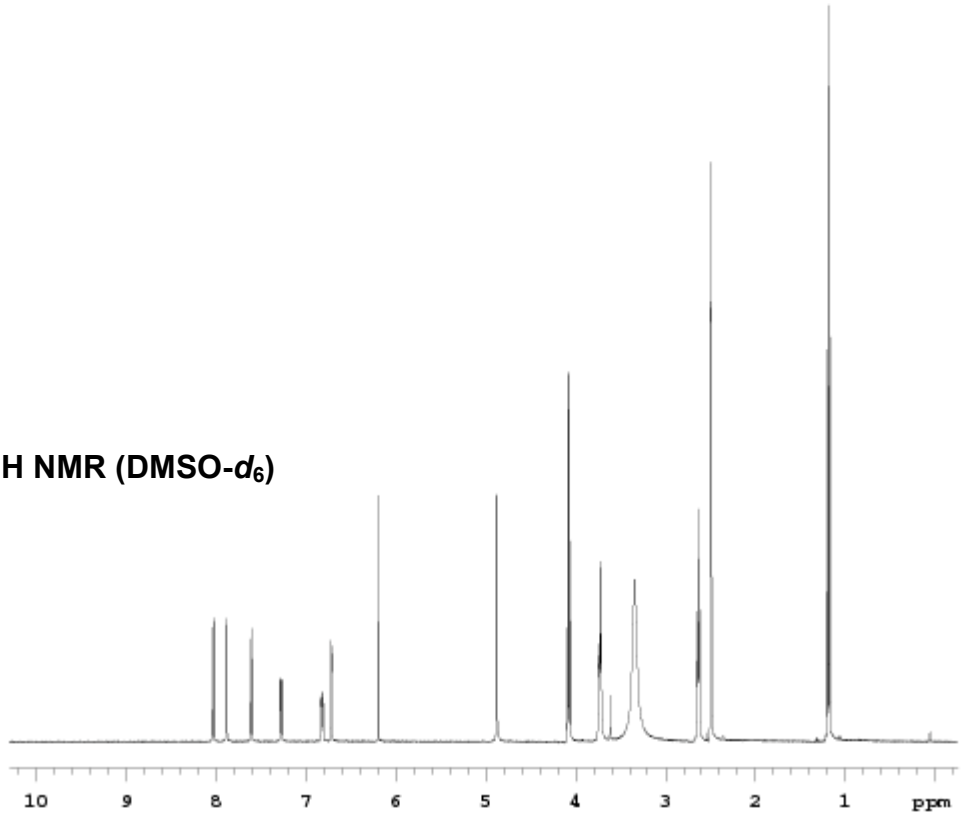

^{13}C NMR (DMSO-d_6)

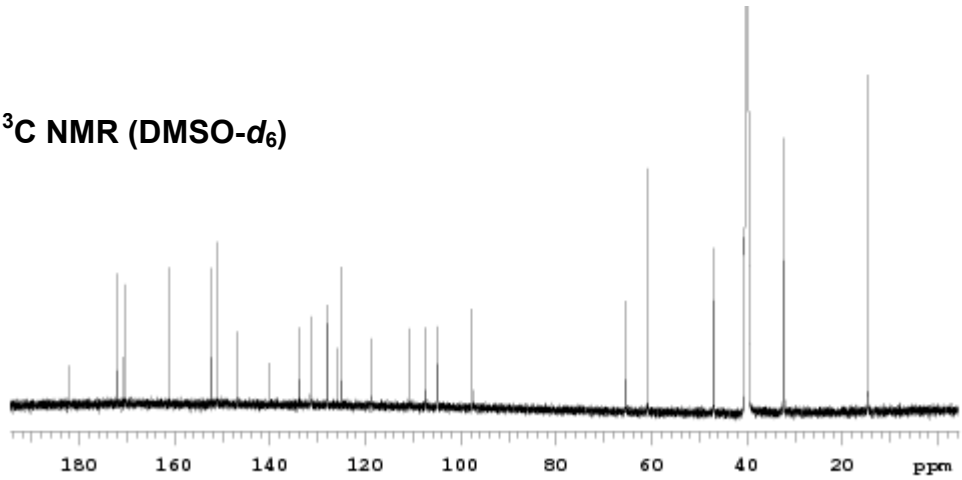

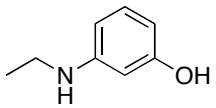

15

A solution of 3-aminophenol **14** (4.0 g, 37.0 mmol) and K_2CO_3 (5.0 g, 37.0 mmol) in DMF (20 mL) was stirred at 25 ºC for 15 min. Iodoethane (5.6 g, 37.0 mmol) was then added and heated at 100 ºC for 2 h. The reaction mixture was cooled to 25 ºC and filtered to remove solid impurities. Water (20 mL) was added to the filtrate and extracted with EtOAc (20 mL × 2), then the combined organic layer was concentrated under reduced pressure and the residue was purified by flash chromatography eluting with 20–50 % EtOAc/hexanes to afford **15** as a brown oil (3.5 g, 70 %). R_f 0.5 (50 % EtOAc/hexanes). **^{1}H NMR** (300 MHz, $CDCl_3$) d 7.07 (t, 1H, J = 8.0 Hz), 6.32–6.28 (m, 2H), 6.16 (s, 1H), 3.09–3.05 (m, 2H), 1.21 (t, 3H, J = 7.5 Hz); **^{13}C NMR** (125 MHz, $CDCl_3$) d 157.2, 149.9, 130.6, 106.9, 106.0, 101.5, 39.3, 14.8; **MS (ESI)** m/z 137.08 $(M+H)^+$.

^{1}H NMR ($CDCl_3$)

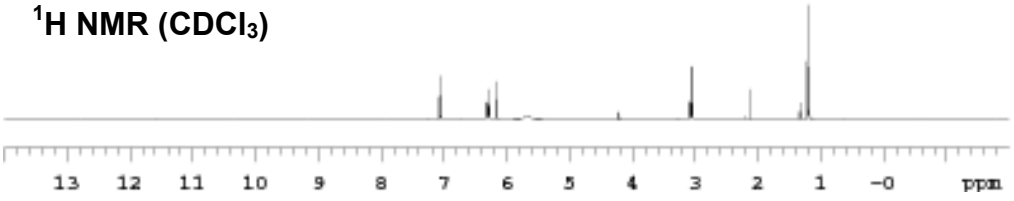

^{13}C NMR ($CDCl_3$)

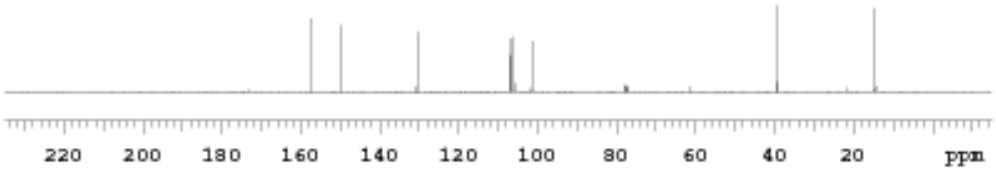

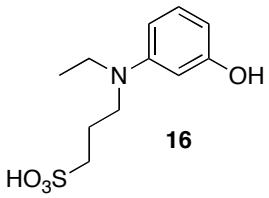

16

Compound **15** (3.5 g, 25.5 mmol) and 1,3-propanesultone (3.36 g, 27.5 mmol) were dissolved in ^{i}PrOH (20 mL) and refluxed for 3 h. The reaction mixture was cooled to room temperature and the precipitate was filtered and washed with cold distilled water to remove any unreacted propanesultone to afford product **16**[66] as a colorless powder (2.6 g, 60 %). R_f 0.3 (10 % MeOH/EtOAc). **^{1}H NMR** (300 MHz, DMSO-d_6) δ 11.22 (br, 1H), 10.21 (br, 1H), 7.36 (t, 1H, J = 4.8 Hz), 7.04 (m, 2H), 6.91 (s, 1H), 3.63–3.53 (br, 4H), 2.60–2.58 (m, 2H), 1.81–1.74 (br, 2H), 1.00–0.95 (m, 3H); **^{13}C NMR** (75 MHz, DMSO-d_6) δ 159.7, 140.1, 131.8, 117.3, 113.9, 110.4, 57.9, 53.4, 49.4, 22.1, 11.2; **MS (ESI)** m/z 258.02 $(M–H)^-$.

^{1}H NMR (DMSO-d_6)

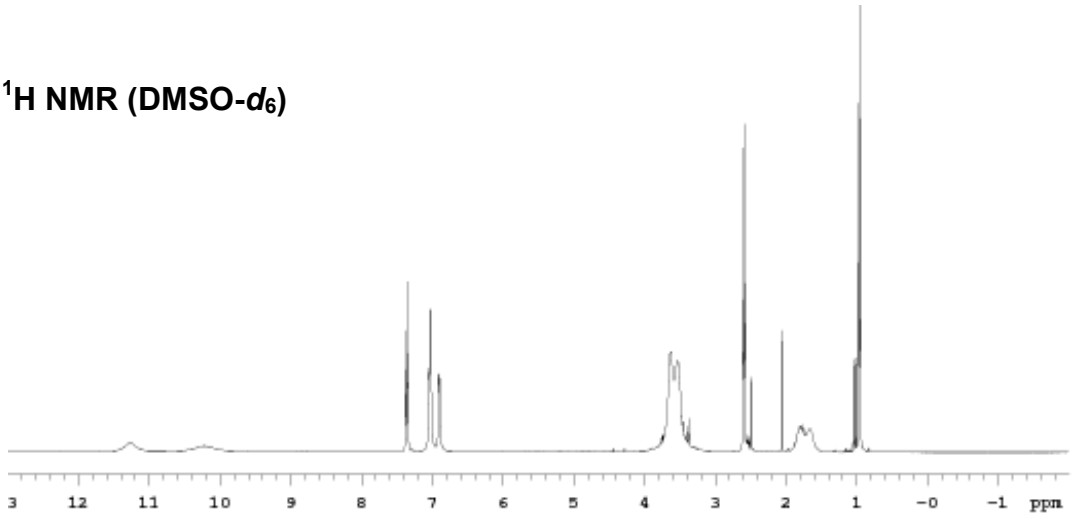

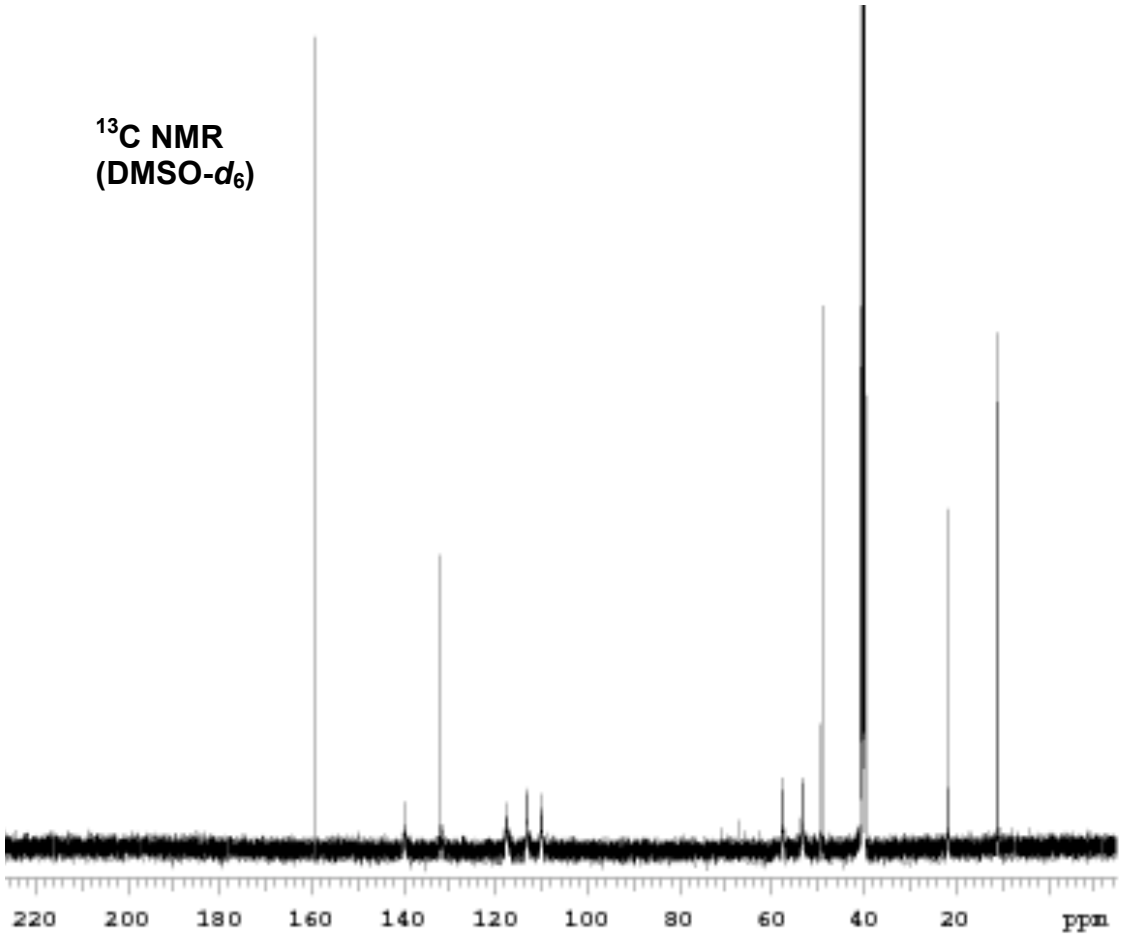

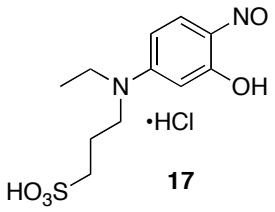

17

Compound **16** (1.0 g, 3.9 mmol) in HCl (10 mL, 10 M) and distilled water (5 mL) was cooled to 0 ºC. Sodium nitrite (0.13 g, 1.8 mmol) in distilled water (2 mL) was added over a period of 10 min using a syringe pump at the rate of 0.2 mL/min. The mixture was stirred at 0 ºC for 3 h and filtered to remove residual impurities. The filtrate was evaporated under reduced pressure to yield product **17** (1.05 g, 80 %) as a yellow solid.[66] The crude product was very moisture sensitive and therefore directly used without further purification for the next step.

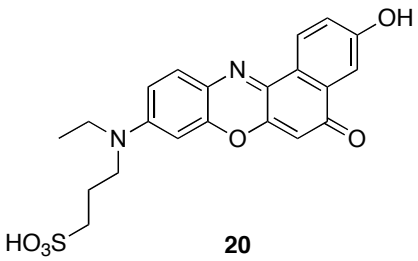

20

The nitroso compound **17** (1.0g, 3.1 mmol) and 1,7-dihydroxynaphthol **19** (0.5 g, 3.1 mmol) was dissolved in dry DMF (20 mL) and heated to 140 ºC for 4 h. The reaction mixture was cooled to 25 ºC and DMF removed under reduced pressure. The residual material was purified by column chromatography eluting with 1/1 MeOH/EtOAc to afford **20** as a blue solid (0.94 g, 71 %). R_f = 0.3 (10 % MeOH/EtOAc). **^{1}H NMR** (500 MHz, CD_3OD) δ 8.55 (d, 1H, *J* = 8.8 Hz), 7.65 (d, 1H, *J* = 8.7 Hz), 7.56 (s, 1H), 7.23 (dd, 1H, *J* = 8.7, 2.7 Hz), 6.95 (dd, 1H, *J* = 8.7, 2.7 Hz), 6.74 (s, 1H), 6.35 (s, 1H), 3.66 (t, 2H, *J* = 8.3 Hz), 3.59 (q, 2H, *J* = 6.8 Hz), 2.92 (t, 2H, *J* = 8.3 Hz), 2.15 (br, 2H), 1.26 (t, 3H, 6.8 Hz); **^{13}C NMR** (125 MHz, CD_3OD) δ 184.3, 172.0, 159.9, 152.7, 151.3, 146.6, 138.9, 133.2, 130.7, 126.0, 125.9, 120.1, 110.9, 109.9, 104.3, 96.5, 49.4, 48.3, 45.2, 23.0, 11.5. **MS (ESI)** m/z $(M-H)^-$ 427.02. **IR (neat)** 3397, 2931, 1689 cm^{-1}.

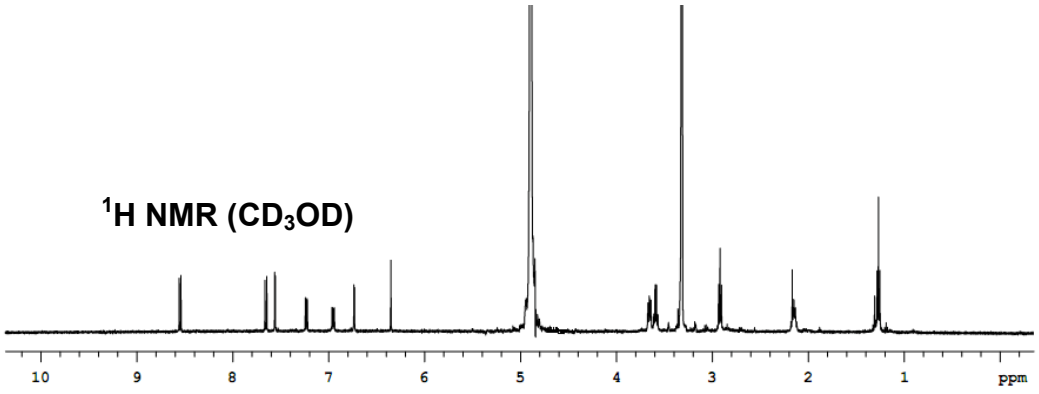

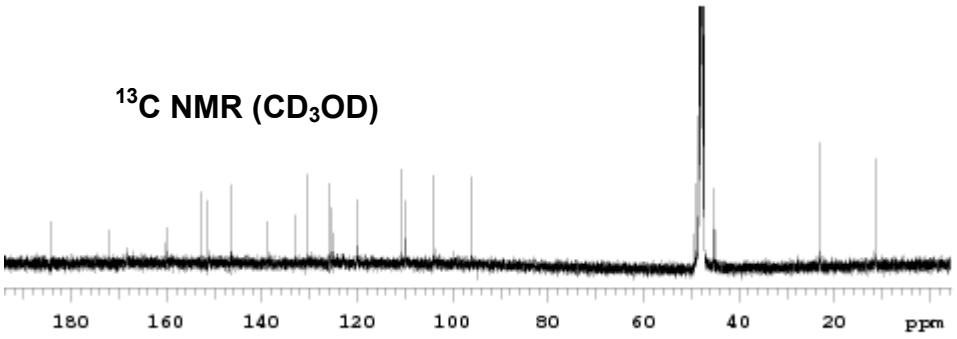

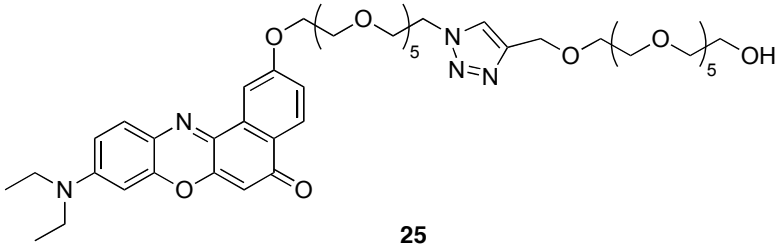

25

2-Hydroxy Diethyl Nile Red **24** (50.0 mg, 0.15 mmol) and K_2CO_3 (103.0 mg, 0.75 mmol) were dissolved in CH_3CN (5 mL). **23** (162.0 mg, 0.18 mmol) in CH_3CN (2 mL) was added drop wise in 5 min. to above solution at 25 ^oC. The reaction mixture was heated to 50 ^oC for 4 h. After completion of reaction the solvent was evaporated and residue was subjected to flash chromatography eluting with 30-40 % acetone/EtOAc and then with 10 % MeOH/CH_2Cl_2 to afford 150.0 mg of red colored material. Flash chromatography was performed to remove excess **23**.

Above red material (60.0 mg, 0.06 mmol) was dissolved in TFA/CH_2Cl_2 (1/1, 3 mL) and stirred at 25 ^oC for 1 h. Solvent was removed under reduced pressure and the residual material was dissolved in 5 mL of water. This solution was filtered to remove solid impurities and the filtrate was purified by reverse phase medium pressure liquid chromatography (MPLC) eluting with 30 % CH_3CN/H_2O to afford **25** as a dark red solid (35.0 mg, 58%). **^{1}H NMR** (500 MHz, CD_3OD) δ 8.06 (d, 1H, *J* = 8.9 Hz), 8.01 (s, 1H), 7.97 (d, 1H, *J* = 3.0 Hz), 7.54 (d, 1H, *J* = 8.9 Hz), 7.17 (dd, 1H, *J* = 9.2, 3.0 Hz), 6.79 (dd, 1H, *J* = 9.2, 3.0 Hz), 6.54 (d, 1H, *J* = 3.0 Hz), 6.17 (s, 1H), 4.61 (s, 2H), 4.55 (t, 2H, *J* = 5.0 Hz), 4.32-4.29 (br, 2H), 3.93 (br, 2H), 3.89 (t, 2H, *J* = 5.0 Hz), 3.77-3.74 (br, 2H), 3.70-3.68 (br, 2H), 3.66-3.52 (m, 40H), 1.27 (t, 6H, *J* = 7.0 Hz); **^{13}C NMR** (75

MHz, CD_3OD) δ 183.7, 161.9, 152.8, 151.8, 147.1, 144.6, 143.8, 138.1, 134.3, 131.3, 127.3, 125.1, 124.7, 118.1, 110.7, 106.4, 103.7, 96.0, 72.5, 70.7, 70.5, 70.4, 70.3, 70.2, 70.1, 69.6, 69.2, 67.9, 63.8, 61.0, 50.2, 44.9, 11.8; **MS (ESI)** 944.49 $(M+H)^+$ 966.45 $(M+Na)^+$; **IR (neat)** 3435, 2925, 1641 cm^{-1}.

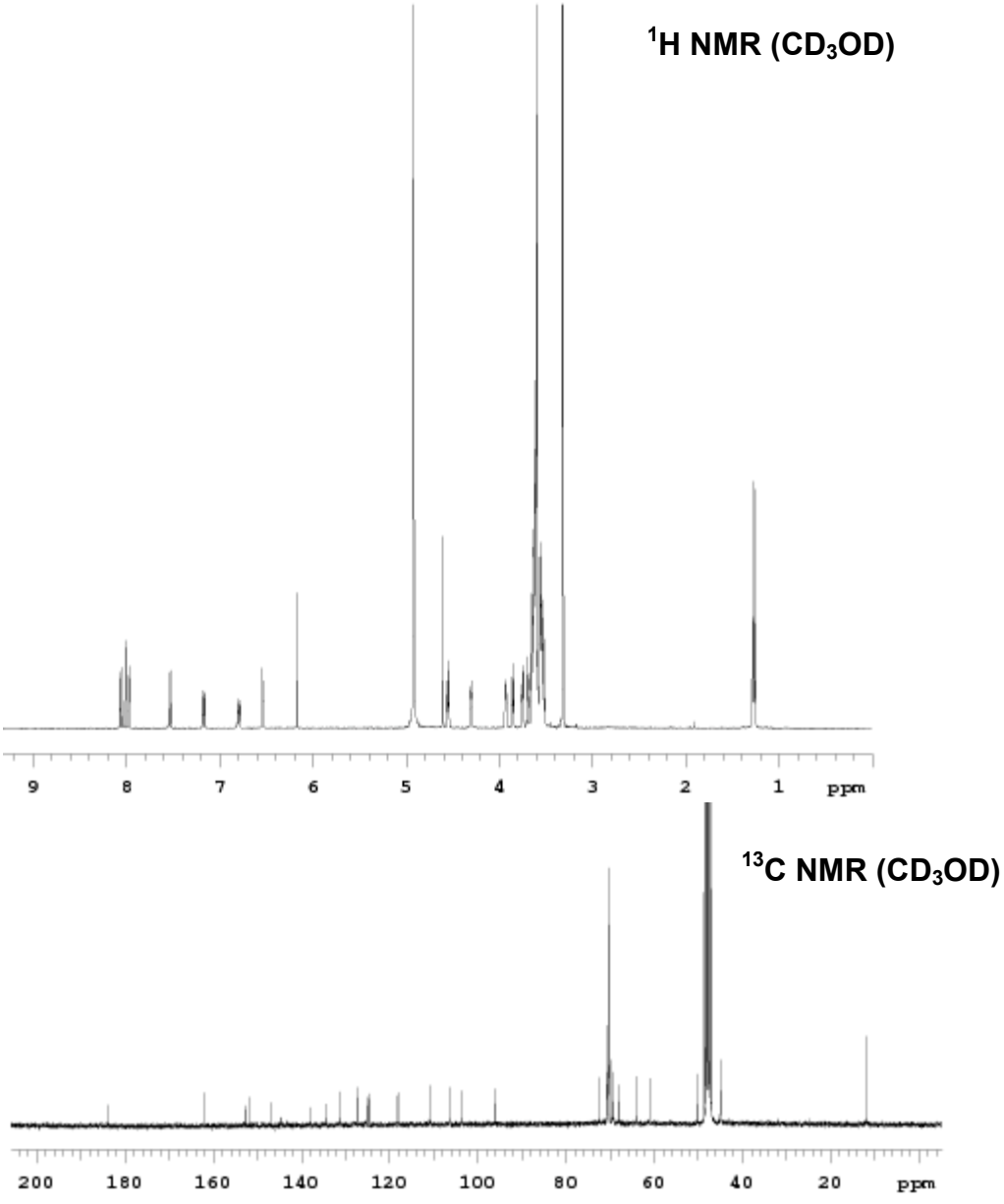

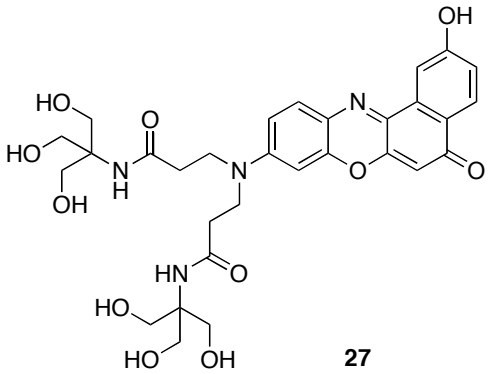

27

Compound **26** (25 mg, 0.06 mmol) and activating agent EDCI (28 mg, 0.24 mmol) was dissolved in pyridine (2 mL). Tris(hydroxymethyl)aminomethane **21** (43 mg, 0.36 mmol) was added and reaction continued at 25 ºC for 24 h. The solvent was evaporated and residue purified by reverse phase medium pressure liquid chromatography (MPLC) eluting with 3/2 CH_3CN/H_2O to afford **27** as a dark red solid (22 mg, 59 %). **^{1}H NMR** (500 MHz, DMSO-d_6) δ 7.96 (d, 1H, J = 10.0 Hz), 7.87 (s, 1H), 7.61 (d, 1H, J = 10.0 Hz), 7.39 (s, 2H), 7.08 (dd, 1H, J = 10.0, 5.0 Hz), 6.84 (dd, 1H, J = 10.0, 5.0 Hz), 6.68 (s, 1H), 6.19 (s, 1H), 4.73 (br, 6H), 3.65 (br, 4H), 3.53 (s, 12H), 2.51 (br, 4H); **^{13}C NMR** (125 MHz, DMSO-d_6) δ 182.4, 172.1, 152.2, 152.2, 151.3, 146.9, 140.1, 134.4, 131.4, 128.2, 124.8, 119.2, 110.8, 110.2, 109.2, 105.2, 97.4, 63.2, 61.2, 48.1, 34.6. **MS (ESI)** m/z $(M+H)^+$ 629.23. **IR (neat)** 3412, 3316, 1693 cm^{-1}.

^{1}H NMR (DMSO-d_6)

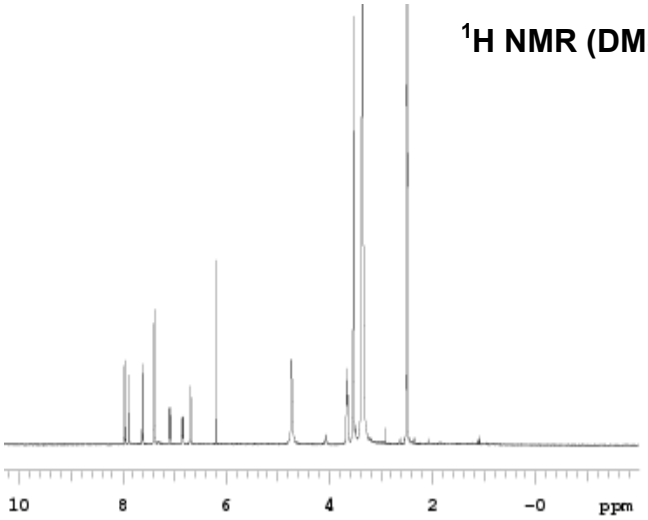

^{13}C NMR (DMSO-d_6)

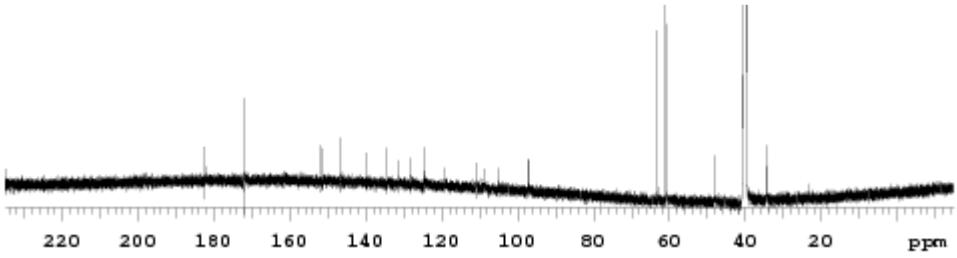

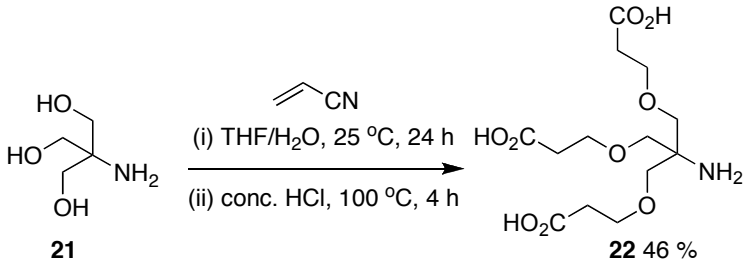

21 **22** 46 %

Tris(hydroxymethyl)aminomethane **21** (2g, 16.5 mmol) was dissolved in THF (10 mL) and aqueous 40 % KOH (1mL). Acrylonitrile (5.4 mL, 82.5 mmol) was added to the above solution and stirred at 25 ^{o}C for 24 h. The solvent was evaporated and water (10 mL) added. The aqueous layer was extracted with dichloromethane (5 x 5 mL) and dried over Na_2SO_4. The residue obtained was purified by flash chromatography eluting with 10% MeOH/EtOAc to obtain cyano derivative as a yellow oil (2.8 g, 61%).

^{1}H NMR (500 MHz, CD_3OD) δ 3.70 (t, 6H, *J* = 8.8 Hz), 3.48 (s, 6H), 2.74 (t, 6H, 8.8 Hz); **^{13}C NMR** (125 MHz, CD_3OD) δ 118.8, 71.8, 66.1, 56.1, 18.1. **IR (neat)** 3378, 2290, 1732, 1616 cm $^{-1}$. Above cyano derivative (1 g, 3.6 mmol) was dissolved in concentrated HCl (3 mL) and refluxed at 100 ^{o}C for 4 h. The reaction mixture was cooled to 25 ^{o}C and diluted with water (20 mL). The solvent was evaporated and residue purified by reverse phase medium pressure liquid chromatography (MPLC) eluting with 1/4 CH_3CN/H_2O to afford **22** as a colorless viscous solid (0.91 g, 75 %). **^{1}H NMR** (500 MHz, D_2O) δ 3.56 (t, 6H, *J* = 6.1 Hz), 3.43 (s, 6H), 2.41 (t, 6H, *J* = 6.1 Hz); **^{13}C NMR** (125 MHz, D_2O) δ 177.6, 68.1, 67.4, 59.7, 35.3. **MS (ESI)** m/z $(M)^+$ 337.18. **IR (neat)** 2927, 1732, 1615 cm^{-1}.

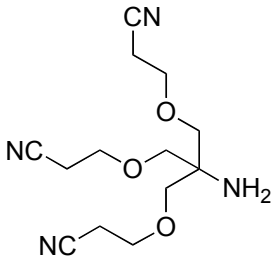

^{1}H NMR (CD_3OD)

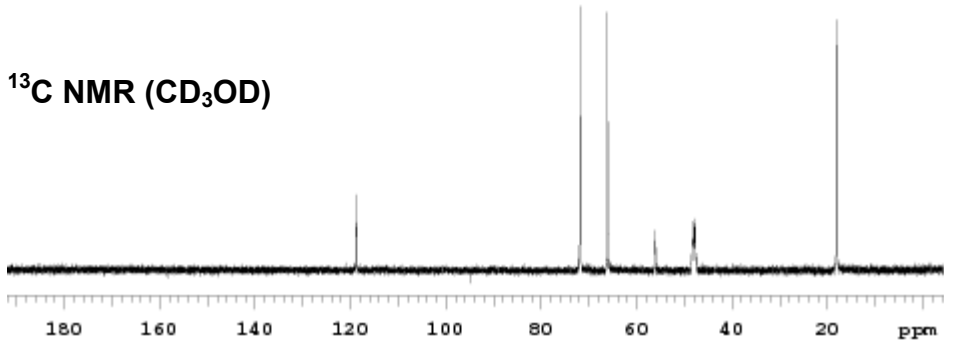

^{13}C NMR (CD_3OD)

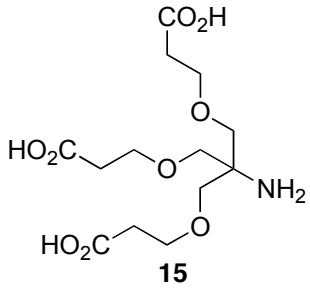

15

^{1}H NMR (D_2O)

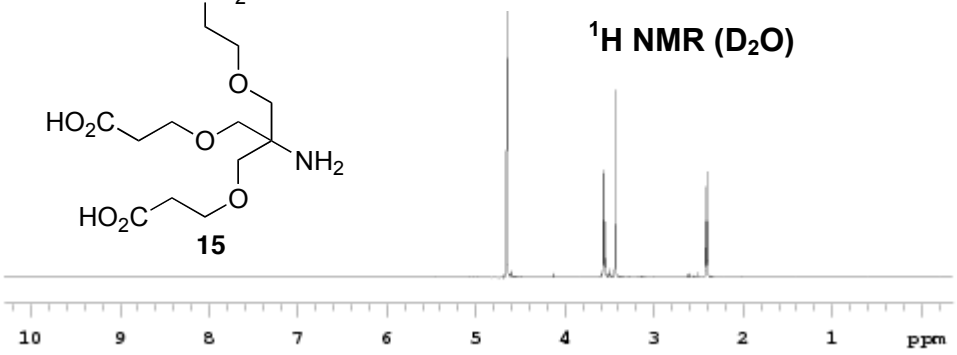

^{13}C NMR (D_2O)

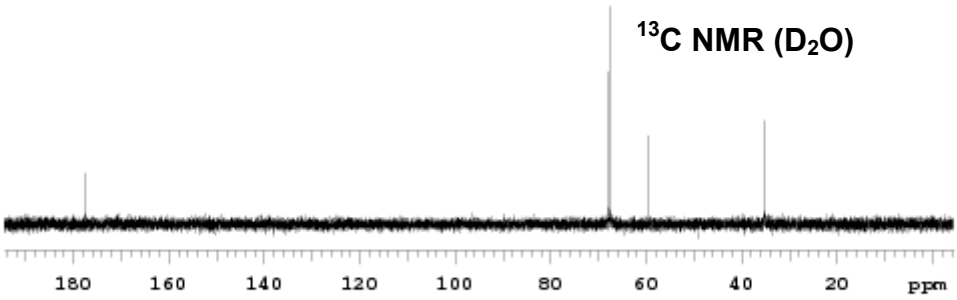

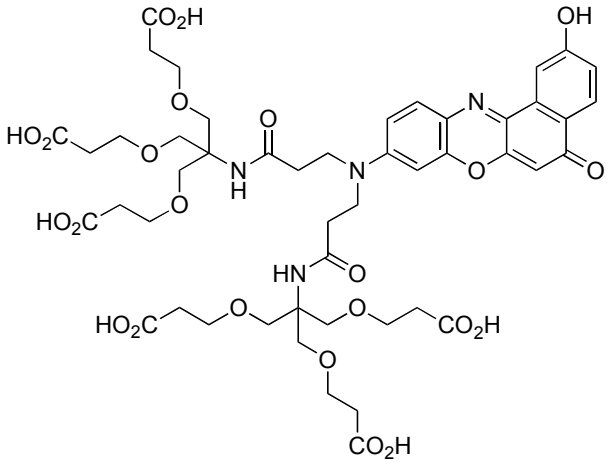

28

Compound **26** (60 mg, 0.14 mmol), *N*-hydroxysuccinimide (81 mg, 0.7 mmol) and *N,N'*-diisopropylcarbodiimide (88 mg, 0.7 mmol) were dissolved in dry DMF (2 mL) and stirred at 25 ºC for 24 h. Solvent was evaporated under reduced pressure and residue dissolved in EtOAc (5 mL) and washed with water (5 mL x3). The organic layer was dried over $MgSO_4$ and solvent evaporated to obtain a red colored material.

The above red colored material was dissolved in DMF (2 mL) along with tricarboxylic acid **22** (479 mg, 1.4 mmol), DMAP (1 mg, 0.01 mmol) and triethylamine (0.2 mL, 1.4 mmol). The reaction mixture was stirred at 25 ºC for 48 h. After removal of DMF under reduced pressure the residue was dissolved in water (2 mL) and washed with EtOAc (2 mL x 3). The aqueous layer containing crude product was loaded on to a reverse phase MPLC column and purified using 3/2 CH_3CN/H_2O solvent mixture. The solvent was evaporated to afford **28** as a dark purple solid (43 mg, 28 %). **^{1}H NMR** (500 MHz, CD_3OD) δ 8.04 (br, 1H), 7.94 (br, 1H), 7.56 (br, 1H), 7.08 (br, 1H), 6.91 (s, 1H), 6.74 (s, 1H), 6.20 (s, 1H), 3.76 (br, 4H), 3.67 (br, 24H), 2.75 (br, 4H), 2.47 (s, 12H); **^{13}C NMR** (125 MHz, CD_3OD) δ 183.9, 175.6, 172.4, 161.0, 152.5, 151.3, 146.5, 139.1, 134.3, 130.8, 127.3, 125.1, 123.9, 118.0, 110.8, 108.4, 103.6, 96.9, 68.5 (2C), 67.2, 60.9, 35.4, 34.2; **MS (MALDI)** m/z 1063.35 $(M+3H)^+$. **IR (neat)** 2942, 1722, 1621 cm^{-1}.

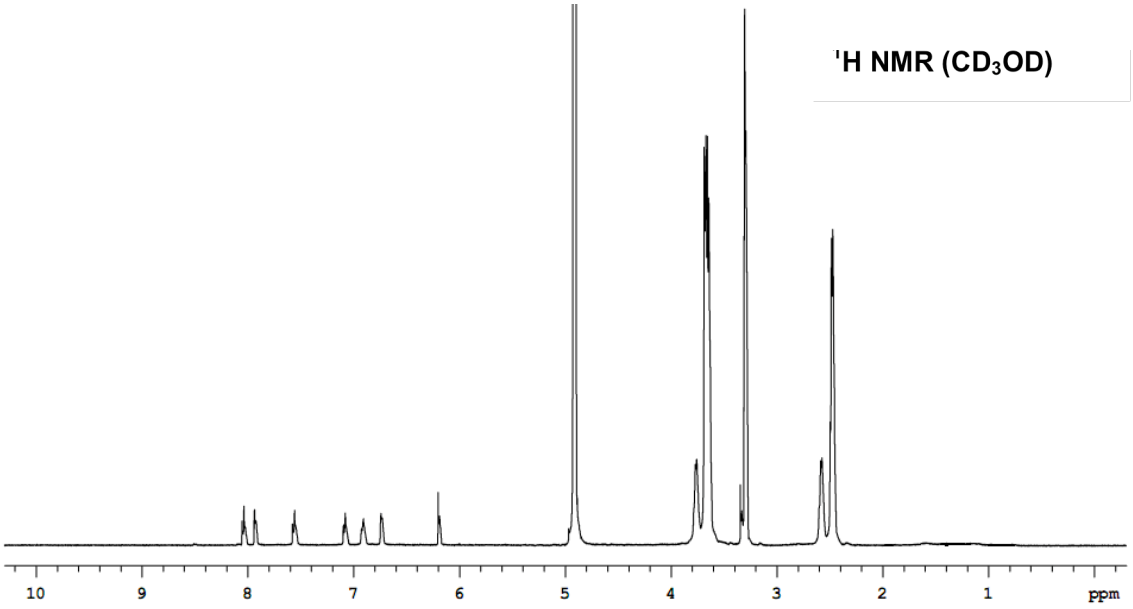
^{1}H NMR (CD_3OD)
10
9
8
7
6
5
4
3
2
1
ppm

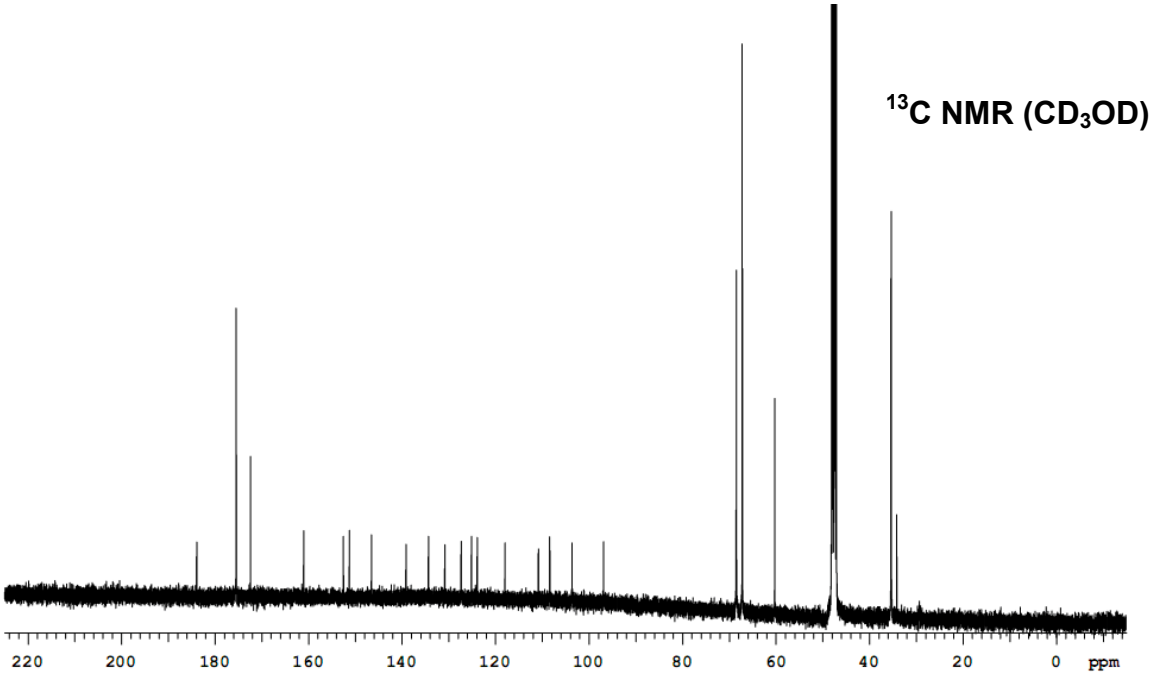
^{13}C NMR (CD_3OD)
220
200
180
160
140
120
100
80
60
40
20
0
ppm

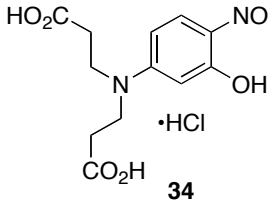

34

Compound **9**[86] (2.0 g, 7.9 mmol) in HCl (20 mL, 10 M) and distilled water (10 mL), was cooled to 0 ºC. Sodium nitrite (0.59 g, 8.5 mmol) dissolved in distilled water (5 mL) was added over a period of 50 min using a syringe pump at the rate of 0.2 mL/min. The mixture was stirred at 0 ºC for 3 h and filtered to remove residual impurities. The filtrate was evaporated under reduced pressure to yield product **34** (1.93 g, 77 %). The crude product was very moisture sensitive and therefore directly used without further purification for the next step.

General Procedure for The Synthesis of Nile Blue Derivatives (32a-b and 33a-b)

Nitroso compound **17** or **34** (0.3 mmol) was dissolved in 5 mL of dry distilled DMF and 5-amino-2-naphthol **36a** or **36b** (0.3 mmol) was added while stirring. The reaction mixture was heated to 90 ºC for 5 h and cooled to room temperature. DMF was removed under reduced pressure and the residual material was dissolved in 10 mL of water. This solution was filtered to remove solid impurities and the filtrate was purified by reverse phase medium pressure liquid chromatography (MPLC) eluting with 1/1 CH_3CN/H_2O to afford the corresponding Nile Blue derivatives as a dark blue solid.

Nile Blue Derivative 32a

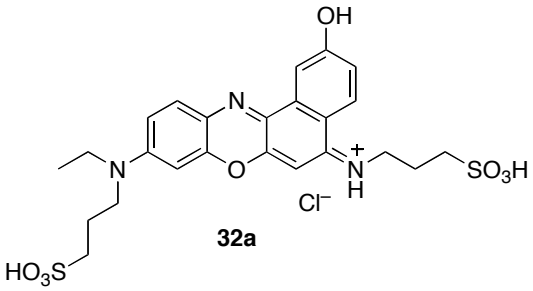

32a

Dark blue solid (120 mg, 68 %). **^{1}H NMR** (500 MHz, CD_3OD) δ 7.87 (d, 1H, *J* = 9.0 Hz), 7.83 (m, 1H), 7.53 (d, 1H, *J* = 9.0 Hz), 7.15 (d, 1H, *J* = 9.0 Hz), 7.00 (dd, 1H, *J* =

9.0, 2.0 Hz), 6.71 (s, 1H), 6.69 (s, 1H), 3.81 (t, 2H, *J* = 7.0 Hz), 3.77 (t, 2H, *J* = 6.5 Hz), 3.68-3.65 (m, 2H), 3.07 (t, 2H, *J* = 6.5 Hz), 2.98 (t, 2H, *J* = 7.5 Hz), 2.34-2.31 (m, 2H), 2.21-2.19 (m, 2H), 1.33 (t, 3H, *J* = 7.0 Hz); **^{13}C NMR** (75 MHz, CD_3OD) δ 161.2, 158.4, 154.8, 152.0, 148.1, 134.0, 133.8, 132.9, 129.1, 125.3, 118.9, 115.8, 114.9, 108.7, 96.4, 92.3, 49.8, 45.9 (2C), 43.5, 43.4, 24.1, 23.6, 11.9; **MS (ESI)** m/z 548.03 $(M–2H)^-$; **HR-MS (ESI)** m/z calculated for $(M–2H)^-$ 548.1167 found 548.1170; **IR (neat)** 3361, 3059, 1627 cm^{-1}.

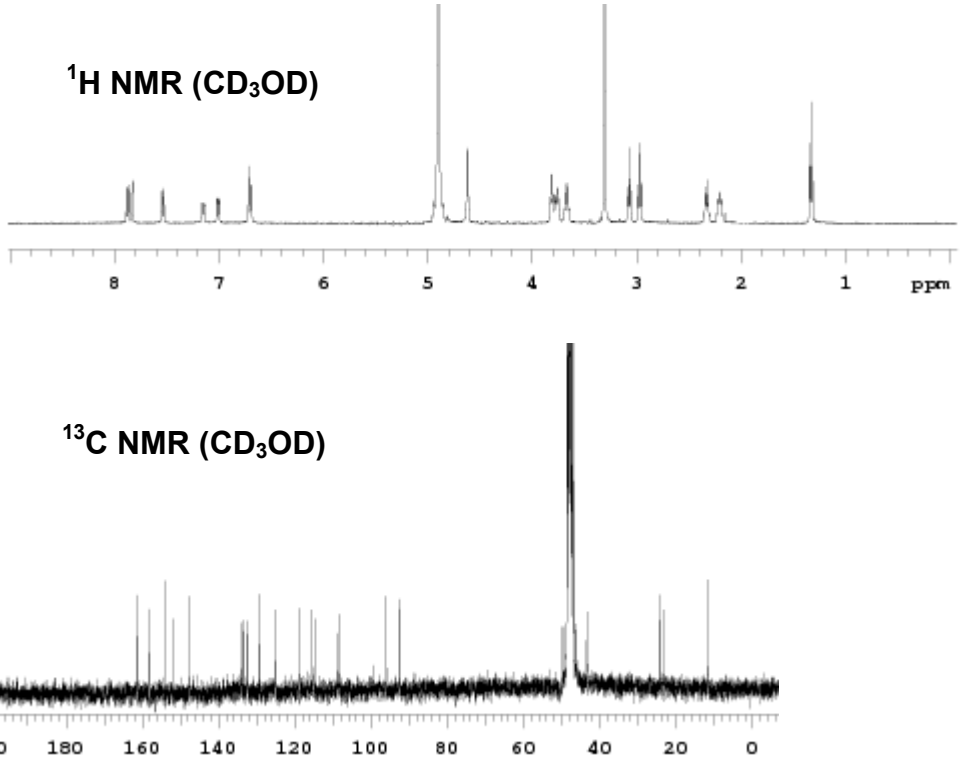

Nile Blue Derivative 32b

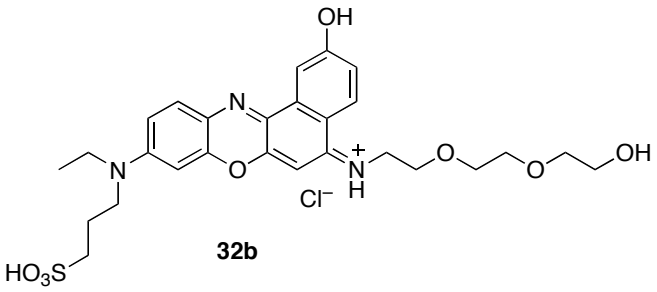

32b

Dark blue solid (82 mg, 46 %). **^{1}H NMR** (500 MHz, CD_3OD) δ 8.08-8.01 (m, 1H), 7.96 (d, 1H, *J* = 3.0 Hz), 7.61-7.57 (m, 1H), 7.24-7.21 (m, 1H), 7.17 (dd, 1H, *J* = 2.5, 10.0 Hz), 6.83 (s, 1H), 6.51 (d, 1H, *J* = 10.0 Hz), 4.32 (t, 2H, *J* = 4.0 Hz), 3.98-3.96 (m, 2H), 3.83-3.67 (m, 10H), 3.61-3.60 (m, 2H), 2.96 (t, 2H, *J* = 7.0 Hz), 2.21-2.19 (m, 2H), 1.33 (t, 3H, *J* = 7.0 Hz); **^{13}C NMR** (75 MHz, CD_3OD) δ 169.2, 163.6, 161.9, 160.6, 154.2, 150.8, 147.4, 133.7, 132.4, 128.7, 125.7, 118.6, 115.9, 114.7, 105.8, 96.0, 72.5, 70.6, 70.3, 69.4, 68.0, 61.0, 49.9, 46.4, 35.8, 23.7, 11.0; **MS (ESI)** m/z 558.12 $(M–2H)^-$; **HR-MS (ESI)** m/z calculated for $(M–2H)^-$ 558.1916 found 558.1915; **IR (neat)** 3348, 3049, 2938, 1587 cm^{-1}.

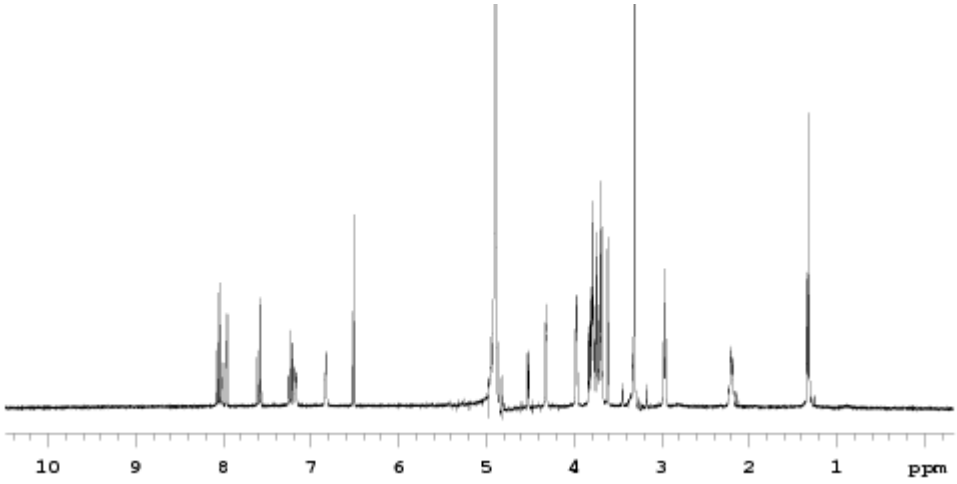

^{13}C NMR (CD_3OD)

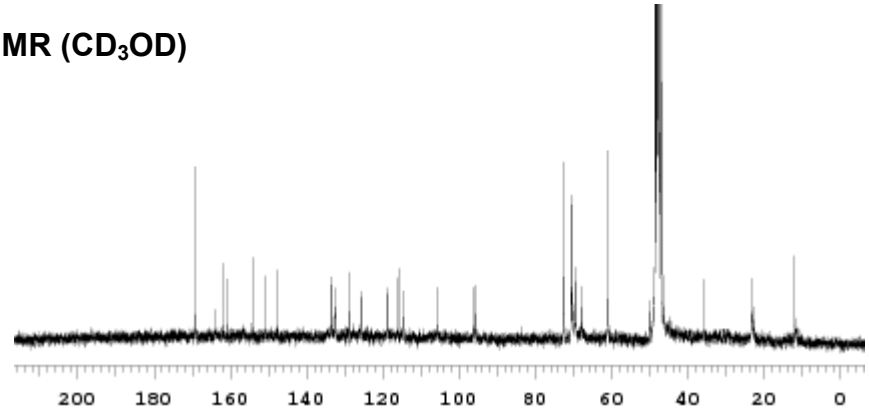

Nile Blue Derivative 33a

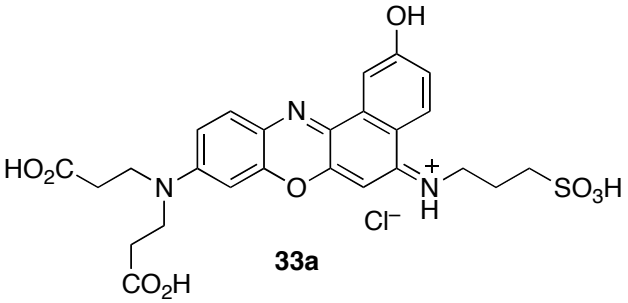

33a

Dark blue solid (115 mg, 66 %). **^{1}H NMR** (500 MHz, CD_3OD) δ 7.99 (d, 1H, *J* = 8.5 Hz), 7.94 (m, 1H), 7.62 (d, 1H, *J* = 9.0 Hz), 7.22 (m, 1H), 7.10 (m, 1H), 6.77 (s, 2H), 3.94 (t, 2H, *J* = 8.0 Hz), 3.85 (t, 2H, *J* = 7.0 Hz), 3.07 (t, 2H, *J* = 7.0 Hz), 2.63 (t, 2H, *J* = 8.0 Hz), 2.34 (m, 2H); **^{13}C NMR** (125 MHz, CD_3OD) δ 177.08, 161.7, 158.5, 154.2, 152.2, 147.8, 134.4, 133.5, 132.3, 129.3, 125.1, 118.9, 115.8, 114.9, 108.7, 96.4, 92.4, 48.6, 44.7, 43.5, 34.8, 24.4; **MS (ESI)** m/z 542.05 $(M–2H)^-$; **HR-MS (ESI)** m/z calculated for $(M–2H)^-$ 542.1239 found 542.1237; **IR (neat)** 3358, 3187, 2924, 1584 cm^{-1}.

^{1}H NMR (CD_3OD)

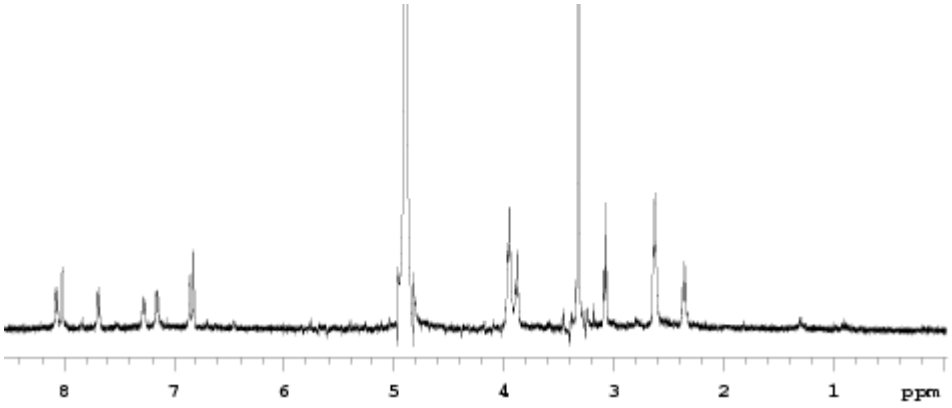

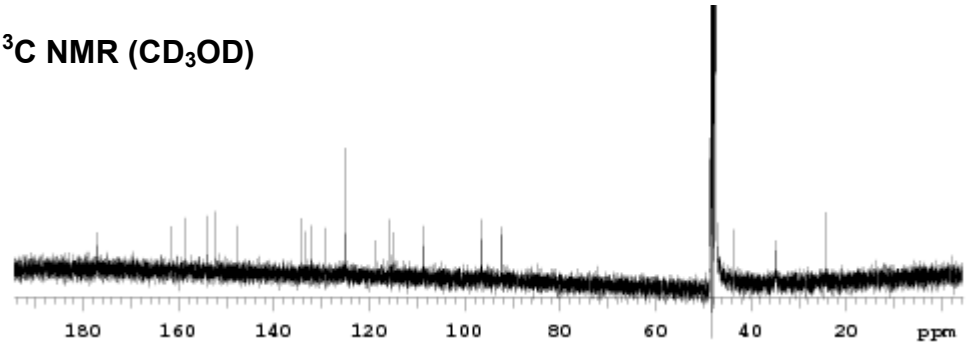

Nile Blue Derivative 33b

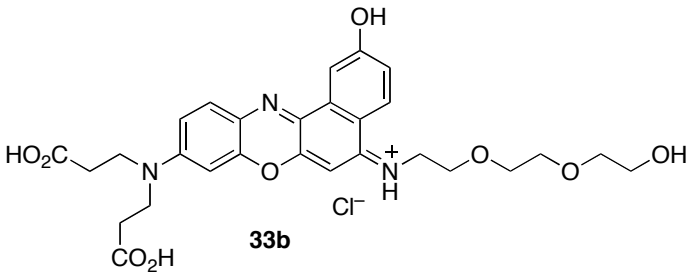

33b

Dark blue solid (78 mg, 44 %). **^{1}H NMR** (500 MHz, CD_3OD) δ 8.24-8.21 (m, 1H), 8.19 (d, 1H, *J* = 9.0 Hz), 7.83-7.80 (m, 1H), 7.38 (dd, 1H, *J* = 2.5, 9.0 Hz), 7.2 (dd, 1H, *J* = 2.5, 10.0 Hz), 6.92 (s, 1H), 6.71 (s, 1H), 4.4 (t, 2H, *J* = 4.5 Hz), 3.97 (t, 4H, *J* = 6.5 Hz), 3.82-3.78 (m, 4H), 3.72 (t, 2H, *J* = 2.5 Hz), 3.67 (t, 2H, *J* = 5.0 Hz), 3.59 (t, 2H, *J* = 5.0 Hz), 2.76 (t, 4 H, *J* = 7.5 Hz); **^{13}C NMR** (75 MHz, CD_3OD) δ 172.0, 161.4, 160.7, 152.3, 150.7, 146.3, 134.1, 133.0, 131.0, 127.3, 124.5, 117.6, 115.1, 112.8, 105.5, 95.2, 94.7, 71.0, 69.1, 68.7, 67.8, 66.7, 59.4, 45.8, 30.2; **MS (ESI)** m/z 554.20 $(M)^+$; **HR-MS (ESI)** m/z calculated for $(M)^+$ 554.2133 found 554.2136; **IR (neat)** 3227, 2984, 1604 cm^{-1}.

^{1}H NMR (CD_3OD)

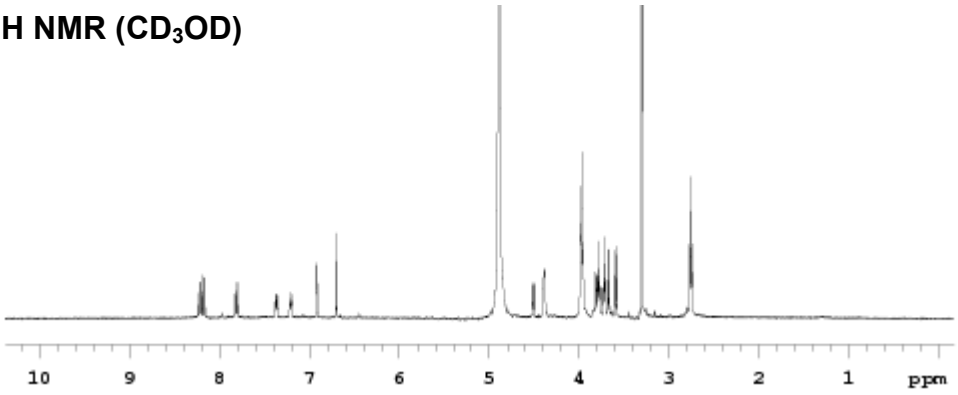

^{13}C NMR (CD_3OD)

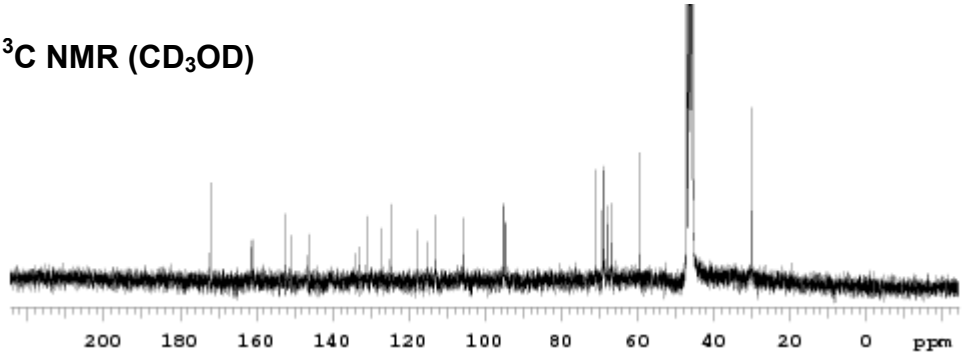

APPENDIX B

EXPERIMENTAL DATA FOR CHAPTER III

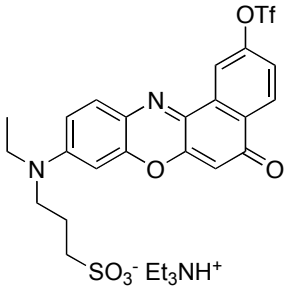

50

Phenyl triflamide (0.21 g, 0.60 mmol) was added gradually over a period of 10 minutes to a solution of **55** (0.10 g, 0.24 mmol) and triethylamine (0.13 mL, 0.96 mmol) in 5 mL dry distilled THF. The mixture was stirred at 25 ^{o}C for 24 h. Reaction mixture was diluted with EtOAc and was washed with 0.1 M HCl (2 x 10 mL). Organic layer was evaporated under reduced pressure and purified by flash chromatography eluting with 1/1 EtOAc /hexanes to afford **50** as a red solid (0.07 g, 55 %). R_f = 0.2 (1/1 EtOAc/hexanes). **^{1}H NMR** (300 MHz, CD_3OD) δ 8.49 (s, 1H), 8.24 (d, 1H, J = 6.3 Hz), 7.69-7.61 (br, 2H), 6.94 (dd, 1H, J = 6.3 Hz, J = 3.2 Hz), 6.70 (s, 1H), 6.23 (s, 1H), 3.71-3.54 (m, 4H), 3.21(br, 6H), 2.96 (t, 2H, J = 7.2 Hz), 2.19-2.10 (br, 2H), 1.32-1.29 (br, 12H); **^{13}C NMR** (75 MHz, CD_3OD) δ 182.0, 153.6, 152.2, 151.9, 146.7, 136.3, 134.1, 132.0, 131.2, 128.9, 125.7, 122.5, 118.2, 115.3, 111.6, 103.9, 96.8, 49.3, 49.1, 45.3(2C), 22.3, 10.9, 10.1. **^{19}F NMR** (282 MHz, CD_3OD) δ 104.1. **IR (neat, cm^{-1})** 3402, 2917, 1644; **MS (ESI)** m/z 558.95 $(M)^-$

^{19}F NMR (CD_3OD)

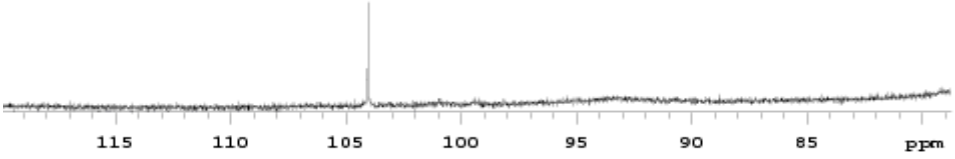

^{1}H NMR (CD_3OD)

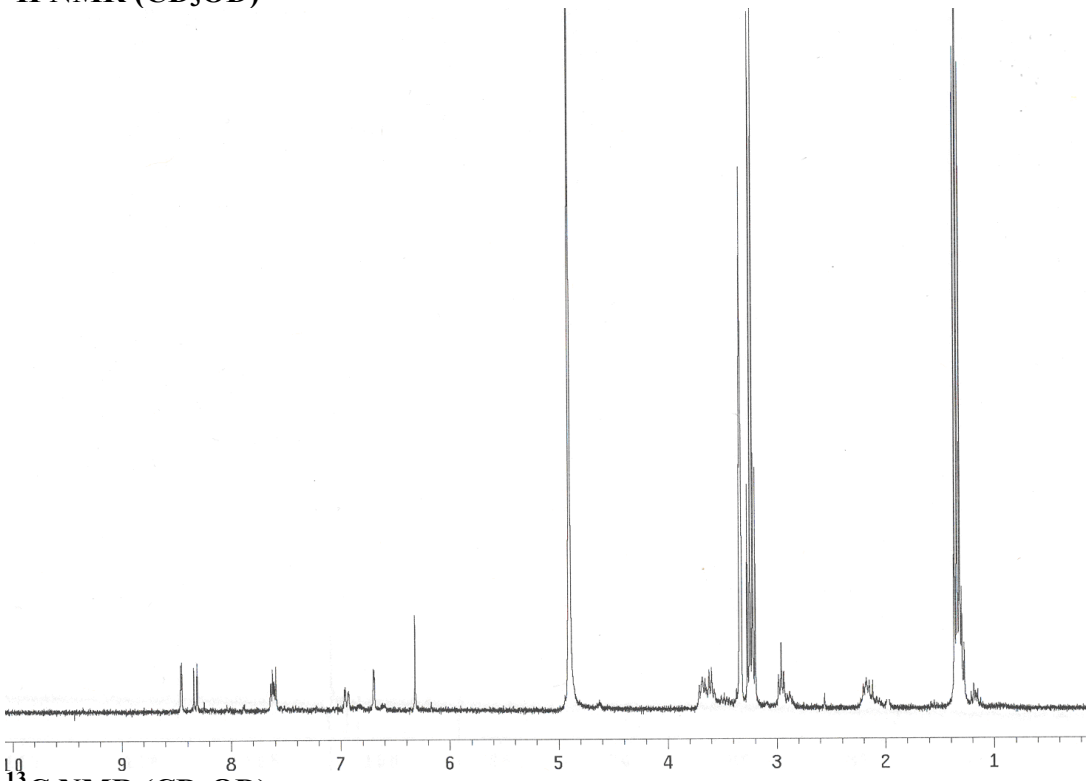

^{13}C NMR (CD_3OD)

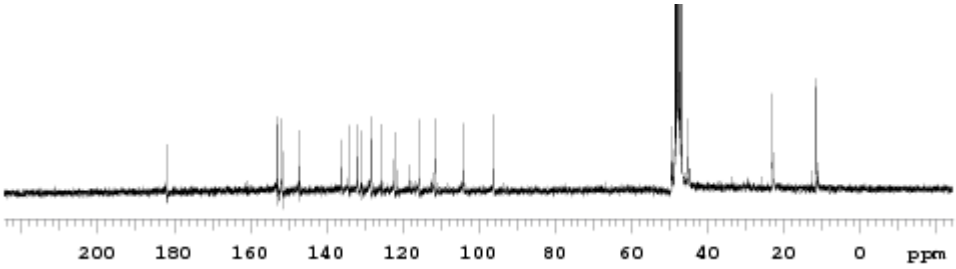

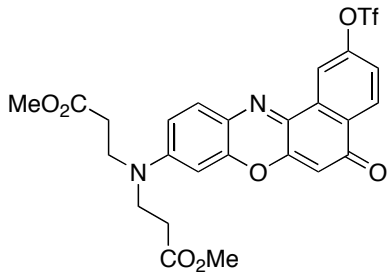

51

Phenyl triflamide (1.9 g, 5.5 mmol) was added gradually over a period of 10 minutes to a solution of **56** (1.0g, 2.2 mmol) and triethylamine (1.2 mL, 8.8 mmol) in 20 mL dry distilled THF. The mixture was stirred at 25 ^{o}C for 24 h. Reaction mixture was diluted with EtOAc and washed with 0.1 M HCl (2 x 10 mL). Organic layer was evaporated under reduced pressure and purified by flash chromatography eluting with 1/1 EtOAc/hexanes to afford **51** as a red solid (0.67g, 52 %). R_f = 0.4 (1/1 EtOAc/hexanes) **^{1}H NMR** (300 MHz, acetone-d_6) δ 8.57 (s, 1H), 8.38 (d, 1H, J = 8.4 Hz), 7.79 (d, 1H, J = 8.4 Hz), 7.70 (d, 1H, J = 9.3 Hz), 6.98 (d, 1H, J = 9.3 Hz), 6.79 (s, 1H), 6.30 (s, 1H), 3.93 (t, 4H, 7.2 Hz), 3.67 (s, 6H), 2.78 (t, 4H, J = 7.5 Hz) **^{13}C NMR** (75 MHz, acetone-d_6) δ 181.9, 173.1, 153.3, 152.0, 151.8, 146.3, 139.8, 135.7(2C), 133.7, 129.1, 124.3, 123.4, 118.1(2C), 111.1, 106.8, 98.2, 60.36, 49.3, 33.4. **^{19}F NMR** (282 MHz, acetone-d_6) δ 104.4. **IR (neat, cm^{-1})** 3421, 2938, 1638; **MS (ESI)** m/z 582.09 (M^+).

^{19}F NMR (acetone-*d6*)

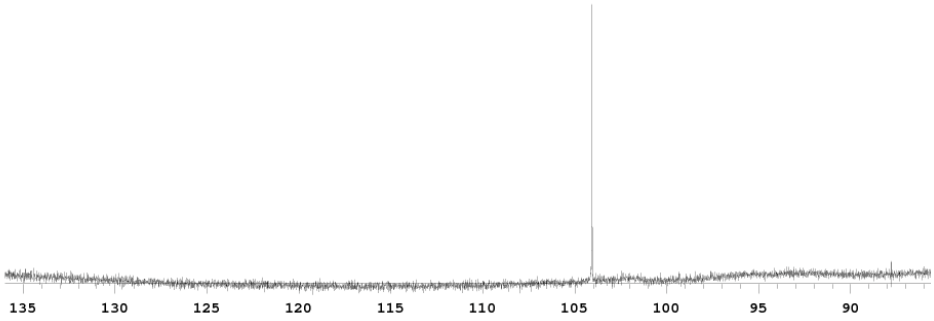

^{1}H NMR (acetone-d_6)

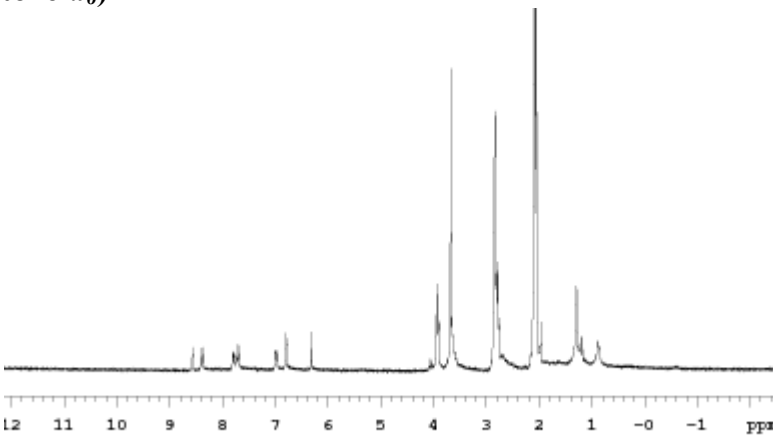

^{13}C NMR (acetone-d_6)

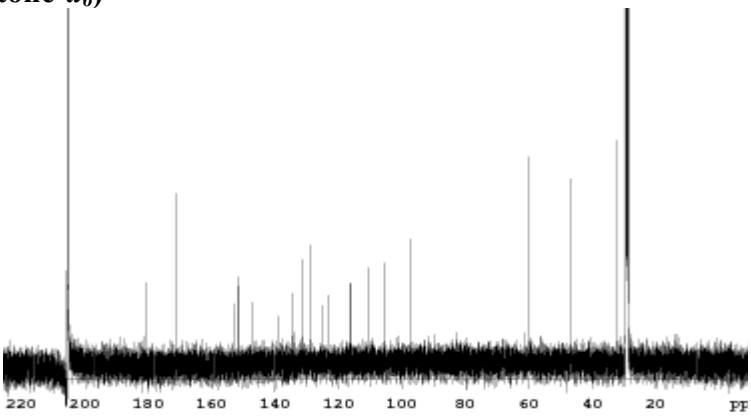

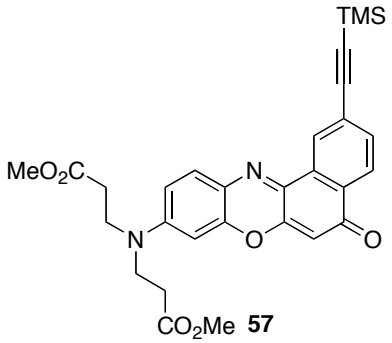

57

$Pd(PPh_3)_4$ (50.0 mg, 0.04mmol), CuI (8.2 mg, 0.04 mmol) was added to a solution of **51** (200mg, 0.4 mmol) in 5 mL of dry DMF. To the above mixture was added an excess of TMS alkyne (0.6 mL, 4.30 mmol) and triethyl amine (0.6 mL, 4.3 mmol). Reaction mixture was freeze-pump-thawed three times with nitrogen after cooling to -78 ^{o}C in an

acetone/dry ice bath. The acetone/dry ice bath was removed and the temperature was allowed to rise to 25 ^{o}C and then heated to 80 ^{o}C for 24 h. Filtered through a sintered glass funnel and organic layer evaporated under reduced pressure. Purified by flash chromatography using 30% EtOAc/hexanes to obtain **57** (125 mg, 73%) as a red solid. R_f = 0.6 (30 % EtOAc/hexanes) **^{1}H NMR** (300 MHz, acetone-d_6) δ 8.62 (s, 1H), 8.14 (d, 1H, J = 8.1 Hz), 7.72 (d, 1H, 6.3 Hz), 7.66 (d, 1H, J = 8.1 Hz), 6.90 (d, 1H, J = 6.3 Hz), 6.70 (s, 1H), 6.22 (s, 1H), 3.89 (t, 4 H, J = 7.5 Hz), 3.62 (s, 6H), 2.77 (t, 4H, J = 6.9 Hz), 0.31 (s, 9H). **^{13}C NMR** (75 MHz, acetone –d_6) δ 181.7, 171.9, 152.4, 151.2, 146.9, 139.7, 132.9, 131.4, 127.1, 126.2, 125.9, 125.3, 110.7, 105.6, 104.3, 100.1, 97.39, 51.3, 47.0, 31.8, 0.7. (2C missing). **MS (ESI)** m/z 530.14 (M^+).

^{1}H NMR (acetone-d_6)

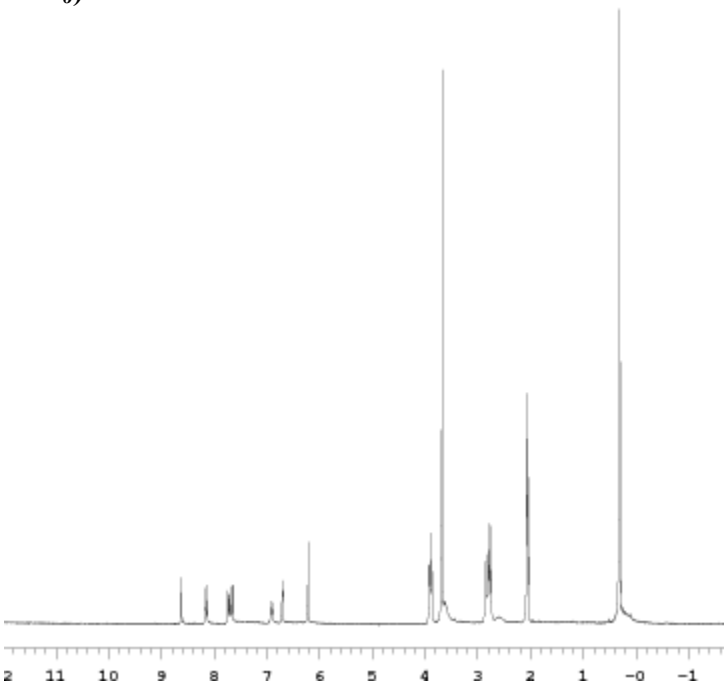

^{13}C NMR (acetone-d_6)

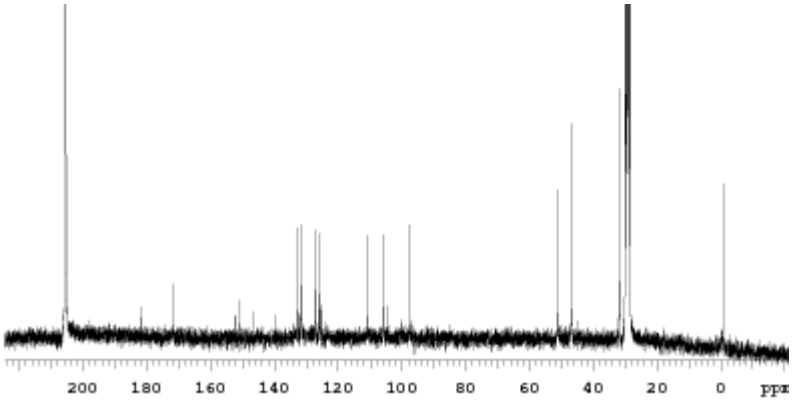

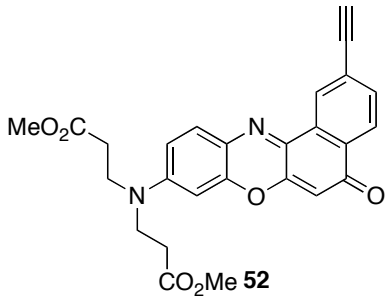

52

TBAF (1.0 M solution in THF, 0.6 mL, 0.6 mmol) was added to a solution of **57** (100 mg, 0.17 mmol) in 10 mL of dry distilled THF at -78 ^{o}C. The reaction mixture was allowed to warm to 25 ^{o}C for 30 min. The reaction mixture was diluted with EtOAc and excess TBAF was removed by washing with water (2 x 10.0 mL) and organic layer evaporated under reduced pressure. The residue was purified by flash chromatography using 1/1 EtOAc/hexanes to yield **52** (63 mg, 80%) as a red solid. R_f = 0.4 (1/1 EtOAc/hexanes) **^{1}H NMR** (300 MHz, $CD_3OD/CDCl_3$) δ 8.80 (s, 1H), 8.22 (d, 1H, 8.0 Hz), 7.72 (d, 1H, J = 8.0 Hz), 7.68 (br, 1H), 6.83 (d, 1H, J = 6.5 Hz), 6.60 (s, 1H), 6.49 (s, 1H), 3.71 (s, 6H), 3.60 (t, 4H, J = 6.5 Hz), 3.53 (s, 1H), 2.72 (t, 4H, J = 6.5 Hz). **^{13}C NMR** (75 MHz, DMSO–d_6) δ 181.8, 172.4, 153.8, 152.8, 147.5, 137.85, 133.2, 132.4, 131.8, 131.4, 127.2, 126.3(2C), 125.6, 125.4(2C), 105.4, 84.2, 83.4, 52.2, 39.1, 34.8; **MS (ESI)** m/z 459.15 $(M+H)^+$.

^{1}H NMR ($CD_3OD/CDCl_3$)

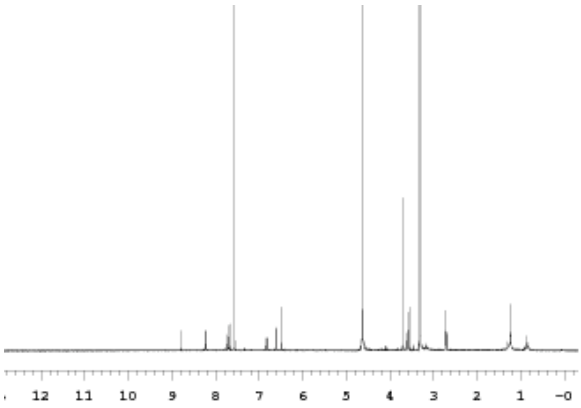

^{13}C NMR (DMSO-d_6)

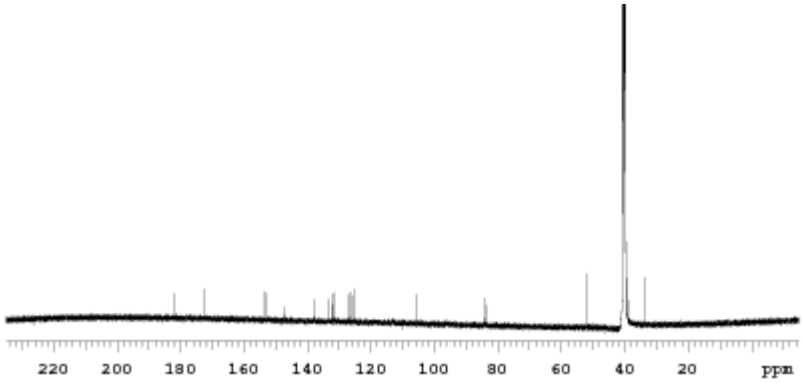

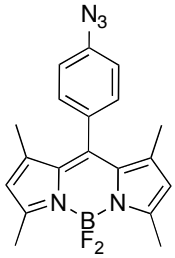

48

Nitro BODIPY **54** (*provided by Mrs. Lingling Li*,100.0 mg, 0.27 mmol) and hydrazine (0.2 mL) along with 10 % Pd/C (38.0 mg, 0.36 mmol) were dissolved in EtOH (4 mL) and refluxed for 30 min. The reaction mixture was cooled to 25 ^{o}C and filtered through celite to remove Pd/C and any solid impuritues. The filtrate obtained was then

evaporated under reduced pressure and purified by flash column chromatography using 1/1 EtOAc/hexanes as eluent. The yellowish orange solid (54.0 mg) obtained was dissolved in 1/1 HCl (1.0 M)/MeOH (3 mL) and cooled to 0 ^{o}C for 10 min. Sodium nitrite (31.0 mg, 0.44 mmol) in H_2O (0.5 mL) was added drop wise in 5 min and stirred at 0 ^{o}C for 1 h. Sodium azide (57.0 mg, 0.88 mmol) in water (1 mL) was added and the reaction mixture stirred for further 1 h at 25 ^{o}C. The solvent was evaporated and crude product purified using flash chromatography eluting with 30 % EtOAc/hexanes to yield **48** as an yellowish orange solid (47.0 mg, 38 %) R_f = 0.6 (30 % EtOAc/hexanes). **^{1}H NMR** (500 MHz, $CDCl_3$) δ 7.25 (br, 2H), 7.15 (br, 2H), 5.98 (s, 2H), 2.56 (s, 6H), 1.41 (s, 6H); **^{13}C NMR** (125 MHz, $CDCl_3$) δ 155.7, 142.9, 141.0, 140.6, 131.5, 129.6, 121.4, 119.7, 119.6, 14.6; **MS (ESI)** m/z 372.18 $(M+ Li)^+$.

^{1}H NMR ($CDCl_3$)

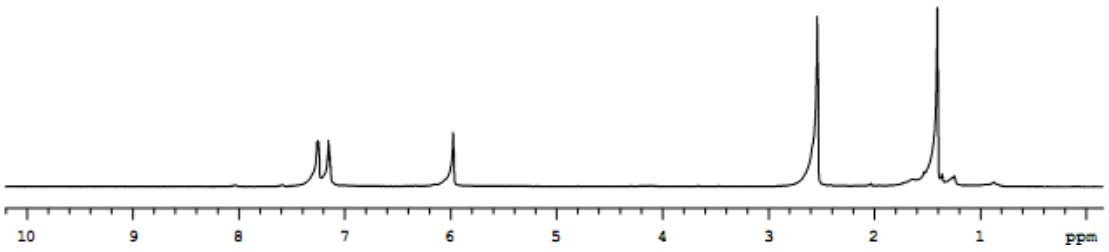

^{13}C NMR ($CDCl_3$)

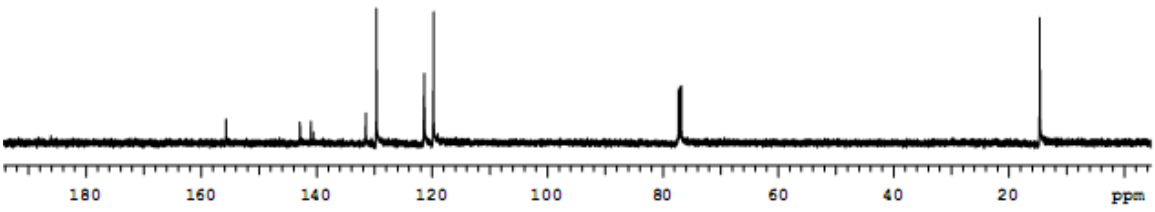

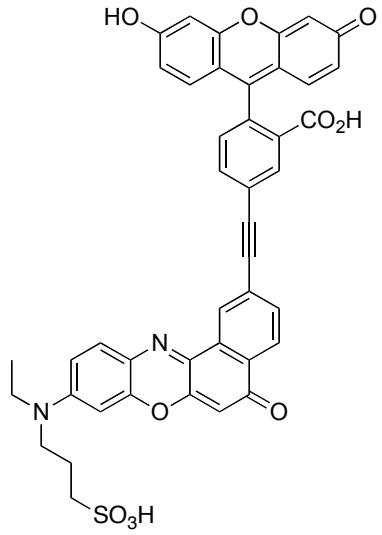

39

Compound **50** (40.0 mg, 0.08 mmol), **45** (38.0 mg, 0.12 mmol), $Pd(PPh_3)_4$ (8.0 mg, 0.008 mmol), copper(I)iodide (1.4 mg, 0.08 mmol) and triethylamine (0.10 mL, 0.8 mmol) were dissolved in 4 mL dry distilled DMF. The solution was freeze-pump-thawed three times with nitrogen after cooling to -78 ^{o}C in an acetone/dry ice bath. The acetone/dry ice bath was removed and the temperature was allowed to rise to 25 ^{o}C and then heated to 130 ^{o}C for 12 h. The solution was concentrated *in vacuo* and purified by flash chromatography eluting with 30% MeOH/EtOAc to afford **39 (**27.0 mg, 49%) as a red solid. R_f = 0.2 (1/1 EtOAc/hexanes). **^{1}H NMR** (500 MHz, CD_3OD) δ 8.91 (s, 1H), 8.53 (d, 1H, *J* = 3.1 Hz), 8.22 (br, 2H), 7.89(s, 1H), 7.79-7.71 (br, 2H), 7.32 (t, 3H, *J* = 6.1 Hz), 7.09-7.01 (br, 2H), 6.71 (s, 1H), 6.63 (br, 3H, 6.4), 3.77-3.63 (br, 4H), 2.92 (q, 2H, *J* = 6.7 Hz), 2.19-2.096 (br, 2H), 1.32-1.29 (br, 3H); **^{13}C NMR** (125 MHz, CD_3OD) δ 179.8, 168.3, 161.7, 153.5, 153.3, 152.4, 152.2, 147.1, 137.8, 134.2, 133.9, 131.8, 131.7, 128.9, 128.1, 125.6, 125.5, 123.7, 122.6, 118.6, 118.4, 113.1, 111.8, 109.6, 108.4, 102.9, 98.7, 96.5, 96.4, 82.1, 80.2, 75.3, 49.4, 49.3, 45.4, 23.7, 10.8. **IR (neat, cm^{-1})** 3451, 2887, 2911, 1657; **MS (ESI)** m/z 764.99 $(M-H)^-$

^{1}H NMR (CD_3OD)

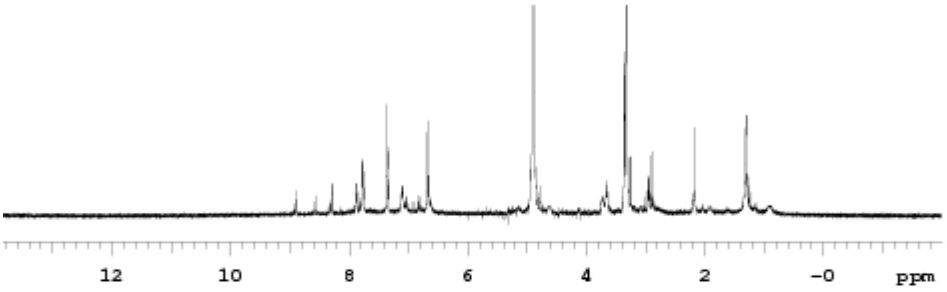

^{13}C NMR (CD_3OD)

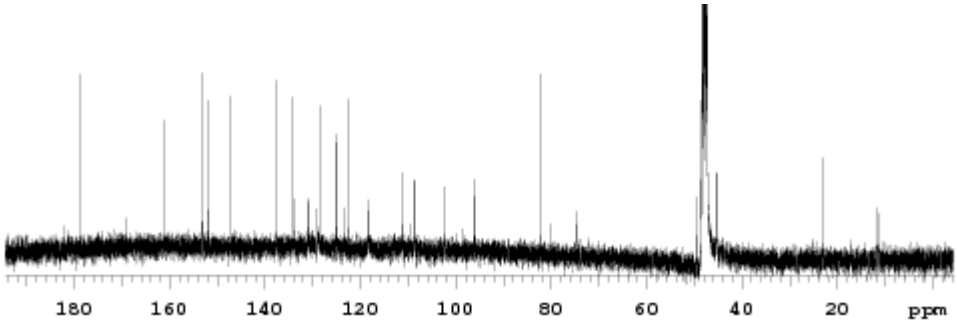

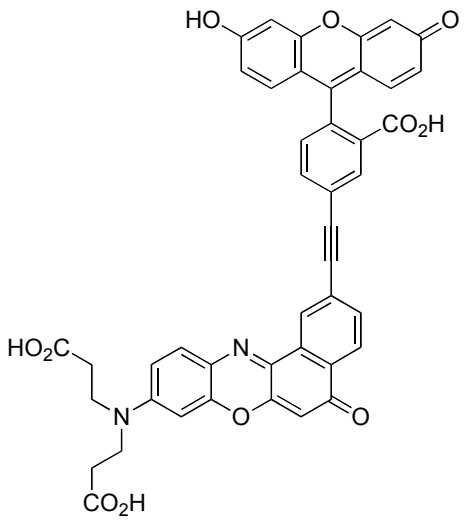

40

Compound **50 (**110.0 mg, 0.2 mmol), **45** (101.0 mg, 0.3 mmol), $Pd(PPh_3)_4$ (22.0 mg, 0.02 mmol), copper(I)iodide (3.6 mg, 0.02 mmol) and triethylamine (265.0 mg, 1.9 mmol) were dissolved in 10 mL dry distilled DMF. The solution was freeze-pump-

thawed three times with nitrogen after cooling to -78 ^{o}C in an acetone/dry ice bath. The acetone/dry ice bath was removed and the temperature was allowed to rise to 25 ^{o}C and then heated to 130 ^{o}C for 12 h. The solution was concentrated *in vacuo* and purified by flash chromatography eluting with 30% MeOH/EtOAc to afford 111.0 mg of red solid. R_f = 0.3 (1/1 EtOAc/hexanes).

Above Red solid (30 mg, 0.04 mmol) and potassium carbonate (66.7 mg, 0.48 mmol) was dissolved in MeOH/water (5 mL, 1/1) and heated to 40 ^{o}C for 12 h. The solution was filtered to remove solid impurities and concentrated *in vacuo*. The crude residue was dissolved in 5 mL water and washed with ethyl acetate (5 mL x 3) to remove any organic impurities. The pH of the aqueous layer was adjusted to 6 by careful drop wise addition of HCl (5 to 6 drops, 1.0 M). The aqueous layer was then extracted with 2/1 $CHCl_3$/*iso*-propanol (5 mL x 3). The organic extract was dried with magnesium sulfate and solvent evaporated. The residue obtained was further purified by reverse phase preparative HPLC (20-95 % CH_3CN/1 % TFA in H_2O) to afford the desired product **40** as dark blue solid (22.0 mg, 59 %). **^{1}H NMR** (500 MHz, DMSO-*d6*) δ 8.72(s, 1H), 8.24(s, 1H), 8.17(d, IH, *J* = 7.8 Hz), 8.01(d, 1H, *J* = 7.8 Hz), 7.90 (d, 1H, *J* = 8.9 Hz), 7.68(d, 1H, *J* = 8.9 Hz), 7.35 (d, 1H, *J* = 8.7 Hz), 6.88 (d, 1H, *J* = 8.8 Hz), 6.75 (s, 1H), 6.68 (m, 2H), 6.63 (m, 2H), 6.56 (m, 2H), 6.33 (s, 1H), 3.73 (m, 4H), 2.65 (t, 4H, *J* = 7.3 Hz). **^{13}C NMR** (125 MHz, DMSO-*d6*) δ 182.0, 172.4, 168.6, 160.3, 153.3, 152.8, 152.5, 151.4, 147.0,139.1, 133.3, 132.8, 132.4, 132.1, 131.7, 131.4, 129.9,129.4, 128.4, 127.6, 127.3, 126.5, 125.6, 125.4, 124.9, 124.4, 113.6, 111.5, 109.9, 105.7, 103.0, 97.9, 90.7, 47.0, 32.1. **IR (neat, cm^{-1})** 3424, 3061, 2931, 1641, 2887; **MS (ESI)** m/z 379.02 $(M-2H)^{2-}$ **MS (MALDI)** m/z 763.21 $(M+3H)^{+}$

^{1}H NMR (DMSO-*d6*)

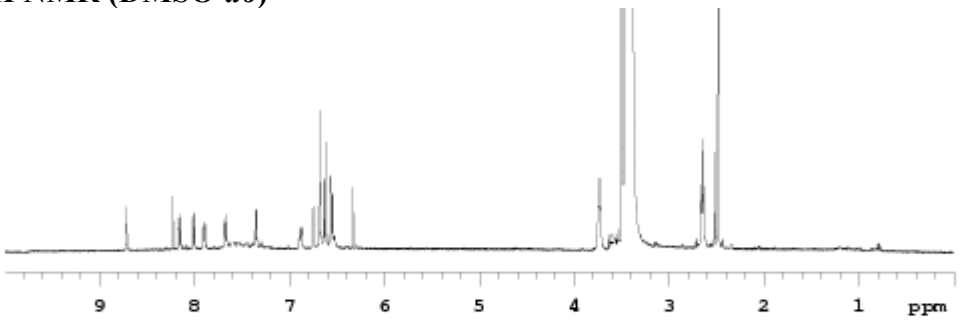

^{13}C NMR (DMSO-*d6*)

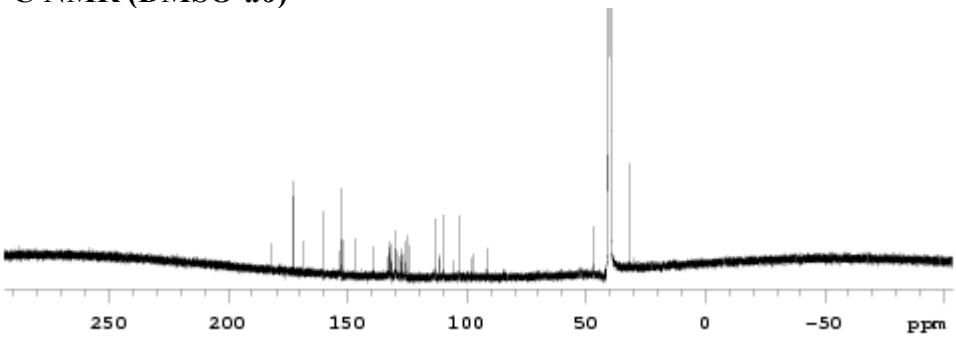

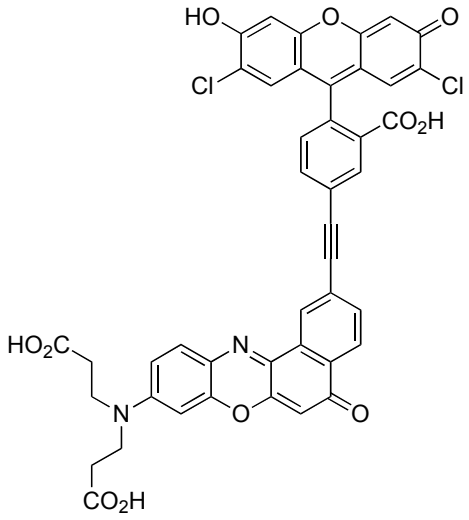

41

Compound **51** (50.0 mg, 0.09 mmol), **46** (50.0mg, 0.11 mmol), $Pd(PPh_3)_4$ (10.0 mg, 0.009 mmol), copper(I)iodide (2.0 mg, 0.009mmol) and triethylamine (0.12 mL, 1.9 mmol) were dissolved in 5 mL dry distilled DMF. The solution was freeze-pump-thawed three times with nitrogen after cooling to -78 ^{o}C in an acetone/dry ice bath. The

acetone/dry ice bath was removed and the temperature was allowed to rise to 25 ^{o}C and then heated to 130 ^{o}C for 12 h. The solution was concentrated *in vacuo* and purified by flash chromatography eluting with 30% MeOH/EtOAc to afford 21.0 mg of red solid. R_f = 0.3 (1/1 EtOAc/hexanes).

Above red solid (20.0 mg, 0.02 mmol) and potassium carbonate (19.0 mg, 0.14 mmol) was dissolved in MeOH/water (5 mL, 1/1) and heated to 40 ^{o}C for 12 h. The solution was filtered to remove solid impurities and concentrated *in vacuo*. The crude residue was dissolved in 5 mL water and washed with EtOAc (5 mL x 3) to remove any organic impurities. The pH of the aqueous layer was adjusted to 6 by careful drop wise addition of HCl (5 to 6 drops, 1.0 M). The aqueous layer was then extracted with 2/1 $CHCl_3$/*iso*-propanol (5 mL x 3). The organic extract was dried with magnesium sulfate and solvent evaporated. The residue obtained was further purified by reverse phase preparative HPLC (20-95% CH3CN/1 % TFA in H_2O) to afford **41** (9.0 mg, 12 %) as a dark blue solid. **^{1}H NMR** (500 MHz, DMSO-d_6) δ 11.17 (br, 2H), 8.74 (s, 1H), 8.24 (s, 1H), 8.18 (d,1H, J = 8.6 Hz), 8.05 (d, 1H, J = 8.1 Hz), 7.91 (d,1H, J = 8.1 Hz), 7.70 (br, 1H), 7.43 (br, 2H), 6.91 (br, 2H), 6.81 (br, 2H), 6.75 (s, 1H), 6.35 (s, 1H), 3.73 (br, 4H), 2.57 (t, 4H, J = 7.1 Hz). **^{13}C NMR** (125 MHz, DMSO-d_6) δ 181.7, 173.3, 167.9, 155.7, 152.6, 152.0, 151.3, 150.5, 146.8, 139.1, 138.7, 132.9, 132.3, 132.1, 131.6, 131.5, 131.2, 128.9, 127.3, 127.0, 126.2, 125.2, 125.1, 124.5, 116.8, 111.3, 110.4, 105.9, 104.1, 97.3, 90.9, 90.8, 82.3, 47.1, 32.3; **IR (neat, cm^{-1})** 3416, 3023, 2897, 1703; **MS (ESI)** m/z 415.06 $(M+2H)^{2+}$ **MS (MALDI)** m/z 830.18 $(M+2H)^{+}$

^{1}H NMR (DMSO-*d6*)

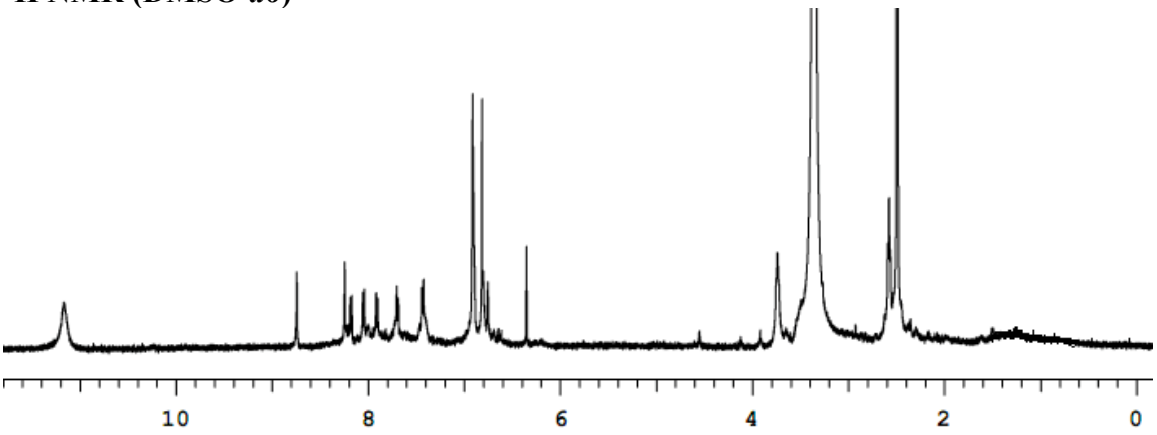

^{13}C NMR (DMSO-*d6*)

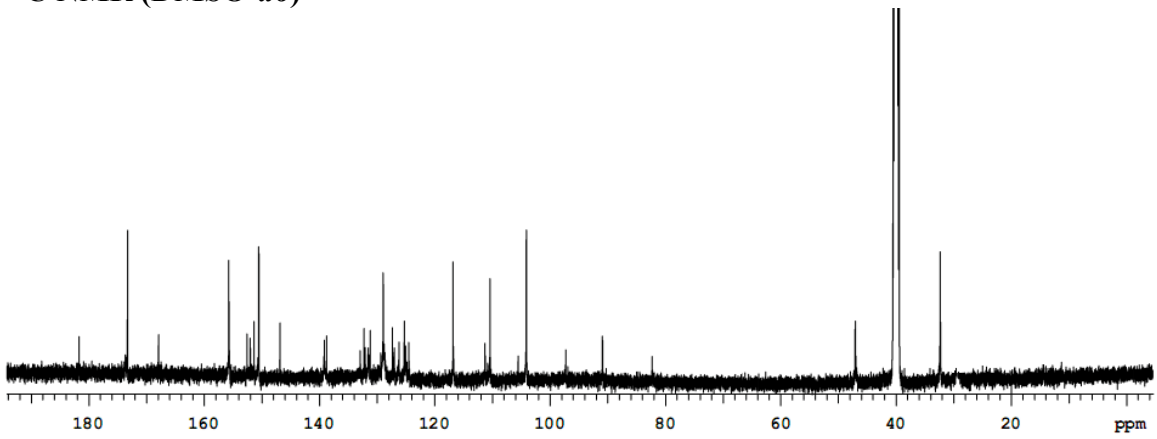

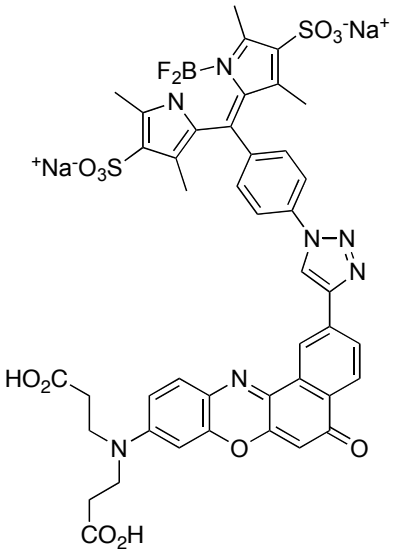

42

Compound **47** (42.0 mg, 0.07 mmol) and alkyne **52** (68.0 mg, 0.14 mmol) along with copper metal (5.0 mg, 0.07 mmol), $CuSO_4$ (0.1 mL, 0.1 M) and tris (1 - benzyl - 1H - 1,2,3 - triazol - 4 - yl) methyl amine (TBTA) (1.0 mg, 0.02 mmol) were taken in THF/H_2O mixture (5 mL, 4/1) and stirred at 25 ^oC for 24 h. The reaction mixture was filtered through celite to remove metallic copper. The filtrate obtained was evaporated under reduced pressure and columned on flash chromatography using CH_2Cl_2/MeOH as eluent. The red colored material obtained (60.0 mg) was dissolved in MeOH/H_2O (4 mL, 1/1) along with K_2CO_3 (33.0 mg, 0.24 mmol) and heated at 40 ^oC for 12 h. The solvent was evaporated and residue dissolved in water (2 mL) and washed with EtOAc (1 mL) three times to remove any organic impurities. The aqueous layer was purified on a reverse phase medium pressure liquid chromatography (MPLC) C-18 column using CH_3CN/H_2O (1/1) as eluent. The solvent was evaporated and dried under vacuum overnight to obtain product **42** as a dark purple colored material (27 mg, 39 %); **^{1}H NMR** (500 MHz, DMSO-d_6) δ 9.83 (s, 1H), 9.18 (s, 1H), 8.26 (br, 4H), 7.75 (d, 1H, J = 8.2 Hz), 7.68 (d, 2H, J = 9.7 Hz), 6.91 (d, 1H, J = 7.3 Hz), 6.78 (br, 1H), 6.34 (s, 1H), 3.74 (br, 4H), 2.65 (s, 6H), 2.53 (br, 4H), 1.61 (s, 6H); **^{13}C NMR** (125 MHz, DMSO-d_6) δ 182.8, 172.4, 166.9, 155.1, 152.5, 151.0, 147.1, 146.7, 142.6, 140.0, 138.3, 137.5, 135.2, 133.6, 132.7, 131. 4, 131.1, 130.3, 130.0, 126.6, 125.2, 121.7, 121.2, 120.4,

111.1, 105.4, 97.4, 47.2, 31.9, 14.2, 13.2 (1 carbon missing); **MS (ESI)** m/z 475.24 $(M-2H)^{2-}$.

^{1}H NMR (DMSO-*d*$_6$)

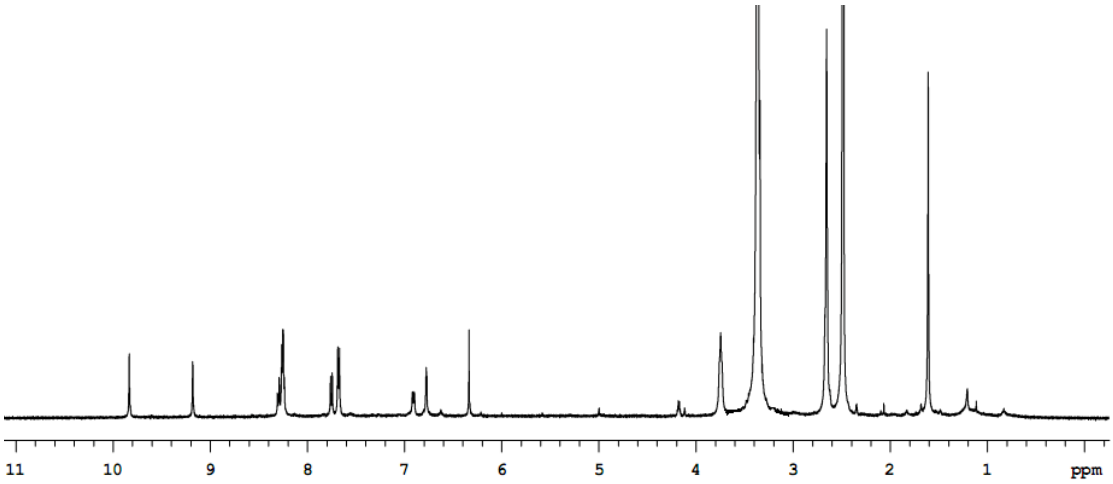

^{13}C NMR (DMSO-*d6*)

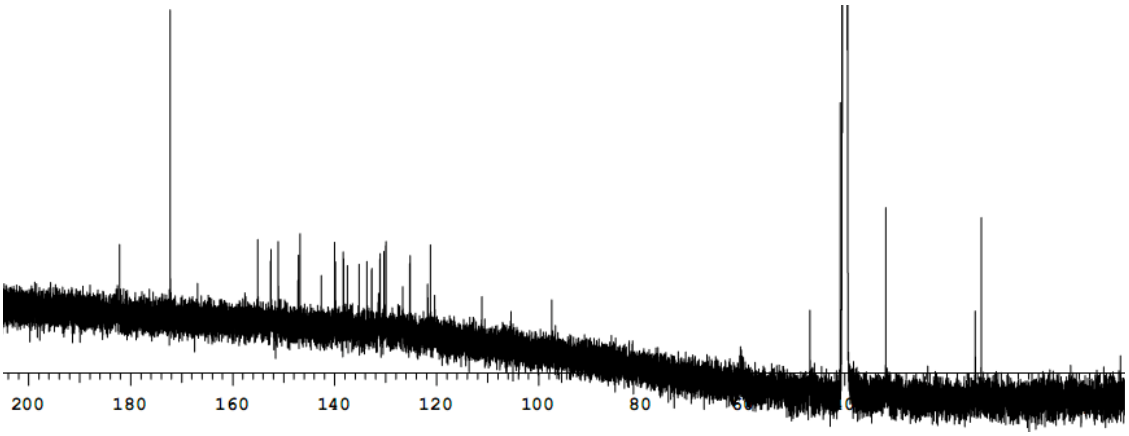

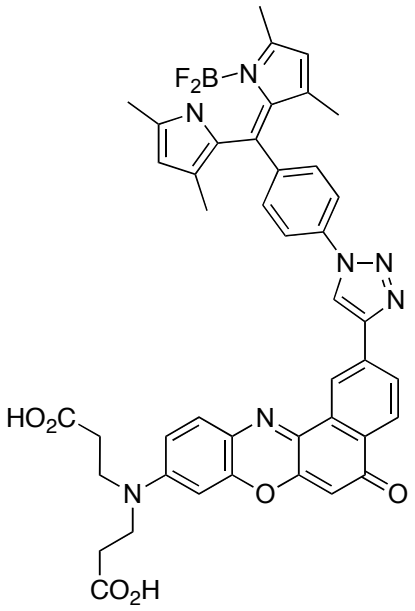

43

BODIPY azide **48** (35.0 mg, 0.1 mmol) and alkyne **52** (65.0 mg, 0.14 mmol) along with copper metal (6.0 mg, 0.1 mmol), $CuSO_4$ (0.1 mL, 0.1 M) and tris (1 - benzyl - 1H - 1,2,3 - triazol - 4 - yl) methyl amine (TBTA) (1.0 mg, 0.02 mmol) were taken in THF/H_2O mixture (5 mL, 4/1) and stirred at 25 ^oC for 24 h. The reaction mixture was filtered through celite to remove metallic copper. The filtrate obtained was evaporated under reduced pressure and residue obtained dissolved in CH_2Cl_2 (5 mL) and washed with water (2 mL) three times and organic layer dried over sodium sulfate. The solvent was evaporated and flash chromatography performed on silica gel with EtOAc/hexanes (1/1) to obtain a red colored material after solvent evaporation under reduced pressure and drying. The red material (42.0 mg), and K_2CO_3 (28.0 mg, 0.2 mmol) were dissolved in MeOH/H_2O (4 mL, 1/1) and heated at 40 ^oC for 12 h. The blue solution obtained was evaporated under reduced pressure and residue purified by flash chromatography eluting with EtOAc/hexanes (1/1) and then with EtOAc/MeOH (4/1) to obtain a dark purple colored material which was further purified on a reverse phase medium pressure liquid chromatography (MPLC) C-18 column using CH_3CN/H_2O (7/3) as eluant. The solvent was evaporated and dried under vacuum overnight to obtain product **43** as a dark purple colored material (23 mg, 30 %) **^{1}H NMR** (500 MHz, $CDCl_3$) δ 9.15 (s, 1H), 8.59 (br,

1H), 8.38 (br, 1H), 8.25 (s, 1H), 8.08 (br, 2H), 7.69 (br, 1H), 7.56 (br, 2H), 6.72 (s, 1H), 6.51 (d, 1H, J = 4.7 Hz), 6.42 (d, 1H, J = 4.7 Hz), 6.02 (s, 2H), 3.81 (t, 4 H, J = 8.8 Hz), 2.71 (t, 4 H, J = 8.8 Hz), 2.58 (s, 6H), 1.48 (s, 6H); **^{13}C NMR** (125 MHz, $CDCl_3$) δ 183.1, 171.8, 156.2, 152.0, 150.0, 147.9, 146.6, 142.8, 141.0, 139.5, 137.4, 135.8, 133.0, 132.5, 131.5, 131.3, 131.2, 130.0, 127.5, 126.7, 125.6, 124.8, 121.6, 121.0, 118.7, 110.1, 106.3, 97.3, 47.1, 32.1, 14.8; **MS (ESI)** m/z $(M-H)^-$ 794.21.

^{1}H NMR ($CDCl_3$)

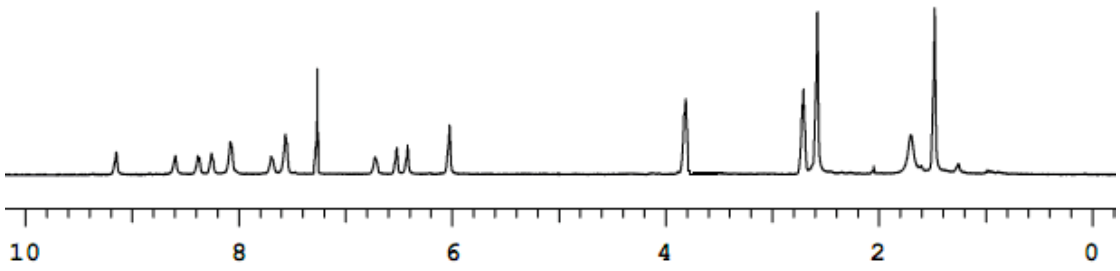

^{13}C NMR ($CDCl_3$)

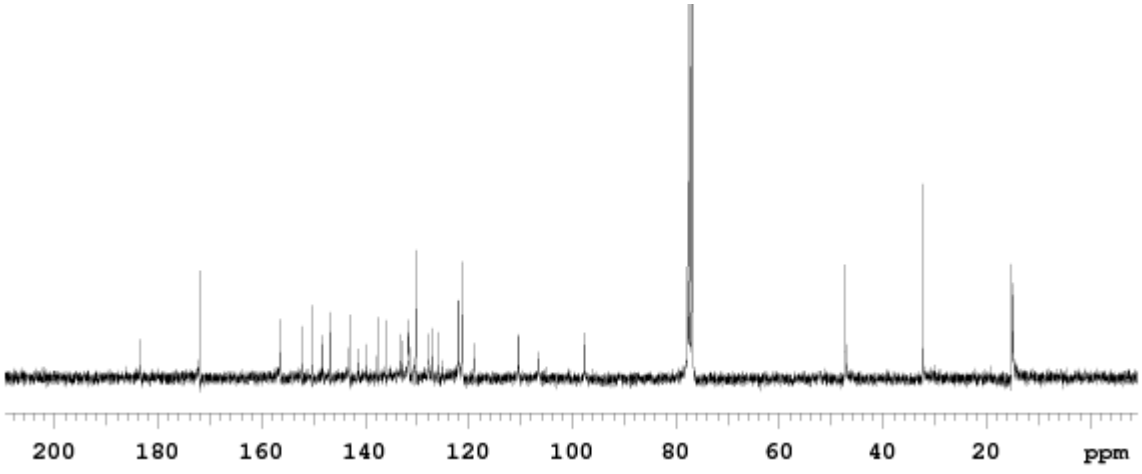

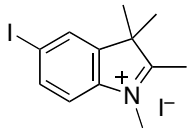

59

This compound was synthesized following a previously published procedure.[204] *para*-iodo-phenylhydrazine (2.0 g, 8.46 mmol) and *iso*-propylmethyl ketone (0.92 mL, 8.46 mmol) was dissolved in acetic acid (5 mL) and heated to 105 ^{o}C for 3 h. The reaction mixture was cooled to 25 ^{o}C and diluted with water (10 mL) and pH adjusted to 7 by adding solid $NaHCO_3$. The indole formed was then extracted with diethyl ether (10 mL) three times and organic layer dried with sodium sulfate followed by solvent evaporation to obtain a brown oil (2.37 g, 8.30 mmol). This oil was dissolved in methanol (10 mL) along with iodomethane (1.12 mL, 17.95 mmol) and heated at 110 ^{o}C in a sealed tube for 6 h. The reaction mixture was cooled to 25 ^{o}C and filtered and washed with methanol and dried to obtain the product **59** as a brown colored solid (1.37 g, 38 %).

^{1}H NMR (500 MHz, DMSO-d_6) δ 8.27 (s, 1H), 7.98 (d, 1H, J = 5.0 Hz), 7.70 (d, 1H, J = 5.0 Hz), 3.92 (s, 3H), 2.72 (s, 3H), 1.50 (s, 6H); **^{13}CNMR** (125MHz, DMSO-d_6) δ 196.8, 144.9, 142.6, 138.7, 132.9, 117.8, 96.8, 55.0, 35.5, 22.5, 15.3.

^{1}H NMR (DMSO-d_6)

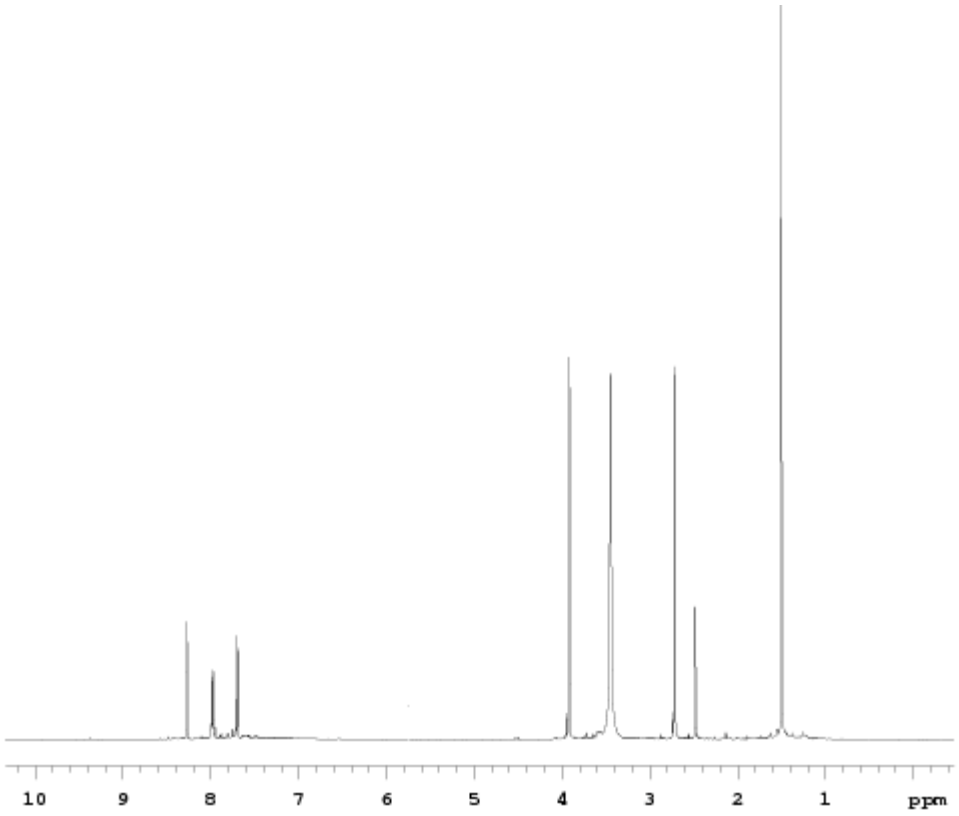

^{13}C NMR (DMSO-d_6)

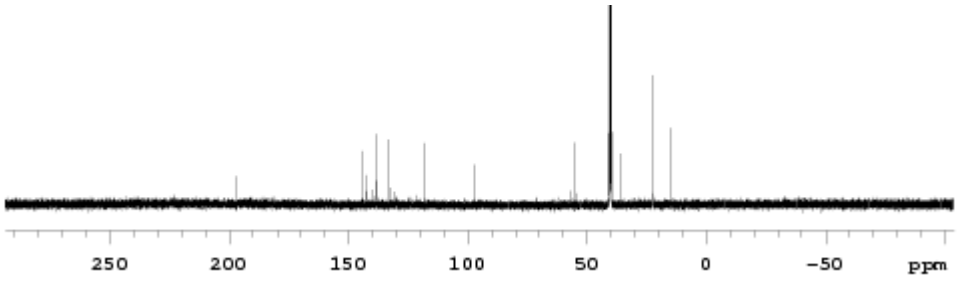

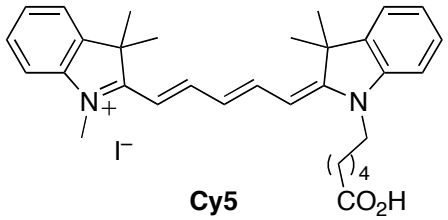

Cy5

This compound was synthesized following a previously published procedure.[205] A solution of indolinium bromide **58** (100 mg, 0.28 mmol) and *N*,*N*'-diphenylformamidine (88 mg, 0.34 mmol) in Ac_2O (1 mL) was heated at 120 ºC for 30 min. The reaction mixture was cooled to room temperature and a solution of indolinium iodide (119 mg, 0.34 mmol) in pyridine (1.5 mL) was added. The reaction mixture was stirred at 25 ºC for 30 min. Ether (100 mL) was added and dark red oil was obtained after the remove of ether. The residue was purified by flash chromatography eluting with 100 % EtOAc and 10 % to 15 % MeOH/CH_2Cl_2 to afford product **Cy5** as a dark purple solid (128 mg, 74 %). R_f 0.3 (10 % MeOH/CH_2Cl_2). **^{1}H NMR** (500 MHz, $CDCl_3$) δ 8.05 (t, 2H, J = 10.0 Hz) 7.39-7.34 (br, 4H), 7.24-7.21 (br, 2H), 7.15-7.12 (br, 2H), 6.94 (t, 1H, J = 10.0 Hz), 6.43 (d, 1H, J = 5.0 Hz), 6.36 (d, 1H, J = 5.0 Hz), 4.08 (m, 2H), 3.71 (s, 3H), 2.44 (t, 4H, J = 7.0 Hz), 1.84 (m, 2H), 1.74 (s, 6H), 1.72 (s, 6H), 1.57 (m, 2H); **^{13}CNMR** (125 MHz, $CDCl_3$) δ 173.8, 172.9, 172.2, 153.6, 153.5, 143.2, 142.2, 141.5 (2C), 141.2, 129.0, 126.9, 125.4, 122.5, 122.4, 110.7, 110.6, 104.6, 104.0, 49.5, 49.4, 44.5, 34.3, 32.7, 28.4, 28.3, 27.2, 26.5, 24.6. (1 carbon overlapping)

^{1}H NMR ($CDCl_3$)

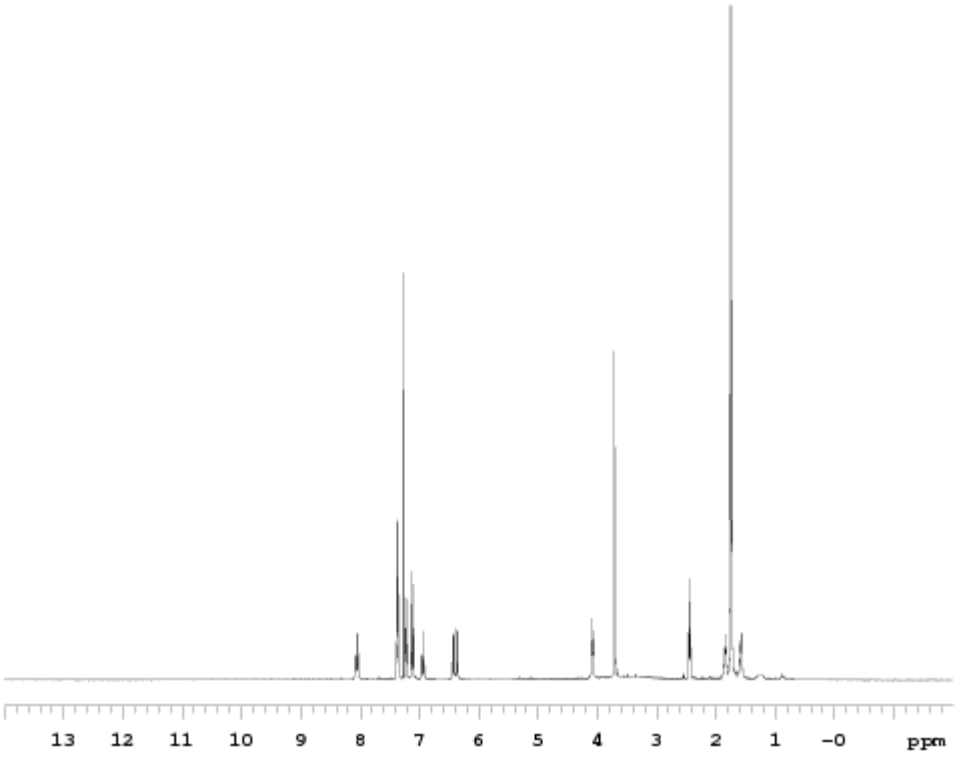

^{13}C NMR ($CDCl_3$)

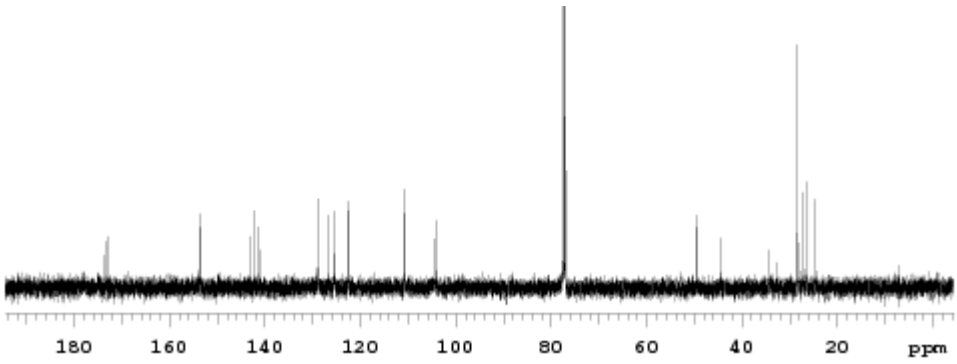

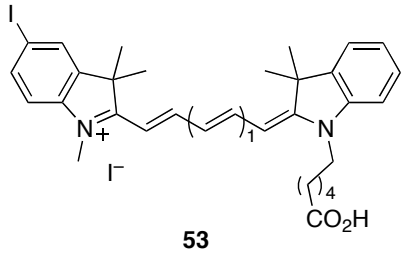

53

A solution of indolinium bromide **58** (150 mg, 0.43 mmol) and *N*,*N*'-diphenylformamidine (132 mg, 0.51 mmol) in Ac_2O (1.2 mL) was heated at 120 ºC for 30 min. The reaction mixture was cooled to 25 ^{o}C and a solution of indolium iodide **59** (254 mg, 0.59 mmol) in pyridine (1.2 mL) was added. The reaction mixture was stirred at 25 ºC for 30 min. Ether (25 mL) was added and the reaction mixture was filtered off to afford **53** as dark blue solid. The residue was purified by flash chromatography eluting with 100 % EtOAc and 5 % to 15 % MeOH/CH_2Cl_2 to afford product as a dark purple solid (203 mg, 65 %). R_f = 0.4 (10 % MeOH/CH_2Cl_2). **^{1}H NMR** (500 MHz, $CDCl_3$) δ 8.09 (t, 1H, *J* = 10.0 Hz), 8.02 (t, 1H, *J* = 10.0 Hz), 7.63 (dd, 1H, *J* = 5.0 Hz, *J* = 1.0 Hz), 7.57 (d, 1H, *J* = 1.0 Hz), 7.40-7.35 (m, 2H), 7.24-7.19 (m, 2H), 6.95 (t, 1H, *J* = 5.0 Hz), 6.88 (d, 1H, *J* = 5.0 Hz), 6.48 (d, 1H, *J* = 7.5 Hz), 6.29 (d, 1H, *J* = 7.5 Hz), 4.14 (m, 2H), 3.62 (s, 3H), 2.40 (m, 2H), 1.79-1.74 (m, 4H), 1.74 (s, 6H), 1.72 (s, 6H), 1.57 (m, 2H); **^{13}CNMR** (125MHz,$CDCl_3$) δ 174.2, 171.4, 154.5, 153.0, 152.9, 143.2, 143.0, 142.0, 141.7, 137.9, 131.4, 129.1, 127.3, 125.7, 122.6, 112.4, 111.6, 105.3, 103.8, 87.9, 50.0, 49.1, 45.0, 34.8 (2C), 30.1, 28.3, 27.5, 26.7, 24.8. **MS** (ESI) m/z 609.15 $(M)^{+}$.

^{1}H NMR ($CDCl_3$)

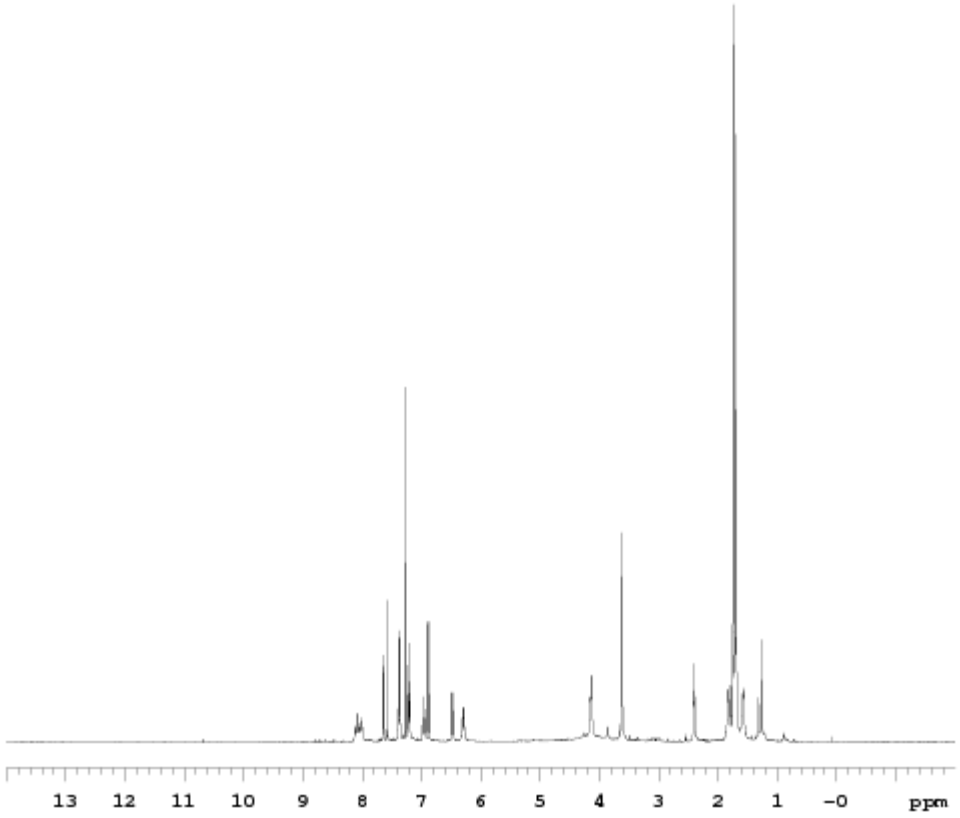

^{13}C NMR ($CDCl_3$)

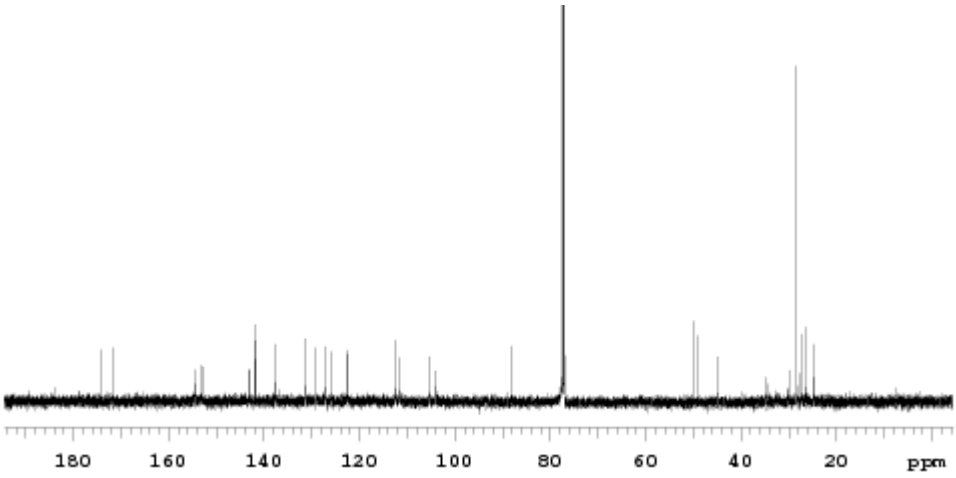

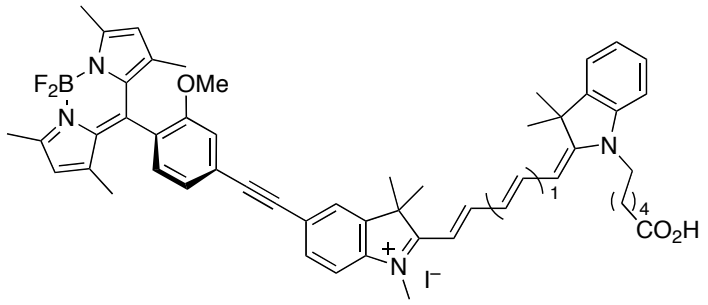

44

A solution of 5-iodo-Cy5 **53** (62 mg, 0.084 mmol), 4-ethynyl BODIPY **49** (54 mg, 0.14 mmol), $Pd(PPh_3)_4$ (20 mg, 0.020 mmol), CuI (3.0 mg, 0.020 mmol) in DMF (2 mL) was freeze-pump-thawed at –78 ºC (3 times). Et_3N (58 μL, 0.42 mmol) was added to a solution and the reaction mixture was stirred at 40 ºC for 1 h under nitrogen. Ether (60 mL) was added to a reaction mixture and reaction mixture was filtered off to afford product **44** as a dark purple solid. The residue was purified by flash chromatography eluting with 100 % EtOAc and 10 to 50 % MeOH/CH_2Cl_2 to afford product as a dark purple solid (21 mg, 26 %). R_f = 0.5 (10 % MeOH/CH_2Cl_2). **^{1}H NMR** (500 MHz, CD_3OD) δ 8.35-8.21 (m, 2H), 7.67 (s, 1H), 7.60 (d, 1H, *J* = 10.0 Hz), 7.55 (d, 1H, *J* = 5.0 Hz), 7.45 (t, 1H, *J* = 10.0 Hz), 7.39 (d, 1H, 5.0 Hz), 7.35-7.31 (m, 3H), 7.28 (d, 1H, *J* = 10.0 Hz), 7.20 (d, 1H, *J* = 5.0 Hz), 6.68 (t, 1H, *J* = 10.0 Hz), 6.42 (d, 1H, *J* = 15.0 Hz), 6.24 (d, 1H, *J* = 15.0 Hz), 6.07 (s, 2H), 4.22-4.17 (m, 2H), 3.87 (s, 3H), 3.60 (s, 3H), 2.49 (s, 6H), 2.37-2.33 (m, 2H), 1.88-1.83 (m, 2H), 1.75 (s, 6H), 1.73 (s, 6H), 1.66-1.63 (m, 2H), 1.54 (s, 6H), 1.39-1.34 (br, 2H); **^{13}CNMR** (125 MHz, CD_3OD) δ 176.1, 173.8, 172.3, 157.1, 156.2 (2C), 153.9, 142.3, 142.1, 138.9, 133.1, 133.0, 131.7, 131.5, 130.2, 128.9, 126.1, 125.8, 124.9, 124.7, 124.3, 124.1 (2C), 123.0, 121.9, 119.3, 114.2, 111.9, 110.8, 105.6, 104.3, 80.2, 79.7, 68.2, 65.7, 55.8, 49.7, 44.1, 39.2, 26.6, 26.4, 25.1, 24.9, 14.1; (1 carbon missing). **MS** (MALDI) m/z 859.29 $(M)^+$.

^{1}H NMR (CD_3OD)

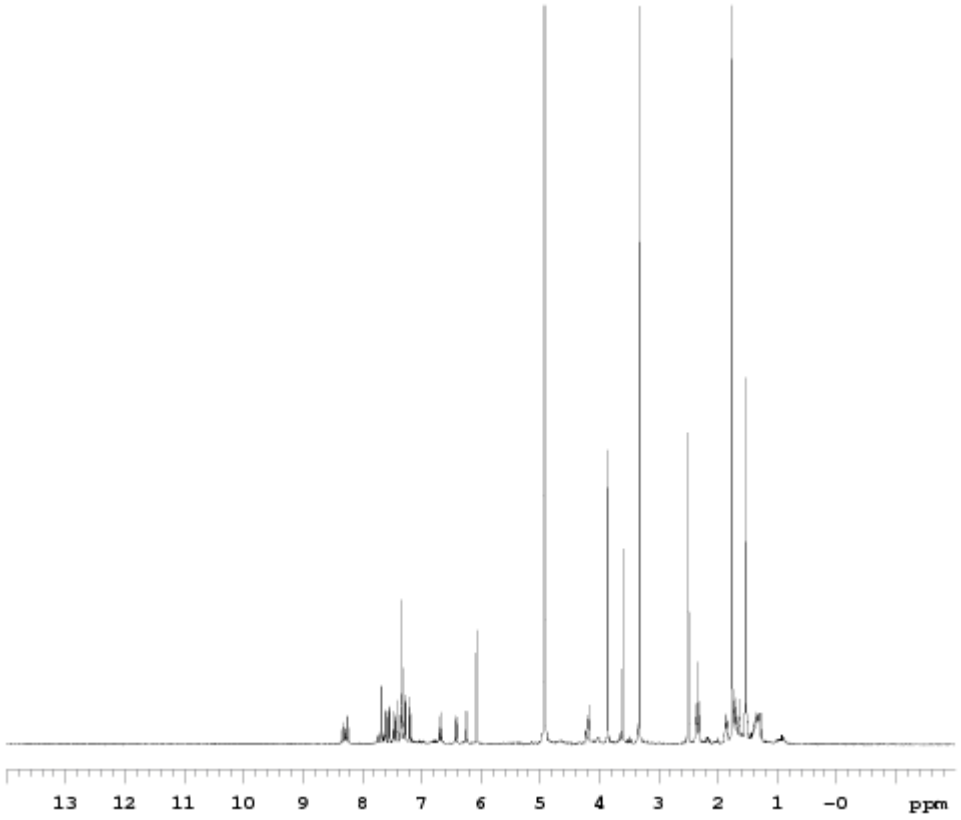

^{13}C NMR (CD_3OD)

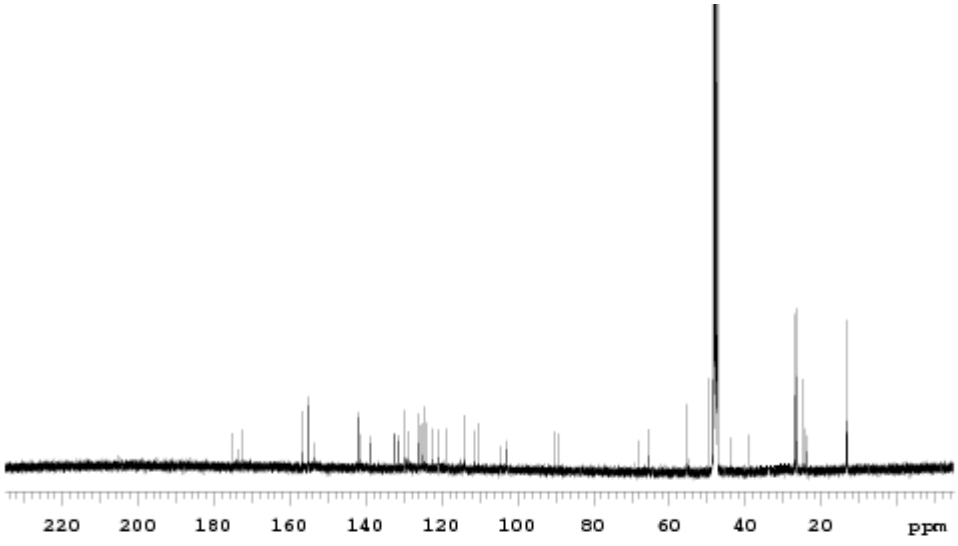

APPENDIX C

EXPERIMENTAL DATA FOR CHAPTER IV

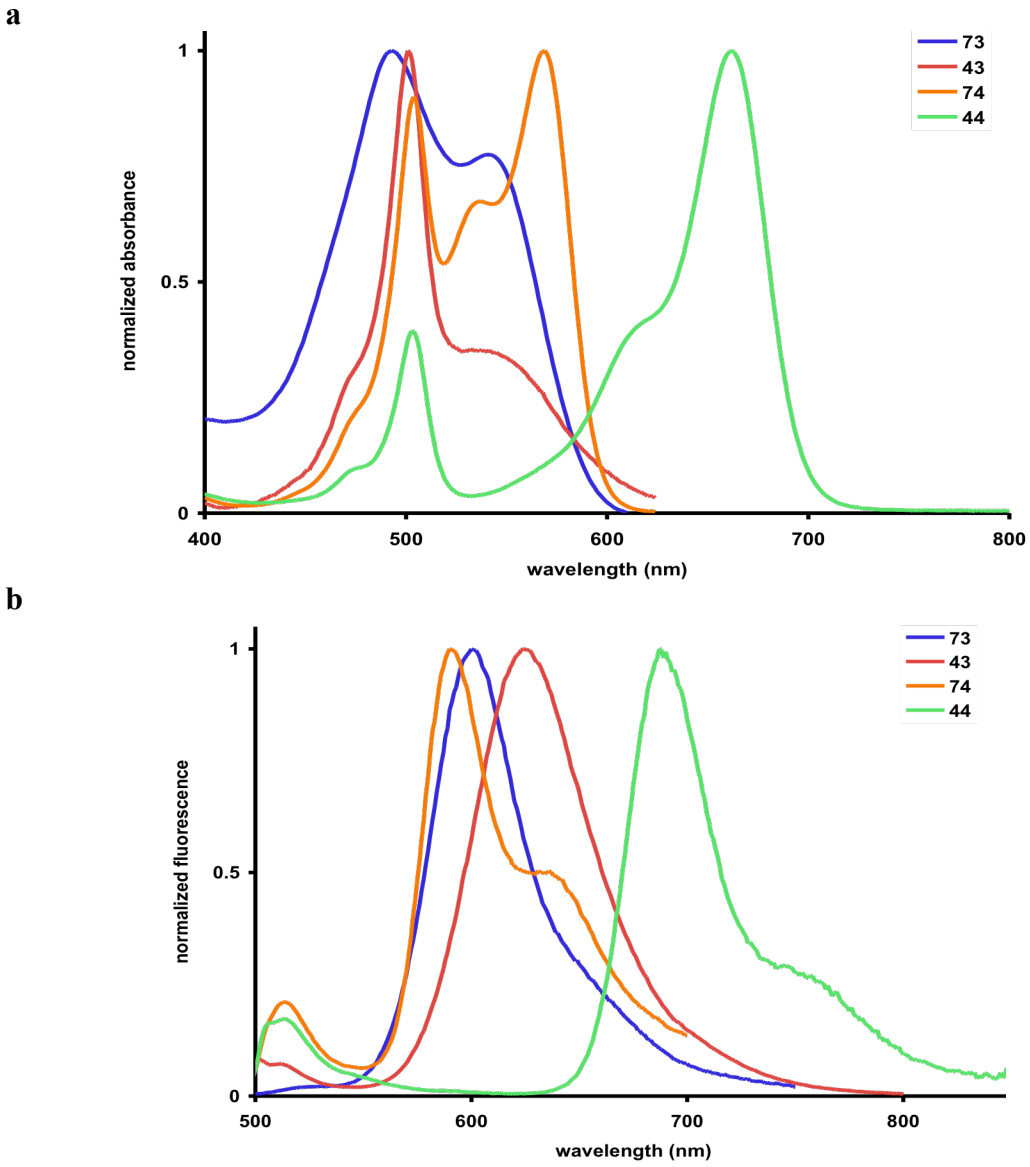

Figure C.1. Normalized absorbance (**a**) and fluorescence (**b**) spectra of cassettes in EtOH (at 10^{-6} and 10^{-7} M for absorbance and fluorescence measurements, respectively). All cassettes were excited at their corresponding donor absorption maxima.

Table C.1. Energy transfer efficiency of bare cassettes in EtOH.

dye	λ_{abs}(nm)	$\lambda_{em.}$(nm)	Φ_D[a]	Φ_A	ETE % (Φ_D/Φ_A)
73	498, 543	600	0.46+/-0.02	0.48+/-0.01[a]	96
43	502, 533	624	0.36+/-0.02	0.37+/-0.01[a]	97
74	504, 569	590	0.20+/-0.01	0.22+/-0.02[b]	90
44	504, 662	687	0.35+/-0.02	0.40+/-0.03[c]	87

Φ_D: quantum yield of cassette when excited at the donor absorption maxima. Φ_A: quantum yield of cassette when excited at the acceptor absorption maxima. Standards used for quantum yield measurement: [a]rhodamine 6G (Φ 0.92 in EtOH); [b]rhodamine 101 (Φ 1.0 in EtOH); [c]Nile Blue (Φ 0.27 in EtOH). Quantum yields were measured three times and averaged.

Table C.2. Energy transfer efficiency of cassettes encapsulated in silica in EtOH.

dye	λ_{abs}(nm)	$\lambda_{em.}$(nm)	Φ_D[a]	Φ_A	ETE % (Φ_D/Φ_A)
73	492,542	600	0.36+/-0.03	0.37+/-0.02[a]	97
43	501, 539	624	0.22+/-0.01	0.29+/-0.01[a]	76
74	504, 568	592	0.23+/-0.01	0.25+/-0.02[b]	92
44	504, 659	687	0.34+/-0.01	0.37+/-0.02[c]	92

Φ_D: quantum yield of cassette when excited at the donor absorption maxima. Φ_A: quantum yield of cassette when excited at the acceptor absorption maxima.Standards used for quantum yield measurement: [a]rhodamine 6G (Φ 0.92 in EtOH); [b]rhodamine 101 (Φ 1.0 in EtOH); [c]Nile Blue (Φ 0.27 in EtOH). Quantum yields were measured three times and averaged.

a

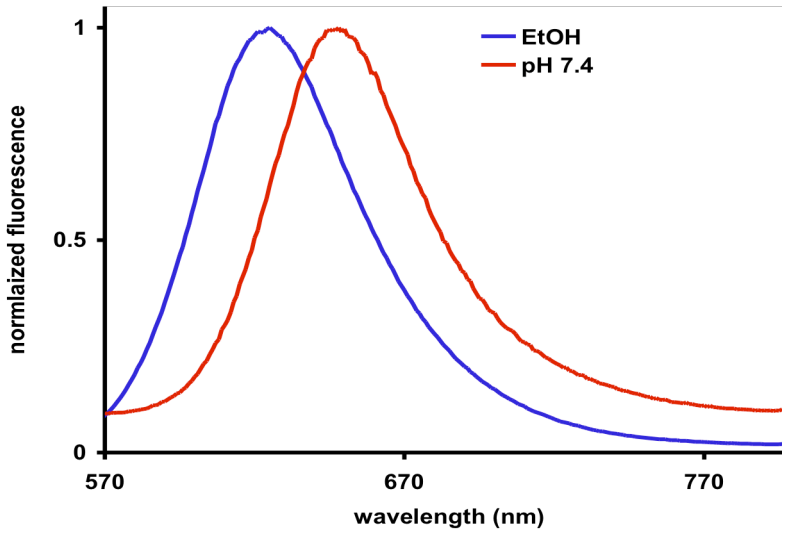

b

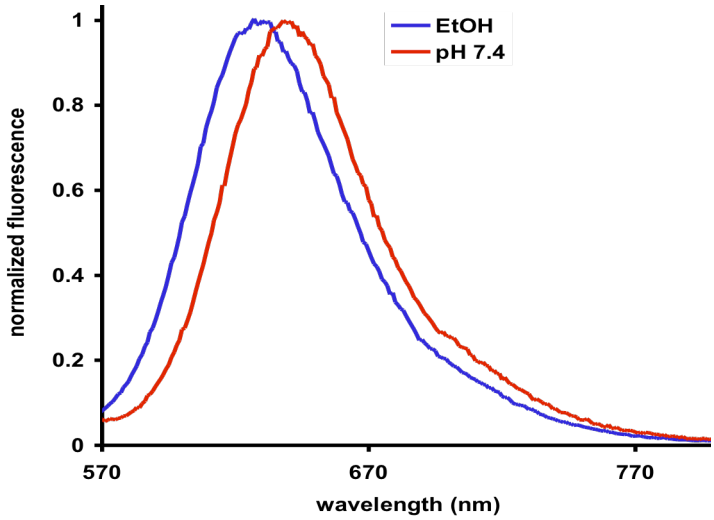

Figure C.2. Normalized fluorescence of acceptor **26** (**a**) and acceptor **26** (**b**) encapsulated in silica in different solvents. The solvent dependent change in emission is much reduced in acceptor encapsulated in silica. Fluorescence was measured after matching absorbance intensities for bare and encapsulated cassettes. (**c**) Comparison of solid state emission of acceptor **26** and acceptor **26** encapsulated in silica.

c

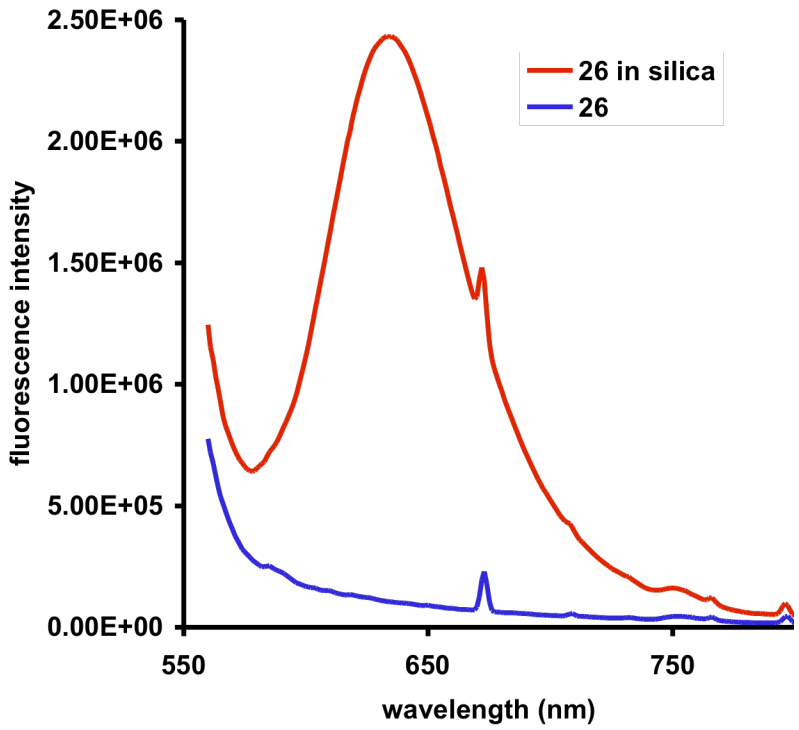

Figure C.2. Continued

Transmission electron microscopy (TEM)

Sample preparation and measurement: A few drops of silica nanoparticles in ethanol were placed on a TEM grid. The TEM grid is made of copper meshes and covered with a thin film of amorphous carbon. The grid is dried and mounted on a specimen holder and loaded on to the TEM. Measurements were made on a JEOL 2010 TEM instrument. The JEOL 2010 is fitted with a LaB_6 thermal emission gun and a Gatan Sc1000 ORIUS slow-scan charge-coupled device (CCD) camera (Model 832 with 4008x2672 pixels). Bright filed TEM images were obtained with JEOL 2010.

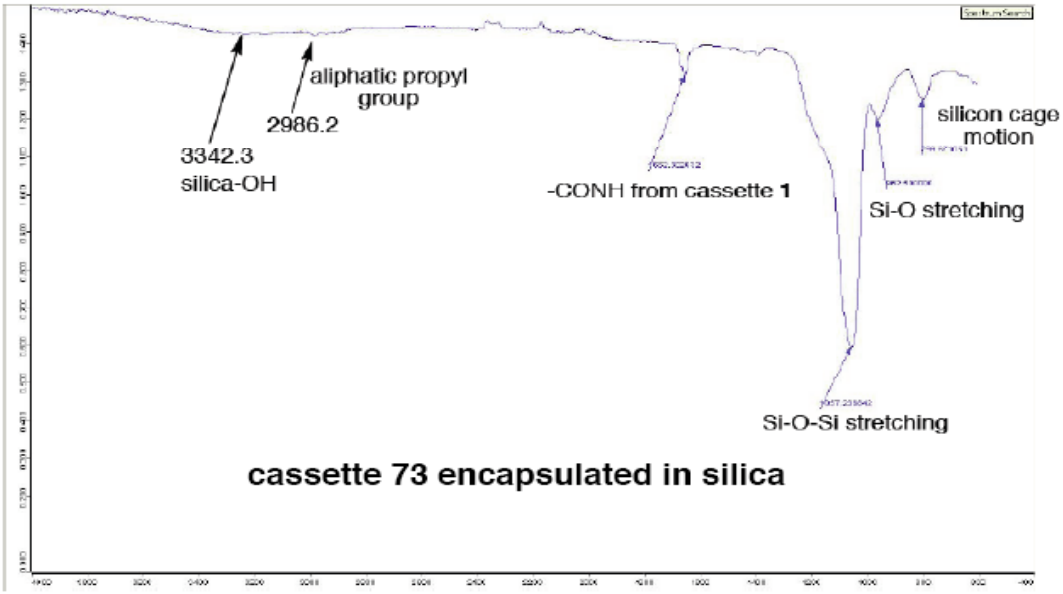

Figure C.3. FTIR spectra of cassette **73** doped silica nanoparticles.

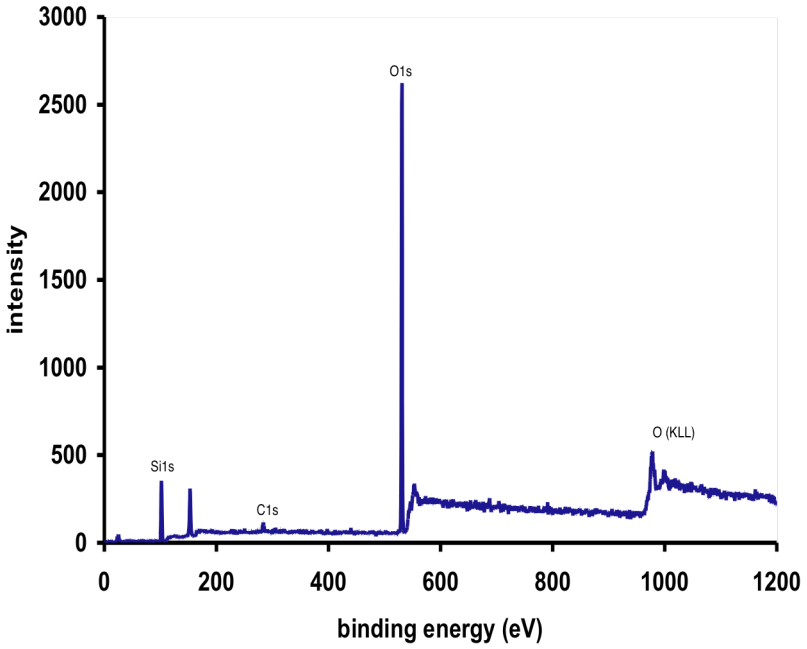

Figure C.4. X-ray photon electron spectroscopy (XPS) whole range spectrum of cassette **73** doped silica nanoparticles.

Photostability Measurement of Silica Nanoparticles

The photostability measurements of the silica nanoparticles were performed in the dry state. A few drops of silica nanoparticle suspension (1mg/mL) or dye in ethanol (concentration 10^{-6} M) were placed on a 2cm x 2cm glass slide and air dried. An argon ion laser (Spectra-Physics) fitted with a filter to select 488 nm wavelength light was used to perform the photostability studies. The 488 nm wavelength light with power density of 12W/cm^2 within fwhm of beam diameter was focused on the dried sample on the glass slide. A biconvex lens was used to concentrate the beam on the sample. The fluorescence output form the sample upon irradiation was collected using a microscope objective lens. The collected fluorescence output was passed through a filter to remove any stray light below 500 nm and to a collimator that was connected to a Peltier-cooled charged coupled device (CCD) spectrometer (Ocean Optics, QE65000).

In Vitro Cellular Imaging Studies

a Cell culture

COS-7 cells (American Type Culture Collection) were cultured as subconfluent monolayers on 75 cm^2 culture flask with vent caps in DMEM supplemented with 10 % fetal bovine serum (FBS) in a humidified incubator at 37 ºC with 5 % CO_2. Cells grown to subconfluence were enzymatically dissociated from the surface with trypsin and plated 2-3 days prior to the experiments in Lab-Tek two well chambered coverglass slides (Nunc).

b Fluorescence microscopy for cassette **1** doped silica nanoparticles (Figure 6a).

Uptake and subcellular localization of the silica nanoparticles were studied on living COS7 cells using a Bio-Rad 2000MP system (Bio-Rad Laboratories, Hercules, CA) equipped with a Nikon T300 inverted microscope with a 60x (NA1.2) water immersion objective lens and an Argon laser tuned to 488 nm wavelength. Images were collected using 488 nm excitation wavelength. Emission from the donor (GFP analog) was collected using a 560 DCLP XR dichroic mirror and a HQ 528/50 –nm emission filter whereas emission of the acceptor (BODIPY; FRET channel; acceptor signal) was

collected using a HQ 600/50-nm filter. COS7 cells were incubated for 2 hours at 37 ºC in ACAS with 0.02 mg/mL of doped nanoparticles (1 mg/mL stock solution in PBS 7.4). After the incubation period, the cells were washed with phosphate-buffered saline (PBS, pH 7.4) several times before imaging.

(c) Fluorescence microscopy for cassette **3** (Figure 6b) doped silica nanoparticles. Uptake and subcellular localization of the silica nanoparticles were studied on living COS7 cells using a Zeiss 510 META NLO Multiphoton Microscope System consisting of an Axiovert 200 MOT microscope. Digital images of BODIPY-Cy3 and Cy3 doped nanoparticles were captured with a 40x / 1.3 oil objective with the following filter sets: Excitation 488 nm and 543 nm for the cassette and Cy3 alone, respectively; Emission BP 500-530 for BODIPY; Emission BP 565-615 for Cy3. COS7 cells were incubated for 2 hours at 37 ºC in ACAS with 0.01 mg/mL of doped nanoparticles (solution in PBS). After the incubation period, the cells were washed with phosphate-buffered saline (PBS, pH 7.4) several times before imaging.

Synthesis of Calcium Phosphate Nanoparticles

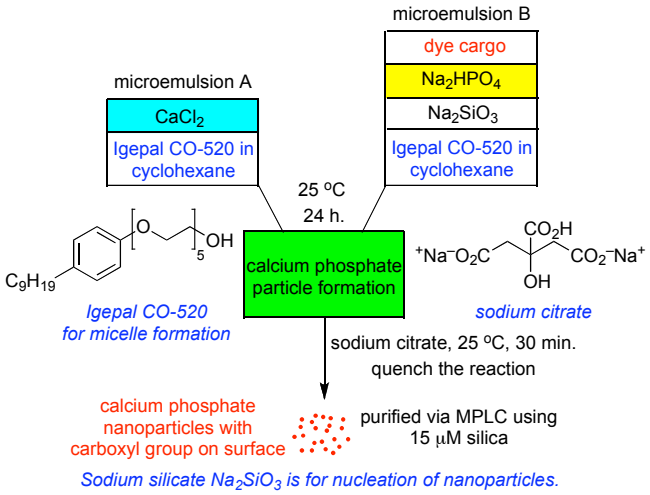

Figure C.5. Synthesis of calcium phosphate nanoparticles

Synthesis of calcium phosphate nanoparticles was based on a previously reported procedure from Adair *et al* (Figure C.5). Briefly two reverse microemulsions were

formed from Igepal CO-520 in cyclohexane and water. 650 μL of freshly prepared 10^{-2} M $CaCl_2$ was added to 14 mL of 29 vol % of Igepal CO-520 in cyclohexane under constant stirring to form microemulsion A. 650 μL of freshly prepared 6 x 10^{-3} M disodium phosphate and 65 μL 8.3 x 10^{-4} M of disodium silicate were added sequentially under constant stirring to 14 mL of 29 vol % of Igepal CO-520 in cyclohexane to form microemulsion B. The dye solution, 1mL of 10^{-3} M was added to microemulsion B. Both microemulsions were stirred at 25 ^{o}C for 1 h. Microemulsion A was added drop wise to microemulsion B in 10 min and the combined microemulsion C stirred at 25 ^{o}C for 24 h. The reaction was quenched by addition of 225 μL of 10^{-3} M sodium citrate at 25 ^{o}C and stirring for 30 min.

The micelles were broken by addition of 50 mL EtOH and purified via medium pressure liquid chromatography (MPLC) using silica microbeads (Stellar phases Inc., Langhorne, PA, dimension15 μm average diameter and 59 Angstrom pore size). EtOH was used as an eluent to remove any free dye and all reaction precursors. The polarity of the solvent was increased to 7/3 EtOH/H_2O to elute the calcium phosphate nanoparticles. A portion of the collected calcium phosphate nanoparticles were dialyzed against water in a Spectra/por molecular membrane tubing MWCO: 6000-8000, flat width: 50 mm and diameter: 32 mm (Spectrum LABS, Houston, TX) for 8 h and then for further 8 h against pH 7.4 (0.1 M sodium phosphate buffer).

APPENDIX D

SYNTHESIS OF CASSETTE WITH A SPACER

As mentioned in the introductory chapter unlike through space systems, through bond energy transfer cassettes benefits from both FRET as well as through-bond energy transfer (TBET). In order to make sure that through-bond energy transfer predominates in such systems, we attempted the synthesis of a cassette with a saturated linker to avoid through-bond energy transfer (Figure D.1). We intend to study the fluorescence emission of such a system and compare it to a similar through-bond energy transfer cassette.

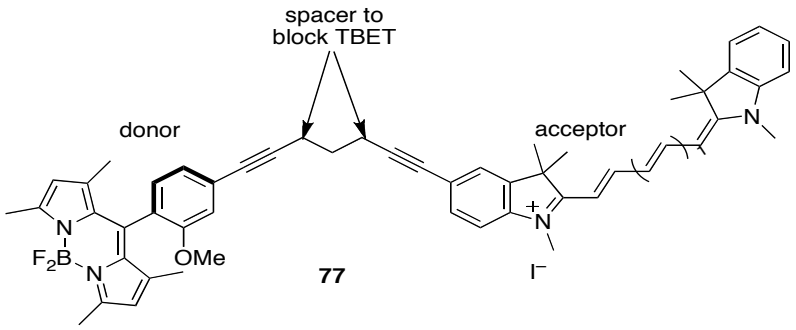

Figure D.1. Cassette with spacer to block TBET.

Synthesis of the above cassette is shown in scheme D.1. The donor fragment was constructed following palladium catalyzed cross coupling reaction of BODIPY **79** (from Dr. Yuichiro Ueno) and alkyne **78**, which was prepared by following a published procedure.[206] Deprotection of trimethylsilane using TBAF afforded the donor BODIPY **80** in 70 % yield. The acceptor fragment iodocyanine was prepared by condensation of indole at 120 ^{o}C in acetic anhydride with *N*,*N*'-diphenylformamidine and treatment of the intermediate with iodoindole in pyridine at 25 ^{o}C fro 30 min. Standard Sonogashira protocol[207] was followed to couple the donor and the acceptor fragment to obtain the cassette **77**. The yield of the reaction is low due to the instability of the acceptor cyanine

in DMF for prolonged period. Attempted reaction at 40 °C for 1 h resulted in complete decomposition of the acceptor fragment.

Scheme D.1. Synthesis of (**a**) donor fragment **80** (**b**) acceptor fragment **82** and (**c**) cassette **76** with spacer.

a

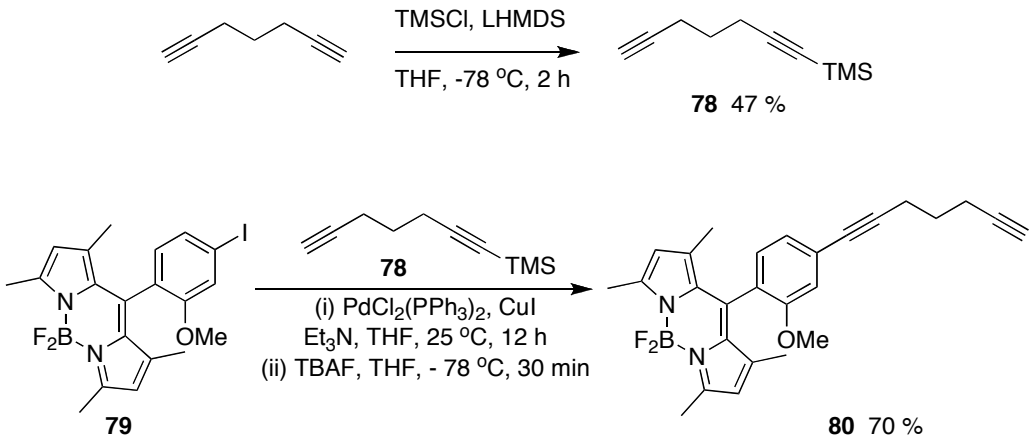

b

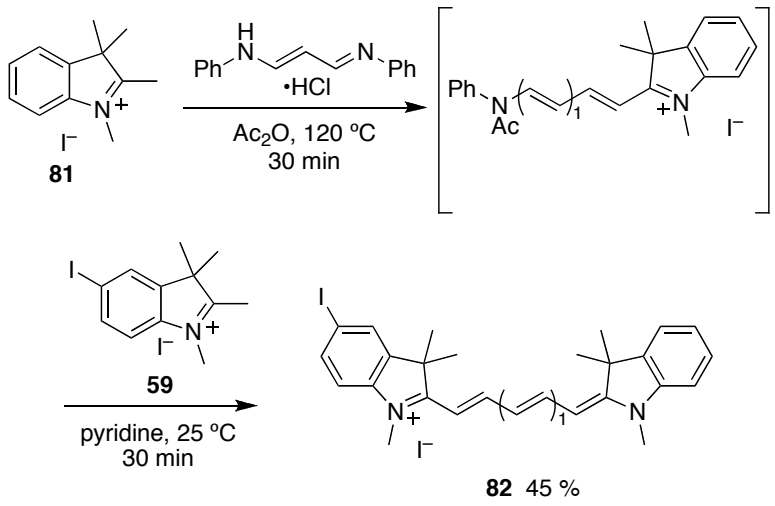

c

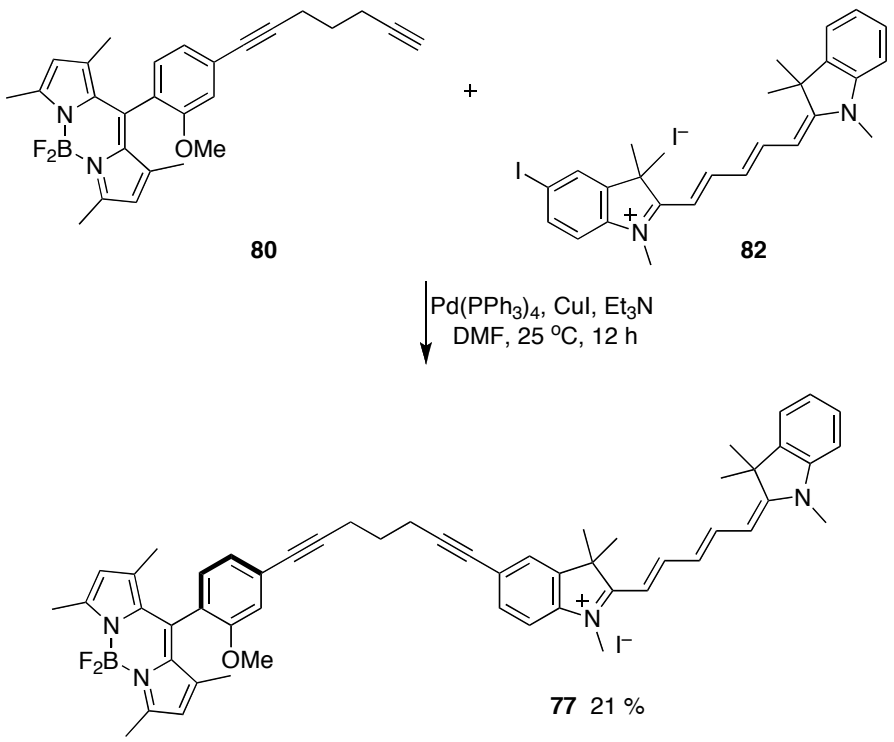

Photophysical properties of the cassette were measured in EtOH. The absorbance of the cassette with spacer is similar to absorbance of TBET cassette showing two distinct absorbtion corresponding to donor BODIPY and acceptor cyanine Cy5 (Figure D.2a). The fluorescence emission of the cassette with spacer was very different from the TBET system (Figure D.2b). When excited at the donor absorbance (504 nm), very little emission is seen from the acceptor fragment (688 nm) and a huge emission peak corresponding to donor fragment is also seen. This is exactly opposite to TBET cassette, which upon excitation at donor absorbance (504 nm) shows good energy transfer to the acceptor. In order to make sure that the emission seen in cassette with spacer is not arising from the acceptor itself, we excited the acceptor Cy5 alone at 504 nm and as expected it did not show any emission at 688 nm. This proves that the emission seen in cassette with spacer arises from only FRET. The TBET cassette on the other hand shows emission, which is a sum of both FRET and TBET. The superior emission observed in TBET systems is a great advantage in applications such as multiplexing wherein

excitation at a single wavelength is used to observe different fluorescently colored regions of the cell or any organelle.

a

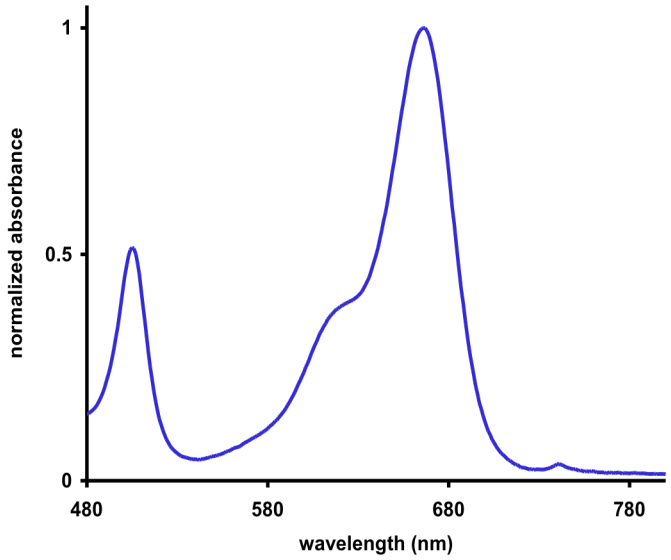

b

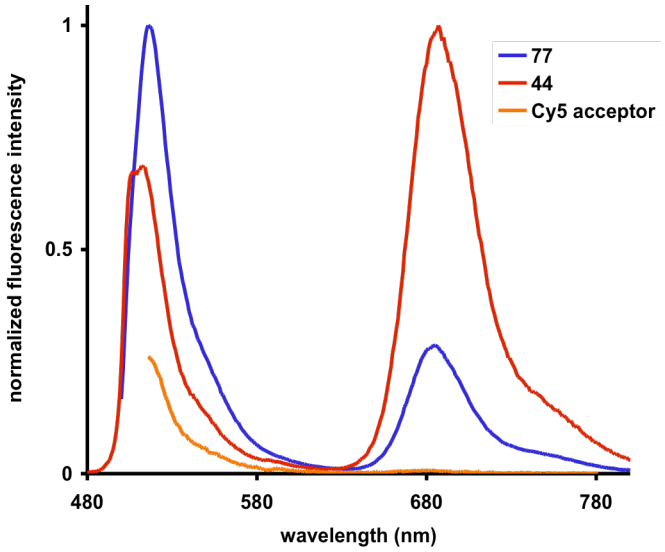

Figure D.2. (a) Normalized absorbance of cassette with spacer **77** in EtOH (concn: 10^{-6} M) (b) comparison of normalized fluorescence intensity of cassette with spacer **77** with TBET cassette **44** and **Cy5** acceptor in EtOH (concn: 10^{-7} M). All solutions excited at 504 nm.

APPENDIX E

EXPERIMENTAL FOR APPENDIX D

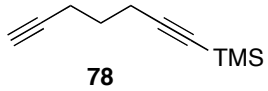

78

This compound was prepared following a reported procedure.[206] 1,6-heptadiyne (1 g, 10.9 mmol) in THF (20 mL) was cooled to -78 ^{o}C and LHMDS (1.0 M solution in THF, 12.0 mL, 13.0 mmol) added. The reaction mixture was stirred for 1 h at -78 ^{o}C and trimethyl silylchloride (1.65 mL, 13.0 mmol) added. The reaction mixture was further stirred at -78 ^{o}C for 2 h and saturated ammonium chloride solution (20 mL) was added to quench the reaction. The reaction mixture was extracted with CH_2Cl_2 (20 mL x 2), dried over anhydrous sodium sulfate and solvent evaporated at 25 ^{o}C. The semisolid obtained was purified by flash chromatography using EtOAc/hexanes 1/4 as eluent to afford **78** as a yellow semisolid (0.83 g, 47 %) after solvent evaporation and drying for 2 h. R_f = 0.4 (EtOAc/hexanes 1/4). **^{1}H NMR** (300 MHz, $CDCl_3$) δ 2.31 (m, 4H), 1.95 (t, 1H, J = 2.6 Hz), 1.72 (m, 2H), 0.13 (s, 9H); **^{13}C NMR** (125 MHz, $CDCl_3$) δ 105.9, 85.1, 83.4, 68.7, 27.4, 18.8, 17.4, 0.0.

^{1}H NMR ($CDCl_3$)

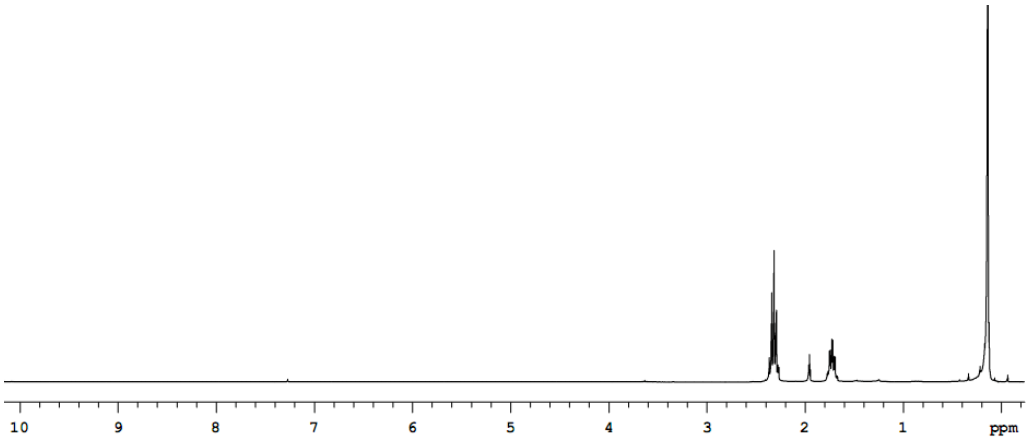

^{13}C NMR ($CDCl_3$)

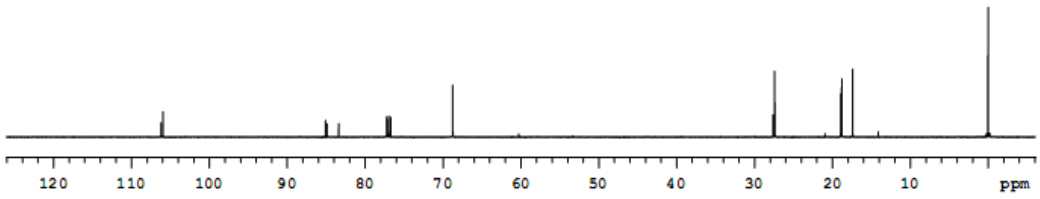

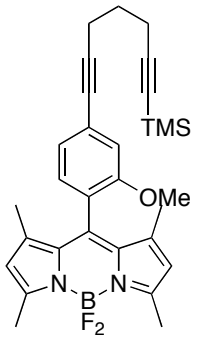

79a

BODIPY **79** (100 mg, 0.21 mmol) along with alkyne **78** (171 mg, 1.0 mmol), $PdCl_2(PPh_3)_2$ (15 mg, 0.02 mmol), copper iodide (4 mg, 0.02 mmol), and triethylamine (0.3 mL, 2.0 mmol) was dissolved in THF (4 mL) and stirred at 25 ^oC for 12 h. The reaction mixture was filtered through celite to remove solid impurities and filtrate obtained evaporated under reduced pressure. The residue obtained was purified via flash chromatography using EtOAc/hexanes 3/7 as eluent to afford **79a** as an orange solid (142 mg, 88 %) after solvent evaporation and drying. R_f = 0.6 (EtOAc/hexanes 3/7). **^{1}H NMR** (300 MHz, $CDCl_3$) δ 7.15 (d, 1H, J = 7.6 Hz), 7.07 (s, 1H), 7.03 (d, 1H, J = 7.6 Hz), 5.97 (s, 2H), 3.77 (s, 3H), 2.55 (s, 6H), 2.44 (t, 2H, J = 7.0 Hz), 1.86 (m, 4H), 1.46 (s, 6H), 0.17 (s, 6H); **^{13}C NMR** (125 MHz, $CDCl_3$) δ 165.1, 156.3, 155.2, 142.6, 131.5, 129.6, 126.2, 125.0, 123.8, 121.0, 114.3, 106.3, 90.6, 85.5, 80.8, 55.8, 27.8, 19.3, 18.7, 14.2, 0.3**; MS (ESI)** m/z 517.26 $(M+H)^+$.

^{1}H NMR ($CDCl_3$)

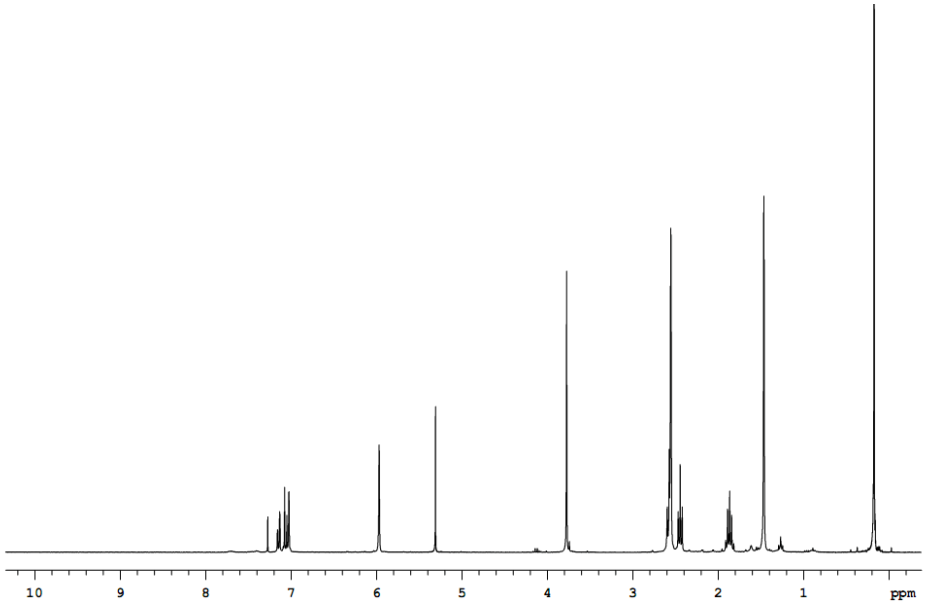

^{13}C NMR ($CDCl_3$)

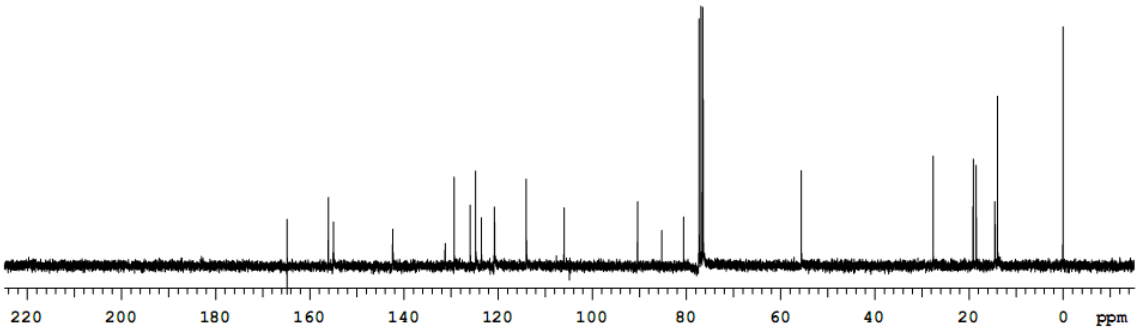

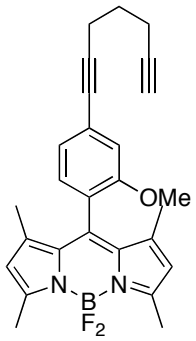

80

BODIPY **79a** (150 mg, 0.29 mmol) was dissolved in THF (4 mL) and cooled to -78 ^{o}C. TBAF (0.3 mL, 0.3 mmol) was added to the above solution and stirred at -78 ^{o}C for 30 min. The reaction was quenched by addition of deionized water (10 mL) and organic

layer extracted with CH_2Cl_2 (5 mL x 3). The CH_2Cl_2 layer obtained was again washed with deionized water (5 mL x 3) and dried over anhydrous sodium sulfate. The solvent was evaporated under reduced pressure and residue obtained purified via flash chromatography using EtOAc/hexanes 3/7 as eluent to afford **80** as an orange solid (102 mg, 79%) after solvent evaporation and drying. R_f = 0.4 (EtOAc/hexanes 3/7).

^{1}HNMR (300 MHz, $CDCl_3$) δ 7.13 (d, 1H, *J* = 4.7 Hz), 7.06 (d, 1H, *J* = 4.7 Hz), 7.02 (s, 1H), 5.96 (s, 2H), 3.76 (s, 3H), 2.59 (t, 2H, *J* = 4.2 Hz), 2.55 (s, 6H), 2.41 (m, 2H), 2.01 (s, 1H), 1.86 (t, 2H, *J* = 4.2 Hz), 1.46 (s, 6H); **^{13}C NMR** (125 MHz, $CDCl_3$) δ 156.2, 155.1, 142.5, 138.1, 131.8, 129.5, 126.0, 124.9, 123.7, 120.9, 114.1, 90.3, 83.4, 80.8, 69.1, 55.7, 27.5, 18.5, 17.7, 14.1; **MS (ESI)** m/z 445.27 $(M+H)^+$.

^{1}HNMR ($CDCl_3$)

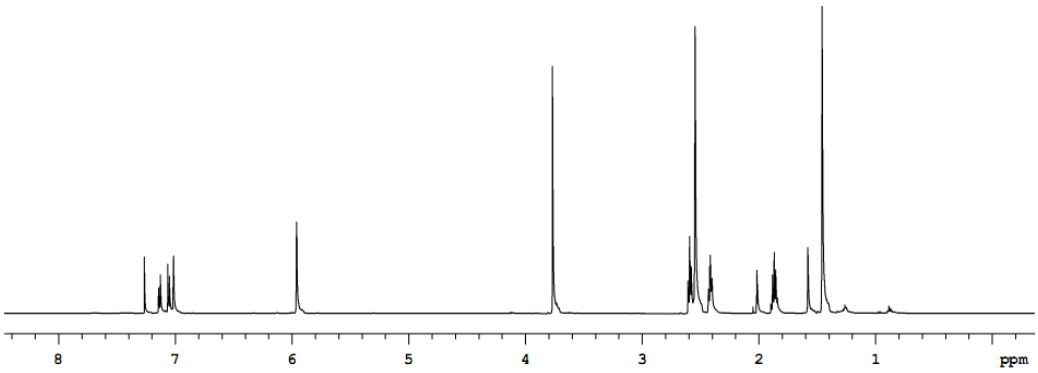

^{13}C NMR ($CDCl_3$)

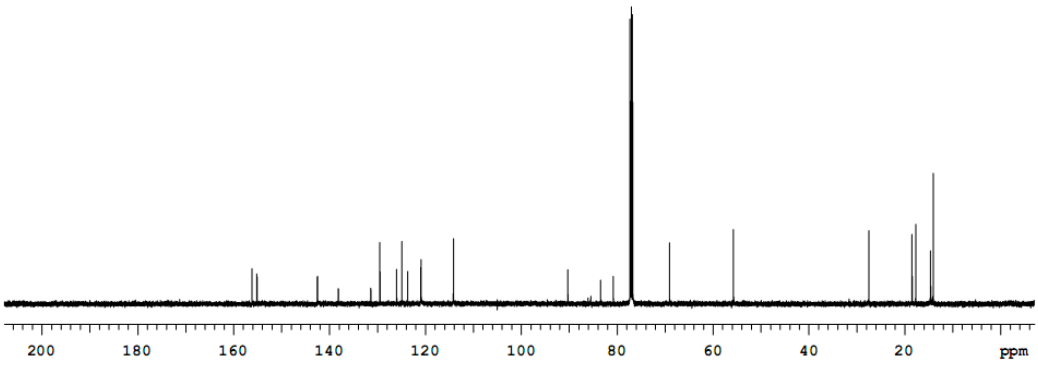

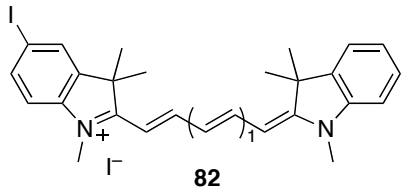

82

A solution of indolinium salt **81** (200 mg, 0.66 mmol) and *N*,*N*'-diphenylformamidine (206 mg, 0.80 mmol) in Ac_2O (2 mL) was heated at 120 ºC for 30 min. The reaction mixture was cooled to 25 ^{o}C and a solution of indolinium iodide **59** (393 mg, 0.92 mmol) in pyridine (2 mL) was added. The reaction mixture was stirred at 25 ºC for 30 min. Ether (25 mL) was added and the reaction mixture was filtered off to afford as dark blue solid. The residue was purified by flash chromatography eluting with 100 % EtOAc and 5 % to 10 % MeOH/CH_2Cl_2 to afford product **82** as a dark purple solid (189 mg, 45 %). R_f = 0.5 (10 % MeOH/CH_2Cl_2). **^{1}H NMR** (500 MHz, $CDCl_3$) δ 8.18 (br, 2H), 7.66 (t, 1H, *J* = 8.5 Hz), 7.60 (br, 1H), 7.49 (s, 1H), 7.40 (t, 1H, *J* = 8.5 Hz), 7.26 (br, 1 H), 7.17 (d, 1H, *J* = 7.6 Hz), 6.86 (br, 2H), 6.47 (d, 1H, *J* = 12.7 Hz), 6.25 (d, 1H, *J* = 12.7 Hz), 3.77 (s, 3H), 2.19 (s, 3H), 1.76 (br, 12H); **^{13}C NMR** (125 MHz, $CDCl_3$) δ 174.6, 171.3, 142.3, 141.5, 137.4, 137.1, 131.2, 131.0, 129.5, 128.8, 128.0, 125.8, 124.8, 122.5, 122.3, 114.0, 111.9, 110.9, 87.8, 49.7, 31.4, 29.7, 27.9, 27.2; **MS (ESI)** m/z 509.14 (M^+).

^{1}H NMR ($CDCl_3$)

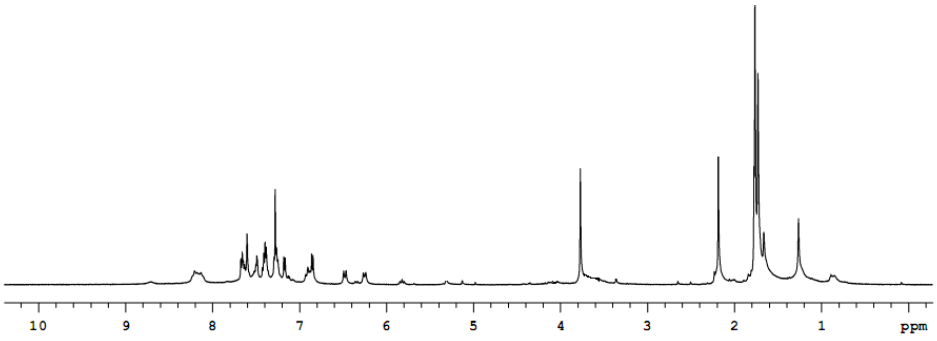

^{13}C NMR ($CDCl_3$)

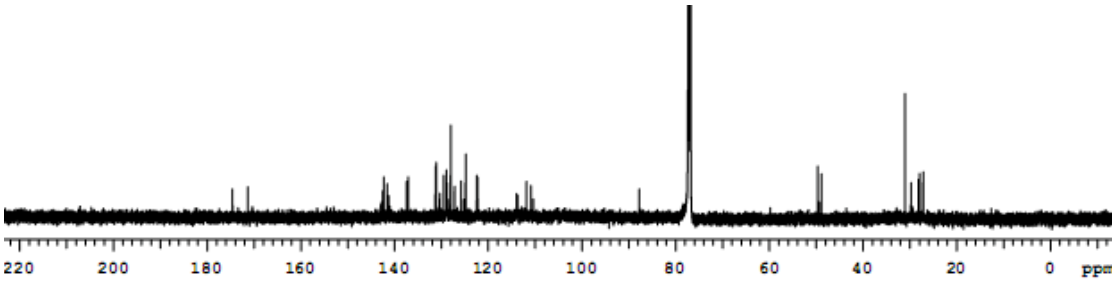

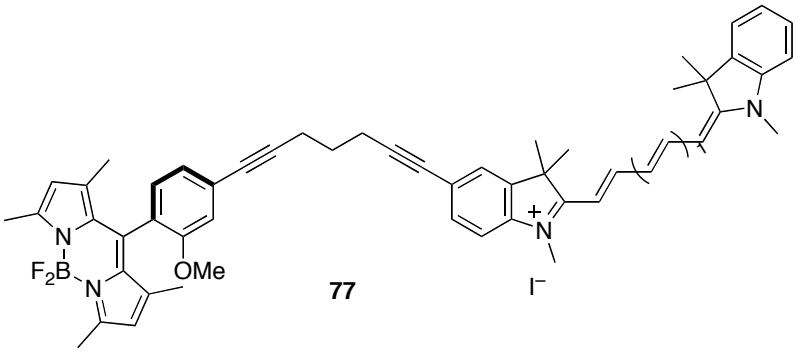

77

A solution of 5-iodo-Cy5 **82** (20 mg, 0.03 mmol), BODIPY **80** (30 mg, 0.07 mmol), $Pd(PPh_3)_4$ (7 mg, 0.006 mmol), CuI (1 mg, 0.006 mmol) in DMF (1.0 mL) was freeze-pump-thawed at –78 ºC (x 3 times). Et_3N (42 μL, 0.3 mmol) was added to a solution and the reaction mixture was stirred at 25 ºC for 12 h under nitrogen. Ether (20 mL) was added to a reaction mixture and reaction mixture was filtered off to afford product as a dark purple solid. The residue was purified by flash chromatography eluting with 100 % EtOAc and 10 to 30 % MeOH/CH_2Cl_2 to afford **77** as a dark purple solid (6 mg, 21 %) in 90 % purity. R_f 0.7 (10 % MeOH/CH_2Cl_2). **^{1}H NMR** (500 MHz, $CDCl_3$) δ 7.67 (br, 3H), 7.55 (d, 2H, J = 7.3 Hz), 7.48 (br, 3H), 7.08 (br, 4H), 6.82 (br, 3H), 5.97 (s, 2H), 3.78 (s, 3H), 3.65 (br, 3H), 2.66 (m, 2H), 2.55 (s, 6H), 2.35 (br, 2H), 2.18 (s, 3H), 1.82 (br, 2H), 1.71 (br, 12H), 1.47 (s, 6H); could not obtain carbon for this sample. **MS (MALDI)** m/z 825.46 (M^+).

^{1}H NMR ($CDCl_3$)

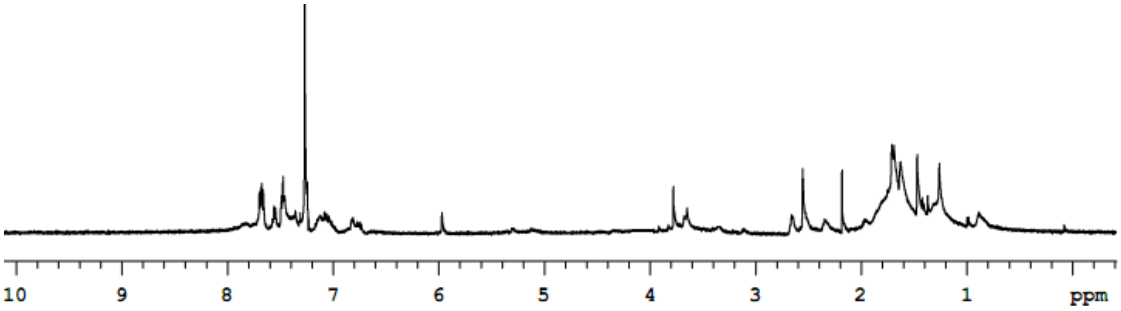

MS (MALDI)

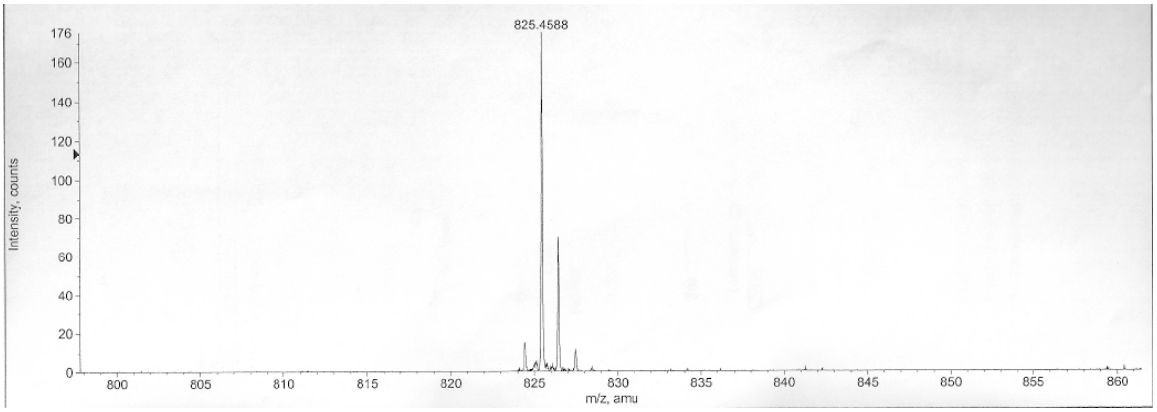

VITA

Name:		Jiney Jose
Permanent Address:		Department of Chemistry c/o Dr. Kevin Burgess Texas A&M University College Station, TX 77443-3255
Education:	2006-2009	Ph.D., Chemistry, Texas A&M University College Station, TX, U.S.A.
	2003-2006	M.S., Chemistry, Texas A&M University College Station, TX, U.S.A.
	1998-2002	B.Tech., Dyes & Intermediates, U.I.C.T. Mumbai, India
Experience:	2002-2003	Plant Manager (Trainee) Gharda Chemicals, Inc. Thane, India